Title
Shear Alfv&#65533;n Waves in Two-Ion Plasmas: Polarization, Dispersion, and Species Mix Diagnostic

Author
Robertson, Jeffrey Scott

Publication Date
2020

Peer reviewed|Thesis/dissertation

UNIVERSITY OF CALIFORNIA
Los Angeles

Shear Alfvén Waves in Two-Ion Plasmas: Polarization, Dispersion, and Species Mix Diagnostic

A dissertation submitted in partial satisfaction
of the requirements for the degree
Doctor of Philosophy in Physics

by

Jeffrey Scott Robertson

2020

ABSTRACT OF THE DISSERTATION

Shear Alfvén Waves in Two-Ion Plasmas: Polarization, Dispersion, and Species Mix Diagnostic

by

Jeffrey Scott Robertson
Doctor of Philosophy in Physics
University of California, Los Angeles, 2020
Professor Troy Carter, Chair

Understanding the physics of shear Alfvén waves in two-ion species plasmas, and the consequent interaction of the waves with the plasma, is important for explaining many observations in both laboratory and space plasmas. In this dissertation, the propagation and polarization of shear Alfvén waves in two-ion species plasmas is investigated under a wide range of conditions in the Large Plasma Device (LAPD) at UCLA. The primary motivation of this thesis is two-fold: (1) to quantify and understand the propagation and polarization of shear waves in two-ion plasmas, both theoretically and experimentally, and (2) to explore the shear wave's viability as a diagnostic tool in two-ion plasmas.

Waves are injected into a mixed helium-neon plasma using a magnetic loop antenna, for frequencies spanning the ion cyclotron regime. Two distinct propagation bands are observed, bounded by $\omega < \Omega_{Ne}$ and $\omega_{ii} < \omega < \Omega_{He}$, where ω_{ii} is the ion-ion hybrid frequency and Ω_{He} and Ω_{Ne} are the helium and neon cyclotron frequencies, respectively. Expanding on the work of previous authors [102], the ion-ion hybrid parallel cutoff frequency is systematically measured under a wide range of plasma conditions. A new diagnostic technique

and accompanying algorithm is developed in which the measured parallel wavenumber $k_{\|}$ is numerically fit to the predicted shear Alfvén wave dispersion in order to resolve the local ion density ratio. A major advantage of this algorithm is that it only requires a measurement of $k_{\|}$ and the background magnetic field in order to be employed. This diagnostic is tested on the Large Plasma Device (LAPD) at UCLA and is successful in yielding radially-localized measurements of the ion density ratio.

The polarization of shear waves in mixed helium-neon plasmas is investigated in detail, both theoretically and experimentally. While the lower frequency band's ($\omega < \Omega_{Ne}$) polarization is found to be in good agreement with a dispersion-based theory, the upper band ($\omega_{ii} < \omega < \Omega_{He}$) is found to be significantly more left-handed than theory or simulations predict. This behavior is observed using several different antenna configurations and a wide range of plasma conditions, showing that this feature is not unique to a given antenna geometry. The possibility of asymmetrical spatial damping is explored, but measurements show that the left-handed component of the upper band damps faster than the right, eliminating damping as a possible cause.

In order to better understand the effects of antenna geometry on wave coupling and polarization, an analytic model is developed for determining the electromagnetic field of a current-driven antenna immersed in a cold plasma. The model is numerically solved for both an electric dipole antenna as well as a magnetic loop antenna, and shows excellent agreement with previously published simulation studies. The mathematical model presented here may be advantageous over other methods, as it allows the user to solve parts of the problems analytically, thereby cutting down significantly on computation time.

The dissertation of Jeffrey Scott Robertson is approved.

Christoph Niemann

Walter Gekelman

George Morales

Stephen Vincena

Troy Carter, Committee Chair

University of California, Los Angeles

2020

To Katy. I wouldn't be where, or who, I am today without your unwavering love and support, and that is something I will forever be grateful for.

TABLE OF CONTENTS

LIST OF FIGURES

LIST OF TABLES

TABLE OF FREQUENTLY USED VARIABLES

Variable	**Name**	**Definition**
e	elementary charge	1.602×10^{-19} C
m_e	electron mass	9.109×10^{-31} kg
m_p	proton mass	1.673×10^{-27} kg
c	speed of light	2.998×10^{8} m/s
μ_0	permeability of free space	$4\pi \times 10^{-7}$ m·kg/C^2
ε_0	permittivity of free space	$1/(\mu_0 c^2)$
q_i	charge of ion species i	
Z_i	charge number of ion species i	q_i/e
m_i	mass of ion species i	
T_e	electron temperature	
B_0	background magnetic	
n_i	particle density of ion species i	particles/m^3
n_e	particle density of electrons	$\sum_{ions} Z_i n_i$ (quasineutral plasma)
f_i	fractional density of ion species i	$Z_i n_i / n_e$
Φ_p	plasma potential	
$v_{Th,s}$	Thermal speed of species s	$\sqrt{T_s/m_s}$
ν_e	Electron collision frequency	
I_{sat}	ion saturation current	
V_f	floating potential	
u_i	flow speed of particle species i	
Ω_{cj}	cyclotron frequency of species j[1]	$q_j B_0/m_j$
Φ_p	plasma potential	
ω_{pj}	plasma frequency of species j	$\sqrt{q_j^2 n_j/\varepsilon_0 m_j}$
$c_{s,i}$	sound speed of ion species i	$\sqrt{Z_i T_e/m_i}$

c_s	system sound speed	$c_s^2 = \sum_{ions} f_i c_{s,i}^2$
λ_{De}	electron Debye length	$v_{Th,e}/\omega_{pe}$
$\rho_{s,i}$	sound gyroradius of ion species i	$c_{s,i}/\Omega_{ci}$
ρ_s	system sound gyroradius	$\rho_s^2 = \sum_{ions} f_i \rho_{s,i}^2$
ω	frequency (rad/s)	
ω_{ii}	ion-ion hybrid frequency	$\omega_{ii}^2 = \frac{\omega_{p1}^2\Omega_{c2}^2 + \omega_{p2}^2\Omega_{c1}^2}{\omega_{p1}^2 + \omega_{p2}^2}$
ω_x	inertial Alfvén wave crossover frequency	$\omega_x^2 = \frac{\omega_{p1}^2\Omega_2^3 + \omega_{p2}^2\Omega_1^3}{\omega_{p1}^2\Omega_2 + \omega_{p2}^2\Omega_1}$
$k_\perp$	perpendicular wavenumber (rad/m)	
$k_\parallel$	parallel wavenumber (rad/m)	
κ	Spatial damping of wave	$\mathrm{Im}\left[k_\parallel\right]$
$\overleftrightarrow{\sigma}$	plasma conductivity tensor	
$\overleftrightarrow{\varepsilon}$	plasma dielectric tensor	$\overleftrightarrow{\varepsilon} = \overleftrightarrow{I} + (i\varepsilon_0\omega)\overleftrightarrow{\sigma}$
$\vec{E}$	electric field	
$\vec{J}$	current density	
S	ion polarization dielectric response (cold limit)	$S = 1 - \sum_s \frac{\omega_{ps}^2}{\omega^2 - \Omega_{cs}^2}$
D	$E \times B$ dielectric response (cold limit)	$D = \sum_s \frac{\Omega_{cs}}{\omega} \frac{\omega_{ps}^2}{\omega^2 - \Omega_{cs}^2}$
P	parallel dielectric response (cold limit)	$P = 1 - \sum_s \frac{\omega_{ps}^2}{\omega^2}$
L		$S - D$
R		$S + D$
n_j	refractive index in direction j	(ck_j/ω)
δ_e	electron skin depth	c/ω_{pe}
v_A	Alfvén speed	$v_A^{-2} = \frac{\mu_0}{B^2} \sum_{ions} n_i m_i$

$J_\nu(x)$	Bessel function, order ν	
$I_\nu(x)$	modified Bessel function, order ν	
$\zeta_{n,s}$		$\dfrac{\omega - n\Omega_{c,s}}{\sqrt{2}v_{Th,s}k_\parallel}$
ρ_j	Larmor radius of species j	$v_{Th,j}/\Omega_{c,j}$
λ_j		$k_\perp^2\rho_j^2$
$Z(\zeta)$	plasma dispersion function	See equation C.11

[1]This dissertation uses the "algebraic" form of the cyclotron frequency, meaning the electron cyclotron frequency is negative.

ACKNOWLEDGMENTS

I would first like to thank my advisor Professor Troy Carter, for his unbounding patience and support over the last six years. Even after all these years, I am still in absolute awe at his seemingly endless knowledge of plasma physics. It truly has been an honor to work under him, and in my time here I have come to know him not only as a mentor but also a friend. His enthusiasm for the field is contagious (rivaled only, perhaps, by his love of cycling and IPAs), and was warmly welcomed during the many times I was feeling beyond burnt out from the drudgery of grad school. To me he is the embodiment of what it means to be an accomplished physicist - the kind of physicist I aspire to be - and the last six years have been a privilege working under him.

A huge thanks must also be given to Doctor Steve Vincena, who in my many years here has basically become a second advisor to my work. Steve knows more about Alfvén waves and the inner workings of a lab than I could hope to learn in ten lifetimes, and I have benefited immensely from his guidance and feedback. Early on in my graduate career I identified him as someone I could bounce ideas off of, largely due to his down-to-earth and approachable demeanor, and I'm truly grateful for our countless discussions.

Thank you to the man who first taught me plasma physics, Professor George Morales, for the many years of wisdom and feedback on my work. You have always held me to a high standard, something which I grew to appreciate with time and have always strove to achieve.

Thank you to Professors Walter Gekelman and Christoph Niemann, for their time and feedback as my committee members.

Thanks to Zoltan Lucky, Marvin Drandell, Tai Ly, Avdit Kohli, and Patrick Pribyl for all their work and assistance in the lab. Anyone who has come through here knows that they are truly the life force of the lab, tirelessly working to keep everything up and running.

Thanks to Doctor Shreekrishna Tripathi for the many late night talks, and for always encouraging me to go home when I was working way later than any sane person rightfully

should.

Thanks to Meg Murphy for taking care of all the real life stuff, when I was simply too caught up with work. It takes a special kind of person to be able to take care of an office full of clueless physicists.

Thanks to Kunal Sanwalka, aka the lab's Petra-M guru, for all his help and patience with running Petra-M full wave simulations.

And thanks to the many graduate students, old and new, that have helped keep me sane over the years, of whom there are simply too many to individually credit. But a special thanks is owed to Giovanni Rossi for patiently guiding me through my first experiment ("is it righty-tighty or lefty-loosy?") and for all the subsequent years of teaching me the ins and outs of the lab. And thanks to Shawn Tang for her friendship over the years, and for always being a much needed source of laughter and positivity.

VITA

2008–2012 B.S. Mechanical Engineering
B.S. Physics
Loyola Marymount University, Los Angeles, CA

2013–2020 Graduate Researcher
Department of Physics and Astronomy
University of California, Los Angeles

PUBLICATIONS

J. Robertson, T. A. Carter, and S. T. Vincena. Propagation of shear Alfvén waves in a two-ion plasma and application as a diagnostic for the ion density ratio. *Journal of Plasma Physics*. Accepted May 2020.

J. Robertson, T. A. Carter, and S. T. Vincena. Polarization of Shear Alfvén Waves in a Two Ion Plasma. *Journal of Plasma Physics*. To be submitted May 2020.

J. Robertson. Semi-Analytic Model for the Electromagnetic Field of a Current-Driven Antenna in a Cold, Magnetized Plasma. *Journal of Plasma Physics*. Accepted March 2020.

CHAPTER 1

Introduction, History, and Motivation

1.1 Alfvén Waves in Multi-Ion Species Plasmas

In 1942, a groundbreaking paper by Swedish physicist Hannes Alfvén predicted the existence of an *electromagnetic-hydrodynamic* wave which may propagate in a magnetized plasma [2]. It was speculated that these *Alfvén waves*, as they would soon be called, could be responsible for many observed astrophysical phenomena, such as the migration of sunspots in the sun's photosphere. Alfvén waves were first successfully created in a laboratory environment in 1949 [67], and have since been observed in countless laboratory and space plasmas. It is now understood that Alfvén waves play a central role in the transport of electromagnetic energy in magnetized plasmas, as well as communicate information about the currents and fields within it [38]. Alfvén waves typically exist at frequencies well below the ion cyclotron frequency, and can be separated into two distinct modes - namely, the compressional and shear waves. In the low frequency limit, shear wave energy propagates along the background magnetic field lines while the energy of the compressional wave radiates outward in a sphere from its source [22]. The majority of this dissertation is concerned with the physics of the shear wave.

1.1.1 In Space Plasmas

Alfvén waves exist pervasively throughout nature, and have been observed in both the solar wind and magnetosphere. Magnetohydrodynamic waves were first observed in the inter-

planetary medium in 1962 by the Mariner 2 spacecraft [58, 59], and a few years later were confirmed to be consistent with the predicted behavior of Alfvén waves made nearly two decades earlier [12, 99]. The observed Alfvén waves in the solar wind follow a Kolmogorov power-law type spectra [63], which is a typical feature of turbulent fluids, and so are often referred to as *Alfvénic turbulence*. Much of the literature tends to agree that the source of Alfvénic turbulence originates near the sun, although there are still many unanswered questions regarding the underlying mechanism that gives rise to these Alfvén waves [108]. Some observations have suggested that the resonant absorption of ion-cyclotron waves with their respective species may act as a significant source of heating and acceleration in the corona and solar wind [9]. This means that the inclusion of additional ion species, even just as a minority species, may have a significant impact on the resulting dynamics of the solar wind. This was supported by numerical simulations of Alfvén waves in the solar corona, with minor ion species of O^{5+} and He^{++}, which also linked the resonant interaction of minority ion species to the power law spectrum of the Alfvénic turbulence [109] in the solar wind. Therefore a better understanding of the behavior of Alfvén waves in multi-ion species plasmas may play a pivotal role in understanding both the generation and dynamics of turbulence in the solar wind.

In 1958, the scientific community discovered the existence of two radiation belts in the earth's upper atmosphere - now known as the upper and lower Van Allen radiation belts [98]. The radiation belts are formed by the interaction of the solar wind with the earth's magnetosphere. The earth's magnetic field lines "pinch" on either pole of the planet, effectively forming a "magnetic mirror" which traps particles within them. The resulting trapped particles collectively act as a magnetized plasma, and are able to facilitate the propagation of various types of plasma waves. One example of such a wave that has been studied in great detail is the *Electromagnetic Ion Cyclotron* (EMIC) wave, a type of plasma wave which propagates along the magnetic field at frequencies just below each ion cyclotron frequency. When particles move along the field with a speed equal to the phase velocity of the wave,

they will undergo particle-wave interactions which may result in an exchange of momentum and energy, leading to particle scattering as well as growth or damping of the wave [97]. Every new ion species introduced to the plasma creates an additional cutoff frequency, which resides between the two ion cyclotron frequencies. The precise location of the cutoff frequency is determined by the relative mixes of the ion species, meaning the phase velocity of the wave is sensitive to the precise ion mix of the plasma. Therefore precise knowledge of the ion composition plays a critical role not only in the dispersion and phase velocity of the wave, but also in its resonant interactions with energetic particles.

1.1.2 In Burning Tokamak Plasmas

The understanding of Alfvén waves in multi-ion species plasmas is also important in the context of burning tokamak reactors, which typically consist of mixtures of deuterium and tritium. Alfvén waves are naturally occurring in tokamaks, and play a large role in turbulence and transport. It is understood that shear Alfvén waves in a tokamak can be spontaneously driven by the free energy of superthermal energetic particles [45]. Due to the periodic nature of a toroid's geometry, a tokamak will only permit a discrete set of parallel wavelengths for the shear wave. Two common manifestations of this effect are the Global Alfvén Eigenmode (GAE) and Toroidal Alfvén Eigenmode (TAE). The latter has been observed to be detrimental to overall particle confinement, sometimes leading to catastrophic consequences [107]. Therefore a better understanding of the basic physics of shear waves in multi-ion plasmas is of fundamental importance in furthering our understanding of turbulence and transport in tokamaks, so that greater levels of particle confinement may be achieved.

Compressional Alfvén waves have been explored extensively in tokamaks, largely as a potential heating scheme. Previous theoretical works have shown that significant particle-wave interactions are expected to occur near the ion cyclotron frequencies, as well as their harmonics, resulting in substantial energy absorption [93, 76]. This method of energy absorption has been investigated in great detail at the fundamental cyclotron frequency [83], as

well as at higher harmonics. Second harmonic ion cyclotron radio frequency (ICRF) heating is intended to be used on the International Thermonuclear Experimental Reactor (ITER) when it goes live, by targeting the second cyclotron harmonic of tritium. ICRF heating has the two-fold advantage of being able to preferentially heat the ions, as well as being able to penetrate into and heat the core of the plasma. There are still many challenges to overcome, which are outside the scope of this dissertation, but ICRF heating remains an active area of research in the quest for nuclear energy.

1.1.3 The Ion-Ion Hybrid Frequency (ω_{ii})

It can be shown from the basic plasma physics theory that each new ion species introduced to the plasma brings with it an additional resonance and cutoff frequency with it. For a plasma with two ion species, there exists a resonance frequency for waves which propagate across the field, known as the *ion-ion hybrid frequency*, or ω_{ii}:

$$\omega_{ii}^2 = \frac{\omega_{p1}^2\Omega_{c2}^2 + \omega_{p2}^2\Omega_{c1}^2}{\omega_{p1}^2 + \omega_{p2}^2} \tag{1.1}$$

Where ω_{pj} and Ω_{cj} are the plasma frequency and ion cyclotron frequency, respectively, of ion species j. The ion-ion hybrid frequency is unique to a plasma with two ion species, and always exists between the fundamental ion cyclotron frequencies of the two species. At the ion-ion hybrid frequency, the ion polarization currents of the two ion species oscillate π out of phase while the electrons remain relatively stationary - similar to the mode of a two spring system. Because of this, ω_{ii} resonance has been explored as a potential ion heating scheme in D-T tokamaks [16, 76]. Even outside the context of tokamak heating, the ion-ion hybrid frequency has a direct impact on the dispersion properties of Alfvén waves, and so it is in the interest of nuclear and space physicists alike to better understand the behavior of waves at these frequencies.

1.1.4 The Motivation for ω_{ii} as a Diagnostic

In laboratory plasmas with low enough energy densities, where direct measurements by probes is possible, the time-honored method of measuring local plasma density has been via the *ion saturation current*. When an electrode is inserted into a plasma, it will draw a current from the plasma - the magnitude of which can be determined by the underlying plasma physics equations. If a sufficiently low electrical bias is applied to the probe, the current response will consist entirely of ions. There is an upper limit to this current, which is determined by the thermal distribution of the ions, meaning increasingly lower voltages won't draw additional current.

An expression for the ion saturation current can be derived by considering the physics of sheath formation around an electrostatic boundary. When an electrode is immersed in a plasma, one might naively think that the potential of the electrode would change to match the surrounding plasma potential Φ_p. In actuality, the increased mobility of the electrons (with respect to the much heavier ions) results in the electrode finding an equilibrium voltage that is lower than the surrounding plasma potential - this equilibrium point is commonly known as the *floating potential*. This results in a positively-charged "sheath" which forms around the electrode, shielding the quasineutral plasma from the negative potential of the electrode. It can be shown [80] that the formation of a sheath is only possible if ions enter the sheath at a velocity approximately equal to the ion sound speed $c_s = \sqrt{T_e/m_i}$. Therefore a crude expression for the ion saturation current I_{sat} in a single ion species plasma can be expressed as follows:

$$I_{sat} = A_{eff} q_i n_i \sqrt{\frac{T_e}{m_i}} \tag{1.2}$$

Where A_{eff} is the effective area of the probe tip. Since I_{sat} is proportional to the ion density n_i (and, by virtue of quasineutrality, n_e), it provides a robust method for measuring plasma density. Equation 1.2 comes from what is known as the *Bohm criterion*. The situation

of sheath formation becomes more complicated when more than one ion species is present, however. The generalization of the Bohm criterion to multi-ion species plasmas has been explored in great detail [10, 32], as well as the specific case of two ion species [66]. In weakly-collisional plasmas, the generalized Bohm criterion can be expressed as:

$$\sum_i \frac{n_i}{n_e} \frac{c_{si}^2}{u_i^2} \leq 1 \tag{1.3}$$

Where $c_{si} = \sqrt{T_e/m_i}$ and u_i are the sound speed and fluid flow speed, respectively, of ion species i. Therefore we run into a problem when more than one ion species is present, as the Bohm criterion alone does not give a closed form expression for the ion saturation current.

As mentioned previously, the ion-ion hybrid frequency is a resonance frequency in two-ion species plasmas for cross-field propagation. It can be shown that, for shear waves with large $k_\perp$, it also doubles as a *cutoff* frequency. This lends motivation as a diagnostic tool, since equation 1.1 can alternatively be expressed as:

$$\frac{\omega_{ii}}{\Omega_2} = \sqrt{\frac{1 + \dfrac{m_2}{m_1}\dfrac{n_2}{n_1}}{1 + \dfrac{m_1}{m_2}\dfrac{n_2}{n_1}}} \tag{1.4}$$

Therefore, if one can measure ω_{ii}, they would be able to determine the ratio of ion densities n_2/n_1. This information could then be used in conjunction with another diagnostic, such as the ion saturation current, to resolve the density profiles of each individual ion species. For tokamak physicists, knowledge of the ion density ratio is valuable in its own right, as the fuel efficiency of nuclear reactions as well as overall plasma confinement is sensitive to the ratio of deuterium and tritium [26, 27].

Previous experiments on shear wave propagation in the Large Plasma Device (LAPD) have noted the existence of a cutoff frequency between the two ion cyclotron resonances. A theoretical analysis of Cherenkov radiation in two-ion species plasmas demonstrated that the shear wave is separated into two propagation bands, with the upper band being bounded

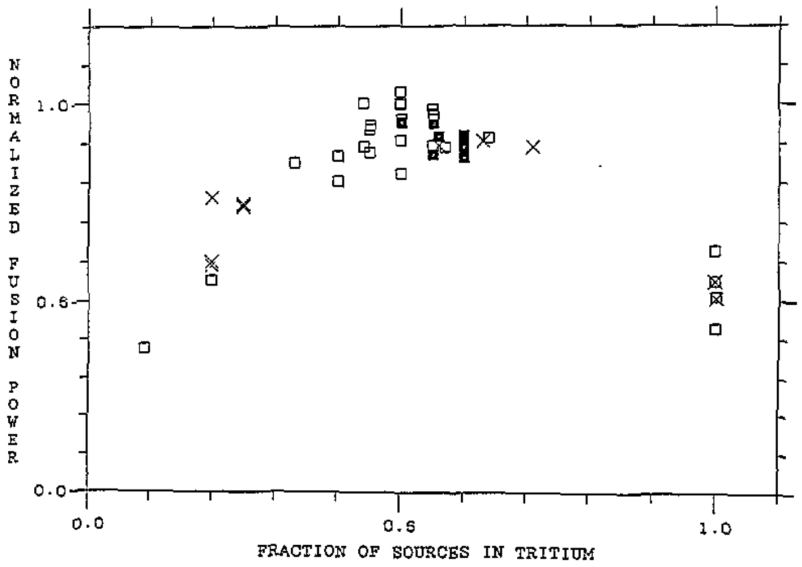

Figure 1.1: Fusion power of a D-T plasma as a function of the fractional beam energy of tritium, in the Tokamak Fusion Test Reactor (TFTR). [26].

by the ion-ion hybrid cutoff frequency [29]. A propagation gap was previously observed in the power spectrum of a helium-neon mixed plasma, whose cutoff frequency was found to scale consistently with the ion mix ratio and background field [103]. Theoretical modeling predicted the propagation gap to fill in with increasing ion temperature, due to finite ion Larmor radius (FLR) effects, which would make it more difficult to resolve the precise bounds of the gap [30]. The spatial pattern of the wavefront was also measured and compared to previous studies on the spatial structure of shear Alfvén waves in single ion species plasmas [39]. Another experiment was able to successfully create an "ion-ion hybrid Alfvén resonator" in the LAPD by exploiting the fact that ω_{ii} is proportional to the background field [101]. By creating a magnetic well geometry, it was shown that particular eigenmodes of the shear wave became trapped in the well, which were consistent with theoretical models. This information has relevance in the physics of the magnetosphere, as the earth's magnetic field acts as a magnetic mirror and may excite particular Alfvén eigenmodes as a direct result of the ion-ion hybrid cutoff physics.

1.2 Outline of Dissertation

The layout of the rest of the dissertation is as follows. Chapter 2 discusses the details of the experimental equipment, including an overview of the LAPD as well as the various antennas and diagnostics used. In chapter 3, we develop an analytic framework for determining the radiation field emitted by current-driven antennas in a cold, magnetized plasma, and successfully use it to calculate the field due to a 1-D electric dipole antenna. In chapter 4, a new diagnostic technique and accompanying algorithm is developed in which the measured parallel wavenumber $k_{\parallel}$ of the shear Alfvén wave is numerically fit to the predicted shear Alfvén wave dispersion in order to resolve the local ion density ratio. This diagnostic is tested on the Large Plasma Device (LAPD) at UCLA and is successful in yielding radially-localized measurements of the ion density ratio. Finally, in chapter 5 we take a closer look at the polarization of shear Alfvén waves in a two-ion plasma, and show that while the lower band's polarization behaves as predicted from dispersion physics, the upper band is much more left-hand dominant than expected. It is shown experimentally that neither damping nor antenna coupling can adequately explain the observed left-hand dominance, and full wave simulations predict the upper band to be much closer to linearly polarized than what is observed.

With the exception of chapters 1 and 2, each chapter in this dissertation is based on a standalone publication of the respective subject matter, with the addition of some more detailed results that were otherwise too nuanced for the published papers. As such, each chapter is fairly self-contained, and has its own introduction and theory section which goes into more detail on the specific contents of that chapter. Chapter 6 gives an overarching summary of the entire thesis, as well as some concluding remarks and possible directions for future research.

CHAPTER 2

Experimental Methods

2.1 The Large Plasma Device (LAPD)

The experiments described in this dissertation were performed in the Large Plasma Device (LAPD), a linear plasma research device located at the Basic Plasma Science Facility (BaPSF) at UCLA. The device, which was originally built in 2001, consists of a cylindrical stainless steel vacuum vessel, approximately 20 meters in length and 1 meter in diameter. The chamber contains over 360 radial ports along the machine, of varying size and shape, so that it can accommodate a wide variety of plasma probes and diagnostics. In any discussion involving Cartesian coordinates, the z direction is always assumed to point along the background magnetic field, whereas the y direction points in the vertical direction (away from the floor).

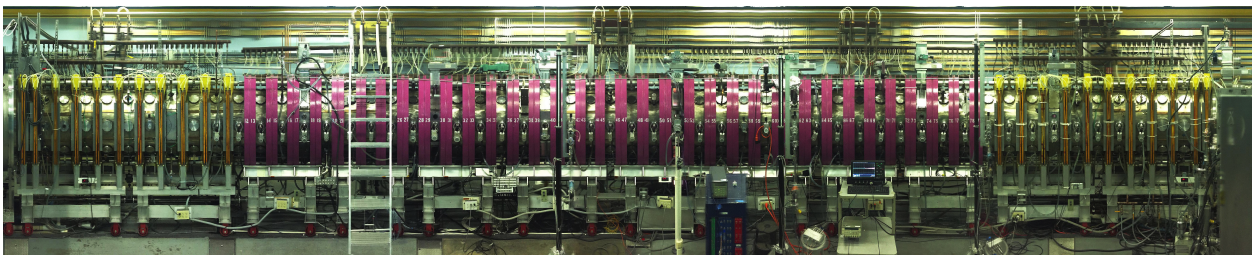

Figure 2.1: Panorama of the large plasma device (LAPD).

2.1.1 Plasma Creation

The LAPD has two plasma sources, capable of achieving different temperature and density regimes. Both plasma sources consist of a heated cathode and mesh anode, and rely on the principle of thermionic emission to produce a stream of free-flowing electrons in order to ionize the gas within the chamber and create a plasma. The barium oxide (BaO) cathode consists of a 60 centimeter nickel substrate and is coated with a thin layer of BaO ($\sim 50\ \mu m$) in order to boost the cathode's emissivity [35]. A 50% transparent molybdenum mesh anode is located 50 cm away, and a DC voltage of 40 - 70 V is applied between the anode and cathode. The cathode is heated up to around 900° C, resulting in a stream of primary electrons which are emitted off the surface. Approximately half of the streaming electrons pass through the mesh anode, ionizing the gas throughout the rest of the chamber. The BaO cathode is capable of achieving plasma densities on the order of $10^{10} < n < 2 \times 10^{12}\ cm^{-3}$ and electrons temperatures on the order of $T_e \sim 5\ eV$.

A second plasma source exists on the opposite end of the chamber, and consists of a 20 cm × 20 cm square lanthanum hexaboride (LaB_6) cathode and similar molybdenum mesh anode. The LaB_6 cathode is maintained at 1850° C for maximum emission, and is capable of producing much hotter and denser plasmas ($n_{max} \sim 3 \sim 10^{13}\ cm^{-3}$ and $T_e \sim 12\ eV$). Both plasma sources are backed by their own respective power supplies, which consist of a discharge capacitor bank that is triggered by a series of transistor switches. The switch is configured to discharge at a rate of 1 Hz (although this can be changed by the experimenter), and lasts up to 15 ms. The resulting plasma is highly reproducible from shot to shot, granting the experimenter the ability to take detailed spatially-resolved measurements of the plasma that would otherwise not be possible. Figure 2.3 shows a typical time trace of the discharge current and resulting plasma density from the BaO cathode.

A gas feed system is installed in the center of the machine, capable of supplying the chamber with steady rates of hydrogen, helium, neon, and argon. Each gas is connected

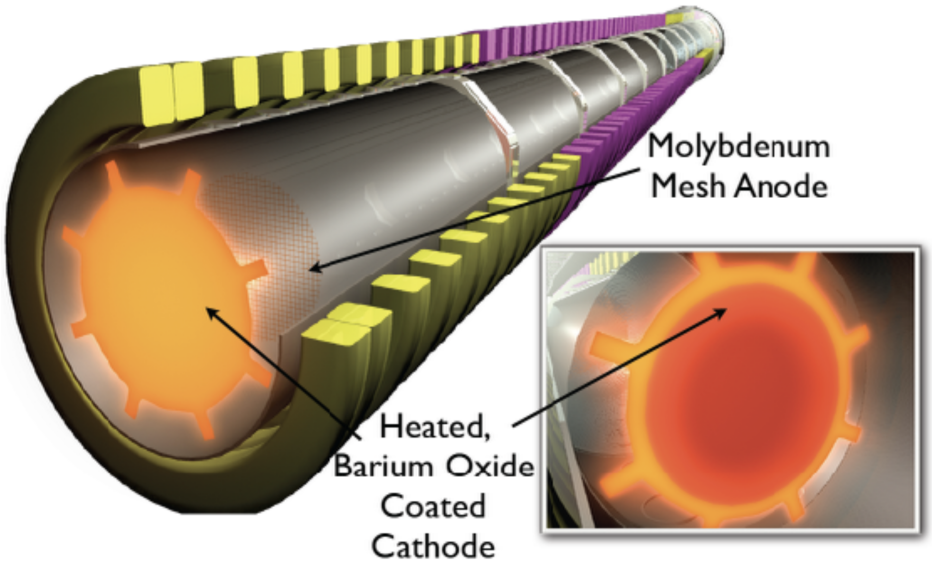

Figure 2.2: CAD model of the BaO-coated cathode and molybdenum mesh anode. The cathode is heated up to 900° C and electrons are released via thermionic emission. A fraction of the electrons pass through the mesh anode, ionizing the neutral gas throughout the rest of the chamber.

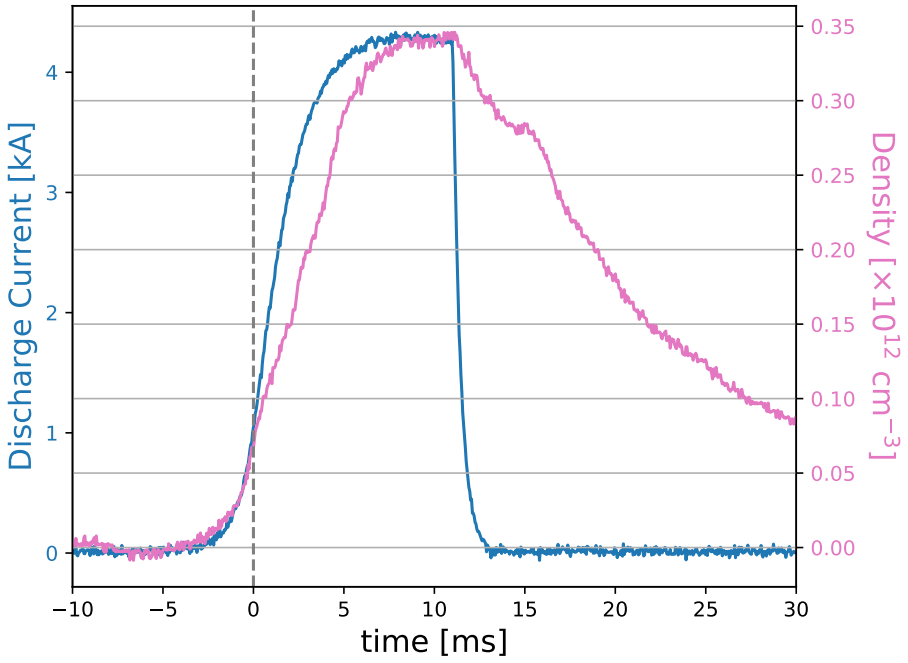

Figure 2.3: Discharge current vs. time for the BaO discharge, and the resulting plasma density vs. time. Density data is a line-integrated average taken from an interferometer about 15.5 meters from the cathode. The "t=0" trigger for the machine begins when the discharge current exceeds 1 kA.

to its own mass flow controller (MFC), allowing the experimenter to precisely control the gas mix, and the partial pressures of each gas is measured using a residual gas analyzer (RGA). Many of the experiments in this dissertation explore the behavior of Alfvén waves for various mix ratios of helium and neon. The neutral pressure ratio is frequently used as a proxy for estimating the ion density ratio of the plasma. Although it is not assumed (or even expected) that these two quantities be equal, it serves as a satisfactory reference point for investigating different ion mixes.

2.1.2 Magnetic Field

The cylindrical chamber is surrounded by 56 electromagnetic coils, and are powered in steady state in order to create a highly uniform axial magnetic field ($\delta B/B < .5\%$) within the chamber. The magnets are powered in parallel by seven independent power supplies, allowing axial variation of the magnetic field if desired (such as in magnetic mirror experiments [104, 105]). The LAPD is capable of producing magnetic fields ranging from 50 G – 2 kG. The upper bound is limited by the heat generation of the coils, whereas the lower bound is limited by the gyroradius of the confined ions (i.e. if the Larmor radius becomes comparable to the diameter of the vacuum vessel, the plasma becomes effectively unmagnetized).

2.1.3 Data Acquisition

There are two overarching data acquisition systems used by the LAPD. The first one, dubbed the "housekeeper", is connected to a variety of global diagnostics and sensors which are constantly monitoring the machine/plasma. The primary purpose of the housekeeper is to provide a general overview of the LAPD and contained plasma, as well as monitor the health of the machine in order to protect it from damage. Examples of data recorded by the housekeeper include interferometer time traces available at various axial positions (as seen in figure 2.3), magnetic coil currents and temperatures, and RGA readings of the neutral

fill pressure. Various safety switches are programmed into the housekeeper, so that different parts of the machine will be shut off automatically in order to prevent damage to the machine in the event something goes wrong.

The second data acquisition system, dubbed the "DAQ", is responsible for the acquisition of data collected by diagnostics that are specific to a given experiment. Analog data is collected from a given probe, in the form of a voltage between ± 2.5 V. This voltage is then read across an internal 50Ω resistor in the DAQ, and digitized at a rate of up to 10^8 samples/second. Data is typically digitized for part or all of the length of the plasma pulse, and this is repeated for as many shots of the plasma as desired. The DAQ contains 32 channels (4 boards, 8 channels each), allowing the simultaneous measurement/digitization of up to 32 diagnostics in parallel. The process is automated by custom in-house software (written in LabVIEW) so that data can be automatically acquired without the physical presence of the experimenter. Data is stored in a Hierarchical Data Format (hdf5) file on a local server, which can then be accessed remotely for subsequent data analysis.

2.2 Probes and Diagnostics

2.2.1 Magnetic Field (B-dot) Probe

Time-varying fluctuations in the magnetic field are measured using a three-axis magnetic induction probe, or B-dot probe for short. The probe utilizes Faraday's law to detect magnetic field fluctuations via the induced emf across a loop of wire. Each component of the probe contains two, oppositely wound twenty-five turn coils, whose signals are fed through a differential amplifier in order to subtract out any electrostatic pickup in the coils [28]. This is then done for three orthogonal loops, which are mounted on a 1 mm^3 polymer cube, to measure all three vector components of the field. Since the measured emf is proportional to $\partial_t B$, the signal must be integrated to get $B(t)$ - this is most easily done in the frequency domain, where $\partial_t \rightarrow -i\omega$. The magnetic field fluctuations can be retrieved from the measured

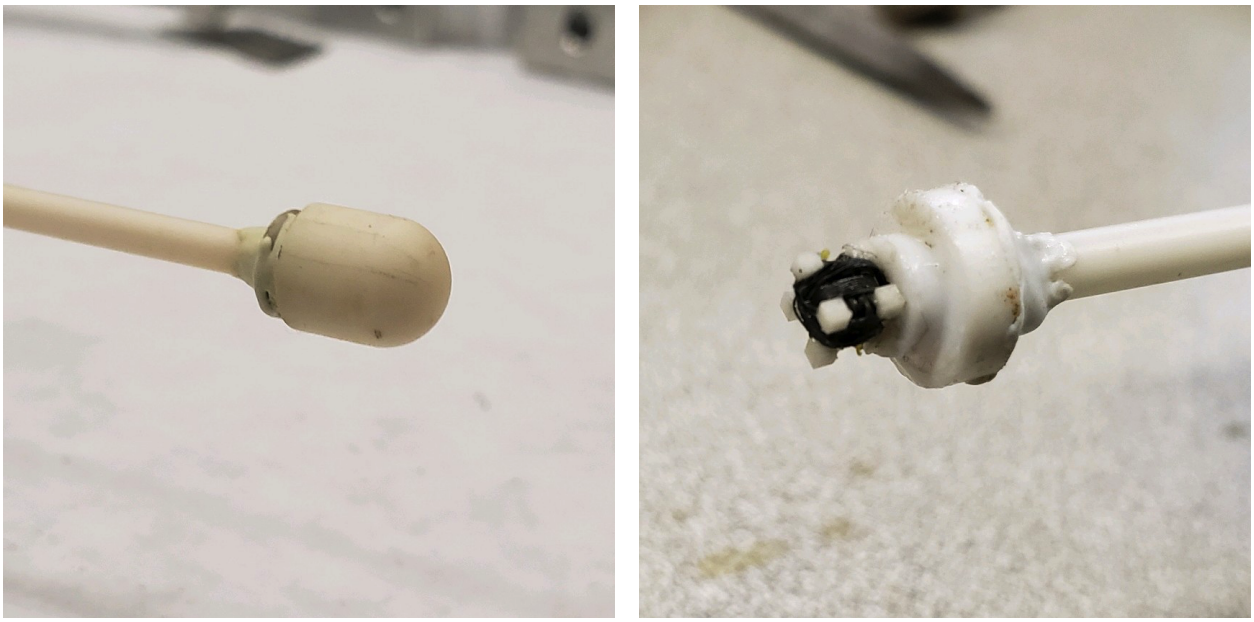

Figure 2.4: (Left) B-dot probe with insulating cap on. (Right) B-dot probe with cap removed, showing the 3 orthogonal loops of wire to measure the fluctuating magnetic field in three directions.

signal on the DAQ by the following expression[1]:

$$\tilde{B}(\omega) = -\frac{\tilde{V}_{DAQ}(\omega)}{i\omega ANg} \tag{2.1}$$

Where A is the area of the B-dot coil, N is the number of turns (typically 50 or 10), and g is the gain on the differential amplifier used. $\tilde{V}_{DAQ}(\omega)$ is the signal recorded by the DAQ, Fourier transformed into the frequency domain. Note that equation 2.1 ignores any modifications to the measured signal due to internal probe circuitry effects, which in practice must be accounted for at higher frequencies. A full circuit analysis of the internal workings of the B-dot probe (such as internal capacitance, self/mutual inductance, etc) can be found in a previous paper [28], and will not be covered here. Explicit knowledge of every internal

[1]Equation 2.1 assumes the convention $\partial_t \rightarrow -i\omega$, which is typical of plasma literature. Many forward FFT algorithms, however, use the opposite sign convention, in which case the negative of equation 2.1 would have to be used.

probe effect is not necessary, however, as the entire probe can be equivalently represented by a complex-valued impedance. The impedance of the probe can be accounted for in equation 2.1 by replacing the area A with a complex-valued "effective area" A_{eff}:

$$A_{eff}(\omega) = |A_{eff}(\omega)|\, e^{i\theta(\omega)}$$

The magnitude and phase of $A_{eff}(\omega)$ can be found empirically by creating a known magnetic field configuration and comparing the expected value to the value measured by the B-dot probe. This was done with a homemade Helmholtz coil, due to the uniformity of the field it creates. At higher frequencies ($>$ 1 MHz), the inductance of the Helmholtz coil begins to impact the current in the coil and reduces the sensitivity of this calibration method, although we are generally at low enough frequencies where this isn't an issue. The Helmholtz coil and B-dot probe are connected to a network analyzer, which reads out the magnitude M (in dB) and phase θ of the B-dot signal relative to the input signal. Using the known expression for the magnetic field at the center of a Helmholtz coil, an expression can be derived to find A_{eff} from the network analyzer readout:

$$A_{eff}(\omega) = \left(\frac{5}{4}\right)^{\frac{3}{2}} \frac{rR_H \times 10^{\frac{M}{20}}}{\mu_0 n N \omega g_H} e^{i\theta} \tag{2.2}$$

Where r, R_H, and n are the radius, resistance, and numbers of windings in the Helmholtz coil, respectively, N is the number of windings in the B-dot probe, and g_H is the gain of the differential amplifier used in the calibration. It's important to note that the signals outputted from the two windings of the B-dot probe must go through the same length of cables to the network analyzer, otherwise there will be a phase mismatch between the two that will give an erroneous contribution to θ.

2.2.2 Langmuir Probe

The Langmuir probe is one of the most common diagnostics used in laboratory plasma experiments, due to both its simplicity and versatility. The most basic type of Langmuir probe works by inserting an electrode (such as a biased wire tip) directly into the plasma. The probe tip will draw a certain amount of current from the plasma, depending on the bias applied to it. Various physical properties of the plasma can then be inferred from the measured current and voltage, such as plasma potential (Φ_p), electron temperature (T_e), and ion density (n_i). Multiple probe tips can be combined in various configurations in order to measure additional plasma properties as well.

When a Langmuir probe is connected to a high impedance resistor ($\sim 1M\Omega$), very little net current is able to be drawn from the plasma. The plasma current consists of an ion and electron current, with the latter generally being much larger due to the electrons having a much higher thermal velocity. In order for the net current drawn into the probe to be zero, the potential of the probe tip will change in order to reach an equilibrium value where the ion and electron currents are equal and opposite. This value is known as the floating potential V_f. Assuming a Maxwellian plasma, V_f is related to the plasma potential Φ_p by the following expression:

$$V_f = \Phi_p - \frac{1}{2} T_e ln \left(\frac{2m_i}{\pi m_e} \right) \tag{2.3}$$

Where m_i and m_e are the ion and electron mass, respectively.

Next, suppose the Langmuir tip is connected to a much smaller resistor, which is then connected to earth ground. The drawn plasma current is no longer required to be zero, as it has a low resistance path to travel out. If a very large negative voltage is applied to the probe tip (several times greater than the electron temperature), then electrons will be repelled by the tip and only ions will be collected. This characteristic current is known as the *ion saturation current*, I_{sat}. The Bohm sheath criterion states that the formation of a

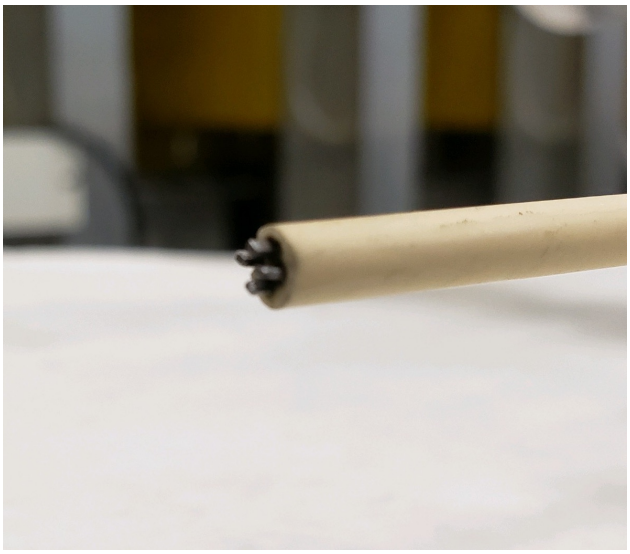

Figure 2.5: A Langmuir probe with 4 tips, which can be wired in parallel to make multiple measurements simultaneously.

sheath is only possible if ions enter the sheath at a velocity approximately equal to or less than the ion sound speed $c_s = \sqrt{T_e/m_i}$ [80]. For a plasma with one ion species, this gives a direct relationship between I_{sat} and the ion density n_i:

$$I_{sat} = A_{eff} q_i n_i \sqrt{\frac{T_e}{m_i}} \tag{2.4}$$

Where q and m_i are the ion charge and mass, respectively, and A_{eff} is the effective surface area of the probe tip. The reason *effective* area is used here is because a large bias will create a Debye sheath on the surface of the probe tip, effectively increasing its collection area. As long as the Debye length of the plasma is much smaller than the physical size of the probe tip, however, it is generally fair to assume $A_{eff} \sim A$.

In practice we are often interested in the fluctuating part of a given signal. If we separate each of the measurable plasma properties into their fluctuating and nonfluctuating components, we can expand equations 2.3 and 2.4 to first order to get the following expressions:

$$\begin{aligned} \delta V_f &\approx \delta\Phi_p - \frac{1}{2}\delta T_e ln\left(\frac{2m_i}{\pi m_e}\right) \\ \delta I_{sat} &\approx qAn_i\sqrt{\frac{Te}{m_i}}\left(\frac{\delta n_i}{n_i} + \frac{1}{2}\frac{\delta T_e}{T_e}\right) \end{aligned} \tag{2.5}$$

Where a δ denotes the fluctuating component of the variable that follows it. Assuming the relative size of temperature fluctuations are much smaller than the density fluctuations (i.e. $\delta T_e/Te \ll \delta n_i/n_i$), we can drop the δT_e term in the δI_{sat} expression. Therefore it is common to use ion saturation fluctuation measurements as a proxy for density fluctuations. Similarly, floating potential fluctuation measurements are typically used as a proxy for plasma potential fluctuations.

A crucial note must be made here that equations 2.3–2.5 are all derived from the Bohm sheath criterion, which assumes a single ion species. The situation becomes much more complicated when there are multiple ion species. This problem has been studied in detail [10, 32], including the specific case of a plasma with two ion species [66]. More information on the multi-ion Bohm criterion can be found in section 1.1.4. Despite this pitfall, physicists typically use V_f and I_{sat} fluctuations as proxies for Φ_p and n_i, respectively, even when multiple ion species are present.

2.3 Antennas

Antennas in plasmas rely on the same basic principle as traditional antennas - an interface is immersed in a dielectric medium, excited harmonically, and electromagnetic waves are radiated out. The complicated frequency response of the plasma dielectric (compared to, say, air) allows for a wide variety of modes and wave structures that would not be possible in any other material. The shape and excitation method of an antenna plays a significant role in the resulting radiation pattern emitted, and so different antennas find their niche in different areas of plasma physics. This section will explain the physical makeup, electronics, and operational use of the various antennas used in this dissertation.

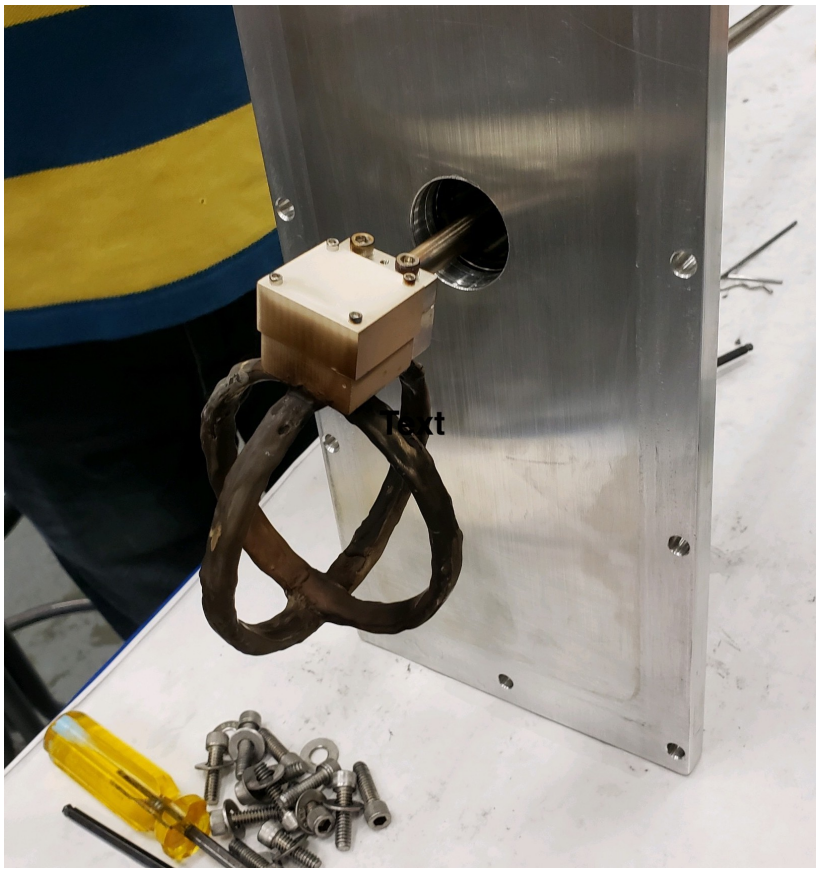

Figure 2.6: Rare shot of the RMF antenna outside of the machine. Two orthogonal coils are wired in parallel, so that elliptical waves with arbitrary polarization can be generated. The epoxy around the coils is blackened from months of ion bombardment.

2.3.1 Rotating Magnetic Field (RMF) Antenna

The rotating magnetic field (RMF) antenna was built and designed to study the propagation of circularly polarized shear Alfvén waves [41]. The antenna consists of two coils, each with three turns of .25 cm thick copper wire, and with diameters of roughly 8 and 9 cm. The coils are mounted orthogonal to each other (in LAPD coordinates, they lie in the XZ and YZ planes), with a coaxial current feed that enters the plasma from the top of the machine. The two coils are wired separately so that they can be driven independently from one another. The antenna coils are epoxied and electrically isolated from the plasma, so they rely on

inductively coupling to the plasma in order to excite waves. They are typically driven with equal magnitude sinusoidal waves, $\pm\pi/2$ out of phase, in order to launch left or right handed waves (see appendix A for a detailed description of circular polarization). For each coil, a low amplitude sinusoidal waveform is created by an Agilent waveform generator. The signal is then fed through an RF amplifier and the outputted current goes to the antenna. The Agilent can be connected to the local network where the user can remotely program a sequence of frequencies for the waveform to incrementally go through, allowing the experimenter the ability to systematically investigate a wide range of frequencies.

Many of the experiments in this dissertation used only the horizontal loop of the RMF antenna in order to excite waves, making it identical in functionality to a magnetic dipole (or loop) antenna.

2.3.2 Magnetic Dipole (Loop) Antenna

A smaller loop antenna was constructed and mounted on a radial probe drive, such that the propagation of shear waves could be investigated at various positions in the plasma. This antenna consists of a 2.5 cm diameter loop, containing three loops of insulated copper wire and oriented in the XZ plane of the LAPD. A picture of this antenna can be seen in figure 2.7.

2.3.3 Mesh Disk Exciter

The disk exciter is one of the most basic antenna designs, and similar designs have been used to investigate Alfvén wave propagation in the LAPD for over 25 years [72, 73, 38, 39]. Two identical disk exciters were fabricated for the purpose of this study, one of which can be seen in figure 2.8. Each exciter consists of a circular disk of stainless steel wire mesh (1 cm diameter, $\sim$ 1 mm thick, transparency $\sim$ 50%), spot welded to a stainless steel ring for structural stability. Mesh was chosen over a solid disk in order to allow the passage of

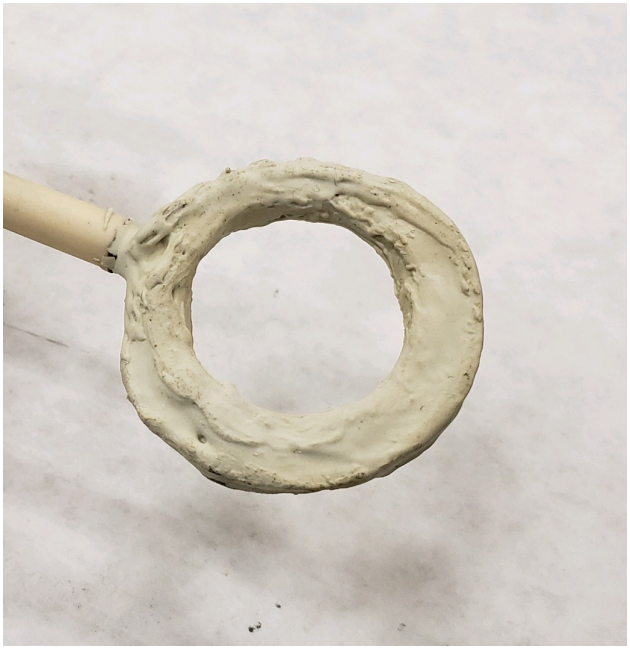

Figure 2.7: Magnetic dipole antenna, approximately 2.5 cm diameter, which can be mounted on a radial probe drive to launch Alfvén waves at different radial positions.

primary electrons from the cathode and minimize the effect of shadowing. The ring is spot welded to a thin steel rod that is surrounded by a ceramic shaft, such that the only part of the antenna in direct electrical contact with the plasma is the circular disk. The steel rod is then crimped to the inner conductor of a coaxial cable, with the outer conductor grounded to help mitigate any unwanted electrostatic pickup.

Since the disk is in direct electrical contact with the plasma, a carefully chosen DC bias should be applied (in addition to the AC signal) so that the disk is drawing a healthy balance of ion and electron currents. If the DC bias is too low, then the disk will only be drawing ion saturation current, and if the bias is too high, the disk can actually drain the connecting field lines of electrons. Figure 2.9 shows a typical circuit diagram for a single disk exciter. For the setup with two disk exciters (figure 2.10), the two disks are connected to both leads of the secondary coil, to ensure both signals are equal in magnitude and π out of phase. The DC bias is then center tapped onto the secondary.

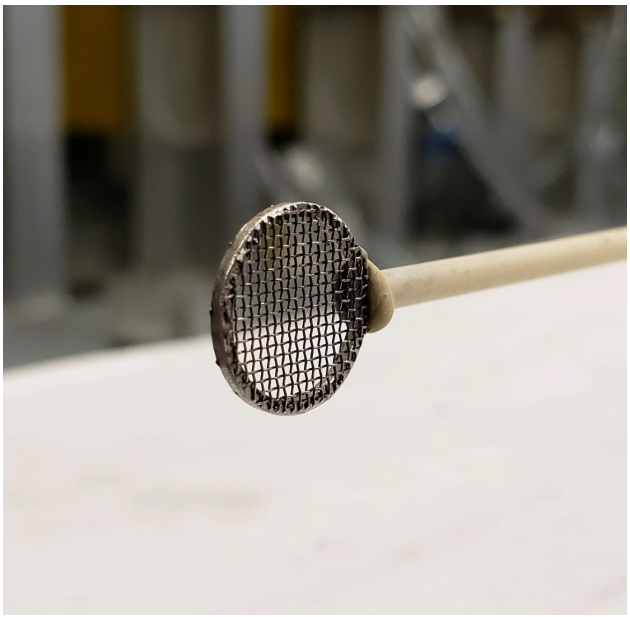

Figure 2.8: One of the two stainless steel mesh disk exciters used to launch shear Alfvén waves. The metal disk is in direct electrical contact with the plasma, allowing it to easily excite plasma currents.

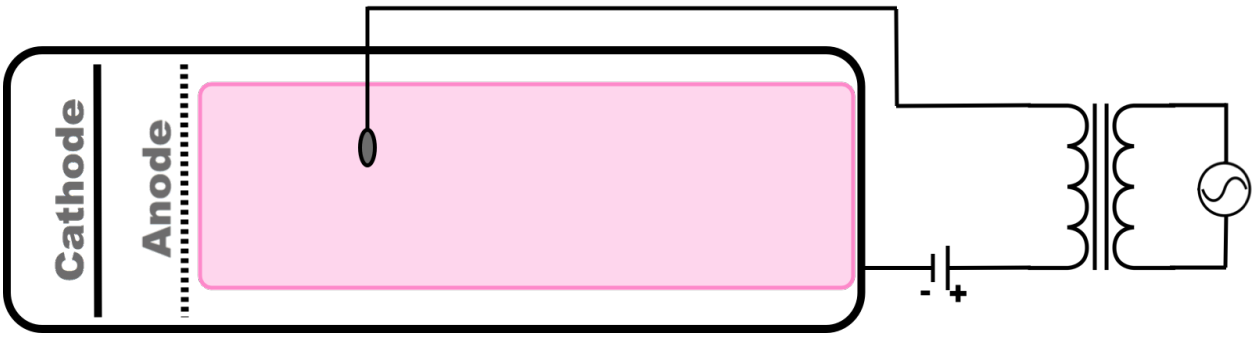

Figure 2.9: Schematic for a single disk exciter. The AC from the waveform generator goes through a 1:1 isolating transformer, so that a new ground bias can be designated on the outgoing side.

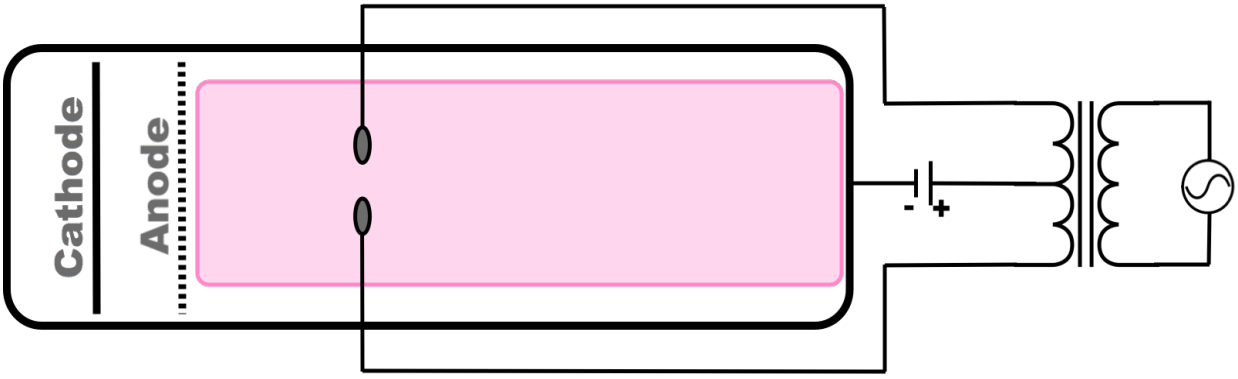

Figure 2.10: The two disks are biased against each other to ensure their resulting waveforms are equal and opposite. The DC bias is center tapped onto the secondary coil.

2.3.4 Square Disk Exciter

The square disk exciter consists of two mesh 1 cm^2 squares, separated by about half a centimeter. The antenna was rotated such that the normal of the plane pointed in the z direction. Both squares were driven by the same sinusoidal signal, making the antenna functionally identical to the mesh disk exciter but with different geometry. This antenna was originally designed and intended for investigating cross-field excitation by driving an oscillating voltage between the two and measuring the current response - hence the second, redundant mesh square. A picture of this antenna can be seen in figure 2.11.

2.3.5 Four Strap Antenna

A four strap antenna for studying fast waves was developed by TAE Technologies and installed in the LAPD. Four curved, horizontal copper straps can be seen in figure 2.12, which cup the edge of the plasma. Each of the four straps can be driven independently, allowing the experimenter to preferentially target certain values of $k_{\parallel}$ and granting them greater control over the desired waveform. Fast waves are typically launched at frequencies well above the ion cyclotron frequency, due to the fact that at low frequency the fast wave's dispersion relation demands cross-field wavelengths that are much greater than the size of the machine.

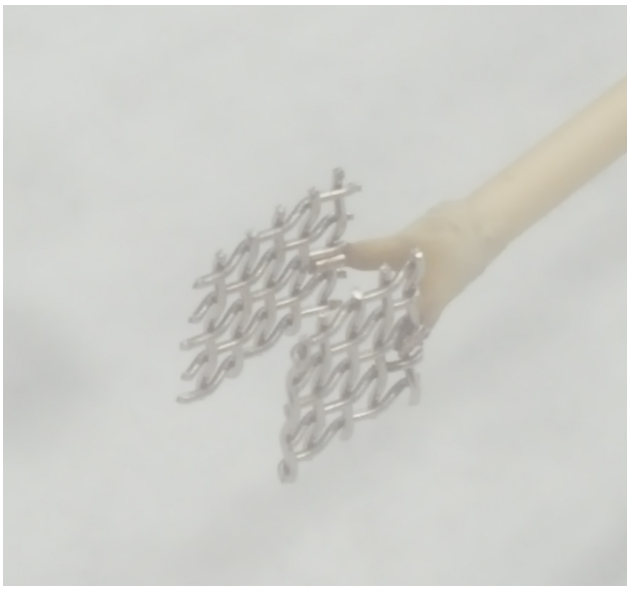

Figure 2.11: Antenna with two 1 cm^2 mesh squares, driven with the same alternating bias.

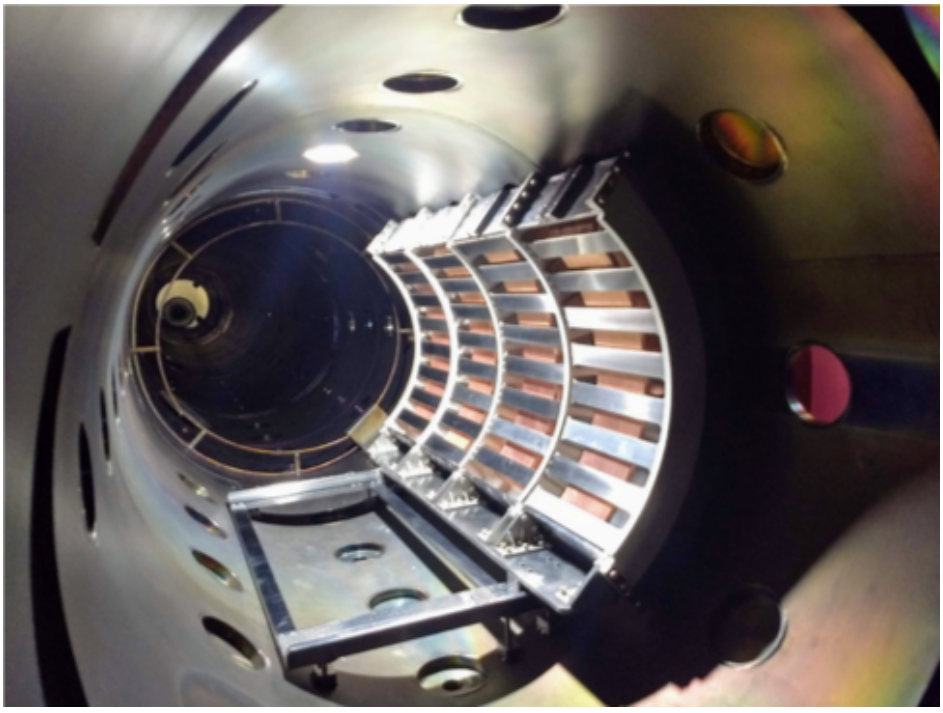

Figure 2.12: The four strap antenna developed by TAE Technologies to study fast wave propagation in the LAPD. Four copper straps can be seen, which are partially covered by a Faraday shield.

Motivated by investigations into the ion-ion hybrid frequency ω_{ii}, a single strap of the antenna was used to launch waves into the BaO plasma in the ion cyclotron regime. Fast wave coupling is extremely weak in this frequency band, but the antenna is capable of large enough currents that it can overcome the weak coupling and create a highly coherent wave nonetheless.

2.3.6 Directly vs. Indirectly Coupled Antennas

The antennas previously described fall into two distinct categories - those which are in direct electrical connection with the plasma, and those which rely on indirect coupling to the plasma (such as inductive or capacitive coupling).

Directly coupled antennas, such as the mesh disk and square exciters, rely on an electrode being in direct contact with the plasma. Assuming the antenna's external circuitry has an accessible ground path, the antenna is able to freely add or remove current from the plasma - essentially acting as an AC-driven Langmuir probe. The ability to directly excite plasma currents is great for easily exciting shear waves, but the drawback is that the waveform of the antenna current is susceptible to warping due to ion and electron saturation. In order to minimize this effect, the antenna should be DC biased such that it falls somewhere in the "middle" of the Langmuir curve, where the slope of the I-V curve is approximately linear. But even then, there is an upper limit to the maximum allowed amplitude of the wave, before the waveform becomes severely warped due to ion/electron saturation effects. Figure 2.13 shows the current response due to a sinusoidal voltage applied to the square mesh exciter, for two different input voltages. In both cases the plasma conditions are similar, and the only difference is one of the signals has a much greater applied AC voltage than the other. You can see in the case with the larger AC voltage that the current response becomes severely warped at the peaks. This is due to the fact that the amplitude of the applied voltage is so large it is beginning to sample both the electron and ion saturation regions of the Langmuir curve.

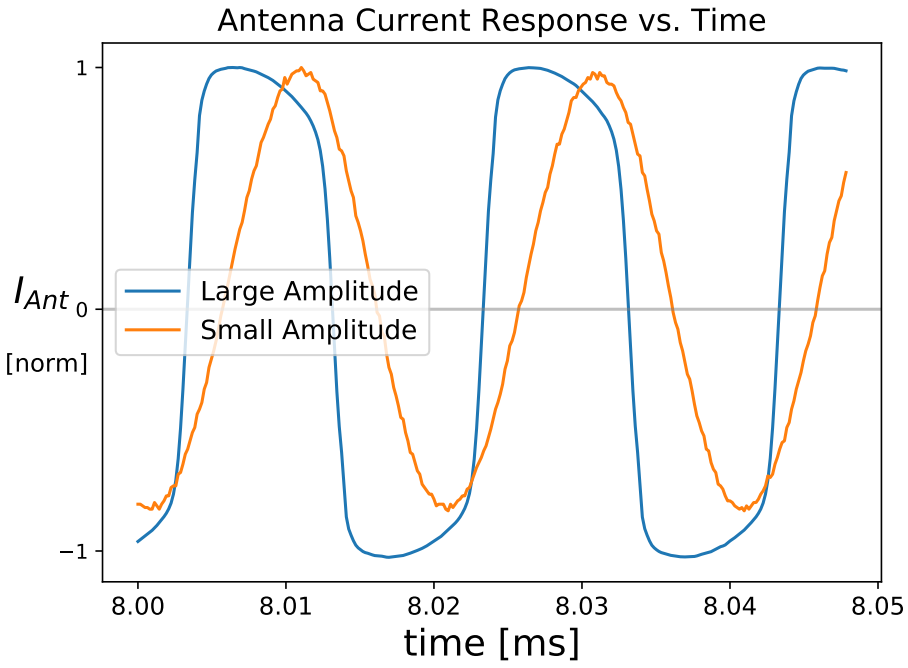

Figure 2.13: Current response vs. time of the square mesh exciter, for both small and large applied AC voltages. The larger bias results in warping of the current's waveform at the peaks, due to the limitations of ion (and electron) saturation.

Indirectly coupled antennas, in general, have much weaker coupling than electrostatic antennas. The trade-off is that since they don't draw any current from the plasma, they are not limited by the electron and ion saturation regions and are therefore capable of driving much larger amplitude waves.

CHAPTER 3

Semi-Analytic Model for the Electromagnetic Field of a Current-Driven Antenna in a Cold, Magnetized Plasma

In this semi-analytic study we develop a mathematical model for determining the electromagnetic field due to a current-driven antenna immersed in a cold, magnetized plasma, valid for frequencies below the electron plasma frequency. At every point in the plasma, it is shown that the vacuum electric field of the antenna couples to the plasma conductivity tensor and acts as an infinitesimal source term to drive plasma currents - the total field is then found from the aggregate sum of these point sources, which is expressed as an integral across the vacuum field. A general solution is provided for both azimuthally-symmetric cylindrical coordinates as well as a fully generalized Cartesian solution. As an example of how this general solution may be applied, we solve for the field due to an electric dipole antenna of length ℓ, aligned along the background field, at frequencies below the ion cyclotron frequency. It is found that the near-field decays exponentially with increasing $k_\perp z$, whereas the far-field exhibits wavelike behavior. The radiation zone exhibits propagation cones emanating from either end of the dipole, with a propagation angle that is consistent with past analytic studies of inertial Alfvén waves. The mathematical model presented here may be advantageous over other numerical methods, as it allows the user to solve parts of the problems analytically, thereby cutting down significantly on computation time, as well as offering physical insight into the system that may not be evident with other numerical solvers.

3.1 Introduction

Understanding the behavior and propagation of plasma waves is of fundamental importance in both laboratory and space plasmas. In laboratory plasmas, waves are a naturally occurring phenomena that arise due to various mechanisms, such as via superthermal energetic particles in tokamaks [45], although they can also be deliberately excited via external circuitry. There are many reasons one would want to excite plasma waves in a laboratory environment, although the two most common applications are for the purposes of plasma heating and diagnostics. As the exceedingly high energy densities found in the core of burning tokamak plasmas prevent direct diagnostic measurements, many fusion diagnostic tools rely on exciting waves along the edge of the plasma, and then inferring the various physical properties of the plasma from the resulting wave propagation. Some examples of this include laser interferometry [11] and Doppler reflectometry [49]. The predictive capability of antenna-based diagnostics is only as good as our understanding of the underlying physics, as well as our ability to effectively and accurately recreate the measured results in a simulated environment.

In general, plasma antennas fall into two major categories: those in direct electrical contact with the plasma, and those which rely on indirect (i.e. inductive or capacitive) coupling. Alfvén waves excited by direct coupling have been explored in great detail in the Large Plasma Device (LAPD) at UCLA [36], and was in fact one of the original motivations for the machine being built [35]. Early studies of shear (or slow) Alfvén waves used a small metal disk in order to drive plasma currents and excite waves [38]. In the inertial (cold) regime, the resulting wavefront was observed to emanate from the disk in a narrow conical pattern, mediated by electrons in the parallel direction and a smaller ion polarization current across the background field [40]. A theoretical companion paper, published around the same time, developed an analytic model for determining the spatial structure of inertial Alfvén waves launched by a metal disk exciter, and the predicted results were found to be in

good agreement with experimental measurements [72]. Similar experiments were later done in the kinetic regime using the same antenna [39], and the corresponding theoretical paper again agreed with the results [73]. Both theoretical models take the general solution to the azimuthally-symmetric cold plasma wave equation, and then use the boundary conditions imposed by the antenna (which can either be an equipotential or constant current surface) to uniquely determine the resulting spatial structure of the excited wave. While this methodology is successful for many simple antenna geometries, a generalization to this approach is desired for antennas which cannot be easily mapped to a set of straightforward boundary conditions.

Alfvén waves launched by inductively-coupled antennas have also been studied in detail, in both the lab as well as in simulations. The rotating magnetic field (RMF) antenna, originally designed to study circularly polarized waves, consists of two orthogonal loops of current-carrying wire [41]. Experimental results showed that the RMF antenna excited large parallel electron currents where the antenna's vacuum electric field pointed along the background field. Three dimensional simulations of the RMF antenna were performed, which used a linear two-fluid MHD spectral model, and the results were in good agreement with experiment [60]. A similar semi-analytical model for analyzing inductively-coupled waves was previously devised by [56] and used to model the behavior of RF power deposition in high-density plasma tools. Both of these theoretical models for inductively-coupled antennas are similar in that they treat the external antenna currents as a "source" term to the cold plasma wave equation, which is contrary to the strategy of boundary condition matching that was employed for the electrostatic disk exciter.

A vast array of numerical tools exist for simulating the behavior of plasma waves launched by various antennas. Many tokamak plasmas are adequately described by a single fluid MHD model, and so several ray tracing codes exist to map out wave propagation in this simple regime [90]. On the other end of the complexity spectrum, finite element [42] and full wave [48] models divide space and time up into a discrete grid (or mesh), and solve Maxwell's

equations incrementally to find the full spatial structure of the field. While these sort of calculations are generally very accurate, they can also be extremely computationally expensive, and for simpler plasma systems a more semi-analytical approach may be advantageous. Unfortunately, in many situations where spatial inhomogeneities of the plasma are present and expected to play a large role in wave coupling, such numerical methods may be necessary for yielding accurate results. The ALOHA code [47] is an example of a full-wave simulation tool which was developed to model the coupling of lower hybrid waves to a cold, inhomogeneous plasma, such as those found in the scrape-off layer of tokamak plasmas. An example of a model which handles wave propagation in nonuniform plasmas while retaining a degree of analyticity is given by [18] and [8], and was developed to study helicon waves in cylindrical plasmas.

In this chapter we present a robust semi-analytic model for modelling antenna-driven waves in a cold, uniform plasma. A semi-analytic model has the benefit of rewarding the user with reduced computation time in exchange for being able to solve any of the steps analytically, as well as granting physical insight into the problem that otherwise might not be evident with other numerical solvers. In order to simplify the problem, we will consider antennas which are current-driven by external electronics, meaning any induced fields (either by the active elements of the antenna or the nearby plasma response) have no effect on the antenna currents. In practice, complex antennas will often have passive elements containing induced currents, in addition to the actively driven antenna current, and the total radiated field is then due to the contribution from both current types. The simulation code TOPICA [69], originally developed to establish predictive capability in ICRF heating schemes, is able to account for details in the antenna such as geometry, housing, and shielding, as well as the induced currents within the passive antenna structures and their resulting radiated fields.

The remainder of this chapter is organized as follows. In section 3.2 we solve the antenna wave equation, which is a system of partial differential equations that describes the plasma field excited by an indirectly coupled antenna, for antennas possessing azimuthal symmetry.

In section 3.3 we solve the general solution for the case of an electric dipole antenna of length ℓ, aligned along the background magnetic field, and discuss the resulting radiation (and near-field) behavior. In section 3.4, we forgo all symmetry constraints and find the fully generalized solution to the antenna wave equation in Cartesian coordinates. Finally, in section 3.5 we offer some concluding remarks, including a discussion of the key physical insights gained from this analytic study as well as the advantages of this model in the context of simulations/numerical analysis.

3.2 Derivation of (and General Solution to) the Antenna Wave Equation

3.2.1 The Antenna Wave Equation

Alfvén waves are often discussed in terms of the behavior of their underlying wavevectors $\vec{k}$. A wave described by a single wavenumber $\vec{k}$ corresponds to a plane wave, whose phase-fronts extend out to infinity. Since waves of infinite extent are not physically realistic in any reasonable laboratory setting, the finite spatial structure of the Alfvén wave must be considered in order to fully capture the behavior of its propagation. Of course, any wave of finite extent can be Fourier transformed into $\vec{k}$ space, where it can then be thought of as a superposition of an infinite number of plane waves - this is standard practice in the plasma literature [93]. In this section, we will offer an alternative means of analysis by remaining in configuration space and solving the governing system of partial differential equations for the cold plasma wave equation. The cold plasma wave equation has been solved in full generality before by [89] and others, and showed that the plasma response due to a driven antenna is a superposition of the fast and slow branches. For plasmas in which the fast branch is evanescent below the ion cyclotron frequency (such as in the LAPD), the spatial structure of slow waves excited by a circular disk exciter was solved for both the inertial [72] and kinetic [73] regimes. One of the predictions for the inertial Alfvén wave is that the wave propagates

out in a conical pattern, and this is something we see later in section 3.3.

The derivation that follows is valid for all frequencies below the electron plasma frequency, although in section 3.3 we will specifically consider the Alfvén wave regime. Our starting point is the combination of Ampere's and Faraday's laws, which is given by the following expression:

$$\nabla \times \nabla \times \vec{E} = -\mu_0 \frac{\partial \vec{J}}{\partial t} - \frac{1}{c^2} \frac{\partial^2 \vec{E}}{\partial t^2}. \tag{3.1}$$

We assume a uniform magnetized plasma, with background field $\vec{B_0} = B_0 \hat{z}$, that is infinite and unbounded. Consider an antenna immersed in the plasma, which is harmonically excited via external circuitry at frequency ω. We will also only consider antennas which are electrically insulated such that they can't draw current from the plasma. The electric field can be redefined as $\vec{E} = \vec{E}_{pl} + \vec{E}_0$, where $\vec{E}_0$ is the vacuum field of the antenna and $\vec{E}_{pl}$ is the field due to the plasma's response to the antenna. Inserting these assumptions into equation 3.1 gives the following:

$$\nabla \times \nabla \times \vec{E}_{pl} + \nabla \times \nabla \times \vec{E}_0 = i\omega\mu_0 \vec{J}_{pl} + i\omega\mu_0 \vec{J}_{ext} + \frac{\omega^2}{c^2} \vec{E}_{pl} + \frac{\omega^2}{c^2} \vec{E}_0, \tag{3.2}$$

where $\vec{J}_{ext}$ is the externally-applied antenna current, and $\vec{J}_{pl}$ is the plasma current. Note that we adopted the convention $\partial_t \rightarrow -i\omega$, as is common in the literature. Additionally, we will consider a cold plasma model where the current density can be related to the local electric field by a conductivity tensor $\overleftrightarrow{\sigma}$, such that $\vec{J}_{pl} = \overleftrightarrow{\sigma} \cdot \vec{E}$. Note that the induced plasma current is proportional to the *total* electric field. Inserting these assumptions into equation 3.2 gives the following:

$$\nabla \times \nabla \times \vec{E}_{pl} = i\omega\mu_0 \overleftrightarrow{\sigma} \cdot (\vec{E}_{pl} + \vec{E}_0) + \frac{\omega^2}{c^2} \vec{E}_{pl}. \tag{3.3}$$

Note that in equation 3.3 we subtracted out the vacuum wave equation, given by $\nabla \times$

$\nabla \times \vec{E}_0 = i\omega\mu_0 \vec{J}_{ext} + (\omega^2/c^2)\vec{E}_0$. Defining $\overleftrightarrow{\varepsilon} = \overleftrightarrow{I} + (i\varepsilon_0\omega)\overleftrightarrow{\sigma}$ as the plasma dielectric tensor, equation 3.3 can be rewritten in the following form:

$$\nabla \times \left(\nabla \times \vec{E}_{pl}\right) - \frac{\omega^2}{c^2}\overleftrightarrow{\varepsilon} \cdot \vec{E}_{pl} = i\mu_0\omega\overleftrightarrow{\sigma} \cdot \vec{E}_0. \tag{3.4}$$

For a strongly magnetized plasma, the dielectric tensor is given in cylindrical coordinates by [93]:

$$\overleftrightarrow{\varepsilon} \cdot \vec{E} = \begin{bmatrix} \varepsilon_\perp & \varepsilon_{xy} & 0 \\ -\varepsilon_{xy} & \varepsilon_\perp & 0 \\ 0 & 0 & \varepsilon_\parallel \end{bmatrix} \cdot \begin{pmatrix} E_r \\ E_\theta \\ E_z \end{pmatrix}. \tag{3.5}$$

We will assume a cold plasma in the derivation that follows. In this limit, the components of the dielectric tensor can be expressed as the following:

$$\begin{aligned} \varepsilon_\perp &\equiv S = 1 - \sum_s \frac{\omega_{ps}^2}{\omega^2 - \Omega_{cs}^2}, \\ \varepsilon_{xy} &\equiv -iD = -i\sum_s \frac{\Omega_{cs}}{\omega}\frac{\omega_{ps}^2}{\omega^2 - \Omega_{cs}^2}, \\ \varepsilon_\parallel &\equiv P = 1 - \sum_s \frac{\omega_{ps}^2}{\omega^2}, \end{aligned} \tag{3.6}$$

where the summations are over all particle species. In equation 3.6, ω_{ps} and Ω_{cs} are the plasma and cyclotron frequencies, respectively, and ν_e is the total electron collision frequency. Note that the dielectric tensor defined by equation 3.6 is only valid for a plasma with background field $\vec{B}_0 = B_0\hat{z}$ pointing entirely in the z direction, and is not valid when an azimuthal component of the background field is present (analogous to the background poloidal field commonly found in tokamaks). Previous analytic approaches to the antenna problem [72, 73] have treated the antenna as a boundary condition to the resulting wave pattern, and was shown to be in excellent agreement with experimental observations. Equation 3.4 offers an alternative formulation to the antenna problem. Instead of boundary conditions,

we will show that the source term given by the right hand side of equation 3.4 can be used to uniquely determine the field in the plasma. Therefore we are able to solve problems which do not have straightforward boundary conditions (such as a one-dimensional dipole antenna, which we solve in section 3.3).

Equation 3.4 contains, in principle, all the information required to determine the field due to an antenna in the plasma. In the absence of an antenna, the right hand side of equation 3.4 goes to zero and the resulting differential equation is the cold plasma wave equation, whose solution gives all the wavelike modes predicted by the cold plasma model. The general solution to the cold plasma wave equation in cylindrical coordinates has been calculated before [78], in the context of the scattering of RF plane waves due to a cylindrical density filament. The right-hand side of equation 3.4 can be thought of as a "source" term to the cold plasma wave equation, and is physically interpreted as the vacuum field coupling to the plasma conductivity to excite plasma currents. This is consistent with previous observations of Alfvén waves in the laboratory. Waves launched by a magnetic dipole antenna, lying in the XZ plane, were shown to induce two antiparallel current channels on either end of the dipole, where the vacuum electric field points in $\pm\hat{z}$ [41]. It is speculated that cross-field currents are also excited in front of the antenna, where the vacuum field points in $\hat{x}$, although for antennas of that scale they are generally much smaller than the induced parallel electron currents.

3.2.2 Antenna Wave Equation for an Azimuthally Symmetric Antenna

The cold plasma assumption allows us to solve equation 3.4 in configuration space, as the dielectric tensor is not a function of the wave vector $\vec{k}$. In this section we will consider an antenna possessing azimuthal symmetry in cylindrical coordinates, although the general Cartesian solution is derived in section 3.4. The plasma response field excited by an azimuthally symmetric antenna is assumed to have the following form:

$$\vec{E}_{pl} = \frac{1}{2}[E_r(r,z,\omega)\hat{r} + E_\theta(r,z,\omega)\hat{\theta} + E_z(r,z,\omega)\hat{z}]e^{-i\omega t} + c.c. \tag{3.7}$$

Equation 3.4 can then be expanded out in cylindrical coordinates to give the following system of equations:

$$-\frac{\partial}{\partial z}\left(\frac{\partial E_r}{\partial z} - \frac{\partial E_z}{\partial r}\right) - \frac{\omega^2}{c^2}SE_r + \frac{\omega^2}{c^2}iDE_\theta = \frac{\omega^2}{c^2}(S-1)E_{r0} - \frac{\omega^2}{c^2}iDE_{\theta 0}, \tag{3.8}$$

$$-\frac{\partial^2 E_\theta}{\partial z^2} - \frac{\partial}{\partial r}\left(\frac{1}{r}\frac{\partial}{\partial r}(rE_\theta)\right) - \frac{\omega^2}{c^2}iDE_r - \frac{\omega^2}{c^2}SE_\theta = \frac{\omega^2}{c^2}iDE_{r0} + \frac{\omega^2}{c^2}(S-1)E_{\theta 0}, \tag{3.9}$$

$$\frac{1}{r}\frac{\partial}{\partial r}\left(r\frac{\partial E_r}{\partial z} - r\frac{\partial E_z}{\partial r}\right) - \frac{\omega^2}{c^2}PE_z = \frac{\omega^2}{c^2}(P-1)E_{z0}. \tag{3.10}$$

Note that we dropped the subscript on $\vec{E}_{pl}$ for brevity. Equations 3.8–3.10 can be reduced down to two differential equations if we recast it in terms of the azimuthal and radial magnetic field, given by Faraday's law to be $i\omega B_\theta = (\partial_z E_r - \partial_r E_z)$ and $i\omega B_r = -\partial_z E_\theta$. We can then perform the operations $\partial_z(Eqn.\ 3.8) - (S/P)\partial_r(Eqn.\ 3.10)$ and $\partial_z(Eqn.\ 3.9) - (iD/P)\partial_r(Eqn.\ 3.10)$ to get the following coupled equations:

$$\frac{\partial^2 B_\theta}{\partial z^2} + \frac{\omega^2}{c^2}SB_\theta + \frac{\omega^2}{c^2}iDB_r + \frac{S}{P}\frac{\partial}{\partial r}\left(\frac{1}{r}\frac{\partial}{\partial r}(rB_\theta)\right) = -\frac{\omega^2}{c^2}SB_{\theta 0} - \frac{\omega^2}{c^2}iDB_{r0}, \tag{3.11}$$

$$\frac{\partial^2 B_r}{\partial z^2} + \frac{\partial}{\partial r}\left(\frac{1}{r}\frac{\partial}{\partial r}(rB_r)\right) - \frac{\omega^2}{c^2}iDB_\theta + \frac{\omega^2}{c^2}SB_r - \frac{iD}{P}\frac{\partial}{\partial r}\left(\frac{1}{r}\frac{\partial}{\partial r}(rB_\theta)\right) = \frac{\omega^2}{c^2}iDB_{\theta 0} - \frac{\omega^2}{c^2}SB_{r0}. \tag{3.12}$$

In deriving equations 3.11 and 3.12, we made the assumption that we are at low enough frequencies such that the vacuum displacement current can be neglected in the dielectric (which is to say $\omega \ll \omega_{pe}$). At this point, equation 3.11 could be solved for B_r and then inserted into equation 3.12, resulting in a single fourth order differential equation for $B_\theta(r,z)$.

The result, however, is messy and uninspiring. Instead, lets consider the first order Hankel transform of the field, defined by:

$$B_j\left(r,z,\omega\right)=\int_0^\infty \tilde{B}_j\left(k_\perp,z,\omega\right)J_1\left(k_\perp r\right)k_\perp \mathrm{d}k_\perp \tag{3.13}$$

and its reverse transform:

$$\tilde{B}_j\left(k_\perp,z,\omega\right)=\int_0^\infty B_j\left(r,z,\omega\right)J_1\left(k_\perp r\right)r\mathrm{d}r. \tag{3.14}$$

The conditions for the existence of a Hankel transform are generally satisfied for physically realistic fields. Namely, the field must be defined and piecewise continuous for $r\in(0,\infty)$, and the integral of $\left|B_j(r)\right|r^{1/2}$ across all space should be finite. Invoking Bessel's differential equation, it is straightforward to prove the following identity:

$$\frac{\partial}{\partial r}\left(\frac{1}{r}\frac{\partial}{\partial r}\left(rB_j\right)\right)=-\int_0^\infty \tilde{B}_j\left(k_\perp,z,\omega\right)J_1\left(k_\perp r\right)k_\perp^3\mathrm{d}k_\perp. \tag{3.15}$$

We can then use identities 3.13 and 3.15 to recast our two differential equations in terms of $\tilde{B}_\theta$ and $\tilde{B}_r$. Finally, we substitute equation 3.11 into 3.12 to eliminate $\tilde{B}_r$ and get a single fourth order differential equation for $\tilde{B}_\theta$:

$$\begin{aligned}\frac{\partial^4\tilde{B}_\theta}{\partial z^4}+\alpha\frac{\partial^2\tilde{B}_\theta}{\partial z^2}+\beta\tilde{B}_\theta=&\\ -\frac{\omega^2}{c^2}S\frac{\partial^2\tilde{B}_{\theta0}}{\partial z^2}-\frac{\omega^2}{c^2}iD\frac{\partial^2\tilde{B}_{r0}}{\partial z^2}-\frac{\omega^4}{c^4}\left[RL-Sn_\perp^2\right]\tilde{B}_{\theta0}+iDn_\perp^2\tilde{B}_{r0}&\end{aligned} \tag{3.16}$$

Where $R,L=S\pm D$, $n_j\equiv ck_j/\omega$ is the refractive index in direction j, and α and β are given by the following:

$$\begin{aligned}\alpha&=\frac{\omega^2}{c^2}\left[S\left(1-\frac{n_\perp^2}{P}\right)+S-n_\perp^2\right],\\ \beta&=\frac{\omega^4}{c^4}\left[RL-Sn_\perp^2\right]\left(1-\frac{n_\perp^2}{P}\right),\end{aligned} \tag{3.17}$$

where $n_j \equiv ck_j/\omega$ is the refractive index in direction j. The left-hand side of equation 3.16 can be factored and alternatively expressed as the product of two second order differential operators:

$$\left(\frac{\partial^2}{\partial z^2} + k_{\parallel +}^2\right)\left(\frac{\partial^2}{\partial z^2} + k_{\parallel -}^2\right)\tilde{B}_\theta = \frac{\omega^4}{c^4} f(z), \tag{3.18}$$

where $k_{\parallel +}$ and $k_{\parallel -}$ are given by

$$\left(\frac{c^2}{\omega^2}\right) k_{\parallel \pm}^2 = S - \frac{n_\perp^2}{2}\left(1 + \frac{S}{P}\right) \pm \sqrt{\left(\frac{n_\perp^2}{2}\right)^2 \left(1 - \frac{S}{P}\right)^2 + D^2\left(1 - \frac{n_\perp^2}{P}\right)}, \tag{3.19}$$

where $k_{\parallel -}^2$ and $k_{\parallel +}^2$ correspond to the dispersion relations for the fast and slow waves, respectively, and are the two fundamental modes that exist in a cold plasma. Equation 3.19 has been previously derived in the context of thermal modulation of the cold conductivity tensor [89]. The source term $f(z)$ is given by the right hand side of equation 3.16:

$$f(z) = -\frac{c^2}{\omega^2} S \frac{\partial^2 \tilde{B}_{\theta 0}}{\partial z^2} - \frac{c^2}{\omega^2} iD \frac{\partial^2 \tilde{B}_{r0}}{\partial z^2} - \left[RL - Sn_\perp^2\right]\tilde{B}_{\theta 0} + iDn_\perp^2 \tilde{B}_{r0}. \tag{3.20}$$

Equation 3.18 is identical in principle to equation 3.3, except that it has been reformulated in such a way that the underlying physics is more readily apparent. In the absence of an externally-applied field, $f(z) = 0$ and equation 3.18 can be decoupled into two second order differential equations, whose solutions correspond to the fast and slow waves, and so the general solution is a linear superposition of both modes. But when an externally-applied field is present and $f(z) \neq 0$, the two modes cannot be decoupled and the full fourth order differential equation of equation 3.18 must be considered. In many laboratory plasmas, such as those found in the Large Plasma Device (LAPD) [36], the fast wave is generally evanescent below the ion cyclotron frequency, and so it is common practice to assume that only the slow wave is present in the system. Conversely, it is typical in the context of ICRF heating of tokamaks to ignore the slow wave contribution and assume only the fast wave is present, such

as is done in the semi-analytical code ANTITER II [68]. The implication of equation 3.18, however, is that neither branch can be ignored, as both branches fundamentally alter how the antenna couples to the plasma. In other words, even though the fast wave is evanescent and immeasurably small in the far-field, a portion of antenna energy in the near-field will couple to the fast wave, which in turn will affect the measured wave pattern of the slow wave. Therefore, a proper analytic treatment of the spatial structure of the slow wave must account for fast wave coupling in the near-field, as we have done in equation 3.18.

Equations 3.11 and 3.12 can alternatively be combined to get a similar differential equation for $\tilde{B}_r(k_\perp, z)$:

$$\left(\frac{\partial^2}{\partial z^2} + k_{\parallel +}^2\right)\left(\frac{\partial^2}{\partial z^2} + k_{\parallel -}^2\right)\tilde{B}_r = \frac{\omega^4}{c^4} g(z). \tag{3.21}$$

where $g(z)$ is given by

$$g(z) = \frac{c^2}{\omega^2} iD \frac{\partial^2 \tilde{B}_{\theta 0}}{\partial z^2} - \frac{c^2}{\omega^2} S \frac{\partial^2 \tilde{B}_{r0}}{\partial z^2} - RL\left(1 - \frac{n_\perp^2}{P}\right)\tilde{B}_{r0}. \tag{3.22}$$

Once $\tilde{B}_\theta(k_\perp, z)$ and $\tilde{B}_r(k_\perp, z)$ are known, $\tilde{B}_z(k_\perp, z)$ can be found from $\nabla \cdot \vec{B} = 0$ and then the electric field through the rest of Maxwell's equations.

It's worth mentioning that some authors [3, 96] have followed alternative, but similar, procedures in which equations 3.11 and 3.12 are Fourier transformed in direction z, resulting in a fourth order differential equation in r (analogous to equations 3.18 and 3.21). Either method should lead to similar results. One of the advantages of expressing our system as a differential equation in z is that the math is a lot more tractable in the next section, where we find the Green's function of equation 3.18. Additionally, this method makes it straightforward to consider the behavior of the field at positions z far away from the antenna, which is useful for comparison to experimental studies of antenna-launched shear (or slow) waves in the laboratory [37]. For inhomogeneous plasmas with radially-varying parameters, it may be preferable to Fourier transform in z and consider the differential equation in r

instead, as was done for the study of helicon waves in nonuniform plasmas by [8].

3.2.3 Solution to the Antenna Wave Equation by Method of Green's Functions

Equation 3.18 is essentially a fourth order wave equation, driven by a "source" term $f(z)$. In order to solve this differential equation we will employ the method of Green's functions. Consider the following differential equation:

$$\frac{\partial^4 G}{\partial z^4} + \alpha \frac{\partial^2 G}{\partial z^2} + \beta G = \delta(z - z'). \tag{3.23}$$

$G = G(z, z')$ is physically interpreted as the field due to an infinitesimal point source[1] at $z = z'$. The total magnetic field at position z, then, is found by summing up the field contributions from all of these point sources:

$$\tilde{B}_\theta(k_\perp, z) = \frac{\omega^4}{c^4} \int G(z, z') f(z') dz', \tag{3.24}$$

where the integral of equation 3.24 is taken over all space. When $z \neq z'$, equation 3.23 can be decoupled into two second order differential equations, and the solution is the superposition of both modes of the system:

$$G(z, z') = \begin{cases} Ae^{ik_{\parallel +} z} + Be^{ik_{\parallel -} z} & \text{for } z > z' \\ Ce^{-ik_{\parallel +} z} + De^{-ik_{\parallel -} z} & \text{for } z < z' \end{cases}. \tag{3.25}$$

As our plasma was assumed to be infinite and unbounded, the Green's function given by equation 3.25 is motivated by our request to have radiation at $z \to \pm\infty$, although equation 3.25 can be modified to consider alternative boundary conditions. The coefficients of equation 3.25 can be found by iteratively integrating equation 3.23 across an infinitesimally small region centered on $z = z'$, and gives the following four boundary conditions:

[1]Note that this is a "point source" in the mathematical sense of equation 3.18, and should not be interpreted as a physical point source (such as a point charge).

$$\begin{aligned}
\lim_{\varepsilon\to 0}\left.\frac{\partial^3 G}{\partial z^3}\right|_{z'-\varepsilon}^{z'+\varepsilon} &= 1,\\
\lim_{\varepsilon\to 0}\left.\frac{\partial^2 G}{\partial z^2}\right|_{z'-\varepsilon}^{z'+\varepsilon} &= 0,\\
\lim_{\varepsilon\to 0}\left.\frac{\partial G}{\partial z}\right|_{z'-\varepsilon}^{z'+\varepsilon} &= 0,\\
\lim_{\varepsilon\to 0} G\Big|_{z'-\varepsilon}^{z'+\varepsilon} &= 0.
\end{aligned} \tag{3.26}$$

The discontinuity in the third derivative of G arises from the presence of the Dirac delta function in equation 3.23. Equation 3.25 can be inserted into the above boundary conditions to solve for A, B, C, and D, and gives the following solution for the Green's function:

$$G(z,z') = \begin{cases} \frac{ie^{ik_{\parallel+}(z-z')}}{2k_{\parallel+}(k_{\parallel+}^2-k_{\parallel-}^2)} + \frac{ie^{ik_{\parallel-}(z-z')}}{2k_{\parallel-}(k_{\parallel-}^2-k_{\parallel+}^2)} & \text{for } z > z' \\ \frac{ie^{-ik_{\parallel+}(z-z')}}{2k_{\parallel+}(k_{\parallel+}^2-k_{\parallel-}^2)} + \frac{ie^{-ik_{\parallel-}(z-z')}}{2k_{\parallel-}(k_{\parallel-}^2-k_{\parallel+}^2)} & \text{for } z < z' \end{cases}. \tag{3.27}$$

The general solution of $\tilde{B}_\theta(k_\perp, z)$ can then be found from equation 3.24:

$$\begin{aligned}
\tilde{B}_\theta(k_\perp,z) = \frac{\omega^4}{c^4}\int_{-\infty}^{z}\left[\frac{ie^{ik_{\parallel+}(z-z')}}{2k_{\parallel+}(k_{\parallel+}^2-k_{\parallel-}^2)} - \frac{ie^{ik_{\parallel-}(z-z')}}{2k_{\parallel-}(k_{\parallel+}^2-k_{\parallel-}^2)}\right]f(z')dz' \\
+\frac{\omega^4}{c^4}\int_{z}^{\infty}\left[\frac{ie^{-ik_{\parallel+}(z-z')}}{2k_{\parallel+}(k_{\parallel+}^2-k_{\parallel-}^2)} - \frac{ie^{-ik_{\parallel-}(z-z')}}{2k_{\parallel-}(k_{\parallel+}^2-k_{\parallel-}^2)}\right]f(z')dz',
\end{aligned} \tag{3.28}$$

where $k_{\parallel\pm}^2$ can be found from equation 3.19, and $f(z)$ is given by equation 3.20. The general solution for $\tilde{B}_r(k_\perp, z)$ is the same as equation 3.28, except with $g(z)$ (given by equation 3.22) in place of $f(z)$. Inserting the solution of equation 3.28 into the inverse Hankel transform of equation 3.13 will give the complete general solution of $B_\theta(r, z)$. We emphasize again here that the preceding derivation is predicated on the assumption that the plasma is infinite and spatially uniform, which allowed us to solve the differential equation given by equation 3.3 in configuration space. The TOPICA code, which was developed as a predictive

tool for ICRF antenna systems, contains a much more robust (and, consequently, numerically intensive) Green's function solution, which accounts for a spatially-varying background field and density as well as finite temperature effects [64].

Equation 3.28 is just the magnetic field due to the plasma response - the total magnetic field will be the sum of equation 3.28 plus the vacuum field of the antenna, although the latter is generally much smaller far from the antenna. The general solution for $B_\theta(r, z)$ is a linear superposition of the fast and slow wave branches, which are the two fundamental modes of the cold plasma, and is valid in both the near and far-field of the antenna. At every position in the plasma, the vacuum field of the antenna couples to the plasma conductivity and acts as an infinitesimal point source emitter - the total field is then found by integrating across the entire vacuum field to find the aggregate sum of all these tiny point source fields. The integral of equation 3.28 can be truncated wherever the quantity $f(z)$ or the vacuum field is deemed sufficiently small. For an observation point $+z$ that is sufficiently far away from the antenna, the contribution to the field due to backwards propagating waves (i.e. the second integral in equation 3.28) is vanishingly small and the resulting wave is entirely forward propagating. Points close to the antenna will experience both forward and backward propagating waves, and the resulting interference creates a much more complicated near-field structure in the vicinity of the antenna. We therefore define the radiation zone of the wave as the region far enough from the antenna such that the vacuum field is sufficiently small, and the field, for a given $k_\perp$, is a forward propagating plane wave (or backwards for $z < 0$). Note that this is in contrast with the classical definition of the radiation zone in vacuum, which is typically defined as the region in space several wavelengths from the source [55].

In our discussion of the antenna wave equation 3.18, we asserted that the presence of an antenna couples the slow and fast wave branches, meaning the physics of the two cannot be separated. This is apparent in our solution given by equation 3.28, as the amplitude of the slow wave is a function of the fast wave's dispersion (and vice versa for the fast wave's amplitude). Even when the fast wave is evanescent, a portion of the antenna's field will

couple to the fast branch and this will ultimately affect the radiation pattern of the slow wave. In deriving equation 3.28, it was required that we assume $k_{\parallel+} \neq k_{\parallel-}$. When $k_{\parallel+} = k_{\parallel-}$, the fast and slow waves are virtually identical, and mode conversion may occur [95].

3.2.4 Necessity of the $E \times B$ Current and Radial Magnetic Field

Many previous treatments of the spatial structure of Alfvén waves have either been done in the low frequency ($\omega \ll \Omega_i$) or large $k_\perp$ limits, where the off-diagonal terms of the dielectric tensor approach zero [72, 73]. Physically, the off-diagonal terms embody the current resulting from the differences in the $E \times B$ drift of the ions and electrons - at low frequencies, all species drift with approximately the same velocity and the net current is zero. In this limit, the only contribution to the cross-field current of the wave is the ion polarization current. For an azimuthally-symmetric antenna, then, it can be assumed that $E_\theta \ll E_r$ and, consequently, the resulting magnetic field of the wave (found via Faraday's law) points entirely in the azimuthal direction.

We are interested in the entire ion cyclotron frequency regime, where, in general, the assumption $D \to 0$ is *not* valid. Additionally, one of the primary motivations of this dissertation is to investigate the polarization of Alfvén waves. A wavefront which consists entirely of an azimuthal field, however, can only ever be linearly polarized by definition. Therefore, consideration of B_r is not only more accurate, it's actually *essential* in the context of this study. For an alternative derivation and discussion of the radial magnetic field, in the context of shear waves launched by a disk exciter, see [100].

3.3 Electromagnetic field of an Electric Dipole Antenna in a Cold, Magnetized Plasma

3.3.1 Radiation Field

As an example of how to apply the general solution derived in section 3.2, we will consider the wave pattern resulting from an electric dipole antenna. An infinitely thin dipole of length ℓ is centered on the origin and aligned along the background magnetic field (see figure 3.1), and the two ends are biased against each other at frequency ω. Assume the antenna is externally driven such that the amplitude of the current in the dipole is constant and independent of changing plasma conditions. We are interested in the far-field wave pattern (in the $+z$ direction), and so we can ignore the contribution to equation 3.28 due to backwards propagating waves. Additionally, we will consider frequencies below the ion cyclotron frequency and assume the fast wave to be evanescent, as is typical in many laboratory plasmas at these frequencies. Equation 3.28 can then be written as the following:

$$\tilde{B}_\theta(k_\perp, z) = \frac{ie^{ik_\parallel z}}{2k_\parallel \left(k_\parallel^2 - k_{\parallel -}^2\right)} \frac{\omega^4}{c^4} \int_{-\infty}^{\infty} e^{-ik_\parallel z'} f(z') dz', \tag{3.29}$$

where $k_\parallel$ and $k_{\parallel -}$ are the parallel wavenumbers of the slow and fast waves, respectively, given by equation 3.19, and $f(z)$ is given by 3.20. The full field solution should also include the vacuum field $\tilde{B}_{\theta 0}$, which equation 3.29 does not, but we will assume that far away from the antenna this contribution is negligibly small (this is verified in figure 3.3). The vacuum magnetic field of the dipole is entirely azimuthal, and is identical to that of a finite wire element carrying current I:

$$B_{\theta 0}(r, z) = \frac{\mu_0 I}{4\pi r} \left[\frac{z + \ell/2}{\sqrt{r^2 + (z + \ell/2)^2}} - \frac{z - \ell/2}{\sqrt{r^2 + (z - \ell/2)^2}} \right], \tag{3.30}$$

where a $e^{-i\omega t}$ time dependence is understood. It is straightforward to show via charge

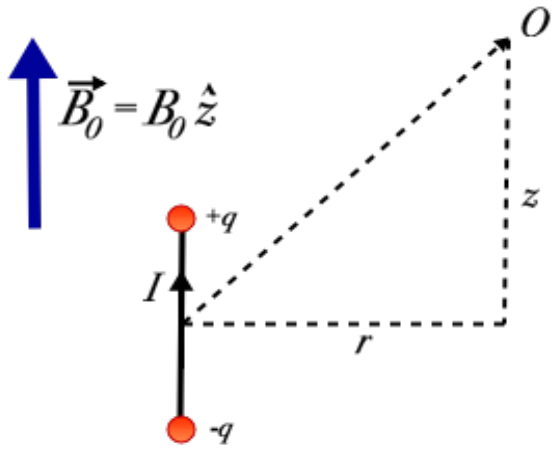

Figure 3.1: An electric dipole of length ℓ, with oscillating point charges $\pm qe^{-i\omega t}$ on either end, is aligned parallel to the background magnetic field $\vec{B} = B_0\hat{z}$. A cylindrical coordinate system is assumed, with the origin centered on the midpoint of the dipole.

conservation that this corresponds to a charge density distribution of $\rho_c = q[\delta(z + \ell/2) - \delta(z - \ell/2)]e^{-i\omega t}$, where $q = I/i\omega$. Note that in deriving equation 3.30 we have assumed the quasi-magnetostatic limit, in which we ignore radiative effects due to the time-retarded vacuum potential [112]. This approximation is valid so long as our region of interest is much closer to the antenna than one vacuum wavelength. At higher frequencies, where the vacuum wavelength of the antenna is of comparable length to the size of the plasma, a more complete radiative theory of the vacuum field should be employed [55].

The first-order Hankel transform of the vacuum field, derived in Appendix C, is:

$$\tilde{B}_{\theta 0}(k_\perp, z) = \frac{\mu_0 I}{2\pi k_\perp} \begin{cases} e^{-k_\perp z} \sinh k_\perp \frac{\ell}{2} & \text{for } z > \ell/2 \\ \left(1 - e^{-k_\perp \frac{\ell}{2}} \cosh k_\perp z\right) & \text{for } -\ell/2 < z < \ell/2 \\ e^{k_\perp z} \sinh k_\perp \frac{\ell}{2} & \text{for } z < -\ell/2 \end{cases} . \tag{3.31}$$

It can be shown that $\tilde{B}_{\theta 0}$ is continuous and differentiable everywhere, although its second

derivative experiences a discontinuity at $z = \pm\ell/2$. Since $\tilde{B}_{\theta 0}$ and its first derivative go to zero at $z \to \pm\infty$, integration by parts can be performed on the $\partial_z^2 \tilde{B}_{\theta 0}$ term of $f(z)$ to express equation 3.29 as the following:

$$\tilde{B}_\theta(k_\perp, z) = \frac{ie^{ik_\parallel z}(Sn^2 - RL)}{2k_\parallel(k_\parallel^2 - k_{\parallel -}^2)} \frac{\omega^4}{c^4} \int_{-\infty}^{\infty} e^{-ik_\parallel z'} \tilde{B}_{\theta 0}(z') dz', \tag{3.32}$$

where $n^2 = n_\perp^2 + n_\parallel^2$. The remaining integral is recognized as the inverse Fourier transform of the vacuum field in z, evaluated at $k_z = k_\parallel$. Inserting equation 3.31 into 3.32, we get the following unsolved integrals:

$$\tilde{B}_\theta(k_\perp, z) = A(k_\perp) \left[\sinh k_\perp \frac{\ell}{2} \int_{-\infty}^{-\ell/2} e^{(k_\perp - ik_\parallel)z'} \mathrm{d}z' + \right.$$
$$\left. \int_{-\ell/2}^{\ell/2} e^{-ik_\parallel z'} \left(1 - e^{-k_\perp \frac{\ell}{2}} \cosh k_\perp z'\right) \mathrm{d}z' + \sinh k_\perp \frac{\ell}{2} \int_{\ell/2}^{\infty} e^{-(k_\perp + ik_\parallel)z'} \mathrm{d}z' \right], \tag{3.33}$$

where

$$A(k_\perp) = \frac{\omega^4}{c^4} \frac{\mu_0 I}{2\pi k_\perp} \frac{ie^{ik_\parallel z}(Sn^2 - RL)}{2k_\parallel(k_\parallel^2 - k_{\parallel -}^2)}. \tag{3.34}$$

The solution to equation 3.33 is as follows:

$$\tilde{B}_\theta(k_\perp, z) = i \frac{\mu_0 I}{2\pi k_\perp} \left(S - \frac{RL}{n^2}\right) \frac{n_\perp^2 e^{ik_\parallel z} \sin k_\parallel \frac{\ell}{2}}{n_\parallel^2(n_\parallel^2 - n_{\parallel -}^2)}. \tag{3.35}$$

While the vacuum magnetic field is entirely azimuthal, the off-diagonal $E \times B$ drift in the plasma response will drive a $\tilde{B}_r$ in the plasma. An expression for $\tilde{B}_r(k_\perp, z)$ can be found by substituting $g(z)$ into equation 3.29 in place of $f(z)$, and yields the following:

$$\tilde{B}_r(k_\perp, z) = \frac{\mu_0 I}{2\pi k_\perp} \frac{Dn_\perp^2 e^{ik_\parallel z} \sin k_\parallel \frac{\ell}{2}}{n^2(n_\parallel^2 - n_{\parallel -})}. \tag{3.36}$$

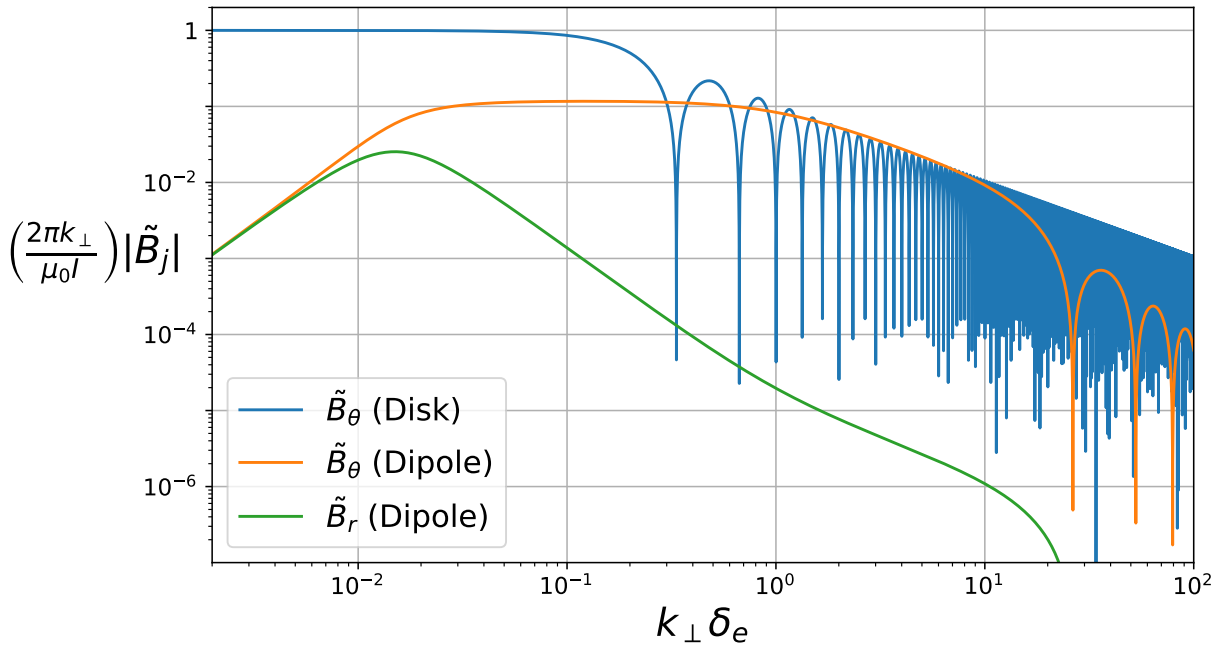

Figure 3.2: Magnitude of the magnetic field resulting from an electric dipole of length ℓ aligned along the background field, in a single-ion species plasma at frequency $\omega = .75\Omega_{ci}$. For comparison, we show the field resulting from a disk exciter with radius $\ell/2$.

Figure 3.2 shows the magnitude of $\tilde{B}_\theta(k_\perp, z)$ and $\tilde{B}_r(k_\perp, z)$, as a function of $k_\perp$, in the radiation zone of a single-ion species plasma. A helium plasma with $B_0 = 1500$ G and $n_0 = 10^{12}$ cm^{-3} was assumed, as these are typical conditions for many laboratory plasmas, such as those found in the LAPD. For the antenna, a frequency of $\omega = .75\Omega_{ci}$ and length $\ell = 20\delta_e$ was assumed, where Ω_{ci} is the ion cyclotron frequency and $\delta_e \equiv c/\omega_{pe}$ is the electron skin depth. We normalized the $k_\perp$ axis to the electron skin depth, as this is the natural cross-field scale length of inertial Alfvén waves [72]. We have also assumed a collisionless plasma ($\nu_e = 0$), in order to elucidate some of the fine-structure features of the wave that would otherwise be washed out by collisions. In the limit $k_\perp \to 0$, $\tilde{B}_\theta$ and $\tilde{B}_r$ are equal in magnitude and $\pi/2$ out of phase. In this limit, the slow wave dispersion of equation 3.19 gives $n_\parallel^2 = R$, which corresponds to a right-handed circularly polarized wave. As $k_\perp$ increases, the relative strength of $\tilde{B}_r$ falls off and the field is almost entirely azimuthal. In this limit, the slow wave's dispersion is approximated by the following expression:

$$n_\parallel^2 = S\left(1 - \frac{n_\perp^2}{P}\right). \tag{3.37}$$

Equation 3.37 is commonly known as the *inertial Alfvén wave*. In the limit $k_\perp \to 0$, the Alfvén wave is mediated entirely by the cross-field ion polarization and $E \times B$ currents. When $k_\perp \neq 0$, a parallel electron current is excited in order to satisfy current closure (i.e. $\nabla \cdot \vec{J} = 0$). When the perpendicular wavelength is of comparable size to the electron skin depth ($k_\perp \delta_e \sim 1$), the induced parallel electron current is so much larger than the cross-field currents that it becomes predominantly responsible for setting the perpendicular magnetic field of the wave - hence the dominant azimuthal magnetic field seen in this regime. From inspection of equations 3.35 and 3.36, the coupled antenna power is zero when $\ell = n\lambda_\parallel$, for integer n, and greatest when $\ell = (\frac{1}{2} + n)\lambda_\parallel$.

Previous analytic studies have been done on the spatial structure of Alfvén waves launched from a metal disk exciter, both in the inertial [72] and kinetic [73] regimes. For a disk exciter of radius a, maintained at a fixed AC voltage, $\tilde{B}_\theta(k_\perp, z)$ was found to have the following form:

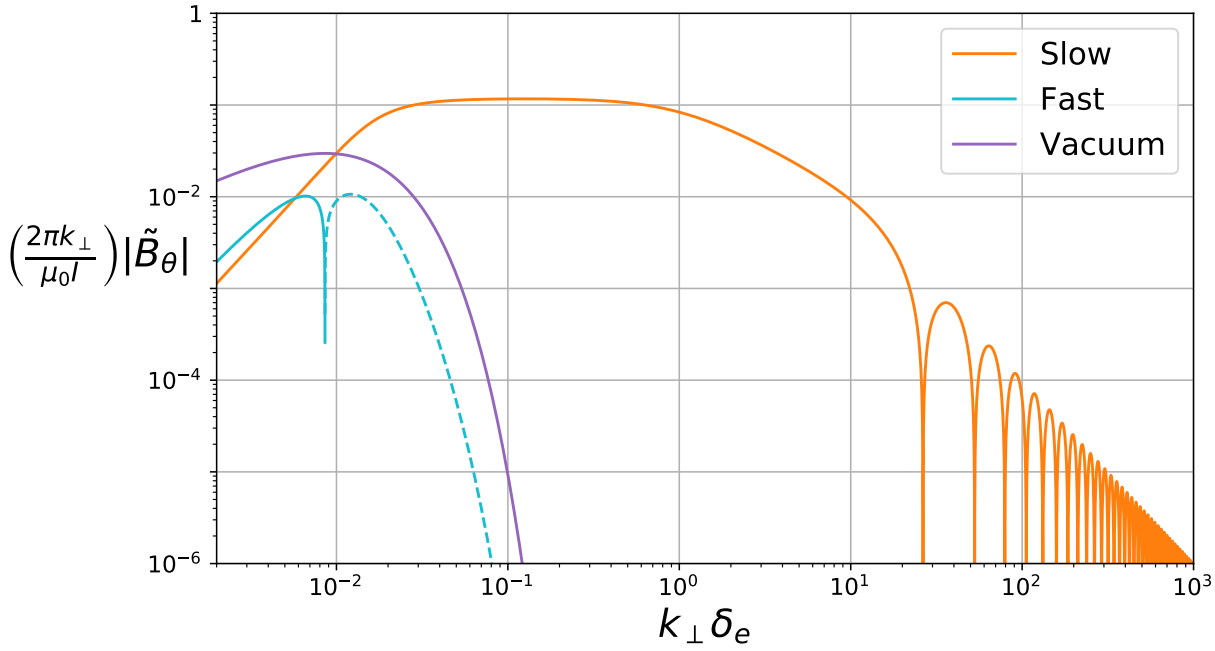

Figure 3.3: Comparison of the azimuthal field of the slow wave, fast wave, and vacuum field, at a distance $z = v_A/\omega$ away from the electric dipole antenna. The same plasma and antenna conditions from figure 3.2 are assumed. The dashed line in the fast wave branch denotes where the wave is evanescent.

$$\tilde{B}_\theta(k_\perp, z) = \frac{\mu_0 I}{2\pi k_\perp} \frac{\sin k_\perp a}{k_\perp a}. \tag{3.38}$$

Figure 3.2 includes $\tilde{B}_\theta(k_\perp, z)$ of a disk exciter antenna, with radius equal to half the dipole length, for comparison. The total integrated power of the disk exciter wave is much greater, which is due in part to the fact that the disk is in direct electrical contact with the plasma, whereas the dipole relies on capacitive coupling. In addition, the dipole experiences worse coupling at lower frequency, while the disk is unaffected.

We previously asserted that the fast wave is evanescent for the plasma parameters being considered, as well as claiming that the vacuum field is much smaller than the radiation field far from the antenna. Figure 3.3 compares the magnitude of the slow wave to both

the fast wave and vacuum field, 1 meter away from the dipole. The dashed line denotes evanescence. The fast wave is seen to be real and propagating at low $k_\perp$, but the vast majority of coupled power exists at values of $k_\perp$ where the wave is heavily evanescent. Additionally, the magnitude of the vacuum field is vanishingly small compared to that of the slow wave. We conclude that, given the assumed plasma conditions, the total magnetic field in the plasma far from the antenna (in the $\hat{z}$ direction) will be due entirely to propagating slow waves.

3.3.2 Near-field Response

In the previous section we solved equation 3.28 for points far away from the antenna, which allowed us to drop the contribution due to backward propagating waves. We will now solve 3.28 everywhere in the plasma. In doing so, our goal is to see how near-field effects modify the resulting field for regions close to the antenna.

Ignoring the fast wave contribution as we did before, equation 3.28 can be written as the following:

$$\tilde{B}_\theta(k_\perp, z) = \tilde{B}_{\theta 0} + \frac{i(\omega^4/c^4)}{2k_\parallel(k_\parallel^2 - k_{\parallel -}^2)} \left[\int_{-\infty}^{z} e^{ik_\parallel(z-z')} f(z') \mathrm{d}z' + \int_{z}^{\infty} e^{-ik_\parallel(z-z')} f(z') \mathrm{d}z' \right]. \quad (3.39)$$

The interference between the forward and backward propagating waves, given by the first and second integrals respectively, is what will give rise to the near-field response. Note that we have included the vacuum field in the above solution. It was shown in the previous section that the vacuum field can be ignored far from the antenna, but we will show here that this is not the case in the near-field.

The source term $f(z)$ can be found by inserting the (Hankel-transformed) vacuum field, given by equation 3.31, into 3.20:

$$f(z) = \frac{\mu_0 I}{2\pi k_\perp} \begin{cases} -RLe^{-k_\perp z} \sinh k_\perp \frac{\ell}{2} & \text{for } z > \ell/2 \\ Sn_\perp^2 - RL(1 - e^{-k_\perp \frac{\ell}{2}} \cosh k_\perp z) & \text{for } -\ell/2 < z < \ell/2 \\ -RLe^{k_\perp z} \sinh k_\perp \frac{\ell}{2} & \text{for } z < -\ell/2 \end{cases} . \tag{3.40}$$

From here it is straightforward to insert the above expression for $f(z)$ into equation 3.39. Because our vacuum field is divided up into three distinct regions, equation 3.39 will have to be solved separately for the three different regions as well. For demonstrative purposes, we will consider the two outer regions first, defined by $|z| > \ell/2$. The solution to equation 3.39 for $z > \ell/2$ and $z < -\ell/2$ are given by the following:

$$\tilde{B}_\theta(k_\perp, z) = \underbrace{i\frac{\mu_0 I}{2\pi k_\perp}\left(S - \frac{RL}{n^2}\right)\frac{n_\perp^2 e^{ik_\parallel |z|}\sin k_\parallel \frac{\ell}{2}}{n_\parallel^2(n_\parallel^2 - n_{\parallel -}^2)}}_{\text{Radiation Field}} + \underbrace{\frac{\mu_0 I}{2\pi k_\perp}\left(1 + \frac{RL}{n^2(n_\parallel^2 - n_{\parallel -}^2)}\right)e^{-k_\perp |z|}\sinh k_\perp \frac{\ell}{2}}_{\text{Near-field Response}} . \tag{3.41}$$

The first term is identified as the radiation field, and is identical to the far-field response derived in the previous section, given by equation 3.35. The second term arises from the inclusion of the contribution from backward propagating waves in the general solution, and can be thought of as the near-field response. The near-field in equation 3.41 is the sum of both the near-field plasma response as well as the vacuum field. The near-field is observed to decay exponentially as one moves away from the antenna, dropping off much more rapidly for larger values of $k_\perp$. Note that the near-field response does *not* propagate as a wave, like the radiation field, but rather is a region around the antenna which pulsates at frequency ω.

The field in the region $-\ell/2 < z < \ell/2$ is found from equation 3.39 to be the following:

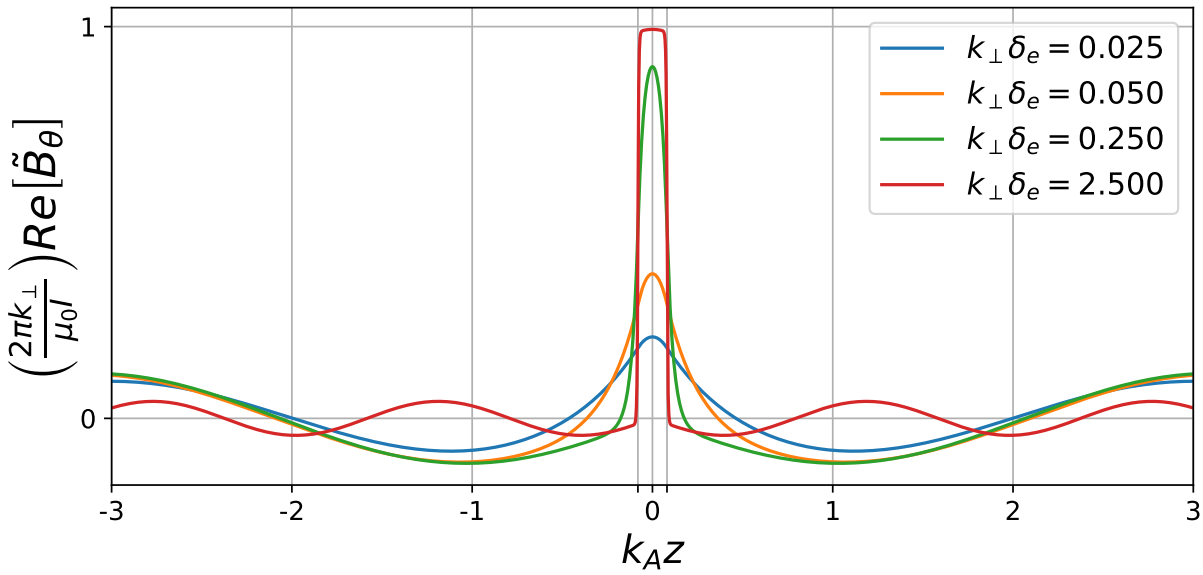

Figure 3.4: Azimuthal magnetic field vs. axial position $k_A z$, due to an electric dipole antenna of length ℓ, for various values of $k_\perp$. In the region $|z| < \ell/2$, near-field effects dominate. The near-field response decays exponentially with increasing $|z|$, and far from the antenna only the radiation field remains.

$$\tilde{B}_\theta(k_\perp, z) = \frac{\mu_0 I}{2\pi k_\perp} \frac{n_\perp^2}{n_\parallel^2(n_\parallel^2 - n_{\parallel-}^2)} \left(S - \frac{RL}{n^2}\right) \left(e^{ik_\parallel \frac{\ell}{2}} \cos k_\parallel z - 1\right) + \frac{\mu_0 I}{2\pi k_\perp} \left(1 + \frac{RL}{n^2(n_\parallel^2 - n_{\parallel-}^2)}\right) \left(1 - e^{-k_\perp \frac{\ell}{2}} \cosh k_\perp z\right). \quad (3.42)$$

Figure 3.4 shows how $\tilde{B}_\theta(k_\perp, z)$ varies with z, for several different values of $k_\perp$. The same plasma and antenna conditions as figures 3.2 and 3.3 were assumed. The field is peaked in the region $-\ell/2 < z < \ell/2$ and drops off exponentially for $|z| > \ell/2$, with larger values of $k_\perp$ experiencing a more abrupt drop-off. The radiation zone for a given $k_\perp$ is defined as the region far enough from the antenna where the field exhibits wavelike motion, as the only remaining field out there is due to the propagating slow wave. In the limit $k_\perp \to \infty$, the field in the vicinity of the antenna converges to a constant value of $\tilde{B}_\theta = \mu_0 I/2\pi k_\perp$, whereas

the radiation field drops off more rapidly with increasing $k_\perp$.

3.3.3 Numerical Results

The spatially-resolved magnetic field is found from the inverse Hankel transform of $\tilde{B}_\theta(k_\perp, z)$. For the radiation field, this amounts to solving the following integral:

$$B_\theta(r,z,\omega) = i\frac{\mu_0 I}{2\pi}\frac{\omega^2}{c^2}\int_0^\infty \left(S - \frac{\omega^2}{c^2}\frac{RL}{k^2}\right)\frac{k_\perp^2 e^{ik_\parallel z}\sin k_\parallel \frac{\ell}{2}}{k_\parallel^2(k_\parallel^2 - k_{\parallel-}^2)} J_1(k_\perp r)\mathrm{d}k_\perp, \tag{3.43}$$

where $k_\parallel$ and $k_{\parallel-}$ are the slow and fast wave dispersions, respectively, and are given by equation 3.19. Equation 3.43 will, in general, need to be solved numerically. The time-resolved field is then found from the real part of $B_\theta(r,z,\omega)e^{-i\omega t}$. Close to the antenna, the near-field solution given by equations 3.41 and 3.42 should be used. The results that follow in this section assume the same plasma conditions as before. Numerical integration of equation 3.43 was done using the algorithm devised by [74], which uses a quadrature formula with the zeros of the Bessel function as nodes.

Figure 3.5 shows the time evolution of the resulting waveform, for two different frequencies. Two conical structures are seen emanating from either end of the dipole, with an angle of propagation that increases with frequency. The cone's propagation angle can be found from the ratio of the wave's perpendicular and parallel group velocities. For antennas whose scale length is on the order of the electron skin depth $\delta_e \equiv c/\omega_{pe}$, the majority of antenna power couples to large enough values of $k_\perp$ where the inertial Alfvén wave dispersion, given by equation 3.37, is valid. The ratio of the inertial wave's perpendicular to parallel group velocities gives the propagation angle of the wave:

$$\tan\theta = \left|\frac{\partial\omega/\partial k_\perp}{\partial\omega/\partial k_\parallel}\right| = \sqrt{\frac{m_e}{m_i}}\frac{\omega}{\sqrt{\Omega_{ci}^2 - \omega^2}}\frac{k_\perp\delta_e}{\sqrt{1+k_\perp^2\delta_e^2}}. \tag{3.44}$$

When $k_\perp\delta_e \gg 1$, the propagation angle approaches an asymptotic limit that is independent of $k_\perp$, resulting in a conical structure. The propagation angle θ_c of the cone is given

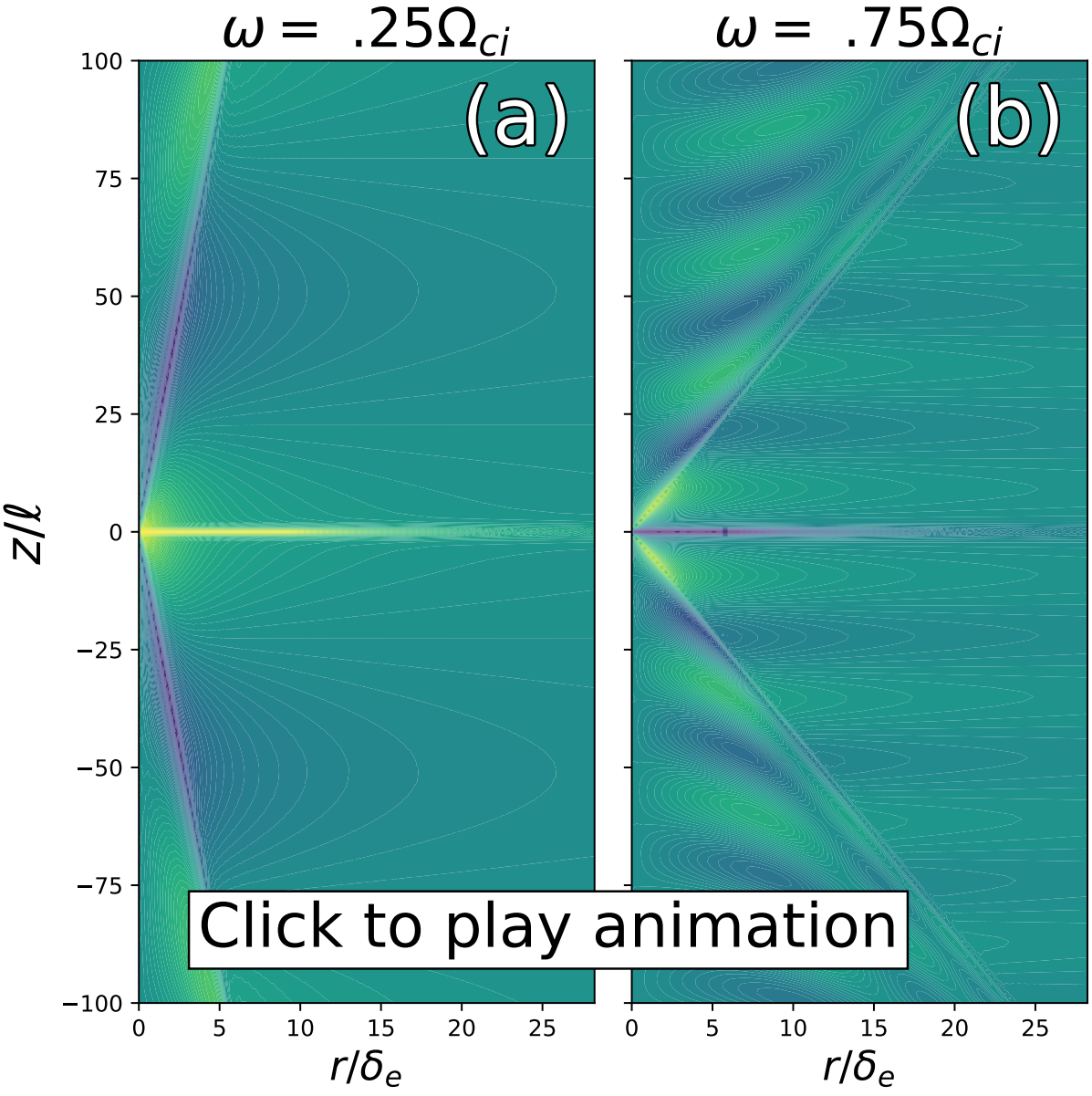

Figure 3.5: Time animation of the azimuthal magnetic field of the slow wave, launched from an electric dipole of length $\ell = 10$ cm, for frequencies (a) $.25\Omega_{He}$ and (b) $.75\Omega_{He}$. The propagation angle of the cones emanating from either end of the dipole can be determined from the inertial Alfvén wave dispersion.

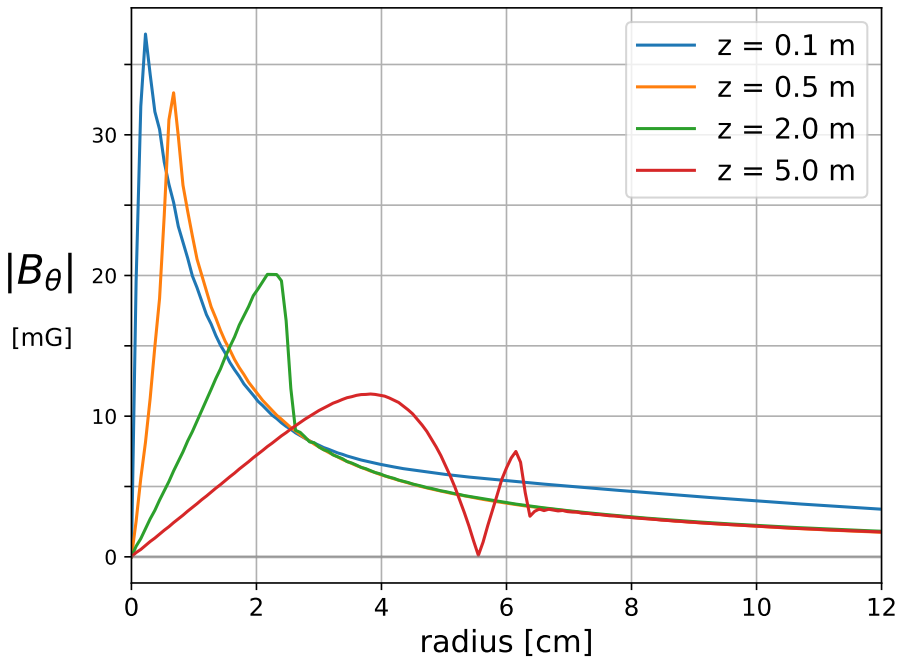

Figure 3.6: Amplitude of the azimuthal magnetic field vs. radius, at various distances from the antenna. The field increases with radius up until a certain point, where it exhibits a $1/r$ drop-off.

by:

$$\tan\theta_c = \sqrt{\frac{m_e}{m_i}}\frac{\bar{\omega}}{\sqrt{1-\bar{\omega}^2}}, \tag{3.45}$$

where $\bar{\omega} = \omega/\Omega_{ci}$. For the two frequencies shown in figures 3.5a and 3.5b, this gives propagation angles of $\theta_c \approx .17°$ and $\theta_c \approx .76°$, respectively, and it's easy to verify that these values agree with the observed propagation angles in figure 3.5. Similar conical spreading was predicted to exist for Alfvén waves launched by a metal disk exciter in a cold plasma [72], and was consequently observed in the lab [38]. The amplitude of the field is shown in figure 3.6 at various axial positions. At each z position, the field is observed to increase with increasing r until it reaches the edge of the cone, where it exhibits a $1/r$ drop-off. The $1/r$ dependence outside the cone suggests that the parallel plasma current excited by the antenna is contained

entirely within the conical region. Additionally, the magnitude of the field outside the cone is constant with z in the radiation zone of the plasma, as the *total* parallel plasma current is conserved with z. The inclusion of electron collisionality, which we have omitted for demonstrative purposes, results in a field outside the cone which decays with z. Far from the antenna, where $k_A z \gg 1$, diffraction patterns begin to emerge in the radial profile. These radial diffraction patterns, as well as the $1/r$ drop off, are known effects that were predicted in previous analytic studies of shear waves launched by a disk exciter antenna [72]. These results are consistent with countless previous experimental studies of inertial Alfvén waves in the LAPD [37]. For a disk exciter antenna whose radius is on the order of the electron skin depth, the wave's radial profile experiences a strong azimuthal magnetic field with an off-axis maximum that spreads out conically with increasing z, eventually producing a radial diffraction pattern far from the disk.

3.3.4 Fast Wave Considerations

In the previous section we asserted that the fast wave was evanescent for the assumed plasma conditions, and therefore focused exclusively on the spatial structure of the slow wave. While it is straightforward to prove the fast wave's contribution is negligible in the far-field, the same is not obvious in the vicinity of the antenna. For the relatively large values of $k_\perp$ imposed by our assumed antenna, it can be shown that the fast wave dispersion, given by the $\pm \to -$ branch of equation 3.19, can be approximated by the following:

$$n_\parallel^2 = S - n_\perp^2. \tag{3.46}$$

Since $n_\perp^2 \gg |S|$, equation 3.46 suggests the fast wave will be almost entirely evanescent. We can find the fast wave's magnetic field from equations 3.41 and 3.42, but with the fast and slow wave dispersions switched. Substituting the above dispersion into these two equations, we get the following approximate form of the field for the fast wave:

$$\tilde{B}_\theta(k_\perp, z) = -\frac{\mu_0 I}{2\pi k_\perp}\frac{S}{n_\perp^2}\begin{cases} e^{-k_\perp|z|}\sinh k_\perp\frac{\ell}{2} & \text{for } |z| > \ell/2 \\ 1 - e^{-k_\perp\frac{\ell}{2}}\cosh k_\perp z & \text{for } |z| < \ell/2 \end{cases}. \tag{3.47}$$

Note that equation 3.47 ignores the small part of the $k_\perp$ spectrum which contributes propagating waves, as can be seen in figure 3.3. Comparing the above equation to the vacuum field, given by equation 3.30, we see that the fast wave is a factor of $S/n_\perp^2$ smaller than the vacuum field's contribution. In the region $|z| > \ell/2$, it is straightforward to show that the exponentially-decaying near-field is dominated by the vacuum field, followed by the evanescent fast wave and then the near-field part of the slow wave. Similarly, in the region $|z| < \ell/2$, the near-field is again dominated by the vacuum field, followed by the slow wave and then the fast wave.

In plasmas with sufficiently high density to permit fast wave propagation, or alternatively at high enough frequencies where $n_\perp^2 \gg |S|$ is no longer satisfied, the physics of the near-field is expected to change drastically and may be dominated by the slow wave, fast wave, or both. Looking at the slow wave solution given by equation 3.41, the slow wave's near-field plasma response will be larger than the vacuum field when the following condition is satisfied:

$$\left|\frac{RL}{n^2(n_\parallel^2 - n_{\parallel-}^2)}\right| > 1. \tag{3.48}$$

Since the approximate form of the fast wave solution, given by equation 3.47, is predicated on the assumption $n_\perp^2 \gg |S|$, a deeper investigation of the fast wave is warranted in order to determine the conditions for fast wave dominance in the near-field.

3.4 Generalized Solution to the Antenna Wave Equation in Cartesian Coordinates

In the preceding sections we found the solution to the antenna equation for an azimuthally symmetric antenna. While this solution was instructive in highlighting the underlying physics, it is useless for antennas which do not possess azimuthal symmetry. In this section we will derive the fully generalized solution to the antenna wave equation in Cartesian coordinates. We will again assume a cold, magnetized plasma and frequencies such that the vacuum displacement current can be ignored, but aside from that we will abstain from making any limiting assumptions about our system. Our starting point is equation 3.4, which can be separated into the following system of equations:

$$in_y\left(in_x\tilde{E}_y - in_y\tilde{E}_x\right) - \frac{\partial}{\partial\bar{z}}\left(\frac{\partial\tilde{E}_x}{\partial\bar{z}} - in_x\tilde{E}_z\right) - S\tilde{E}_x + iD\tilde{E}_y = S\tilde{E}_{x0} - iD\tilde{E}_{y0}, \tag{3.49}$$

$$\frac{\partial}{\partial\bar{z}}\left(in_y\tilde{E}_z - \frac{\partial\tilde{E}_y}{\partial\bar{z}}\right) - in_x\left(in_x\tilde{E}_y - in_y\tilde{E}_x\right) - iD\tilde{E}_x - S\tilde{E}_y = iD\tilde{E}_{x0} + S\tilde{E}_{y0}, \tag{3.50}$$

$$in_x\left(\frac{\partial\tilde{E}_x}{\partial\bar{z}} - in_x\tilde{E}_z\right) - in_y\left(in_y\tilde{E}_z - \frac{\partial\tilde{E}_y}{\partial\bar{z}}\right) - P\tilde{E}_z = P\tilde{E}_{z0}, \tag{3.51}$$

where we dropped the vacuum displacement current, and have defined $\bar{z} \equiv (c/\omega)z$. $\tilde{E}_j(k_x, k_y, z)$ is the Fourier transform of $E_j(x, y, z)$ in the x and y directions, given by:

$$\tilde{E}_j(k_x, k_y, z) = \int_{-\infty}^{\infty}\int_{-\infty}^{\infty} E_j(x, y, z)e^{-ik_x x}e^{-ik_y y}\mathrm{d}x\mathrm{d}y. \tag{3.52}$$

Equations 3.49–3.51 can be expressed in terms of the magnetic field $\vec{B}$ via the following transformations:

$$
\begin{aligned}
(in_yS - n_xD)\Big[\text{Equation 3.49}\Big] - (in_xS + n_yD)\Big[\text{Equation 3.50}\Big],\\
P\frac{\partial}{\partial\bar{z}}\Big[\text{Equation 3.49}\Big] - (in_xS + n_yD)\Big[\text{Equation 3.51}\Big],\\
P\frac{\partial}{\partial\bar{z}}\Big[\text{Equation 3.50}\Big] - (in_yS - n_xD)\Big[\text{Equation 3.51}\Big].
\end{aligned}
\tag{3.53}
$$

The resulting three equations are as follows:

$$
(in_xS + n_yD)\frac{\partial\tilde{B}_x}{\partial\bar{z}} + (in_yS - n_xD)\frac{\partial\tilde{B}_y}{\partial\bar{z}} - (RL - Sn_\perp^2)\tilde{B}_z = RL\tilde{B}_{z0}, \tag{3.54}
$$

$$
\begin{aligned}
(-in_y^2D + n_xn_yS + iDP)\tilde{B}_x + (-n_x^2S + in_xn_yD + SP)\tilde{B}_y -\\
in_yP\frac{\partial\tilde{B}_z}{\partial\bar{z}} + P\frac{\partial^2\tilde{B}_y}{\partial\bar{z}^2} = -iDP\tilde{B}_{x0} - SP\tilde{B}_{y0},
\end{aligned}
\tag{3.55}
$$

$$
\begin{aligned}
(-n_y^2S - in_xn_yD + SP)\tilde{B}_x + (in_x^2D + n_xn_yS - iDP)\tilde{B}_y -\\
in_xP\frac{\partial\tilde{B}_z}{\partial\bar{z}} + P\frac{\partial^2\tilde{B}_x}{\partial\bar{z}^2} = -SP\tilde{B}_{x0} + iDP\tilde{B}_{y0}.
\end{aligned}
\tag{3.56}
$$

Equation 3.54 can be inserted into equations 3.55 and 3.56 to eliminate $\tilde{B}_z$, resulting in two coupled differential equations for $\tilde{B}_x$ and $\tilde{B}_y$:

$$
\begin{aligned}
\left[\frac{in_yP(in_xS + n_yD)}{RL - Sn_\perp^2}\right]\frac{\partial^2\tilde{B}_x}{\partial\bar{z}^2} + \left[\frac{in_yP(in_yS - n_xD)}{RL - Sn_\perp^2} - P\right]\frac{\partial^2\tilde{B}_y}{\partial\bar{z}^2} +\\
\Big[in_y(in_xS + n_yD) - iDP\Big]\tilde{B}_x + \Big[-in_x(in_xS + n_yD) - SP\Big]\tilde{B}_y =\\
\left[\frac{in_yPRL}{RL - Sn_\perp^2}\right]\frac{\partial\tilde{B}_{z0}}{\partial\bar{z}} + iDP\tilde{B}_{x0} + SP\tilde{B}_{y0},
\end{aligned}
\tag{3.57}
$$

$$
\begin{aligned}
\left[\frac{-in_xP(in_xS + n_yD)}{RL - Sn_\perp^2} + P\right]\frac{\partial^2\tilde{B}_x}{\partial\bar{z}^2} + \left[\frac{-in_xP(in_yS - n_xD)}{RL - Sn_\perp^2}\right]\frac{\partial^2\tilde{B}_y}{\partial\bar{z}^2} +\\
\Big[in_y(in_yS - n_xD) + SP\Big]\tilde{B}_x + \Big[-in_x(in_yS - n_xD) - iDP\Big]\tilde{B}_y =\\
\left[\frac{-in_xPRL}{RL - Sn_\perp^2}\right]\frac{\partial\tilde{B}_{z0}}{\partial\bar{z}} - SP\tilde{B}_{x0} + iDP\tilde{B}_{y0}.
\end{aligned}
\tag{3.58}
$$

Equations 3.57 and 3.58 can be decoupled to get a differential equation for either $\tilde{B}_x$ or $\tilde{B}_y$, although the math is rather tedious. The final result is two fourth order differential equations for $\tilde{B}_x$ and $\tilde{B}_y$, given by:

$$\left(\frac{\partial^2}{\partial z^2} + k_{\parallel+}^2\right)\left(\frac{\partial^2}{\partial z^2} + k_{\parallel-}^2\right)\begin{bmatrix}\tilde{B}_x \\ \tilde{B}_y\end{bmatrix} = \frac{\omega^4}{c^4}\begin{bmatrix} f(z) \\ g(z)\end{bmatrix}, \tag{3.59}$$

where $k_{\parallel\pm}$ is given by the following dispersion relation:

$$\left(\frac{c^2}{\omega^2}\right)k_{\parallel\pm}^2 = S - \frac{n_\perp^2}{2}\left(1+\frac{S}{P}\right) \pm \sqrt{\left(\frac{n_\perp^2}{2}\right)^2\left(1-\frac{S}{P}\right)^2 + D^2\left(1-\frac{n_\perp^2}{P}\right)}, \tag{3.60}$$

and $n_\perp^2 = n_x^2 + n_y^2$. Aside from the new definition of $n_\perp^2$, this dispersion relation is identical to the one derived in cylindrical coordinates in equation 3.19. The source terms $f(z)$ and $g(z)$ are given by the following:

$$f(z) = -S\frac{\partial^2\tilde{B}_{x0}}{\partial\bar{z}^2} + iD\frac{\partial^2\tilde{B}_{y0}}{\partial\bar{z}^2} + \left[-in_y(in_yS + n_xD) - RL\left(1-\frac{n_x^2}{P}\right)\right]\tilde{B}_{x0} + \left[in_y(in_xS - n_yD) + n_xn_y\frac{RL}{P}\right]\tilde{B}_{y0}, \tag{3.61}$$

$$g(z) = -iD\frac{\partial^2\tilde{B}_{x0}}{\partial\bar{z}^2} - S\frac{\partial^2\tilde{B}_{y0}}{\partial\bar{z}^2} + \left[in_x(in_yS + n_xD) + n_xn_y\frac{RL}{P}\right]\tilde{B}_{x0} + \left[-in_x(in_xS - n_yD) - RL\left(1-\frac{n_y^2}{P}\right)\right]\tilde{B}_{y0}. \tag{3.62}$$

Alternatively, one can combine equations 3.55 and 3.56 with $\nabla\cdot\vec{B} = 0$, and they will arrive at the same fourth order differential equation given by 3.59 (the math is a bit easier this way). Equation 3.59 is identical to the differential equation that was solved in section 3.2 for cylindrical coordinates, and so its general solution is the same:

$$\begin{bmatrix} \tilde{B}_x(k_x,k_y,z) \\ \tilde{B}_y(k_x,k_y,z) \end{bmatrix} = \frac{\omega^4}{c^4}\int_{-\infty}^{z} \left[\frac{ie^{ik_{\parallel+}(z-z')}}{2k_{\parallel+}(k_{\parallel+}^2-k_{\parallel-}^2)} + \frac{ie^{ik_{\parallel-}(z-z')}}{2k_{\parallel-}(k_{\parallel-}^2-k_{\parallel+}^2)} \right] \begin{bmatrix} f(z') \\ g(z') \end{bmatrix} dz'$$
$$+ \frac{\omega^4}{c^4}\int_{z}^{\infty} \left[\frac{ie^{-ik_{\parallel+}(z-z')}}{2k_{\parallel+}(k_{\parallel+}^2-k_{\parallel-}^2)} + \frac{ie^{-ik_{\parallel-}(z-z')}}{2k_{\parallel-}(k_{\parallel-}^2-k_{\parallel+}^2)} \right] \begin{bmatrix} f(z') \\ g(z') \end{bmatrix} dz'. \quad (3.63)$$

The Cartesian source terms given by equations 3.61 and 3.62 are lengthier than their azimuthally-symmetric counterparts (equations 3.20 and 3.22), but that is the trade-off we make in developing a fully generalized Cartesian solution. When $n_y = 0$, the variable substitutions $x \to r$ and $y \to \theta$ in equations 3.60–3.63 will return the general solution that was derived for the azimuthally-symmetric case in section 3.2. A fully generalized solution to the homogeneous cold plasma wave equation in cylindrical coordinates is given by [78], and consists of an infinite summation of Bessel function eigenmodes. Depending on the geometry of a given antenna, it may be advantageous to use either the generalized Cartesian solution above or the generalized cylindrical solution.

3.5 Discussion and Concluding Remarks

In this chapter we successfully developed a semi-analytic model for determining the electromagnetic field due to a current-driven antenna in a cold, magnetized plasma. We showed in section 3.2 that the vacuum electric field of the antenna couples to the plasma conductivity tensor and acts as a source that drives plasma waves. In section 3.2.3, we derived a general solution to the antenna wave equation for antennas with azimuthal symmetry. The general solution is a superposition of the fast and slow waves, which are the two fundamental modes of the cold plasma. It is typical in many laboratory plasmas for the fast wave to be evanescent, with only the slow wave being measurable far away from the antenna. In spite of this, it was shown that the fast wave physics *cannot* be ignored due to the fact that the antenna will always couple to both branches, even if one of them is evanescent. This is reflected in

the general solution of equation 3.28, which shows that the amplitude of the slow wave is a function of the fast wave dispersion (and vice versa).

At every point in the plasma, the vacuum field of the antenna acts as an infinitesimal point source emitter that launches both forward and backward propagating waves. The total field is then found from the aggregate sum of all these infinitesimal point sources, which is the physical interpretation of the integral across the vacuum field in equation 3.28. For observation points close to the antenna, the interference of forward and backward propagating waves gives rise to what we refer to as the "near-field" of the antenna. Far away from the antenna, the field is shown to be a superposition of propagating plane waves (forward propagating for $z \gg 0$, and backwards for $z \ll 0$). Because of this, we define the radiation zone of the plasma as the region sufficiently far away from the antenna such that the near-field and vacuum field are vanishingly small compared to the propagating part of the field. In deriving equation 3.28, we made the assumption that our plasma is infinite and unbounded, which allowed us to ignore possible complications due to reflected waves. Section 3.2 can be generalized to allow solutions which account for finite plasma boundaries, although this adds an additional layer of complexity that is outside the scope of the present discussion.

In order to show how this model can be applied, we solved it for the case of an electric dipole antenna aligned along the background magnetic field. For plasma conditions that are typical of laboratory plasmas, such as those found in the Large Plasma Device (LAPD), we showed that the magnetic field is almost entirely azimuthal with the majority of its power at large values of $k_\perp$, where the slow wave is commonly known as the *inertial Alfvén wave*. The wave was shown to emit cones out of either end of the dipole, where the angle of propagation is given by equation 3.45. This is consistent with previous analytic studies of inertial Alfvén waves launched by a disk exciter in a cold plasma [72].

To summarize, this model provides a straightforward recipe for determining the plasma field excited by current-driven antennas, given the vacuum field of the antenna. For an azimuthally-symmetric antenna, the steps are as follows:

1. Calculate the first order Hankel transform of the vacuum field, defined by equation 3.13.

2. Calculate the "source" terms $f(z)$ and $g(z)$, given by equations 3.20 and 3.22.

3. Calculate the plasma response field, given by equation 3.28. The total field is then the sum of this solution plus the vacuum field.

4. Calculate the inverse Hankel transform of the above solution to get the radial and azimuthal fields of the plasma, $B_r(r, z)$ and $B_\theta(r, z)$.

5. $B_z(r, z)$ can then be found from $\nabla \cdot \vec{B} = 0$, and everything else from the rest of Maxwell's equations.

While the majority of this chapter focused on antennas with azimuthal symmetry, mostly for demonstrative purposes, in section 3.4 we provided a fully generalized solution for Cartesian coordinates that is similar in format and methodology.

CHAPTER 4

Diagnostic for the Measurement of the Ion Density Ratio in a Two Ion Plasma

In this chapter we propose and test an efficient new diagnostic for determining spatially-resolved measurements of the ion density ratio in a magnetized two-ion plasma. Shear Alfvén waves were injected into a mixed helium-neon plasma using a magnetic dipole antenna, for frequencies spanning the ion cyclotron regime. Two distinct propagation bands are observed, bounded by $\omega < \Omega_{Ne}$ and $\omega_{ii} < \omega < \Omega_{He}$, where ω_{ii} is the ion-ion hybrid frequency and Ω_{He} and Ω_{Ne} are the helium and neon cyclotron frequencies, respectively. A theoretical analysis of the cutoff frequency was performed and shows it to be largely unaffected by kinetic electron effects and collisionality, although it can deviate significantly from ω_{ii} in the presence of warm ions due to ion finite Larmor radius (FLR) effects. A new diagnostic technique and accompanying algorithm was developed in which the measured parallel phase velocity is numerically fit to the predicted inertial Alfvén wave dispersion in order to resolve the local ion density ratio. A major advantage of this algorithm is that, other than a measurement of the parallel phase velocity, it only requires knowledge of the background field in order to be employed. This diagnostic technique was tested on the Large Plasma Device and was successful in yielding radially-localized measurements of the ion density ratio.

4.1 Introduction

The propagation of shear Alfvén waves in a multi-ion species plasma, and the consequent interaction of the waves with the plasma, is important in space and astrophysical settings as well as in the laboratory. Each additional ion species in a magnetized plasma introduces a new resonance (at that ion's cyclotron frequency) and an associated cutoff for the shear Alfvén wave, leading to propagation in a series of frequency bands, one per ion species. Plasma in the Earth's magnetosphere is composed of protons as well as ionized heavier elements such as helium and oxygen. In that setting, shear Alfvén waves propagating in bands near or above the species' gyrofrequencies are called Electromagnetic ion cyclotron waves (EMIC waves) [111, 81, 33]. EMIC waves play an important role in the Earth's radiation belts, where they can be excited by Doppler-shifted cyclotron resonance (DCR) with energetic ions and subsequently can interact with trapped relativistic electrons, causing scattering and precipitation [21, 94, 25]. In magnetically-confined plasmas for fusion energy research, such as tokamaks, Alfvém eigenmodes (AEs) can be excited by energetic particles which could be created by heating schemes (such as neutral beam injection or heating by radio frequency waves) or by fusion reactions (e.g. deuterium-tritium fusion generated alpha particles). AEs can in turn interact with and scatter these energetic particles, leading to their transport [46]. While most current tokamak experiments typically utilize pure deuterium plasmas, fusion reactors are expected to have comparable densities of deuterium and tritium, leading to important changes to the properties of AEs and to wave-particle interactions that can cause transport and loss of energetic particles [1].

For plasmas with two ion species, a resonant frequency exists for perpendicularly propagating waves known as the ion-ion hybrid resonance. This resonant frequency was first predicted by [16] and later observed in experiments by [75]. For waves with cross-field scale lengths comparable to the electron skin depth, it can be shown that the ion-ion hybrid resonance doubles as a cutoff frequency for shear wave propagation [103]. One application of

this is in magnetic fields with mirror-like boundary conditions, such as the magnetosphere, where the reflection of shear waves at the ion-ion cutoff boundary layer can trap waves, effectively creating an ion-ion hybrid wave resonator. [77] investigated measurements taken by GEOS spacecraft, and noted that the results were consistent with waves being reflected at the ion-ion hybrid cutoff boundary layer. A theoretical study done by [43] concluded that the ion-ion hybrid resonator concept in the planetary magnetosphere was plausible, and this was later confirmed experimentally by [101] in the Large Plasma Device (LAPD) at UCLA.

The ion-ion hybrid frequency is of interest in magnetized plasmas with two ion species, such as those found in fusion plasmas with comparable densities of D-T, as it can be used as a diagnostic tool to resolve the ratio of ion densities. While many diagnostics exist for measuring the total ion density in tokamaks, both via direct and indirect measurements, there exist few techniques for locally measuring the density profiles of individual ion species in a multi-ion species plasma. In Section 4.2 we will show that the ion-ion hybrid frequency, ω_{ii}, can be expressed analytically as a function of the ratio of ion densities. This means that, in principle, if one could measure the ion-ion hybrid frequency, they could then use that information in conjunction with an electron density measurement to resolve the individual ion density profiles of a quasi-neutral plasma. Additionally, precise knowledge of the ratio of ion densities is valuable in the optimization of various tokamak heating schemes [57]. This topic has been explored in great detail, both in mixed plasmas [106] as well as single-species plasmas containing impurities [19]. In addition, detection of ω_{ii} by fast wave reflectometry has been proposed as a diagnostic in D-T tokamaks [54].

Previous experiments on the LAPD have investigated the ion-ion hybrid frequency as a possible diagnostic for the mix ratio of a two-ion species plasma. A parallel cutoff frequency has previously been observed in the LAPD for two-ion species plasmas [103], and its potential as a diagnostic has also been explored [102], the latter of which focused primarily on measuring the cutoff via the power spectrum of the wave. The focus of this paper will be on measuring the ion-ion cutoff frequency of two-ion shear Alfvén waves under a much wider

range of conditions, and by a variety of different methods, in order to assess its viability as a diagnostic for measuring the ion density ratio.

The remainder of this chapter is organized as follows. In Section 4.2 we discuss the theory behind the two-ion cutoff frequency, and show that a diagnostic based around measuring ω_{ii} is valid for all electron temperatures as well as ions with negligible finite Larmor radius (FLR) effects. In Section 4.3, we describe the experimental setup of launching and measuring shear Alfvén waves in the LAPD, which consists of a loop antenna and a series of magnetic induction (B-dot) probes. In Section 4.4, we extend the work of [102] by measuring ω_{ii} for a much wider range of plasma parameters, as well as employing a new technique in which we systematically measure the parallel wave phase in order to resolve the cutoff frequency. Additionally, a smaller antenna is constructed as a diagnostic and is successfully used to measure the cutoff frequency (and therefore the ion density ratio) at various radial positions in the plasma. A conclusion and discussion of future work is presented in Section 4.5.

4.2 Theory

In this section we will derive the ion-ion hybrid cutoff frequency [16], which is a cutoff frequency that exists between the two ion cyclotron frequencies for inertial Alfvén waves in a two-ion species plasma. This cutoff frequency is well understood and has been extensively studied in the lab [101, 102, 103]. Previous authors have explored the scaling of the ion-ion hybrid cutoff frequency as various effects outside the scope of the cold plasma model are considered. A generalization of the two-ion cutoff frequency in the presence of ion finite Larmor radius (FLR) effects was derived by [30], for plasma conditions that are expected to be typical in the ITER device. In this section we build upon the work of previous authors by considering the scaling of the ion-ion hybrid cutoff frequency under various non-ideal plasma conditions, in order to assess its viability as a diagnostic tool.

A uniform magnetized plasma, subjected to a small monochromatic perturbation, may

be described by the following system of equations:

$$\nabla \times \nabla \times \vec{E} = \left(\frac{\omega}{c}\right)^2 \overleftrightarrow{\varepsilon} \cdot \vec{E}, \quad \text{where} \quad \overleftrightarrow{\varepsilon} = \begin{bmatrix} \varepsilon_\perp & \varepsilon_{xy} & 0 \\ -\varepsilon_{xy} & \varepsilon_\perp & 0 \\ 0 & 0 & \varepsilon_\parallel \end{bmatrix}, \tag{4.1}$$

and $\vec{E}$ is the electric field of the wave perturbation and $\overleftrightarrow{\varepsilon}$ is the dielectric tensor of the plasma. The cross-field currents due to polarization drift and $E \times B$ slippage are captured by $\varepsilon_\perp$ and ε_{xy}, respectively, while the tensor element $\varepsilon_\parallel$ consists primarily of the parallel electron response. It can be shown that for $\omega \ll \Omega_{ci}$, the $E \times B$ drift of the ions and electrons are nearly identical and the off-diagonal term ε_{xy} is vanishingly small compared to the diagonal elements. As we are interested in the frequency band between the two ion cyclotron frequencies of a two-ion plasma, it's worth emphasizing that this is *not* true for our case, and so these dielectric elements must be preserved. For a cold, fluid-like plasma, the dielectric tensor elements can be expressed in Stix notation [93] as the following:

$$\begin{aligned} \varepsilon_\perp &\equiv S = -\sum_{ions} \frac{\omega_{pi}^2}{\omega^2 - \Omega_{ci}^2}, \\ \varepsilon_{xy} &\equiv -iD = -i\sum_{ions} \frac{\omega}{\Omega_{ci}} \frac{\omega_{pi}^2}{\omega^2 - \Omega_{ci}^2}, \\ \varepsilon_\parallel &\equiv P = -\frac{\omega_{pe}^2}{\omega^2}. \end{aligned} \tag{4.2}$$

We have assumed $\omega \ll \Omega_{ce}$, which allows us to drop the vacuum displacement current, as well as the cross-field electron and parallel ion currents. Additionally, we invoked quasineutrality in order to express the electron $E \times B$ drift in terms of ion currents. The cold plasma dispersion relation can be found from the determinant of equation 4.1 (once it has been Fourier transformed into $\vec{k}$-space), and is given by the following expression:

$$n_\parallel^2 = S\left(1 - \frac{1}{2}\frac{n_\perp^2}{P}\right) - \frac{1}{2}n_\perp^2 \pm \sqrt{\left(\frac{n_\perp^2}{2}\right)^2 \left(1 - \frac{S}{P}\right)^2 + D^2\left(1 - \frac{n_\perp^2}{P}\right)}, \tag{4.3}$$

where $n_j \equiv (c/\omega)k_j$ is the refractive index for direction j, and $n_\perp^2 = n_x^2 + n_y^2$. For the frequencies being considered, it is straightforward to verify that the quantity within the radical of equation 4.3 is positive-definite, meaning $k_\parallel$ must be either purely real or purely imaginary. In other words, the cold, collisionless fluid model does not permit damped propagating wave solutions, and any observed damping must be explained by effects outside the scope of this simple model. The two branches of equation 4.3 are commonly known as the fast and slow waves, due to the relative magnitude of their respective phase velocities, and are the fundamental modes of a cold plasma. In the limit $k_\perp \to 0$, the two modes of equation 4.3 reduce to $n_\parallel^2 = S \pm D$, whose field vectors correspond to right and left handed circularly polarized waves, respectively. In this limit, the wave is mediated entirely by cross-field currents – namely, the ion polarization current and $E \times B$ drift. When $k_\perp \neq 0$, in order to satisfy $\nabla \cdot \vec{J} = 0$, a parallel electron current is introduced. It is the interplay of all three of these currents which result in the dispersion relation of equation 4.3. Below the ion cyclotron frequency, the fast wave is generally evanescent in typical LAPD plasmas, meaning the slow (or shear) Alfvén wave is the only cold plasma wave that can propagate.

Figure 4.1 shows the dispersion relation for the shear Alfvén wave in a 50% He/50% Ne plasma, at various values of $k_\perp$ (normalized to the electron skin depth $\delta_e \equiv c/\omega_{pe}$). An electron density of $n_e = 10^{12}$ cm^{-3} and background field $B_0 = 1500$ G was assumed, as these are typical plasma conditions in the Large Plasma Device (LAPD) [36]. Two propagation bands are observed in figure 4.1, with the lower band defined by $\omega < \Omega_{Ne}$, and the upper band bound by $\omega_{cut} < \omega < \Omega_{He}$, where ω_{cut} is some cutoff frequency that exists between the two ion cyclotron frequencies. The addition of each new ion species to the plasma introduces an additional cutoff frequency and resonance, and so this cutoff frequency is unique to a plasma with two ion species. At sufficiently large $k_\perp$, we note in figure 4.1 that the cutoff frequency of the upper band converges towards a frequency that is independent of $k_\perp$.

The cutoff frequency of the shear wave was numerically found from equation 4.3 for a wide range of $k_\perp$, for several different mixes of He/Ne, and the results are shown in figure 4.2.

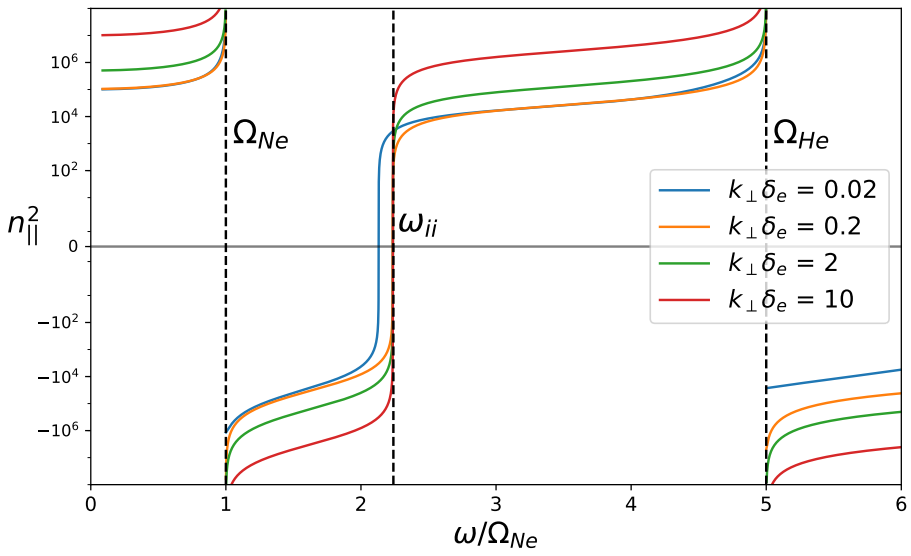

Figure 4.1: Dispersion relation of the shear Alfvén wave, for an evenly mixed He/Ne plasma. Dashed lines mark the locations of the ion cyclotron frequencies and ion-ion hybrid frequency. At sufficiently large $k_\perp$, the cutoff frequency converges to the ion-ion hybrid frequency ω_{ii}.

It can be seen that at large enough $k_\perp \delta_e$, the cutoff frequency converges to an asymptotic value, denoted by a dashed line. An analytic expression for the asymptotic limit of the cutoff frequency can be found by considering the limit where $n_\perp^2 \gg |S|, |D|$ - a regime that is typical for LAPD antenna experiments[1]. In this limit, the shear wave branch of the dispersion relation given by equation 4.3 can be approximated by the following:

$$n_\parallel^2 = \left(S + \frac{D^2}{n_\perp^2} \right) \left(1 + \delta_e^2 k_\perp^2 \right). \tag{4.4}$$

An interesting observation of equation 4.4 is that, for the relatively large values of $k_\perp$ assumed, the $E \times B$ slippage current ultimately manifests as only a tiny contribution to the shear wave, in the form of a correction factor $D^2/n_\perp^2$. Thus, in the limit of large $k_\perp$, the shear wave is mediated almost entirely by the cross-field ion polarization and parallel electron

[1]Note that this limit is not satisfied near the ion cyclotron frequencies, although the cold fluid model isn't valid there anyway.

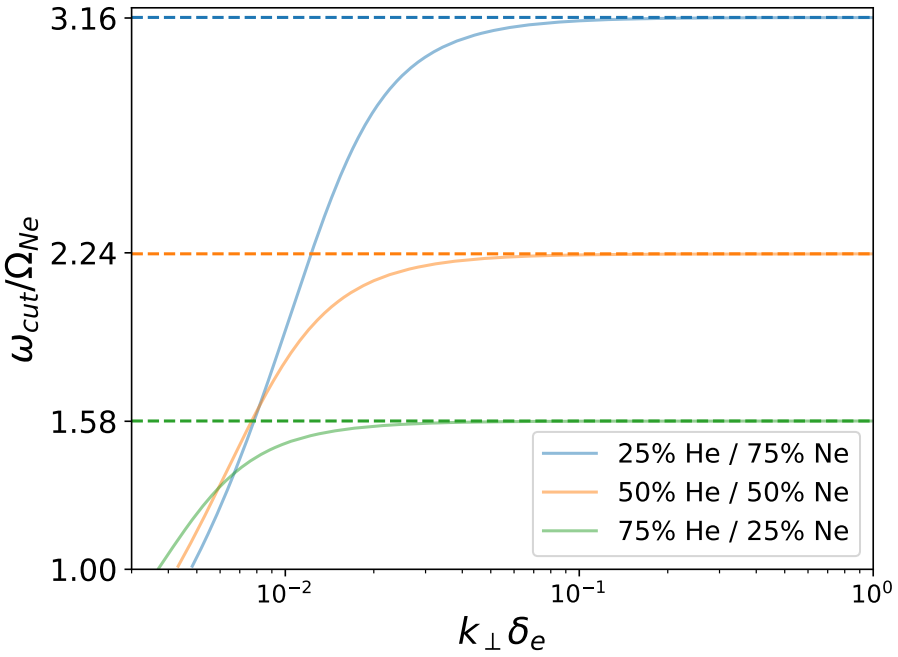

Figure 4.2: Cutoff frequency of the shear wave as a function of $k_\perp$ in a two-ion species plasma, for several mixes of helium/neon. When $k_\perp \delta_e$ is sufficiently large, the cutoff frequency converges to an asymptotic value that is equal to the ion-ion hybrid frequency for that mix ratio (denoted by a dashed line).

currents. Previous authors [72] have noted that the $E \times B$ slippage current vanishes at low frequency (which can be seen by inspection of equation 4.2), which physically corresponds to all particle species having the same $E \times B$ drift, resulting in no net current. For waves with cross-field scale length comparable to the electron skin depth, the $E \times B$ slippage current plays a similarly minuscule role in the dispersion of the wave, although we emphasize in this case that it is due to the largeness of $n_\perp^2$ relative to D. A similar result was derived by [72], and it was concluded that the $E \times B$ contribution is vanishingly small except for a very narrow frequency band around the ion cyclotron frequency. In the absence of the $E \times B$ correction term, equation 4.4 is commonly known as the dispersion relation of the *inertial Alfvén wave*.

For the particular case of a two-ion species plasma, the dispersion relation of the inertial Alfvén wave can be written in the following form:

$$n_\parallel^2 = \frac{(\omega_{p1}^2 + \omega_{p1}^2)(\omega^2 - \omega_{ii}^2)}{(\Omega_{c1}^2 - \omega^2)(\omega^2 - \Omega_{c2}^2)} \left(1 + \delta_e^2 k_\perp^2\right), \quad \text{where} \quad \omega_{ii}^2 = \frac{\Omega_{c1}^2 \omega_{p2}^2 + \Omega_{c2}^2 \omega_{p1}^2}{\omega_{p1}^2 + \omega_{p2}^2}. \tag{4.5}$$

In equation 4.5, ω_{ii} is the *ion-ion hybrid frequency*, and corresponds to the asymptotic limit of the cutoff frequency seen in figure 4.1. It was first discovered as a resonance for cross-field propagation [16], although in the context of parallel propagation we see that it acts as a cutoff. Since ω_{ii} is found from the root of S, physically this corresponds to the frequency where the ion polarization currents of the two ion species are equal in magnitude and oscillate π out of phase, resulting in no net cross-field current. The ion-ion hybrid cutoff is of interest to us as a potential diagnostic, as it can be rewritten to be a function of the ion density ratio:

$$\frac{\omega_{ii}}{\Omega_2} = \sqrt{\frac{1 + \dfrac{m_2}{m_1}\dfrac{n_2}{n_1}}{1 + \dfrac{m_1}{m_2}\dfrac{n_2}{n_1}}}. \tag{4.6}$$

Equation 4.6 suggests that, in principle, if one could measure the ion-ion hybrid cutoff,

they would then be able to resolve the ratio of ion densities. The ability to locally measure ω_{ii}, therefore, would provide a valuable diagnostic and is the primary motivation for the present study. This has been done before by [102] in a hydrogen-helium plasma, where the power spectrum was measured in order to infer the value of the cutoff. Additionally, previous investigations have attempted to measure ω_{ii} in the context of cross-field resonance, both as an impurity diagnostic [19] as well as for evenly mixed plasmas [106], although the latter utilized reflectometry and therefore could only yield global measurements.

Generally speaking, an antenna's power will be distributed across a continuous spectrum of $k_\perp$ waves, each with their own respective cutoff frequency, as seen previously in figure 4.2. The full waveform is then found from the aggregate sum of all these different $k_\perp$ waves. For an azimuthally symmetric wave, this can be written mathematically as the following:

$$E_j(r,z,t) = e^{-i\omega t}\int_0^\infty C(k_\perp)J_1(k_\perp r)e^{ik_\parallel(k_\perp)z}k_\perp dk_\perp \quad + \quad c.c., \tag{4.7}$$

Where $C(k_\perp)$ is, in general, set by the boundary conditions of the antenna used to excite the wave [72, 73]. This would normally be problematic for an experimenter that wishes to measure the cutoff frequency, as each value of $k_\perp$ will contribute its own unique cutoff (as seen in figure 4.2). If the majority of wave power imposed by an antenna, however, is contained at large values of $k_\perp$, where $\omega_{cut} \to \omega_{ii}$, the cutoff frequency should be fairly robust as a measurable quantity. Deviations from the large $k_\perp$ limit, even in a small part of the antenna's $k_\perp$ spectrum, will result in some "filling in" of the propagation gap seen in figure 4.1. Therefore an idealized diagnostic for measuring the ion-ion hybrid cutoff frequency should be constructed such that it imparts nearly all of its power at values of $k_\perp$ which satisfy $n_\perp^2 \gg |S|, |D|$, where the inertial Alfvén dispersion limit of equation 4.5 holds.

In the limit $k_\perp\delta_e \to 0$, where our previous assertion $n_\perp^2 \gg |S|, |D|$ breaks down, we see from figure 4.2 that the cutoff diverges from ω_{ii}. In this limit, the inertial branch turns into the right handed wave $n_\parallel^2 = S + D$, which has no cutoff in the ion cyclotron regime. The

fast wave branch turns into the left handed wave $n_{\parallel}^2 = S - D$, which has the following cutoff frequency for a two-ion species plasma:

$$\omega_{cut} = \frac{\Omega_{c1}^2\omega_{p2}^2 + \Omega_{c2}^2\omega_{p1}^2}{\Omega_{c2}\omega_{p1}^2 + \Omega_{c1}\omega_{p2}^2}. \tag{4.8}$$

While the present study will be considering waves whose energy is almost entirely contained in values of $k_\perp$ where this cutoff isn't valid, it's worth mentioning that equation 4.8 can similarly be written in terms of n_2/n_1 and therefore be used as a diagnostic as well. [106] explored this cutoff frequency as a diagnostic tool, although it was again in the context of cross-field propagation.

4.2.1 Kinetic Considerations - Thermal Effects

The derivation of ω_{ii} as a parallel cutoff frequency in the preceding section is predicated on the assumption that the plasma can be treated as a perfectly cold fluid. If we are to develop a diagnostic around measuring the ion-ion hybrid cutoff frequency, it is in our interest to determine under which plasma conditions ω_{ii} *fails* to accurately approximate the two-ion cutoff frequency. The purpose of this section is to determine the behavior of the two-ion cutoff frequency when plasma effects outside the scope of the cold plasma model are considered. Previous theoretical studies have explored the impact of various kinetic effects on the two-ion cutoff frequency in the context of fusion plasmas [30].

In the context of kinetic theory, deviations from cold fluid theory fall under two major categories: finite ion Larmor radius (FLR) and thermal effects. We will first consider a plasma with negligible FLR effects but arbitrary temperature, whose dielectric components can be written as the following [15]:

$$\begin{aligned}
\varepsilon_\perp &= \frac{1}{2}\sum_s \frac{\omega_{ps}^2}{\omega^2}\zeta_{0,s}\left[Z(\zeta_{1,s}) + Z(\zeta_{-1,s})\right], \\
\varepsilon_{xy} &= -\frac{1}{2}\sum_s \frac{\omega_{ps}^2}{\omega^2}\zeta_{0,s}\left[Z(\zeta_{1,s}) - Z(\zeta_{-1,s})\right], \\
\varepsilon_\parallel &= -\sum_s \frac{\omega_{ps}^2}{\omega^2}\zeta_{0,s}^2 Z'(\zeta_{0,s}),
\end{aligned} \tag{4.9}$$

where $\zeta_{n,s} \equiv (\omega - n\Omega_{c,s})/\sqrt{2}k_\parallel v_{Th,s}$, $Z(\zeta)$ is the plasma dispersion function, and the summations are over all particles species s. We retrieve the cold plasma dielectric of equation 4.2 in the limit $\zeta_{n,s} \gg 1$, although this limit is generally *not* true - particularly for the parallel flowing electrons, as well as the ions near their respective cyclotron frequency. If we avoid frequencies near the ion cyclotron frequencies, then we can expand the plasma dispersion function to first order:

$$\begin{aligned}
\varepsilon_\perp &= -\sum_{ions} \frac{\omega_{pi}^2}{\omega^2 - \Omega_{ci}^2} + \frac{\omega_{pe}^2}{\omega^2}\zeta_{0,e}^2 Z'\left(\frac{\Omega_e}{\sqrt{2}k_\parallel v_{Th,e}}\right), \\
\varepsilon_{xy} &= \sum_{ions} \frac{\Omega_{ci}}{\omega}\frac{\omega_{pi}^2}{\omega^2 - \Omega_{ci}^2} + \frac{\omega_{pe}^2}{\omega^2}\zeta_{0,e} Z\left(\frac{\Omega_e}{\sqrt{2}k_\parallel v_{Th,e}}\right), \\
\varepsilon_\parallel &= -\frac{\omega_{pe}^2}{\omega^2}\zeta_{0,e}^2 Z'(\zeta_{0,e}).
\end{aligned} \tag{4.10}$$

In the above expressions, we made use of the expansion $Z(\zeta) \approx -1/\zeta$ for $|\zeta| \ll 1$. Additionally, we expanded the electron dispersion functions around $\omega \ll |\Omega_{ce}|$ to first order:

$$Z\left(\frac{\omega \pm \Omega_{ce}}{\sqrt{2}k_\parallel v_{Th,e}}\right) \approx Z\left(\frac{\pm\Omega_{ce}}{\sqrt{2}k_\parallel v_{Th,e}}\right) + Z'\left(\frac{\pm\Omega_{ce}}{\sqrt{2}k_\parallel v_{Th,e}}\right)\left(\frac{\omega}{\sqrt{2}k_\parallel v_{Th,e}}\right). \tag{4.11}$$

Exploiting the evenness and oddness of Z' and Z (and ignoring imaginary terms due to Landau and cyclotron resonance), respectively, allows us to arrive at equation 4.10.

If we make the assertion $|\Omega_{ce}| \gg \sqrt{2}k_\parallel v_{Th,e}$ (a condition which is easily satisfied in LAPD plasmas), then the electron contribution to $\varepsilon_\perp$ and ε_{xy} can be dropped, and the resulting

expressions are identical to their cold plasma counterparts from equation 4.2. Therefore the only manifestation of "thermal" electrons in our dispersion relation is in modifying the parallel electron current. Since our polarization and $E \times B$ dielectric terms are the same as for the cold fluid case, we can again make the assertion $n_\perp^2 \gg |S|,\ |D|$ and use the same dispersion relation 4.4 derived for the cold plasma case, but with the warm $\varepsilon_\parallel$ from equation 4.10:

$$n_\parallel^2 = \varepsilon_\perp \left(1 - \frac{n_\perp^2}{\varepsilon_\parallel}\right) = S\left(1 + \frac{\delta_e^2 k_\perp^2}{\zeta_{0,e}^2 Z'\left(\zeta_{0,e}\right)}\right). \tag{4.12}$$

In the limit of very hot electrons, $|\zeta_{0,e}| \ll 1$ and $Z'(\zeta) \approx -2$. Substituting this expression into 4.12 and solving for $n_\parallel^2$, we get the following dispersion for shear Alfvén waves in the limit of hot electrons:

$$n_\parallel^2 = \frac{S}{1 + S k_\perp^2 \lambda_{De}^2}, \tag{4.13}$$

where λ_{De} is the electron Debye length of the plasma. Equation 4.13 is most commonly known as the kinetic Alfvén wave in the literature, and so for the sake of consistency we will call it this as well. We will refer to the more general solution of equation 4.12 as the *warm Alfvén wave*.

We see that the root of the kinetic Alfvén wave still corresponds to $S = 0$, meaning ω_{ii} is still a valid approximation for the cutoff even in the limit of hot electrons. The next step is to determine the cutoff behavior for intermediate values of $\zeta_{n,s}$, where kinetic effects such as Landau resonance are expected to play a larger role. Previous attempts to measure the parallel dispersion for shear waves with finite $k_\perp$ [61] found that a fully generalized complex kinetic solution had the best agreement with experimental data in the LAPD. For simplicity we will continue to assume our dispersion is mediated by cold ions across the field and kinetic electrons along the field, and focus on solving equation 4.12 for $k_\parallel(\omega)$. The Newton-Raphson root-finding method was employed in order to solve 4.12 numerically. For most frequencies,

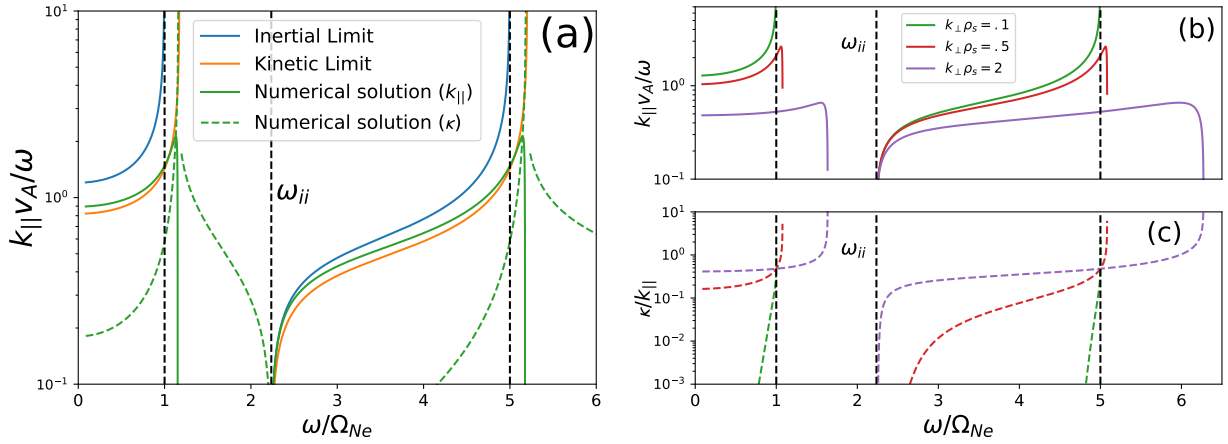

Figure 4.3: (a) Dispersion relation for a 50 % He/50 % Ne plasma with cold ions and warm electrons, compared to the cold and hot limits of the dispersion. Dashed lines mark the ion cyclotron frequencies and ion-ion hybrid frequency. (b) Dispersion relation and (c) spatial damping, for several temperature cases.

the cold plasma dispersion 4.4 was found to be a satisfactory initial estimate of the root in order to allow the algorithm to converge. For frequency bands where $\zeta \ll 1$, however, the kinetic dispersion 4.13 was used as an initial estimate of the root instead.

Figure 4.3a shows $k_\parallel(\omega)$, as found numerically from equation 4.12, alongside its inertial (equation 4.4) and kinetic (equation 4.13) limits. A 50% He/50% Ne plasma was considered, with $B_0 = 1500$ G, $T_e = 5$ eV, $n_e = 10^{12}$ cm^{-3}, and $\lambda_\perp = 4$ cm. In the lower band, the numerical solution most closely matches the kinetic Alfvén wave dispersion. We see that the cutoff frequency is identical for all three dispersion relations, and that the exact solution converges with the inertial Alfvén wave close to the cutoff. This makes sense, as the $\zeta \gg 1$ cold plasma limit is by definition always satisfied near the cutoff, since $k_\parallel \to 0$. A spatial damping $\kappa(\omega)$, defined as the imaginary part of $k_\parallel(\omega)$, is present at all frequencies and is indicated by the dashed lines in figure 4.3. While the damping is small for most frequencies, it becomes substantial close to either resonance and should be accounted for in a laboratory setting. Note that as we have not included ion cyclotron damping in our model, this damping

is due entirely to parallel electron particle-wave interactions in response to the wave's large $k_{\parallel}$.

Figures 4.3b and 4.3c show the predicted wavenumber and spatial damping, respectively, for several different values of $k_{\perp}\rho_s$, where ρ_s is the root-mean-squared ion sound gyroradius of the system, defined by:

$$\rho_s^2 \equiv \sum_{ions} f_i \rho_{s,i}^2 = \sum_{ions} \frac{n_i}{n_e} \frac{c_{s,i}^2}{\Omega_{ci}^2}, \tag{4.14}$$

where f_i is the fractional ion concentration and $c_{s,i}$ is the ion sound speed of species i. An interesting observation is that the existence of increasingly kinetic electrons pushes the boundary of both propagation bands past the ion cyclotron frequencies. It can be seen in figure 4.3 that the upper bound of both propagation bands are identical for the kinetic Alfvén wave as well as the exact solution, although the inclusion of electron Landau damping smooths over the resonance and prevents it from diverging to infinity. Therefore, an analytic expression for the frequency shift of the resonance for either species can be found from the resonances of equation 4.13, and for small deviations from the cyclotron frequency are given by the following:

$$\omega_{Res,i}^2 = \Omega_{ci}^2 + k_{\perp}^2 f_i c_{s,i}^2. \tag{4.15}$$

While increased $k_{\perp}\rho_s$ permits propagation at frequencies past the ion cyclotron frequencies, figure 4.3c suggests that waves in these regions will be heavily damped. But regardless of resonance behavior, figure 4.3 shows that the cutoff frequency is unchanged in the presence of thermal electron effects, lending credence to its viability as a diagnostic for a wide range of electron temperatures.

4.2.2 Kinetic Considerations - Finite Ion Larmor Radius (FLR) Effects

In this section we will consider the behavior of the two-ion cutoff frequency in a cold plasma, but with arbitrary finite ion Larmor radius (FLR) effects. FLR effects can be ignored when $k_\perp \rho_i \ll 1$, where ρ_i is the gyroradius of particle species i. This condition is usually satisfied in LAPD plasmas, but there are some plasma/antenna conditions where this inequality may not hold.

The inclusion of FLR effects means we must include the additional off-diagonal dielectric terms that were previously swept under the rug in establishing equation 4.1. Since we showed in the previous section that the cutoff frequency is the same for all electron temperatures, we will consider the "cold" limit ($Z(\zeta) \to -1/\zeta$) for all particle species, while retaining ion FLR effects. The caveat to this assumption is that it is not valid for frequencies very close to the ion cyclotron frequencies, although it is easily satisfied for frequencies in the vicinity of the cutoff. We will continue to assume negligible electron FLR effects, as well as only considering frequencies $\omega \ll |\Omega_{ce}|$. Additionally, we will rotate our coordinates such that $\vec{n} = n_\perp \hat{x} + n_\parallel \hat{z}$. The generalized version of equation 4.1 can then be written as [15]:

$$\begin{bmatrix} \varepsilon_{xx} - n_\parallel^2 & \varepsilon_{xy} & \alpha n_\parallel + n_\perp n_\parallel \\ -\varepsilon_{xy} & \varepsilon_{yy} - n_\parallel^2 - n_\perp^2 & \beta n_\parallel \\ \alpha n_\parallel + n_\perp n_\parallel & -\beta n_\parallel & \varepsilon_{zz} - n_\perp^2 \end{bmatrix} \cdot \begin{pmatrix} E_x \\ E_y \\ E_z \end{pmatrix} = 0, \tag{4.16}$$

where

$$
\begin{aligned}
\varepsilon_{xx} &= -2\sum_{ions}\omega_{pi}^2\frac{e^{-\lambda_i}}{\lambda_i}\sum_{n=1}^{\infty}\frac{n^2 I_n}{\omega^2-(n\Omega_{ci})^2},\\
\varepsilon_{xy} &= -i\frac{\omega_{pe}^2}{\omega\,|\Omega_{ce}|}-2i\sum_{ions}\frac{\Omega_{ci}}{\omega}\omega_{pi}^2 e^{-\lambda_i}\sum_{n=1}^{\infty}\frac{n^2(I_n'-I_n)}{\omega^2-(n\Omega_{ci})^2},\\
\varepsilon_{yy} &= \varepsilon_{xx}-2\frac{\omega_{pe}^2}{\omega^2}\frac{k_\perp^2 v_{Th,e}^2}{\Omega_{ce}^2}+2\sum_{ions}\frac{\omega_{pi}^2}{\omega}\lambda_i e^{-\lambda_i}\sum_{n=-\infty}^{\infty}\frac{I_n'-I_n}{\omega-n\Omega_{ci}},\\
\varepsilon_{zz} &= -\frac{\omega_{pe}^2}{\omega^2},\\
\alpha &= -\frac{4}{n_\perp}\sum_{ions}\omega_{pi}^2\Omega_{ci}^2 e^{-\lambda_i}\sum_{n=1}^{\infty}\frac{n^2 I_n}{\left[\omega^2-(n\Omega_{ci})^2\right]^2},\\
\beta &= -in_\perp\frac{\omega_{pe}^2 v_{Th,e}^2}{c^2|\Omega_{ce}|\omega}+ik_\perp\sum_{ions}\frac{\omega_{pi}^2 v_{Th,i}^2}{c\Omega_{ci}}e^{-\lambda_i}\sum_{n=-\infty}^{\infty}\frac{I_n'-I_n}{(\omega-n\Omega_{ci})^2},
\end{aligned}
\tag{4.17}
$$

and $\lambda_i \equiv (k_\perp\rho_i/\Omega_{ci})^2$, and $I_n = I_n(\lambda_i)$ is the modified Bessel function of order n. Note that we redefined the dielectric terms $\varepsilon_{xz} \equiv \alpha n_\parallel$ and $\varepsilon_{yz} \equiv \beta n_\parallel$, where α and β are independent of $k_\parallel$. In this way, all the terms defined in equation 4.17 are independent of $k_\parallel$ and the $n_\parallel$ dependence of equation 4.16 is explicitly shown. Although we chose to cast equation 4.16 in Cartesian coordinates, the system of equations is directly analogous to cylindrical coordinates via the variable substitutions $\hat{x} \to \hat{r}$ and $\hat{y} \to \hat{\theta}$ – therefore any analysis performed in Cartesian coordinates is directly transferable to a cylindrical system with azimuthal symmetry.

The dispersion relation of the system is found by taking the determinant of equation 4.16, and the resulting characteristic equation is a quadratic in $n_\parallel^2$:

$$
0 = An_\parallel^4 - Bn_\parallel^2 + C, \tag{4.18}
$$

where

$$
\begin{aligned}
A &= \varepsilon_{zz}+\alpha^2-\beta^2+2\alpha n_\perp,\\
B &= (\varepsilon_{yy}-n_\perp^2)(\varepsilon_{zz}+\alpha^2+2\alpha n_\perp)+\varepsilon_{xx}(\varepsilon_{zz}-n_\perp^2-\beta^2)-2\beta\varepsilon_{xy}(\alpha+n_\perp),\\
C &= (\varepsilon_{zz}-n_\perp^2)\left[\varepsilon_{xx}(\varepsilon_{yy}-n_\perp^2)+\varepsilon_{xy}^2\right].
\end{aligned}
\tag{4.19}
$$

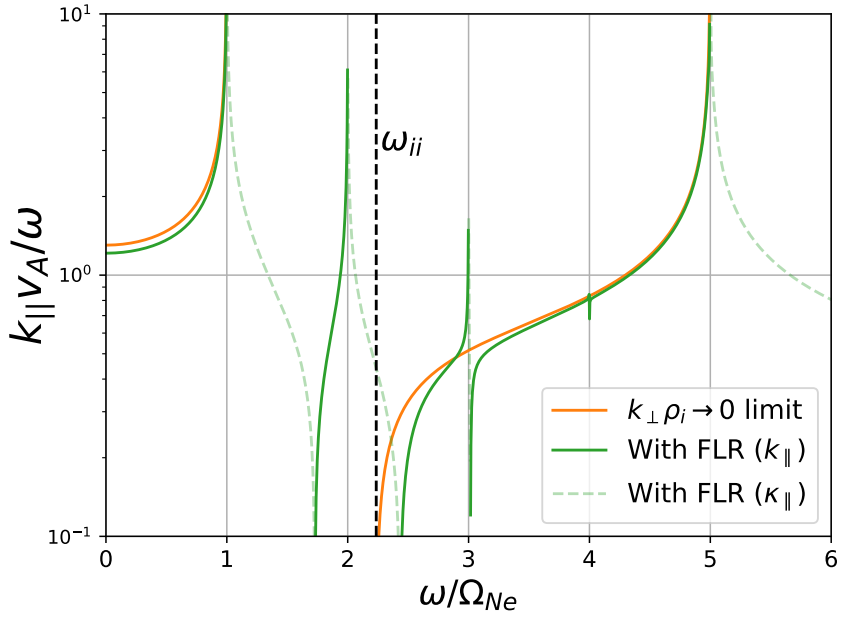

Figure 4.4: Dispersion relation of the inertial Alfvén wave in a 50% He/50% Ne plasma, with and without finite Larmor radius (FLR) effects included in the dielectric tensor.

Equation 4.18 can then be readily solved for $k_\parallel(\omega, k_\perp)$, using the definitions provided by equations 4.19 and 4.17, without having to resort to numerical root-finding methods.

Figure 4.4 shows the resulting dispersion relation for a 50% He/50% Ne plasma, where we have assumed the same plasma conditions as in figure 4.3 (in addition to $T_i = 1$ eV for both ion species). This corresponds to $k_\perp \rho_i \sim .5$ for the heavier of the two ion species, and so FLR effects are expected to be present but not dominating. The first major change we see is the emergence of an additional propagating band, bounded by $1.73\Omega_{Ne} < \omega < 2\Omega_{Ne}$, in a frequency regime which was previously only evanescent. This feature effectively "fills in" part of the previously evanescent region, defined by $\Omega_{Ne} < \omega < \omega_{ii}$, which may make it difficult to experimentally identify the cutoff frequency. Hints of this propagation band have been observed in previous experiments, and was speculated to be due to ion Bernstein modes [103, 102].

An additional change to the dispersion relation in figure 4.4 is that the cutoff frequency

is shifted, from ω_{ii} ($\sim 2.24\Omega_{Ne}$) to about $2.43\Omega_{Ne}$. If one were to naively calculate the mix ratio from this cutoff frequency (via equation 4.6), they would get a result saying the plasma is closer to 56% neon. Therefore FLR effects clearly have a severe impact on the accuracy of such a diagnostic. In the limit $k_\perp \rho_i \to \infty$ (which can be computed using the asymptotic form of $I_n \sim e^{\lambda_i}/\sqrt{2\pi\lambda_i}$), there is no cutoff frequency as all previously evanescent frequency bands can now facilitate propagation.

It is clear that FLR effects have a noticeable impact on the ion-ion cutoff frequency, and so our next goal is to explicitly determine the dependence of the cutoff frequency on $k_\perp$. If we are in a region where $n_\perp^2$ is much larger than each of the terms in the dielectric tensor (with the exception of the parallel dielectric ε_{zz}, which can be comparable to or greater than $n_\perp^2$), we can expand equation 4.18 accordingly and derive an analytic expression for the dispersion relation to lowest order. The result is the following:

$$n_\parallel^2 = \varepsilon_{xx}\left(1 + k_\perp^2 \delta_e^2\right), \tag{4.20}$$

where ε_{xx} is defined in equation 4.17. Equation 4.20 is analogous to the inertial Alfvén dispersion, given by equation 4.4, and so can be thought of as the dispersion relation for inertial Alfvén waves with finite FLR effects[2]. The cutoff frequency corresponds to the root(s) of ε_{xx}, or:

$$\sum_{ions} \omega_{pi}^2 \frac{e^{-\lambda_i}}{\lambda_i} \sum_{n=1}^{\infty} \frac{n^2 I_n(\lambda_i)}{\omega^2 - (n\Omega_{ci})^2} = 0. \tag{4.21}$$

Equation 4.21 will presumably contain multiple roots, due to the higher harmonic resonances. As we are specifically interested in perturbations to the ion-ion cutoff frequency, we will limit ourselves to finding the root within the frequency band bounded by the nearest

[2]Equation 4.20 was numerically compared to the results of figure 4.4 and found to be in extremely close ($< .1\%$) agreement.

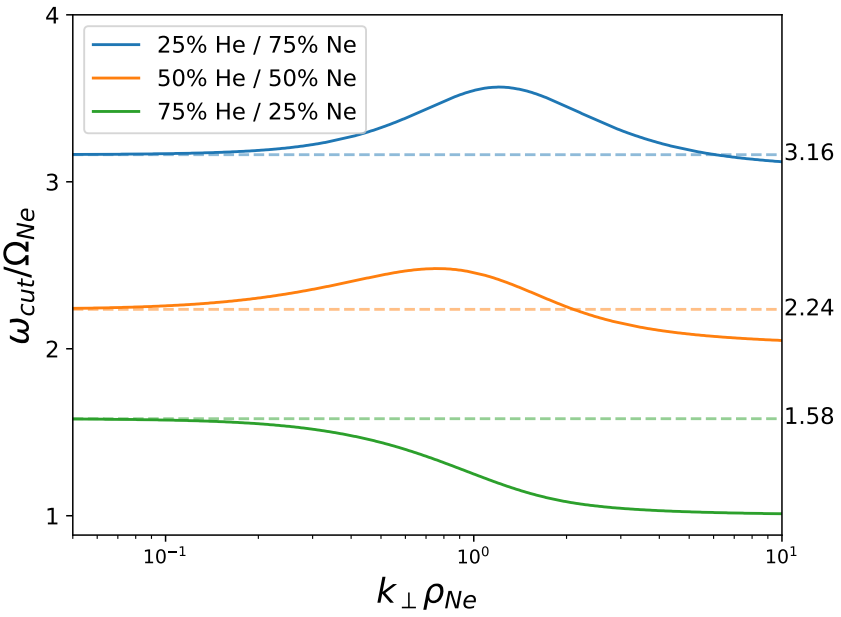

Figure 4.5: Two-ion cutoff frequency of the inertial Alfvén wave as a function of increasing FLR effects, for several mixes. The horizontal dashed line denotes the ion-ion hybrid cutoff for its respective mix, which the cutoff frequency converges to in the limit $k_\perp \rho_i \to 0$.

harmonics above and below ω_{ii} (i.e. for a 50% He/50% Ne plasma, where $\omega_{ii} \approx 2.24\Omega_{Ne}$, we would look for the cutoff in the frequency band $2\Omega_{Ne} < \omega < 3\Omega_{Ne}$).

Figure 4.5 shows the two-ion cutoff frequency (ω_{cut}) as a function of $k_\perp \rho_{Ne}$, where ρ_{Ne} is the neon gyroradius. Note that the values of $k_\perp \rho_{Ne}$ showcased in figure 4.5 reside within the asymptotic region of figure 4.2 – meaning any deviation of the cutoff from ω_{ii} (denoted by a horizontal dashed line) is entirely due to FLR effects, and is a separate phenomena from the $k_\perp \delta_e$ scaling that was previously observed. For all three mixes shown in figure 4.5, the cutoff frequency approaches its respective ion-ion hybrid frequency in the $k_\perp \rho_{Ne} \to 0$ limit, as expected. In the intermediate region, where $k_\perp \rho_{Ne} \ll 1$ is not satisfied, the cutoff frequency deviates significantly from the ion-ion hybrid frequency. In the limit where $k_\perp \rho_{Ne} \to \infty$, the cutoff frequency approaches the nearest cyclotron harmonic. In this limit, FLR effects completely fill in the evanescent gaps in the dispersion, allowing propagation at virtually

all frequencies. Therefore, accurate measurement of the ion-ion hybrid frequency becomes significantly more challenging with increasing $k_\perp \rho_i$.

An interesting consequence of the above analysis is that while $\varepsilon_{xx} = 0$ gives the cutoff frequency as a function of $k_\perp$, it is also the dispersion relation for ion Bernstein waves [85]. This suggests that an inertial Alfvén wave which is incident on an ion-ion hybrid cutoff layer in the plasma may spontaneously mode convert into an ion Bernstein wave [95]. Ion Bernstein waves have been explored previously as a potential diagnostic for both ion temperature and ion minority concentration [79].

4.2.3 Collisionality

Next we pose the question of how collisionality affects the ion-ion cutoff frequency. For simplicity we will again assume a cold, fluid-like plasma, in the regime where ω_{ii} matches the cutoff frequency to good agreement. There are several types of "collisionality", depending on the context - the kind we will consider here is the one responsible for bulk momentum transfer between particle species. A particle travelling through a plasma will periodically come in close contact with another particle, resulting in an exchange of momentum between the two. If we assume the vast majority of these interactions are binary in nature, then the rate of momentum transfer between two particle species can be thought of as the aggregate sum of many binary interactions. Assuming small angle, Rutherford-like scattering events, the collision frequency between electrons and ion species i can be expressed as [17]:

$$\nu_{e,i} = \frac{4\sqrt{2\pi}}{3} \left(\frac{e^2}{4\pi\varepsilon_0} \right)^2 \frac{n_i}{m_e^{1/2} T_e^{3/2}} \ln \Lambda, \tag{4.22}$$

where $\ln \Lambda$ is the Coulomb logarithm, and is typically of the order $\sim$10. For a plasma with $T_e = 5$ eV and $n_i = 5 \times 10^{11}$ cm^{-3}, equation 4.22 predicts an electron-ion collision frequency of around 1.5 MHz - well above the ion cyclotron regime. This is in rough agreement with the empirically measured electron-ion collision frequency of a singly ionized Helium plasma

[7]. This means that the plasma is highly collisional at the frequencies we are interested in, and a proper theoretical treatment should consider collisionality. The equations of motion for electrons and ions are then described by the following:

$$\begin{aligned} m_e n_e \frac{d\vec{u}_e}{dt} &= -e n_e \vec{E} - e n_e \vec{u}_e \times \vec{B}_0 - m_e n_e \sum_i \nu_{e,i}(\vec{u}_e - \vec{u}_i), \\ m_i n_i \frac{d\vec{u}_i}{dt} &= q_i n_i \vec{E} + q_i n_i \vec{u}_i \times \vec{B}_0 - m_i n_i \nu_{i,e}(\vec{u}_i - \vec{u}_e). \end{aligned} \tag{4.23}$$

Conservation of momentum requires that $m_e n_e \nu_{e,i} = m_i n_i \nu_{i,e}$, and so the ion-electron collision frequency will be at least a factor of m_e/m_i smaller than the electron-ion collision frequency and can generally be ignored. As the cross-field currents are mediated primarily by ions, to lowest order they can continue to be treated as collisionless, while the parallel electron current will be modified by collisional effects. The resulting dispersion relation is similar in form to equation 4.4:

$$n_\parallel^2 = S\left(1 - \frac{n_\perp^2}{P^*(\omega)}\right), \quad \text{where} \quad P^*(\omega) = \frac{-\omega_{pe}^2}{\omega(\omega + i\nu_e)}, \tag{4.24}$$

where S is the same cold dielectric element defined in equation 4.2. In equation 4.24, ν_e is the *total* electron collision frequency with all other species, defined by $\nu_e = \sum \nu_{e,i}$. Note that electron-neutral collisions can be accounted for as well by simply including their respective collisional frequencies into this summation.

As $S(\omega)$ is unchanged by Coulomb collisions (at least, to lowest order), the root of equation 4.24 still corresponds to ω_{ii} in a two-ion species plasma, and so the cutoff frequency is unchanged by collisionality. If we were to be more diligent in keeping track of collisional effects in the polarization current, then we would see that $S(\omega)$ is, in fact, weakly dependent on the electron-ion collision frequency and the cutoff frequency would be slightly modified as a result. But these deviations of the cutoff frequency from ω_{ii} would be minuscule in nature, and therefore a more rigorous treatment is not warranted for the present study.

Lastly, electron collisions with neutrals will have a noticeable impact on the wave physics,

but this effect can be absorbed into the collision frequency ν_e described above. Therefore it is common practice to use a "catch-all" collision frequency ν_e that modifies the parallel electron motion, which accounts for electron collisions with both ions and neutral particles. Similar to ion-ion collisions, the collision frequency between ions and neutrals is low enough that it can be ignored.

4.2.4 Summary of Theoretical Results

To summarize this section, we have demonstrated the existence of a cutoff frequency for parallel propagating waves in a two-ion species plasma, which exists between the two ion cyclotron frequencies. For antennas whose size are on the order of the electron skin depth (i.e. $k_\perp \delta_e \sim 1$) or smaller, this cutoff frequency can be approximated by the ion-ion hybrid frequency ω_{ii}, which in turn can be expressed as a function of the ratio of ion densities. Therefore the ion-ion hybrid frequency is of interest to us as a potential diagnostic tool in two-ion species plasmas.

The cutoff frequency was shown to be unchanged by electron thermal effects, suggesting that this diagnostic is valid for all (reasonable) electron temperatures. It was shown, however, that the cutoff frequency deviates from ω_{ii} when $k_\perp \rho_i \ll 1$ is not satisfied, where ρ_i is the ion gyroradius. This does not mean that this diagnostic is unusable in plasmas with non-negligible FLR effects - it just means the cutoff frequency can no longer be accurately modeled by ω_{ii}. If one has information on the $k_\perp$ spectrum of their plasma, then equation 4.21 can, in principle, be solved numerically to find the cutoff frequency as a function of ion mix ratio. One caveat is that large FLR effects introduce additional propagation bands below the ion-ion hybrid cutoff frequency, in the vicinity of the ion cyclotron harmonics. This results in propagating signals at frequencies which, in the cold fluid limit, are typically evanescent, which may make it more difficult to pinpoint the precise location of the cutoff frequency. Finally, the cutoff frequency was shown to be unaffected by collisional effects (to lowest order). All of this suggests that ω_{ii} is fairly robust under a wide range of plasma

conditions, and could serve as a valuable diagnostic in two-ion species plasmas.

4.3 Experimental Setup

4.3.1 General Overview of LAPD

A series of experiments were conducted in the Large Plasma Device (LAPD) at UCLA. The LAPD is a cylindrical stainless steel chamber that is 18 m in length and 1 m in diameter. The chamber is surrounded by 56 electromagnets, capable of producing a highly uniform axial magnetic field ($\delta B/B_0 < .5\%$) up to 3000 G [36]. A DC discharge is applied to a barium oxide (BaO) coated cathode, located on one end of the machine. This produces a stream of primary electrons which pass through a 50% transparent mesh anode, located 52 cm away, ionizing the gas throughout the rest of the chamber. The discharge lasts 12 ms, and is fired at a rate of 1 Hz to create a highly reproducible plasma. An overview of general plasma parameters for this experiment can be seen in table 4.3.1.

A gas feed system is installed in the center of the machine, capable of supplying the chamber with steady rates of hydrogen, helium, neon, and argon. Each gas is connected to its own mass flow controller (MFC), allowing the experimenter to precisely control the gas mix, and the partial pressures of each gas is measured using a residual gas analyzer (RGA). This experiment explores the behavior of shear Alfvén waves for various mix ratios of helium and neon. Throughout this chapter, the neutral pressure ratio is used as a proxy for estimating the ion density ratio of the plasma. Although it is not assumed (or even expected) that these two quantities be equal, it will serve as a satisfactory reference point as we investigate different mixes.

Parameter	*Value*
Ions	He^+ and Ne^+
Gas (fill) pressure	2–3 $\times$ 10^{-5} Torr
Background magnetic field	600–1650 G
Plasma density (interferometer)	2.5 $\times$ 10^{12} cm^{-3}
Electron temperature (T_e)	4–5 eV
Ion temperature (T_i)	<1 eV
Electron cyclotron frequency	1.7–4.6 GHz
Helium cyclotron frequency	228.7–629 kHz
Electron skin depth	3.4 mm
Electron-neutral collision frequency	285 kHz
Ion-neutral collision frequency	100 Hz
Coulomb (electron-ion) collision frequency	4.75 MHz

Table 4.1: Range of plasma parameters considered in this experiment.

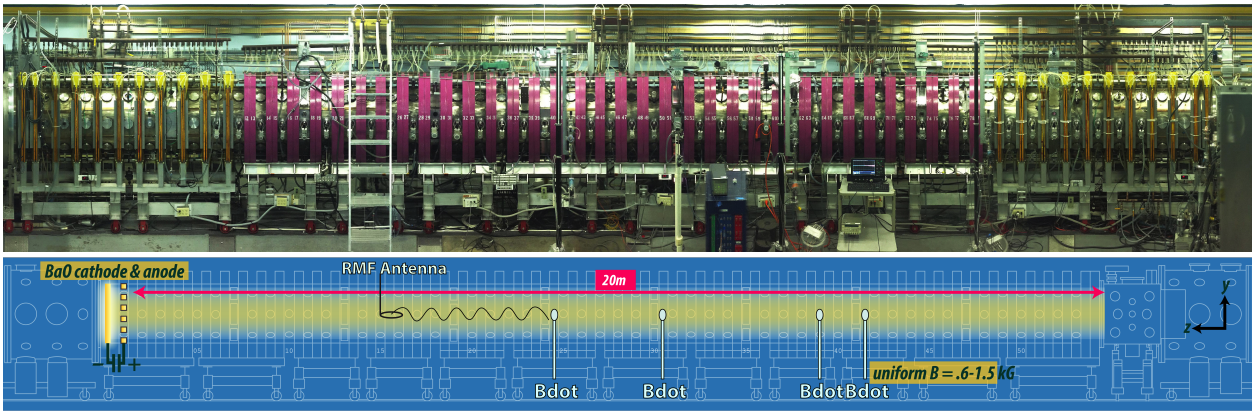

Figure 4.6: Picture (upper) and schematic (lower) of LAPD, showing location of RMF antenna and probes.

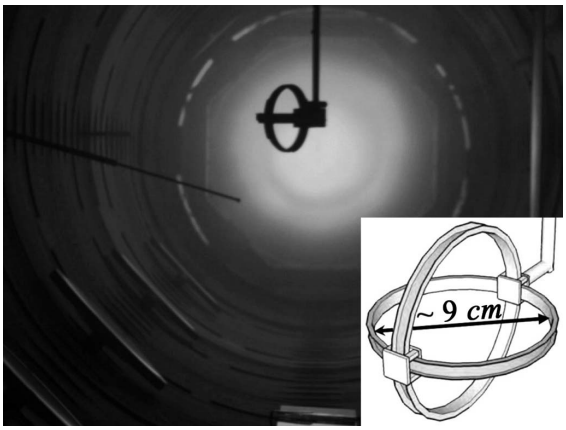

Figure 4.7: Picture of rotating magnetic field (RMF) antenna used to launch shear Alfvén waves, with cathode visible at far end. (inset) Schematic drawing of antenna

4.3.2 Antenna and Probes

Shear Alfvén waves are launched using the rotating magnetic field (RMF) antenna, originally designed to study circularly polarized waves [41]. The majority of the experiment utilizes only the horizontal loop of the antenna, which has a diameter of roughly 9 cm. The antenna is aligned such that the plane of the loop laid in the XZ plane. Previous experiments have shown the antenna to create two antiparallel electron current channels, centered on either end of the loop. At frequencies well below the ion cyclotron frequency, the induced magnetic field of this current configuration creates a plasma wave with a strong linearly polarized magnetic field B_y along the background field line passing through the midpoint of the loop. A second dipole loop antenna was constructed with similar geometry, consisting of a 2.5 cm diameter insulated loop of wire mounted on a movable probe drive, and was used to launch shear Alfvén waves at varying radial positions in the plasma.

The antenna is driven by a sinusoidal waveform generator which was then fed through an RF amplifier capable of delivering several amps of current to the antenna. The amplitude of the resulting Alfvén waves (measured several meters away) is on the order of tens of milligauss. Background fluctuations in the field due to plasma turbulence are typically on the

order of tens of microgauss, resulting in a strong signal to noise ratio for our wave. Previous studies [24] on the LAPD have shown that large enough amplitude shear Alfvén waves can lead to wave current filamentation as well as modifications to the plasma density due to ponderomotive forces, but these nonlinear effects are only significant for wave magnitudes exceeding 10% of the background field. Therefore we are justified in using the linearized theory outlined in section 4.2.

Magnetic field fluctuations are measured with four three-axis magnetic induction (B-dot) probes, located at various axial positions in the plasma. Each component of the probes contains two, oppositely wound twenty-five turn coils, which are fed through a differential amplifier to subtract out any electrostatic pickup in the coil [28]. The locations of the probes, as well as the antenna, are shown in figure 4.6.

4.4 Experimental Results

4.4.1 General Results

A series of frequency scans were performed under a wide range of plasma conditions, using the horizontal loop of the RMF antenna to excite a shear wave along the radial center of the machine. The following measurements were taken with a series of B-dot probes, placed at r=0, for various axial positions in the plasma.

Figure 4.8 shows the power spectrum of the wave as a function of frequency, for varying background field strengths, at two axial positions. All cases are for a plasma with equal fill pressures of helium and neon. Assuming the ion density ratio is equal to the fill pressure ratio (not generally true but a good reference point), equation 4.6 predicts the ion-ion hybrid cutoff to be $\omega_{ii} = 2.24\Omega_{Ne}$, which is labeled in the plots by a vertical dashed line. $B_\perp$ was normalized to the antenna current I_{ant}, as the current provided by the RF power supply was not constant for all frequencies. In order to isolate the antenna-driven signal from the background turbulence of the plasma, the following formula was used to calculate the filtered

power spectrum:

$$|B_j|^2_{filt} \equiv \frac{|\langle B_j(\omega) I^*_{ant}(\omega)\rangle|^2}{\langle |I_{ant}|^2\rangle} = \gamma^2 \langle |B_j|^2\rangle, \tag{4.25}$$

where the brackets denote an ensemble average, and $\gamma(\omega)$ is the coherence between the B-dot signal and antenna current. When background fluctuations are small relative to the antenna-driven signal, $\gamma \sim 1$ and the filtered power spectrum is identical to the regular power spectrum. Equation 4.25 is used in all power spectrum calculations that follow in this chapter, and so the *filt* subscript is dropped in our notation. Since the overall power of the wave is observed to decrease with decreasing field, each spectrum is normalized to itself in order to help illuminate some of the more subtle features. The spectra contain two distinct frequency bands with a propagation gap in the middle, which is in agreement with the predicted dispersion of figure 4.1. The normalized cutoff frequency ω/Ω_{Ne} is constant with changing background field, which is consistent with equation 4.6. The low frequency side of the propagation gap begins to fill in at 900 G, and even more so for the 600 G case. This is consistent with our theoretical prediction from figure 4.3b, which says that as electrons become increasingly kinetic, the upper bounds of the propagation bands can push past their respective cyclotron frequencies. Meanwhile, the high frequency side of the propagation gap also experiences some "filling in" around the expected cutoff. This can be attributed to the previous discussion in section 4.2, in which we asserted that small-$k_\perp$ portions of the wave will have cutoff frequencies below ω_{ii}, resulting in a leakage of some power below the ion-ion hybrid cutoff.

Both the upper and lower frequency bands begin to lose power as they approach their respective resonance. This is consistent with our theoretical prediction in figure 4.3, which suggested that significant kinetic damping is expected just before either cyclotron. Additionally, previous studies [72] have shown that the ratio of perpendicular to parallel group velocities increases rapidly near the resonances, leading to a radial spreading of wave energy and smaller measured signal by the B-dot probe. This behavior has been observed in

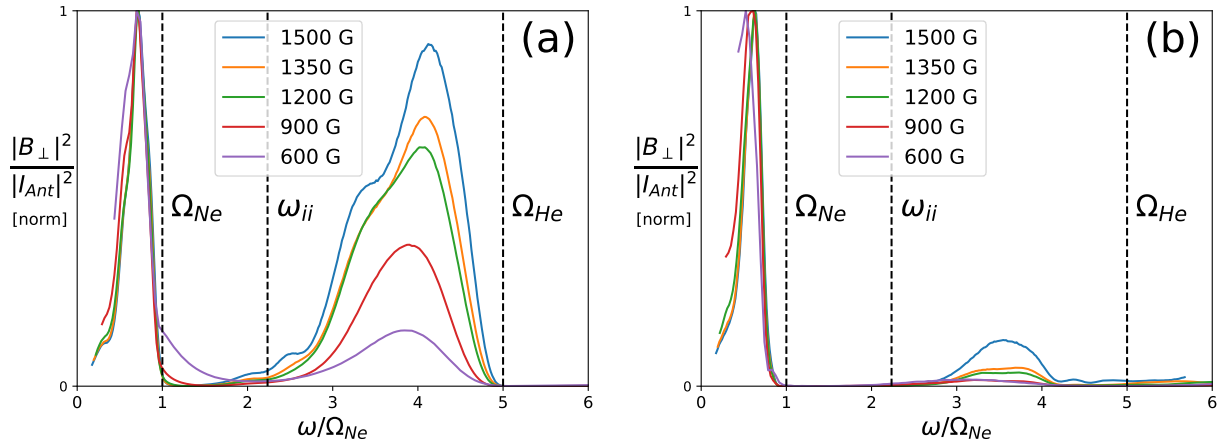

Figure 4.8: Normalized power spectrum of the perturbed magnetic field at (a) 3 m and (b) 9 m from the antenna, for various background fields. Dashed lines, from left to right, mark the locations of the neon cyclotron frequency, ion-ion hybrid cutoff frequency (predicted value for a 50/50 mix), and helium cyclotron frequency.

previous antenna experiments, both in the LAPD [38] as well as in a toroidal device [14].

Having established the existence of a cutoff frequency which scales as expected with background field, our next objective is to vary the mix ratio of the plasma and see if it scales in a way that is consistent with ω_{ii}. Figures 4.9a and 4.9b show the power spectrum of the wave and parallel wavenumber, respectively, for various mix ratios in a background field of $B_0 = 1500$ G. The mix ratio here is again based off the neutral fill pressure of the gas. From equation 4.6, it is expected that ω_{ii} approaches Ω_{He} with increasing neon concentration, and vice versa for increasing helium. This trend can be seen clearly in the power spectra of figure 4.9a, where we have labeled the estimated cutoff frequencies with a colored X. The method for selecting the cutoff frequency is to find the point in the spectrum where the slope rapidly increases, as it is thought that this is the wave transitioning from being "weakly evanescent" to propagating. It is observed that the upper band gets weaker with decreasing helium (relative to the lower band), suggesting that the total power of the two propagating bands scale differently with ion mass. This is likely due to the fact that

neon suffers higher collisional damping at these frequencies than helium. Several peaks can be seen in the spectra, especially for the majority-helium mixes. This has been observed before in the LAPD [71], and it is suspected that this is due to backwards propagating waves reflecting off the cathode and constructively interfering with our forward propagating wave. Calculations using the phase velocity of the wave at these frequencies support this claim.

Figure 4.9b shows the parallel wavenumber, which was calculated from the crossphase of two probes spaced 2.24 meters apart axially [91], for various mix ratios. B_y was used to calculate the phase difference, as this component of the field had the strongest signal-to-noise ratio, but similar results are achieved using B_x. Data points which failed to meet a minimum coherency threshold of $r^2 > .9$ were deemed too noisy and omitted from the plot. The results are in good agreement with the theoretical dispersion plotted in figure 4.1. Looking at the upper band in particular, we see $k_\parallel$ begin to increase past a certain frequency (presumably the cutoff frequency), rising rapidly and then eventually dropping as it approaches the cyclotron resonance. The cutoff frequency for each mixed case was estimated from the local minimum in the dispersion relation, and again labeled with an X. It's observed that most of the measured wavenumbers don't actually cross the zero axis, but rather bottom out at a value above zero. This is speculated to be due to the finite length of the plasma column imposing a minimum fundamental eigenmode on the parallel wavelength, as discussed in [71].

Figure 4.10 compares the measured cutoff frequencies, estimated independently from figures 4.9a and 4.9b, to the predicted values, which were calculated from equation 4.6. The plot of predicted cutoff frequencies in figure 4.10 is based on if the ion density ratio were equal to the neutral fill pressure. While these quantities in general are not expected to be equal, it is assumed that they're similar enough such that the former can serve as a satisfactory proxy for the latter (in lieu of other options). Error bars were included for the ω_{ii} measurements taken from $k_\parallel$, which were obtained from the minimum and maximum values of an ensemble of frequency scans, although the uncertainty tended to be no more

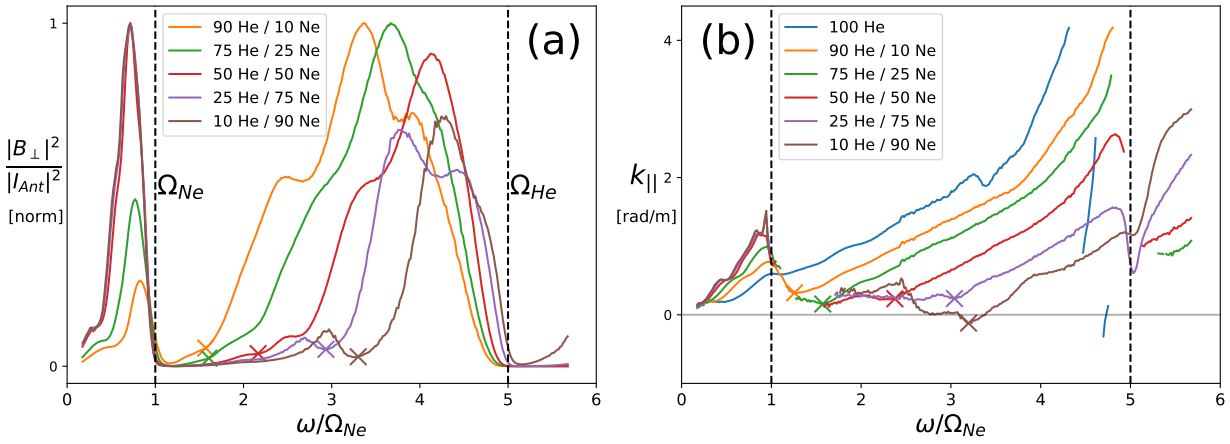

Figure 4.9: (a) Normalized power spectra and (b) parallel wavenumber, for various mix ratios of helium/neon for $B_0 = 1500$ G. The X's mark the estimated cutoff frequency, and were separately identified from both the measured spectra and dispersion.

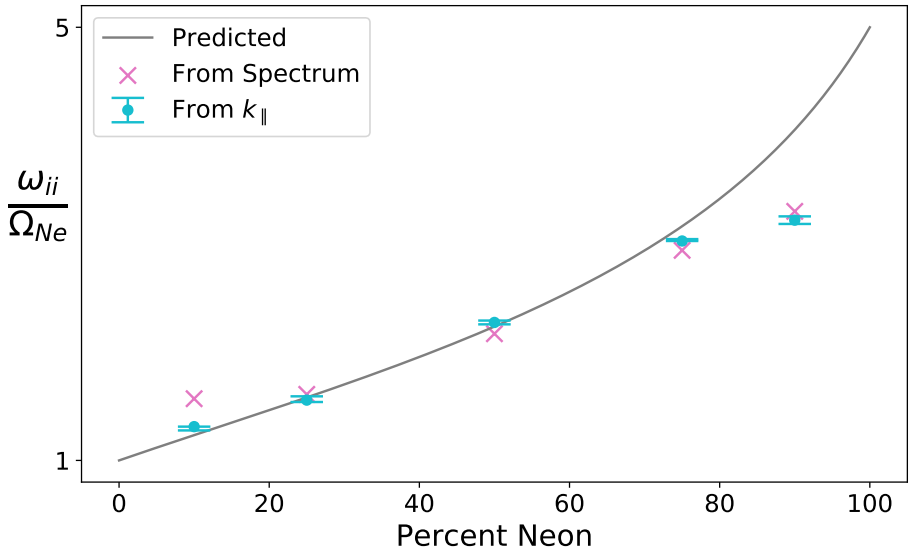

Figure 4.10: Plot of the theoretically predicted ion-ion cutoff frequency in a helium/neon plasma, as a function of percent neon. The measured cutoff frequencies (from both the power spectrum and dispersion) are plotted for comparison.

than a few percent. The observed cutoffs from both the spectra and dispersion relations are observed to scale consistently with the predicted values. For the majority-neon cases, the measured cutoff is below the predicted cutoff, suggesting that there may be less ionized neon in the plasma than the neutral fill pressure would suggest. For the 90% Ne case, the measured cutoff suggests the concentration of ionized neon is actually closer to 78%.

There is a small discrepancy between the cutoffs measured from the spectra vs. the dispersion relations, which can be attributed to uncertainty in picking out the precise cutoff frequencies from figure 4.9. Just below ω_{ii}, the signal is expected to be only very weakly evanescent, and therefore one might expect a measurable portion of the near-field signal to tunnel through to the probe at these frequencies. What this means for the experimenter is that there is some uncertainty when attempting to pinpoint the cutoff frequency from the power spectrum. For several of the mixed cases, there is a "kink" near the predicted cutoff where the slope of the spectrum suddenly increases. It is assumed that this kink is the cutoff frequency, and the rapid change in slope is due to the wave transitioning from being "very weakly evanescent" to propagating. The cutoff frequency measured from $k_{\|}$ avoids the ambiguity brought on by the weakly evanescent region, but it is at the expense of requiring an additional probe to measure.

Next, we attempt to measure the the cutoff frequency from the parallel spatial damping of the wave. Figure 4.11a shows, for a 50% He/50% Ne plasma, how the magnitude of the power spectrum drops off rapidly with distance from the antenna. At each frequency, the spatial damping of the wave was calculated by fitting the power spectra of four axially separated probes to a negative exponential via method of least squares. This was done for all of the cases in figure 4.9, and the resulting plot is shown in figure 4.11b. Frequencies which failed to satisfy a correlation threshold of $r^2 > .9$ were omitted from the plot. Noticeable damping is observed across the entire spectrum, including in the propagating frequency bands where the cold fluid model of equation 4.3 does not predict damping. For all mix cases, a large amount of damping is observed at frequencies approaching either cyclotron, and this is consistent

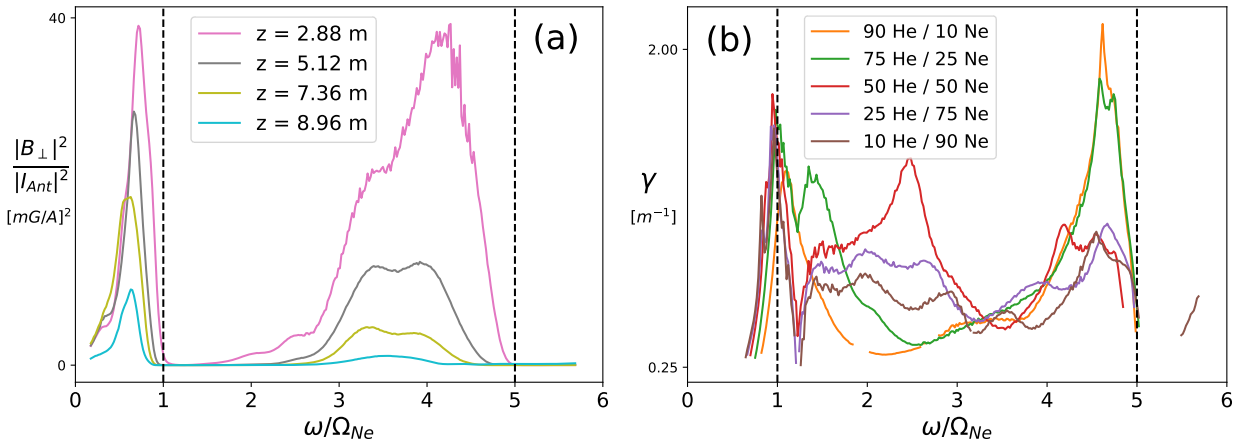

Figure 4.11: (a) The power spectra of a 50% He/50% Ne plasma at 1500 G, showing how the power drops off with increasing distance z from the antenna. (b) The spatial damping as a function of frequency, calculated from fitting the four probe measurements to a decaying exponential.

with the kinetic electron damping predicted in figure 4.3. There are additional dissipative effects which are not captured by our theoretical model, such as collisionality, that likely play a large role in the observed damping. Additionally, experiments with a large fill pressure experience an appreciable drop in plasma density as one moves further away axially from the cathode source, and this is likely to have a noticeable effect on the measured spatial damping. Since negligible kinetic damping is expected in the vicinity of the cutoff, it is clear in this region that the measured damping is dominated by physical effects outside the scope of our theoretical model. For these reasons, the spatial damping does not make a good candidate for measuring the cutoff frequency ω_{ii}.

4.4.2 Estimating the $k_\perp$ spectrum from radial lines

While the methods of determining the cutoff frequency from the local minima of the power spectra or measured parallel wavenumber are able to infer a value that is consistent with theoretical predictions, as shown in figure 4.10, they are still fairly subjective and highly

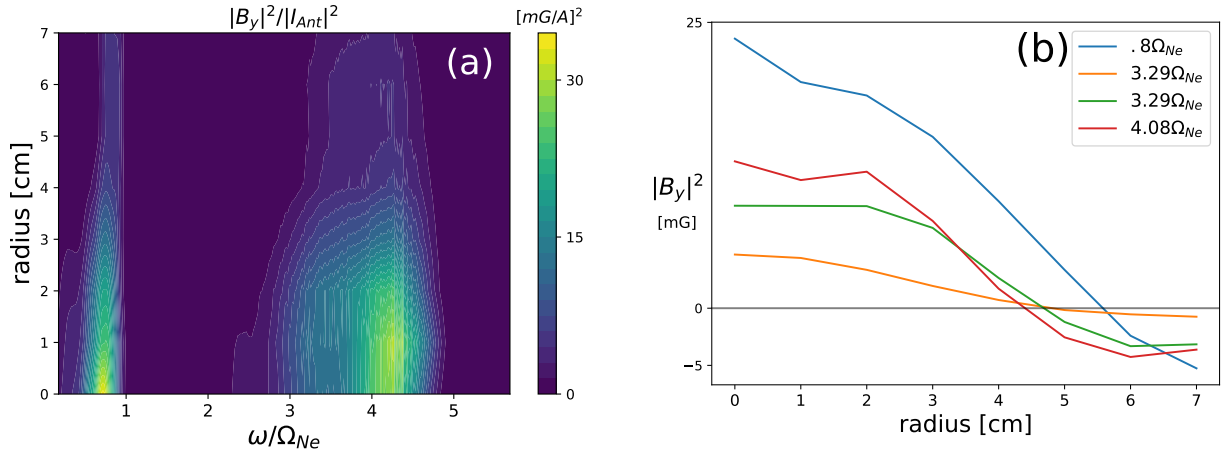

Figure 4.12: (a) Power spectrum of the wave 3 m from the antenna, for a 50% He/50% Ne plasma at 1500 G, measured at various radial distances from the center of the plasma column. (b) Radial profiles of the vertical B-field for several frequencies, taken at a time corresponding to the peak of the signal at $r = 0$.

susceptible to noise interference. A more rigorous method of determining the ion density ratio is to fit the measured dispersion relation from figure 4.9b to the theoretical prediction of equation 4.4. In order to accurately do so, however, we need some idea of the values of $k_\perp$ imposed by the antenna, which can be obtained from radial profiles of the wavefront.

Figure 4.12 shows the power spectrum of a wave launched in a 50 % He / 50% Ne plasma, measured at different radial offsets from the center of the antenna. Due to symmetry, the majority of wave power along this line is in B_y, and so only the vertical component of the field is considered here. For the frequencies of interest, the peak power of the wavefront is located at the center of the antenna. This is reassuring from a diagnostic point of view, as there is no ambiguity in deciding where one should place the B-dot probes relative to the antenna. The radial structure of the wavefronts seen in figure 4.12 is reminiscent of previous antenna experiments, in which two electrostatic disks were driven π out of phase with each other [38]. The effect of the RMF antenna on the plasma, then, can be thought of as two current channels running antiparallel to one another, located along the field lines passing

through either side of the loop at $r = \pm 4.5$ cm. The resulting azimuthal field adds up constructively in between the two current channels, resulting in a strong vertically polarized wave at the midpoint of the antenna. Previous experiments [41] with the same antenna, as well as 2-D simulations [60], have observed current and field patterns which corroborate this idea.

The next step is to determine $k_\perp$, as a function of ω, from the radial profiles of figure 4.12. For simplicity, we will assume the majority of the wave's power to be confined to a small range of $k_\perp$, such that the radial structure of the wavefront can be thought of as the superposition of two first order Bessel functions centered on ± 4.5 cm. Invoking the addition theorem of Bessel functions, we can express the net field of the two sources (along the horizontal plane) in the following alternate form:

$$J_1\left(k_\perp\left(x+R\right)\right) - J_1\left(k_\perp\left(x-R\right)\right) = 4\sum_{1,3,5\ldots} J_n\left(k_\perp R\right) J_n'\left(k_\perp x\right), \tag{4.26}$$

where x is the horizontal distance from the center of the antenna, and R is the antenna's radius. To lowest order, the field is then given by $4J_1(k_\perp R)J_1'\left(k_\perp x\right)$, whose lowest root is approximately where $k_\perp x \approx 1.841$. From this, we are able to formulate a simple linear approximation for finding $\lambda_\perp$:

$$\lambda_\perp \approx 3.4126 x_0, \tag{4.27}$$

where x_0 is the horizontal position at which the vertical field of the wave crosses zero. Numerically, equation 4.27 was found to be accurate within 10% for $k_\perp R < 2.5$. Our method for estimating the value of $\lambda_\perp$, then, is as follows: Find the time-instantaneous radial profile of the wave field (at a time corresponding to the peak of the wave), measure the position at which the field crosses zero, and then use equation 4.27 to calculate $\lambda_\perp$. The results can be seen in figure 4.13a, in which we have plotted the estimated $\lambda_\perp$ as a function of frequency. Figures 4.13b and 4.13c show a comparison of the measured radial profile to the profile

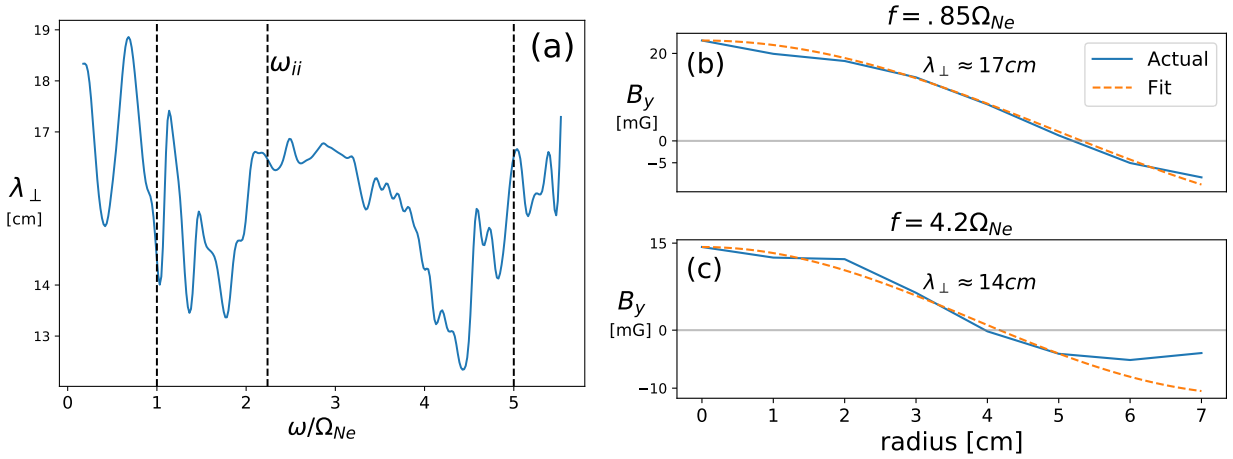

Figure 4.13: (a) Perpendicular wavelength vs frequency, estimated from the radial profiles of the field. (b) Comparison of the measured radial profile to the predicted profile for $f = .85\Omega_{Ne}$ and (c) $4.2\Omega_{Ne}$.

predicted by equation 4.27, for two frequencies which are close to the peaks of the power spectra in the lower and upper band, respectively.

4.4.3 Determining ω_{ii} by Fitting Data to the Predicted Dispersion

In this section we present a robust algorithm for efficiently fitting measured data of the parallel wavenumber to theoretical predictions, in order to determine the local ion density ratio. Consider an inertial Alfvén wave in a weakly collisional two-ion species plasma. The real parallel wavenumber can be written as the following:

$$k_\parallel (\bar{\omega})^2 = -\frac{\omega_{p1}^2 + \omega_{p2}^2}{c^2} \frac{\bar{\omega}^2 (\bar{\omega}^2 - \bar{\omega}_{ii}^2)}{(\bar{\omega}^2 - 1)(\bar{\omega}^2 - m_{21}^2)}, \tag{4.28}$$

where $\bar{\omega} = \omega/\Omega_2$ and $m_{21} = m_2/m_1$. We will assume that m_2 refers to the mass of the heavier ion species, although the derivation that follows in this section works equally well if the opposite is assumed. Equation 4.4.3 can be rewritten in terms of the ion density ratio

$\alpha = n_2/n_1$ as follows:

$$k_{\parallel}\left(\bar{\omega}\right)^2 = \frac{m_e}{m_2}\frac{\bar{\omega}^2}{1+\alpha}\left[\frac{m_{21}}{m_{21}^2-\bar{\omega}^2}+\frac{\alpha}{1-\bar{\omega}^2}\right]\left[\delta_e^{-2}+k_{\perp}^2\right], \tag{4.29}$$

where in deriving equation 4.4.3 we made use of the definition $\bar{\omega}_{ii}^2 = m_{21}(1+m_{21}\alpha)/(m_{21}+\alpha)$. Finally, we define the quantity $\beta^2 = (m_e/m_2)(\delta_e^{-2}+k_{\perp}^2)$ and are able to rewrite our dispersion relation in the following form:

$$k_{\parallel}\left(\bar{\omega}\right) = \beta f(\bar{\omega};\alpha) \tag{4.30}$$

where

$$f(\bar{\omega};\alpha) = \frac{\bar{\omega}}{\sqrt{1+\alpha}}\left[\frac{m_{21}}{m_{21}^2-\bar{\omega}^2}+\frac{\alpha}{1-\bar{\omega}^2}\right]^{1/2}. \tag{4.31}$$

We have rewritten our dispersion relation in terms of two free parameters α and β. We would like to find the values of α and β which give us the best fit of equation 4.4.3 to the experimentally measured parallel wavenumber. We choose to quantify the fit quality using the *least-squares cost function*, given by the following:

$$J = \frac{1}{N}\sum_i \left(y_i - k_{\parallel}\left(\bar{\omega}_i\right)\right)^2, \tag{4.32}$$

where y_i is the measured parallel wavenumber, $k_{\parallel}\left(\bar{\omega}_i\right)$ is the predicted dispersion given by equations 4.4.3, and the sum is over all measured frequencies. Equation 4.4.3 is sometimes referred to as the error function. At this point, the problem can be brute forced in order to find the right combination of α and β which minimizes the value of J above. The problem

can be simplified down substantially, however, by solving for β analytically. A common technique in regression problems is to take the partial derivative of the cost function with respect to the free parameters and set it equal to zero in order to find the local minimum of the cost function. Using equation 4.4.3, we can solve $\partial J/\partial\beta = 0$ to get the following:

$$\beta = \frac{\sum y_i f(\bar{\omega}_i)}{\sum f(\bar{\omega}_i)^2}. \tag{4.33}$$

By combining equation 4.4.3 with equations 4.4.3 and 4.4.3, we can express the predicted dispersion curve $k_\parallel(\bar{\omega})$ in terms of a single free parameter α. The last step, then, is to find the value of α which minimizes the cost function given by equation 4.4.3. A big advantage of this algorithm is that the electron density and $k_\perp$ spectrum are baked into our free parameter β, which we were able to solve for analytically. Therefore we have developed an algorithm in which we are able to predict the ion density ratio without requiring any knowledge about the plasma density or $k_\perp$ spectrum. We don't even need to know the distance between the two probes used to measure the parallel crossphase, as this information can also be absorbed into our β parameter.

Figure 4.14 is the result of employing our best-fit algorithm to the measured dispersion for our $50\%He/50\%Ne$ plasma. Included in the plot is the numerical solution to the dispersion relation with kinetic effects included, to show that the inertial Alfvén wave dispersion is a more than acceptable approximation for the given plasma conditions. The best fit curve is obtained for a value of $\alpha = 1.1$, or around 53% neon. The best fit algorithm was applied only to the upper frequency band, i.e. $\Omega_1 < \omega < \Omega_2$). Two steps were taken in order to filter out noise before applying the best fit algorithm. The first step was to remove data points which had a low coherency with the antenna current (for this example, a threshold of $\gamma^2 = .95$ was chosen). Second, frequencies where either one of the B-dot probe's power was less than 1% of the maximum of the full power spectrum (shown in figures 4.8a and 4.9a) were omitted from the fit as well. These two filtering steps ensure that only data points

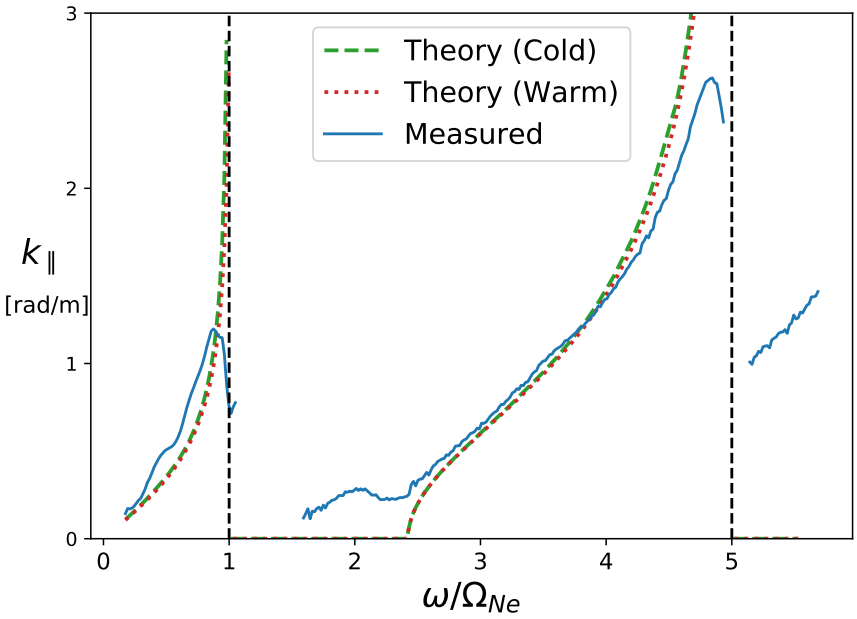

Figure 4.14: Comparison of the measured dispersion, for a plasma with equal fill pressures of He/Ne, to the predicted dispersion relation of a shear Alfvén wave (both exact and in the cold limit). The above theoretical dispersions are for a 47% He/53% Ne plasma, as this mix ratio was found to yield the best fit.

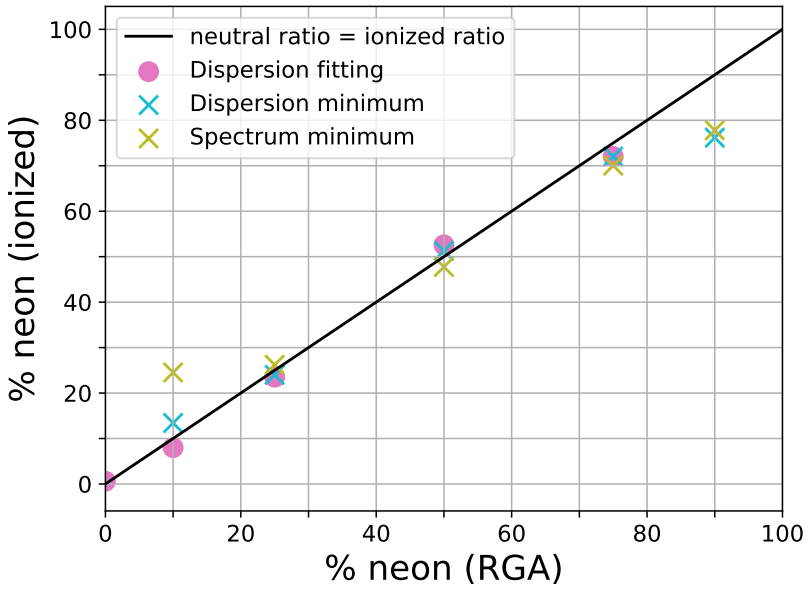

Figure 4.15: Comparison of the three different methods discussed for finding the ion mix. The solid black line is the percent neon corresponding to if the ionized density ratio were to equal the neutral fill pressure.

with a high signal-to-noise ratio are being used in order to fit the predicted dispersion. In addition, the parts of the spectrum below either cyclotron frequency where a drop in the measured wavenumber is observed were ignored, as these dips are not predicted by the cold plasma model and would otherwise add a large amount of unwanted error to the least-squares cost function.

Figure 4.15 shows how the method of least-squares fitting compares to the previously discussed methods of estimating the cutoff from the minimum of the power spectrum and dispersion. We see that the ion density ratios predicted from our best-fit algorithm scale consistently with what we would expect, validating the use of this method. The method was not able to find an adequate fit for the 90% neon case, however, suggesting that this technique might struggle in situations where one of the ions is a minority species.

In order to account for uncertainty in the measurements obtained by this algorithm, we

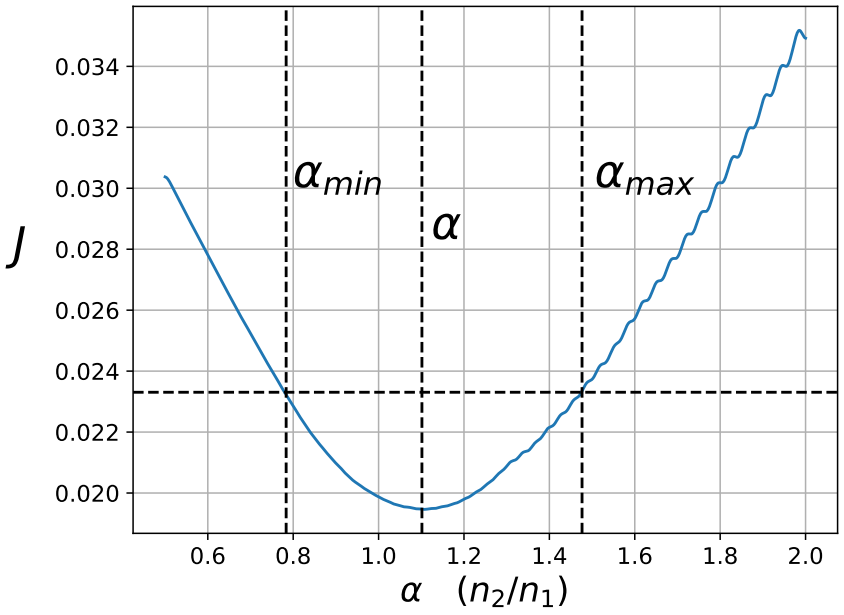

Figure 4.16: Cost function J vs. predicted ion density ratio α for the 50% He/50% Ne plasma. The cost has a minimum around $\alpha = 1.1$, corresponding to $\sim 53\%$ neon. Error bars are defined by the values of alpha corresponding to a 20% increase in the cost on either side of the local minimum.

propose the following technique. From the local minimum in the least squares cost function, find the values of α on either side corresponding to a 20% increase from the local minimum. These values determine the error bars for the α measurement. Cost functions with a sharp valley will have small error bars as a result, whereas cost functions which are slow to find a minimum value will convey this information by having larger error bars. Figure 4.16 shows the cost function vs. α for the 50% He/50% Ne plasma. The predicted value of α as well as the minimum and maximum error bar values are denoted by dashed vertical lines. Note that the 20% threshold that was used is arbitrary - while this value was found to give reasonable results for the dataset shown here, a different percent threshold could be chosen if desired.

4.4.4 Radial diagnostic for determining the ion density ratio

In section 4.4.1 we noted the existence of a cutoff frequency in our data, which was consistent with the predicted ion-ion cutoff frequency in section 4.2. This motivated us to construct a second antenna, consisting of a horizontal loop of wire 2.5 cm in diameter, such that it could be moved radially throughout the plasma. The purpose of this antenna is to look for changes in Alfvén wave propagation at different positions of the plasma, as well as observe the behavior of the ion-ion hybrid cutoff frequency and ultimately determine its viability as a radially localized diagnostic. We will employ the least-squares fitting algorithm derived in section 4.4.3 at each position in order to determine the spatially-resolved ion density ratio.

Figure 4.12a shows the spectrum of waves launched at various radial positions in the plasma, for a 50% He / 50% Ne plasma (based off the neutral fill pressure) with $B_0 = 1500$ G. The loop antenna was incrementally moved to many radial positions, with the B-dot probes always centered on the field line passing through the midpoint of the loop. Looking at figure 4.12a, the strength of the power spectrum tends to drop with increasing radius, presumably due to decreasing plasma density. A shift in the peak of the upper band is seen at $r = 28$ cm, which corresponds to the field lines which pass through the edge of the BaO cathode. Previous studies [82] have shown the existence of an azimuthal shear flow layer in

this region. The shear flow arises spontaneously from the free energy of the pressure gradient in the plasma, which is due to edge conditions imposed by the cathode, and this may be responsible for the frequency shift in the peak of the upper band. Another explanation is simply that the edge plasma is more neon-dominated, as the peak shifting towards the helium cyclotron would correspond to a larger neon concentration. While a gap region can clearly be identified in the spectra, it is difficult to pinpoint a precise value of the cutoff in any objective manner. Therefore, the power spectrum's ability to determine the cutoff frequency is severely limited and not ideal as a diagnostic.

Looking at figure 4.12b, the plasma exhibits similar dispersion behavior in the region $r < 28$ cm. At most of the positions shown, a local minimum can be observed in the frequency band $\omega = 2.5 - 3\Omega_{Ne}$. It is speculated that this minimum corresponds to the cutoff frequency ω_{ii}. The dispersion at $r = 28$ cm is an exception, as no local minimum is apparent in the data. This again may be due to various edge plasma effects not considered here, limiting our ability to resolve a cutoff. Below what we assume to be ω_{ii}, there is a small peak in the dispersion. It is currently unclear what this peak is, as it is not predicted by our theoretical model, although previous papers have noted the existence of small peaks in the gap region as well and speculated them to be Ion-Bernstein Modes [101]. Additionally, it is unclear why $k_{\|}$ drops off rapidly as it approaches the helium cyclotron.

Figure 4.17 shows the result of applying our best-fit algorithm, outlined in the preceding section, to various radial positions in the plasma. The algorithm is performed by taking the predicted dispersion, given by equations 4.4.3, 4.4.3, and 4.4.3, and numerically finding the value of α $(= n_2/n_1)$ which minimizes the least-squares cost function given by equation 4.4.3. Only the frequencies in the upper band were considered for the fitting algorithm. We can see that the measured parallel wavenumbers for the first few positions in the plasma are in excellent agreement with the predicted dispersion curves, to the point of almost completely overlapping. For positions near or outside the edge of the plasma (around r = 28 cm), there is more uncertainty associated with the best fit curve.

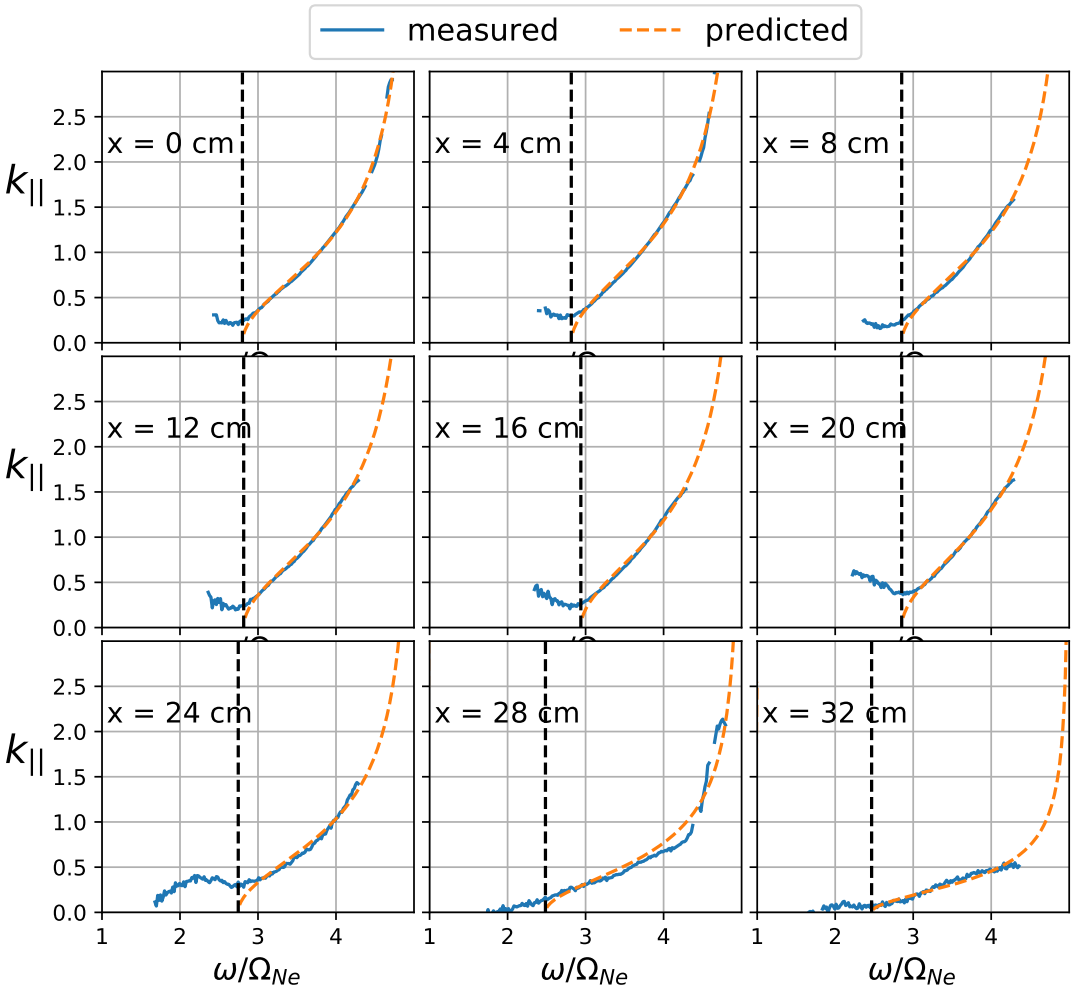

Figure 4.17: Measured parallel wavenumbers and the corresponding best-fit predicted dispersion, for various radial positions. Dashed vertical lines denote the corresponding location of the predicted ion-ion hybrid cutoff.

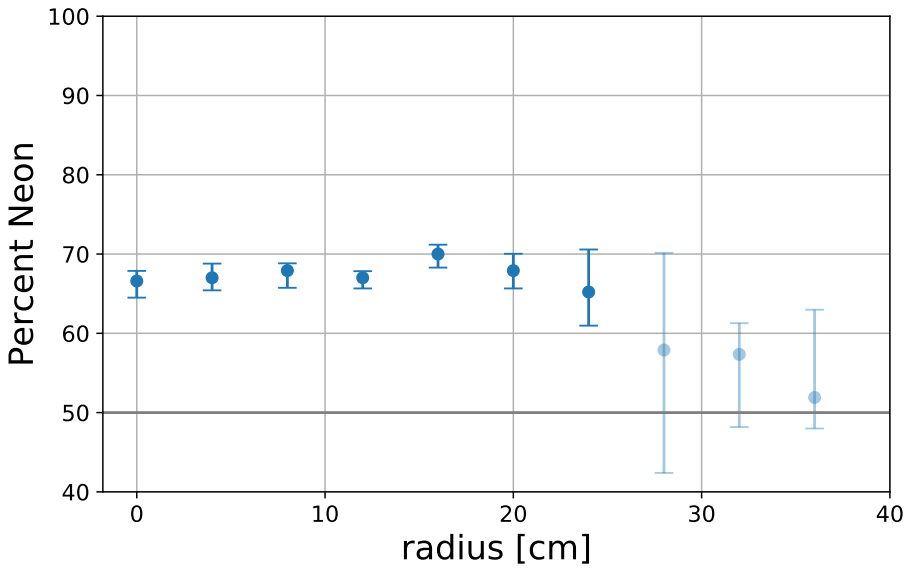

Figure 4.18: Estimated percent ionized neon as a function of radius in the plasma, for a plasma with 50% He/50% Ne neutral pressure.

Figure 4.18 shows the estimated neon mix concentration vs radius in the plasma. Error bars were calculated from the values of α corresponding to a 20% increase from the local minimum in the least-squares cost function. For positions $x \leq 20$ cm, the error bars on the mix are fairly small as the best fit plots are in excellent agreement with the measured parallel wavenumbers, as can be seen in figure 4.17. Figure 4.18 suggests that there is more ionized neon in the plasma (up to 65-70% neon in the core) than the neutral pressure would suggest, which makes intuitive sense given that neon has a lower ionization potential than helium. The error bars are larger for positions $x > 24$ cm, which is understandable given the corresponding best-fit curves seen in figure 4.17. Overall, this diagnostic was successful in determining the ion density ratio as a function of position to rather high accuracy.

It should be noted that the reason the ionized density ratio in figure 4.18 differs so much from the 50% He/50% Ne case shown in figure 4.14 is that these measurements were taken in two different plasmas, several months apart, and while care was taken to reproduce similar plasma conditions, they are clearly not the same.

4.5 Conclusion

The purpose of this study was to investigate the ion-ion hybrid cutoff frequency of shear Alfvén waves in a two-ion species plasma, and evaluate its viability as a diagnostic for the ion density ratio. In section 4.2, theoretical work was done in order to expand the parameter regime in which this diagnostic could be applied. It was shown that for sufficiently large $k_\perp \delta_e$, the cutoff frequency is identical to the ion-ion hybrid frequency ω_{ii}, which can be expressed as a function of the ratio of ion densities. Numerical calculations demonstrated that this cutoff frequency was unchanged by kinetic thermal electron effects, allowing this diagnostic to potentially be used in a wide range of plasmas. In plasmas with significant ion finite Larmor radius (FLR) effects (i.e. where $k_\perp \rho_i \ll 1$ is not satisfied), it was shown that the cutoff frequency deviates from ω_{ii} and this diagnostic may not be valid. An additional caveat of large ion FLR effects is that they tend to excite additional propagation bands near the cutoff, which may mask the exact value of the cutoff frequency and further limit this diagnostic's accuracy. In addition, the cutoff frequency is unaffected by collisionality to lowest order.

Shear Alfvén waves were systematically launched in a helium/neon plasma for a wide range of conditions in the LAPD. In section 4.4, we were able to demonstrate the existence of two distinct propagation bands bounded by $\omega < \Omega_{Ne}$ and $\omega_{ii} < \omega < \Omega_{He}$. The cutoff frequency was measured from a variety of methods, such as the power spectrum and parallel dispersion $k_\parallel(\omega)$, and found to scale consistently with theory. Both methods are limited in their precision, due to various non-ideal effects concealing the exact location of the cutoff. An efficient algorithm was developed, which works by fitting the predicted dispersion relation to the measured $k_\parallel$ via least squares error, and finding the ion density ratio which yields the best fit. One of the advantages of this algorithm is that one does not need to know the electron density, $k_\perp$ spectrum, or even the distance between probes used to measure $k_\parallel$. Given a measured dispersion curve and the local background field, one can quickly and easily

apply this algorithm in order to determine the ion density ratio at this position.

A diagnostic was constructed out of a magnetic loop antenna and two accompanying B-dot probes in order to measure the parallel wavenumber at various positions in the plasma and apply the best-fit algorithm described above. Radial lines showed that for a plasma with equal fill pressures of helium and neon, the ionized neon concentration was estimated to be 65-70% in the core and 50-60% in the edge. Error bars were constructed by looking at the ion density ratios corresponding to a 20% increase from the local minimum in the least-squares error function. Overall, this diagnostic was successfully applied in order to obtain a radial profile of the ion density ratio.

CHAPTER 5

Polarization of Shear Alfvén Waves in Two-Ion Plasmas

In chapter 4, we successfully measured the parallel dispersion of shear waves in two-ion plasmas, and found that it agreed (within reason) with the predicted theory. The dispersion physics of the wave are governed by the underlying currents in the plasma - namely, the ion polarization, $E \times B$, and parallel electron currents - and it is the combination of these currents which facilitate wave propagation. There is one major aspect of wave physics which has been ignored, however, which is the impact of the antenna's geometry on the spatial structure of the wave. The antenna imposes the boundary conditions which set the $k_\perp$-spectrum of the wave, and this can drastically alter the spatial structure of the wave in a way that is not captured by dispersion physics alone. In this chapter we take a closer look at the polarization of two-ion shear waves, and compare it to the theoretical prediction from the dispersion physics. We find that while the lower band is in good agreement with theory, there are discrepancies in the upper band's polarization which cannot be explained by dispersion physics alone.

5.1 Introduction

A better understanding of the polarization of Alfvén waves in multi-ion species plasmas is important for explaining many observations in both laboratory and space plasmas. Electromagnetic ion cyclotron (EMIC) waves are shear Alfvén waves that exist in the earth's magnetosphere, at frequency bands below the ion cyclotron frequencies. It is believed that EMIC waves play an important role in magnetospheric dynamics, such as electron heating

and pitch angle scattering loss of ions and electrons [44, 21]. Measurements made by the GOES-1 and GOES-2 spacecraft suggested that the wave characteristics of EMIC waves, such as frequency and propagation direction, vary greatly depending on plasma density and He^+ concentration [111, 81]. The composition of plasma in the magnetosphere varies depending on many factors, but generally consists of a mix of H^+, He^+, and O^+. The O^+ concentration is typically much smaller than the concentrations of H^+ and He^+, and so the physics of shear waves in two-ion plasmas has direct relevance to developing a better understanding of the behavior of EMIC waves.

Exhaustive measurements in the global distribution of EMIC waves have shown that their polarization varies depending on many factors, such as the magnetic local time (MLT), L value, and propagation band in which they occur [70]. Satellite measurements found that EMIC events in the afternoon mostly occurred in the He^+ band and were left-hand polarized, whereas in the morning sector they occurred more commonly in the H^+ band and were linearly polarized. It was found that the early morning EMIC events experienced significant growth for highly oblique waves ($k_\perp \gg k_\parallel$), which may suggest that the observed linear polarization of these waves may be due to waves generated with large oblique wave vectors [4]. While the helium band tends to excite larger wave vector angles (($\theta_\mathbf{k} = \arctan k_\perp/k_\parallel$)), particularly at dawn, it was clearly observed in both propagation bands that the wave normal angle is small where left hand polarized waves dominate, and large in the region of linear polarization [5, 6].

EMICs are predicted to be most readily excited where the group velocity of the waves is lowest, making the equator the most preferable region for wave generation. Early theoretical studies predicted EMIC waves excited by anisotropic ion temperatures ($T_\perp > T_\parallel$) to be left-hand polarized at generation [20]. More recent simulations have shown that waves generated at the equator by protons with anisotropic temperature are expected to be strongly left-handed, and become increasingly linearly polarized as they propagate towards higher latitudes [51, 52]. Additionally, the simulations showed that angle of the wave's propagation

vector was found to increase as the wave propagated and became increasingly linear, supporting previous observations [4]. Motivated by observations taken by the AMPTE satellite [5, 6], a comprehensive theoretical study of EMIC growth and instabilities in two-ion magnetospheric plasmas suggested that the left-handed waves observed in the afternoon sector near the equator is a generation effect, whereas the linear polarization of the early morning waves may be due to a propagation effect associated with wave reflection [50]. It was further shown that the distribution of wave propagation angles varies with helium concentration. Although these previous theoretical endeavors have made great strides towards a better understanding of the observed global measurements of EMIC polarization, many questions still remain. Controlled laboratory experiments on shear waves in two-ion plasmas may lend additional insight into the behavior of these waves and their measured polarization.

Many experiments have been performed on the Large Plasma Device (LAPD) at UCLA in order to study the propagation and polarization of shear waves. Experiments on single-ion shear waves launched by a small disk exciter showed that the wave was linearly polarized at frequencies well below the ion cyclotron frequency [39]. More recently, a rotating magnetic field (RMF) antenna was built from two orthogonal current loops, which can be driven $\pm\pi/2$ out of phase in order to excite left and right handed circularly polarized waves [41]. One of the motivations for the development of the RMF antenna is to launch shear waves from satellites in order to deplete the earth's inner radiation belts of energetic particles via non-adiabatic scattering [87]. Particle-wave interactions are directly dependent on the handedness of the wave, and so a greater understanding of the polarization of two-ion shear waves would be directly beneficial to the efficacy of such an antenna.

The polarization of two-ion shear waves has relevance in burning tokamak plasmas, which typically consist of mixtures of D-T. Various polarimetry schemes exist for using wave polarization as a diagnostic tool in fusion plasmas. Faraday rotation is a phenomena which causes linearly polarized light waves to rotate when propagating along the background magnetic field, whereas the Cotton-Mouton effect results in cross-field linearly polarized waves to be-

come elliptically polarized [86]. Both effects have been successfully used as an interferometer-polarimeter diagnostic in tokamaks [13]. At Alfvénic frequencies, MHD spectroscopy has been used to make measurements of bulk plasma properties in tokamaks [31], although there is little published data on the use of polarimetry specifically.

The remainder of this chapter is organized as follows. In section 5.2 we derive the polarization of two-ion shear waves, as predicted by dispersion physics. In section 5.3, we outline the experimental setup used to launch shear waves in a laboratory environment. In section 5.4, we share the key results, as they pertain to wave polarization, and compare them to theory. Finally, a conclusion and discussion of future work are presented in section 5.7.

5.2 Dispersion Theory

In this section we review the notion of a circularly polarized coordinate system, something which has been used extensively in the plasma literature for studying magnetized plasmas [53, 84, 93]. We then transform the cold plasma wave equation into circularly polarized coordinates, and derive the ratio of left-to-right handed power for inertial Alfvén waves. For two-ion species plasma, it is shown that a "crossover frequency" exists in the upper band of the inertial Alfvén wave, in which the wave transitions from being majority right-handed to majority left-handed. A similar crossover frequency was derived by [29], although it was in the context of when the fast wave and slow wave have the same phase velocity and mode conversion occurs.

5.2.1 Recasting the Dispersion Matrix in Circularly Polarized Coordinates

Consider a uniform magnetized plasma ($\vec{B_0} = B_0\hat{z}$), subjected to a small monochromatic perturbation. The dispersion of a single wavefront, found from the spatial Fourier transform of equation 4.1, is described by the following system of equations:

$$\begin{bmatrix} \varepsilon_\perp - n_y^2 - n_z^2 & \varepsilon_{xy} + n_x n_y & n_x n_z \\ -\varepsilon_{xy} + n_x n_y & \varepsilon_\perp - n_x^2 - n_z^2 & n_y n_z \\ n_x n_z & n_y n_z & \varepsilon_\parallel - n_x^2 - n_y^2 \end{bmatrix} \cdot \begin{pmatrix} E_x \\ E_y \\ E_z \end{pmatrix} = 0. \tag{5.1}$$

Taking the determinant of equation 5.1 will yield the dispersion relation given by equation 4.3, where $n_\perp^2 = n_x^2 + n_y^2$. This has been previously derived in [89]. In the limit $n_\perp^2 \gg |S|, |D|$, we showed that the dispersion relation of the slow branch reduces to the inertial Alfvén wave, given by equation 4.4, and is the only propagating branch in the LAPD plasmas we are considering.

The natural language of waves in a magnetized plasma is to describe them in terms of their circularly polarized components. We define the left and right handed unit vectors $\hat{l}$ and $\hat{r}$, respectively, as:

$$\begin{aligned} \hat{l} &= \frac{1}{\sqrt{2}} \left(\hat{x} - i\hat{y} \right), \\ \hat{r} &= \frac{1}{\sqrt{2}} \left(\hat{x} + i\hat{y} \right), \end{aligned} \tag{5.2}$$

where $\hat{l}$ represents a unit vector which rotates in the direction of ion gyromotion, and $\hat{r}$ rotates with the electrons [84]. The complex unit vectors $\hat{l}$, $\hat{r}$, and $\hat{z}$ form an orthonormal basis in R^3, and so any 3-dimensional vector field (which has been Fourier transformed into frequency space) can be uniquely expressed in this coordinate basis. The left and right handed components of the electric field can be found by projecting $\vec{E}$ onto $\hat{l}$ and $\hat{r}$ (recall that the inner product for complex vectors is defined by $a \cdot b = \Sigma a_i b_i^*$). The coordinate transformation from Cartesian to circularly polarized, then, is achieved by the following transformation matrix U [53]:

$$\begin{pmatrix} E_L \\ E_R \\ E_z \end{pmatrix} = \mathbf{U} \cdot \begin{pmatrix} E_x \\ E_y \\ E_z \end{pmatrix}, \quad \text{where} \quad \mathbf{U} = \begin{bmatrix} 1/\sqrt{2} & i/\sqrt{2} & 0 \\ 1/\sqrt{2} & -i/\sqrt{2} & 0 \\ 0 & 0 & 1 \end{bmatrix}. \tag{5.3}$$

The transformation matrix U satisfies the condition for unitarity $U \cdot U^{\dagger} = I$, where $\mathbf{U}^{\dagger}$ is the Hermitian of U. Note that our definitions for $\hat{l}$, $\hat{r}$, and $\mathbf{U}$ are based off the convention $\partial_t \rightarrow -i\omega$ (and, consequently, $\nabla \rightarrow i\vec{k}$), which is typical in plasma physics literature [93]. It's worth emphasizing that many FFT algorithms use the opposite sign convention for their forward Fourier transforms, in which case the complex conjugates of equations 5.2 and 5.3 should be used instead. Additionally, equations 5.2 and 5.3 are only valid for $\omega > 0$, and their complex conjugates should be used when dealing with negative frequencies.

The dispersion matrix of equation 5.1 can be recast into circularly polarized coordinates by the transformation $\mathbf{U} \cdot \mathbf{W} \cdot \mathbf{U}^{\dagger}$, where $\mathbf{W}$ is the 3×3 Cartesian matrix in equation 5.1. This gives us the following system of equations:

$$\begin{bmatrix} \varepsilon_L - n_L n_R - n_z^2 & n_L^2 & n_z n_L \\ n_R^2 & \varepsilon_R - n_L n_R - n_z^2 & n_z n_R \\ n_z n_R & n_z n_L & \varepsilon_{\parallel} - 2 n_L n_R \end{bmatrix} \cdot \begin{pmatrix} E_L \\ E_R \\ E_z \end{pmatrix} = 0, \tag{5.4}$$

where $\varepsilon_{R,L} = \varepsilon_{\perp} \pm i\varepsilon_{xy}$. The determinant of equation 5.4 will again yield the same dispersion relations given by equation 4.3.

5.2.2 Polarization Energy of Shear Alfvén Waves

The ratio of left-to-right handed power in the electric field, for a given frequency, can be found by combining the first and second lines of equation 5.4, and gives the following:

$$\frac{|E_L|^2}{|E_R|^2} = \left| \frac{n^2 - \varepsilon_R}{n^2 - \varepsilon_L} \right|^2, \tag{5.5}$$

where $n^2 = n_{\perp}^2 + n_{\parallel}^2$. The handedness of waves is traditionally discussed in the context of the polarization of the wave's transverse electric field. The antenna used in this experiment (described in detail in section 5.3) works by inductively coupling to the plasma in order to drive the x and y components of the magnetic field out of phase, resulting in elliptically

polarized waves [41]. The ratio of the left-to-right handed power of the wave's *magnetic* field can be found by combining equation 5.4 with Faraday's law, and gives the following:

$$\frac{|B_L|^2}{|B_R|^2} = \left| \frac{n^2 - \varepsilon_R + \frac{\varepsilon_{xy}}{\varepsilon_\parallel} n_\perp^2}{n^2 - \varepsilon_L - \frac{\varepsilon_{xy}}{\varepsilon_\parallel} n_\perp^2} \right|^2 . \tag{5.6}$$

Equations 5.6 and 5.5 are similar in form, but differ due to the presence of a parallel electron current. When $n_\perp^2 \to 0$, the polarized power ratios of the electric and magnetic fields are identical. Additionally, in the low frequency limit $\omega \ll \Omega_{c,i}$, where the net $E \times B$ slippage current vanishes, ε_{xy} reduces to zero and equation 5.6 is identical to 5.5. Equation 5.6 is valid for both modes in the system, whose dispersion relations are given by equation 4.3. Since we are specifically interested in the polarization of shear waves, we can insert the inertial Alfvén wave dispersion, given by equation 4.4, into 5.6 to get the following:

$$\frac{|B_L|^2}{|B_R|^2} = \left| \frac{n_\perp^2 \left(1 - \frac{\varepsilon_L}{\varepsilon_\parallel}\right) - \varepsilon_{xy}}{n_\perp^2 \left(1 - \frac{\varepsilon_R}{\varepsilon_\parallel}\right) + \varepsilon_{xy}} \right|^2 . \tag{5.7}$$

Equation 5.6 is the ratio of left-to-right handed energy for the shear wave, in the limit of large $k_\perp$. Figure 5.1 shows the ratio of left-to-right handed power of the shear wave, for various values of $k_\perp \rho_s$, in a 50% He / 50% Ne plasma. Ions were assumed to be cold for this calculation, although accounting for ion FLR effects yields similar results. In calculating $k_\perp \rho_s$, $k_\perp$ was varied while T_e was fixed at 5 eV (typical for LAPD plasmas). The variable ρ_s is the *root-mean-square ion sound gyroradius* of the plasma, defined by:

$$\rho_s^2 = \sum_{ions} f_i \rho_{s,i}^2 = \sum_{ions} \frac{n_i}{n_e} \frac{c_{s,i}^2}{\Omega_{ci}^2}.$$

In order to capture possible kinetic effects in the left-right power ratio, the full dispersion relation given by equation 4.3 was solved numerically, as it is valid for all values of $k_\perp$, and then substituted into equation 5.6. In the dielectric terms, given by equation 4.17, the cold ion limit ($\zeta_{\pm 1,i} \gg 1$) was assumed in order to simplify calculations, although kinetic electron

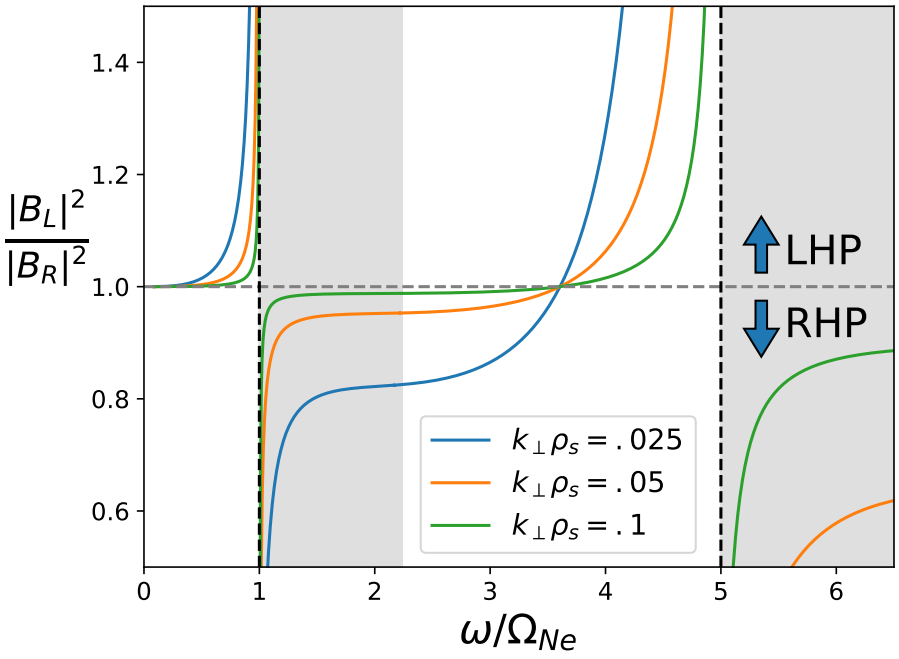

Figure 5.1: Ratio of left-to-right handed power in the magnetic field of the shear Alfvén wave, for several values of $k_\perp$. Greyed out frequency bands indicate regions of evanescence.

effects were preserved. The frequency bands where shear waves are evanescent (as predicted by equation 4.3) are shaded in grey in figure 5.1. Although figure 5.1 doesn't account for ion cyclotron damping, we see the shear wave becomes increasingly left handed as it approaches either cyclotron frequency. In the upper band, the energy is predominantly right handed just above the two-ion cutoff frequency, and then above a certain frequency it flips and becomes left hand dominant. This crossover frequency, which we define as ω_x, can be found by setting equation 5.6 equal to unity:

$$\omega_x^2 = \frac{\omega_{p1}^2\Omega_2^3 + \omega_{p2}^2\Omega_1^3}{\omega_{p1}^2\Omega_2 + \omega_{p2}^2\Omega_1}. \tag{5.8}$$

Equation 5.8 is unique to a plasma with two ion species, and is also the frequency that corresponds to $\varepsilon_R = \varepsilon_L$ in the cold ion limit. Note that this is *not* the same crossover frequency for low-$k_\perp$ waves at which mode conversion occurs due to the fast and slow waves having identical wavelengths [92]. An interesting feature of ω_x is that it is the same for all values of $k_\perp$, as well as being valid for all electron temperatures. This suggests ω_x would be a potentially robust measurable quantity in the lab. The normalized crossover frequency ω_x/Ω_2 can be expressed as a function of the ionized density ratio, offering motivation as a possible diagnostic tool. Previous experiments have investigated measurement of the ion-ion hybrid cutoff frequency ω_{ii} as a diagnostic [101, 102], which can similarly be expressed as a function of the ion density ratio, but the author is not aware of any previous attempts to measure ω_x.

For larger values of $k_\perp$, $|B_L|^2 \sim |B_R|^2$ for nearly all frequencies in this region, corresponding to a linearly polarized wave. The reason for this can be explained through the physics of the shear wave. When $k_\perp \to 0$, the shear wave is mediated entirely by cross-field currents - namely, the ion polarization current and E×B drift. When $k_\perp$ is finite, the necessity of the wave to satisfy $\cdot\vec{J} = 0$ introduces a parallel electron current. All three currents contribute to the wave's perpendicular magnetic field and the resulting polarization, as seen in equation 5.7. When $n_\perp^2 \gg |S|, |D|$, the parallel electron current is so large that its contribution to

the perpendicular magnetic field completely dwarfs the ion polarization and E×B current contributions, resulting in a linearly polarized wave. This can be seen in previous disk exciter studies [72, 73, 39], where the wave's magnetic field was entirely azimuthal.

The results of figure 5.1 are consistent with both simulations and measurements of EMIC waves in the earth's magnetosphere. Early simulations showed that waves with oblique wave vectors ($k_\perp \gg k_\parallel$) were expected to be close to linearly polarized, while parallel propagating wave vectors ($k_\perp \ll k_\parallel$) were much more left handed, which is consistent with the $k_\perp$ scaling shown in figure 5.1. Measurements taken by both the AMPTE and THEMIS spacecraft reported similar findings [5, 6, 70].

5.2.3 Near-field Coupling of a Magnetic Dipole Antenna

The analytic study of the left-to-right handed power ratio of the shear wave is based on the dispersion properties of the wave, which are set by the plasma. We have not considered one other major factor in determining the polarization of the wave, which is the boundary conditions imposed by the antenna. Previous antenna experiments have shown that the plasma tends to create parallel electron currents parallel to the antenna's vacuum electric field. For the case of a disk exciter, the antenna excites a single parallel current channel along the the field [38], while a magnetic dipole antenna has been shown to create two antiparallel current channels along the field lines passing through either edge of the dipole (where the vacuum electric field is parallel to the background magnetic field) [41, 60].

Consider a magnetic dipole, centered on the origin and lying in the XZ plane. If the dipole has an alternating current with frequency ω, a vacuum electric field will form rings around the dipole parallel to the dipole current. At a given position, the component of the vacuum electric field projected onto $\hat{z}$ will couple to the parallel plasma conductivity and induce an electron current, which is generally much larger than the induced cross-field currents. Directly in front of the antenna, along $x = 0$, $y = 0$, the vacuum electric field points in the $\hat{x}$ direction and no parallel current is produced. To lowest order, the resulting

plasma currents excited in front of the antenna can be found from the plasma conductivity tensor $\overleftrightarrow{\sigma}$:

$$\begin{pmatrix} J_x \\ J_y \\ J_z \end{pmatrix} = \begin{bmatrix} \sigma_\perp & \sigma_{xy} & 0 \\ -\sigma_{xy} & \sigma_\perp & 0 \\ 0 & 0 & \sigma_\parallel \end{bmatrix} \cdot \begin{pmatrix} E_0 \\ 0 \\ 0 \end{pmatrix}, \tag{5.9}$$

where the conductivity is related to the plasma dielectric via $\overleftrightarrow{\varepsilon} = \overleftrightarrow{I} + (i/\omega\varepsilon_0)\overleftrightarrow{\sigma}$. This excites an ion polarization in $\hat{x}$ ($J_x = \sigma_\perp E_0$) and E×B drift in $\hat{y}$ ($J_y = -\sigma_{xy} E_0$). The ion polarization and E×B currents induce a magnetic field in $\hat{y}$ and $\hat{x}$, respectively, resulting in an elliptically polarized wave. The ratio of left-to-right handed magnetic energy of the near-field coupling can be found from equation 5.9 and $\times\vec{B} = \mu_0\vec{J}$, and is given by the following:

$$\frac{|B_L|^2}{|B_R|^2} = \frac{|L|^2}{|R|^2}. \tag{5.10}$$

Figure 5.2 shows the ratio of left-to-right handed coupled energy, directly in front of the magnetic dipole antenna, for a 50% He/50% Ne plasma. The regions of evanescence are greyed out, as they have no measurable impact on the far-field of the wave. Note that this is *only* the polarized energy due to the cross-field currents at $x = 0$, $y = 0$. A dipole with radius a lying in the XZ plane will drive two antiparallel current channels along $x = \pm a$, resulting in a linearly polarized magnetic field $B_y\hat{y}$ along the $r = 0$ field line. The addition of the linearly polarized field with the left or right handed polarized field induced by the cross-field currents will result in an elliptically polarized field of the same handedness, and so figure 5.2 is instructive in elucidating the polarization imposed in front of the antenna. We see that the coupled power is linearly polarized at $\omega = 0$ and $\omega = \omega_x$, similar to the dispersion relation, although it is also linearly polarized at the cutoff frequency ω_{ii}. The coupled power right-hand is dominant in the same region of right-hand dominance observed in figure 5.1, for $\omega_{ii} < \omega < \omega_x$, and similarly for the left-handed bands. In other words, there

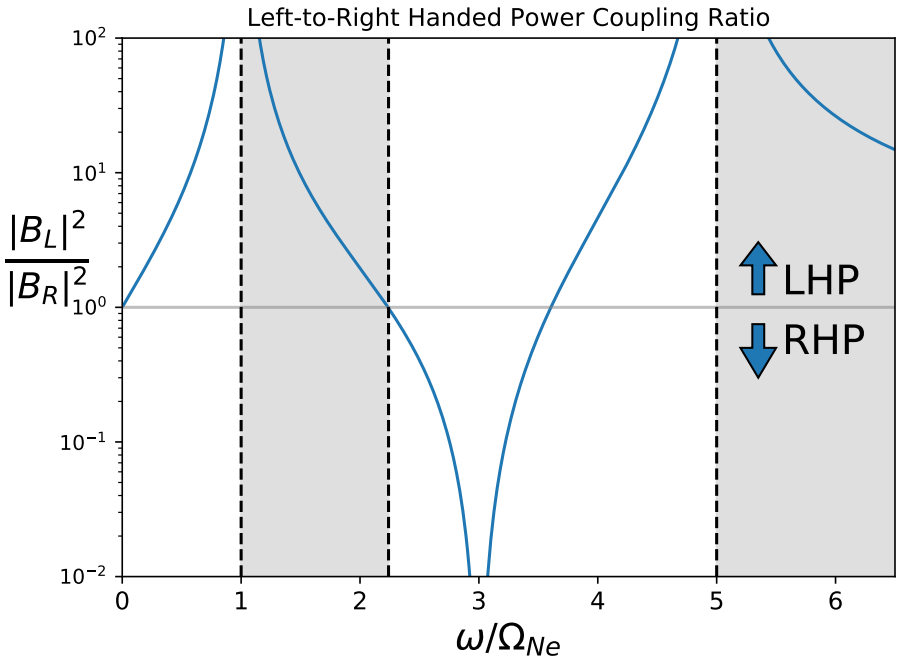

Figure 5.2: Ratio of left-to-right coupled power in the near-field of a magnetic dipole, lying in the XZ plane, due to the induced cross-field currents. This calculation assumes $k_\perp \to 0$. Greyed out frequency bands indicate regions of evanescence.

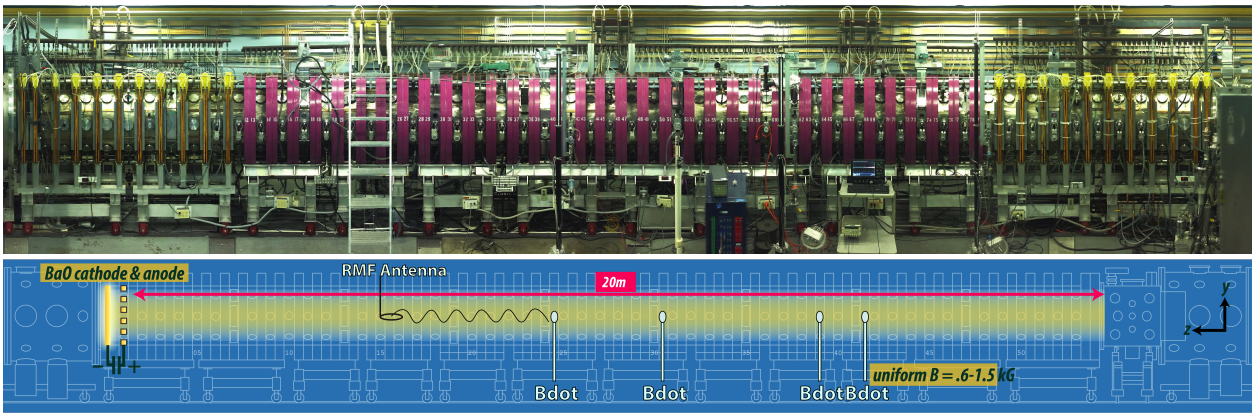

Figure 5.3: Picture (upper) and schematic (lower) of LAPD, showing location of RMF antenna and probes.

are no frequencies at which the wave dispersion (figure 5.1) predicts a certain handedness but the antenna coupling (figure 5.2) "overrides" it and imposes the opposite polarization. Therefore figure 5.1 should be sufficient in predicting the measured polarization of shear waves excited by a magnetic dipole along the $r = 0$ line, at least qualitatively.

5.3 Experimental Setup

5.3.1 Overview of LAPD

A series of experiments were performed in the upgraded Large Plasma Device (LAPD), which is part of the Basic Plasma Science Facility (BaPSF) at UCLA. The LAPD is an 18 meter long, 1 meter diameter cylindrical vacuum chamber. The vessel is surrounded by 56 electromagnets which are capable of producing a highly uniform magnetic field ($\delta B/B_0 <$ .5%) up to 3000 G. A DC discharge is applied to a barium oxide (BaO) coated cathode at one end of the machine to produce a stream of primary electrons. The electron stream passes through a 50% transparent mesh anode located 52 cm away, ionizing the gas throughout the rest of the chamber. The discharge lasts for 12 ms, and is fired once per second to create a highly reproducible plasma column approximately 56 cm in diameter. An overview of basic

Parameter	*Value*
Ions	He^+ and Ne^+
Gas (fill) pressure	$2 - 3 \times 10^{-5}$ Torr
Background magnetic field	600-1650 G
Plasma density (interferometer)	2.5×10^{12} cm^{-3}
Electron temperature (T_e)	4-5 eV
Ion temperature (T_i)	$<$1 eV
Electron cyclotron frequency	1.7-4.6 GHz
Helium cyclotron frequency	228.7-629 kHz
Electron skin depth	3.4 mm
Electron-neutral collision frequency	285 kHz
Ion-neutral collision frequency	100 Hz
Coulomb collision frequency	4.75 MHz

Table 5.1: Range of plasma parameters considered in this experiment.

plasma parameters for this experiment can be found in table 5.3.1.

A gas feed system is located at the center of the machine, capable of providing the chamber with steady supplies of hydrogen, helium, neon, and argon. Mass flow controllers (MFC) allow the experimenter to precisely control the gas mix supplied to the chamber, while a residual gas analyzer (RGA) is used to estimate the neutral partial pressures of each gas. This experiment is performed in various mixes of helium and neon, and for background fields ranging from 600-1500 G.

5.3.2 Antenna and Probes

This experiment uses the rotating magnetic field (RMF) antenna, originally designed to study circularly polarized waves [41]. The RMF antenna consists of two orthogonal loops of wire,

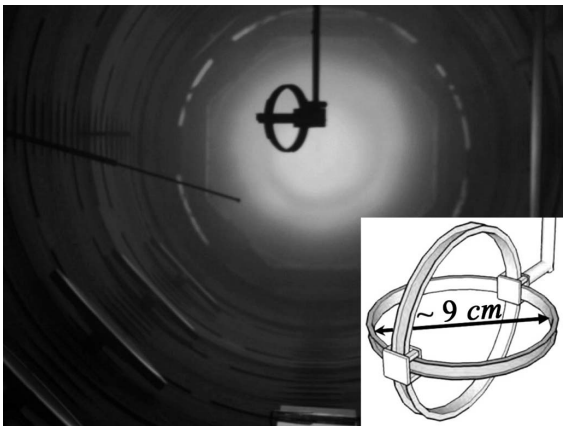

Figure 5.4: Picture of rotating magnetic field (RMF) antenna used to launch shear Alfvén waves, with cathode visible at far end. (inset) Schematic drawing of antenna

approximately 9 cm in diameter, which can be driven out of phase to produce elliptically polarized waves. The majority of this experiment utilizes only the horizontal loop of the antenna (lying in the XZ plane), essentially using it as a magnetic dipole antenna. The antenna is driven by a sinusoidal waveform generator, which is then fed through an RF amplifier capable of delivering several amps of current to the antenna. The amplitudes of the resulting shear waves are on the order of tens of milliGauss, which is 1-2 orders of magnitude above the background turbulent fluctuations of the plasma. The RF amplifier was initiated at the same time offset for every plasma shot, resulting in the wave being phase-locked between shots[1], which allowed detailed 2-D measurements to be taken of the spatial structure of the wave.

Magnetic field fluctuations are measured using four three-axis induction (B-dot) probes, located at various axial positions in the plasma. Each component of the probe contains two, oppositely wound 25 turn coils, which are fed through a differential amplifier to subtract out any electrostatic pickup in the coil [28]. The location of the antenna and B-dot probes are shown in figure 5.3. Previous experiments have shown that magnetic dipole antennas

[1]Small variations in phase may occur from shot to shot, due to slight fluctuations in the density profile, but these phase differences are minute compared to the size of the parallel wavelengths excited.

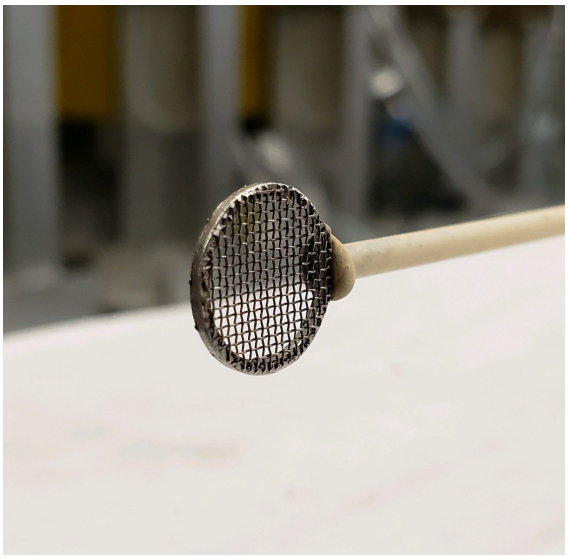

Figure 5.5: One of the two disk exciters used to launch shear waves. The disk is a mesh so as to not obstruct the path of primary electrons from the BaO cathode.

tend to excite large antiparallel electron currents along the field lines at $x = \pm a$, where a is the radius of the dipole [41]. In the absence of cross-field plasma currents, symmetry dictates that this would create a linearly polarized magnetic field $B_y\hat{y}$ along the $r = 0$ field line. This symmetry is taken into consideration in this experiment, as the majority of B-dot measurements are taken along $r = 0$.

In section 5.4.5, we consider the radiation pattern due to two metal disk exciters, located at the same z position and biased with equal and opposite voltage signals. A simplified schematic of the electronics is shown in figure 5.6, as well as a picture of one of the disks in figure 5.5. Both disks are connected to either end of the secondary coil of an isolating transformer, and the secondary coil is center tapped so that a DC bias can be applied to both disks. Without a DC bias, the disk voltages oscillate around the floating potential, and for large amplitude signals the current response would be limited by the ion saturation current of the plasma.

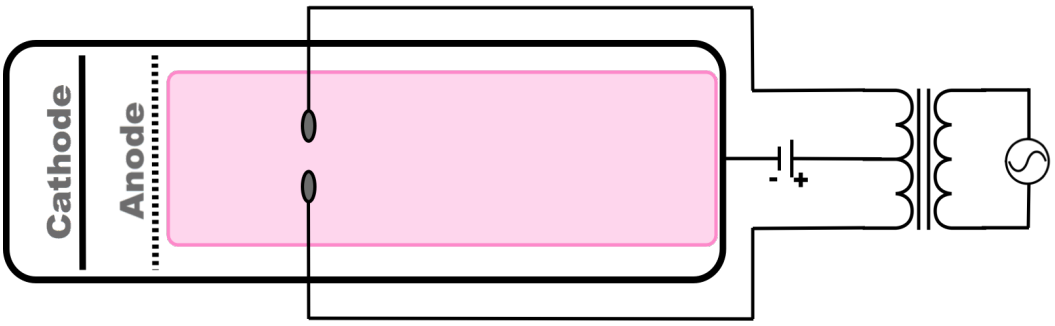

Figure 5.6: Schematic of electronics used to drive two disk exciter antennas with equal and opposite biases. The secondary coil of a 1:1 isolating transformer goes to each of the disks, which are inside the plasma. The secondary is centered tapped with respect to ground in order to bring the DC bias of both disks up out of the ion saturation region.

5.4 Experimental Results

5.4.1 Launching L and R waves with the RMF Antenna

The majority of this paper considers waves excited by driving current through the horizontal loop of the RMF antenna, using it as a magnetic dipole antenna. We then rely on using equation 5.3 to analytically decompose the resulting B-dot signals into their left and right hand polarized (LHP and RHP) constituents. But before doing so, it's essential to have some sort of idea of what kind of spectrum one might expect from launching "pure" L and R waves, so that we can validate the results of using equation 5.3 when used to decompose arbitrary waveforms. The RMF antenna consists of two orthogonal loops, as it was originally designed to excite left and right hand polarized waves. By driving the two loops $\pm\pi/2$ out of phase, previous experiments have shown that the RMF antenna is able to couple nearly all of its energy into either a left or right hand polarized wave [41].

Figure 5.7 compares the spectra of launching "pure" L and R waves, by phasing the two RMF loops, with the spectra that result from analytically decomposing the wave from a single loop into its LHP and RHP constituents. Measurements were taken at $r = 0$

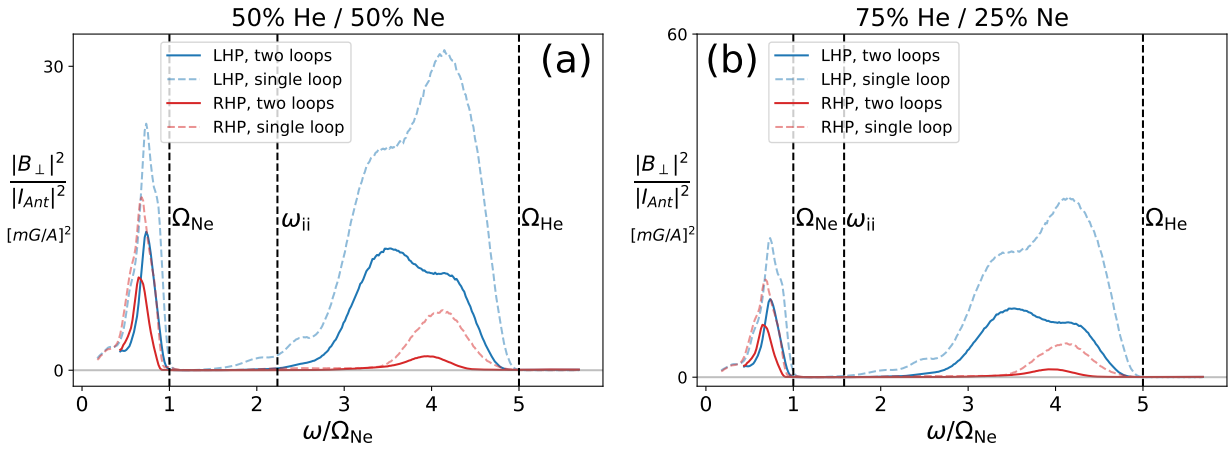

Figure 5.7: Comparison of the spectra resulting from launching pure LHP and RHP waves with a linearly polarized wave which has been analytically decomposed into its LHP and RHP components, for a (a) 50% He / 50% Ne and (b) 75% He / 25% Ne plasma.

cm, which corresponds to the field line passing through the midpoint of the antenna. The power spectra shown are normalized to the antenna current I_{Ant}, as the outputted current by the RF amplifier was not constant with frequency. It's worth noting that the pure and analytically decomposed cases were measured several months apart, and while care was taken to reproduce similar plasma conditions, small differences in overall density and mix are expected. Despite this, the pure L and R spectra are in good qualitative agreement with the analytically decomposed LHP and RHP spectra. Both the L and R waves are observed to contain two distinct propagation bands. For $\omega < .65\Omega_{Ne}$, the decomposed wave consists of nearly equal parts LHP and RHP, suggesting that the wave is linearly polarized at low frequencies. Similar behavior is observed in the pure L and R spectra, suggesting that the plasma is indifferent to wave polarization at these frequencies. Closer to the neon cyclotron frequency, both the pure and decomposed waves are observed to exhibit a preference for LHP waves. This is consistent with figure 5.1, which predicts that shear waves are linearly polarized at low frequency and become increasingly left-hand dominant near the ion cyclotron frequencies.

Above ω_{ii}, the plasma is observed to have a strong preference for left-handed waves in both the pure and decomposed cases. The upper band of the LHP wave is bounded by $\omega_{ii} < \omega < \Omega_{He}$, where ω_{ii} is the ion-ion hybrid cutoff frequency given by the root of equation 4.4. The ion-ion hybrid frequency of each mix was estimated from the ratio of neutral partial pressures, and marked by a vertical dashed line in figure 5.7. An upper band is also observed for the RHP wave, for both the pure and decomposed cases, although it does not appear to share the same cutoff frequency as the LHP wave. Regardless, figure 5.7 shows that the LHP and RHP spectra resulting from analytic decomposition of the linear wave is consistent with the spectra of pure L and R waves.

5.4.2 Scaling of LHP and RHP with Mix and Field

Figure 5.7 showed that the spectra resulting from launching pure L or R waves are consistent with those obtained from a linearly polarized wave, and so the remainder of this paper will only consider linearly polarized waves (launched from the horizontal loop of the RMF antenna) which have been analytically decomposed via equation 5.3. We are interested in how the energy of the shear Alfvén wave is distributed between its left and right handed components, and how the polarization of the wave varies with species mix.

Figures 5.8a and 5.8b show the left and right handed power spectra, respectively, of a decomposed linear wave, for various mix ratios. The mix ratios are based on the fill pressure of the neutral gasses, and are not expected to be equal to the ionized density ratio. Two distinct propagation bands are observed in both the LHP and RHP spectra. The lower band for both components is bounded by $\omega < \Omega_{Ne}$. While both the LHP and RHP spectra have upper bands, they appear to be bounded by different cutoff frequencies. The cutoff frequency of the LHP spectrum scales with mix in a way that is consistent with ω_{ii}, which is the cutoff frequency predicted by equation 4.4 for high-$k_\perp$ shear waves. The RHP spectrum possesses a different cutoff frequency altogether, which also scales with mix. Additionally, the upper band of the RHP spectrum becomes increasingly prominent with increased helium

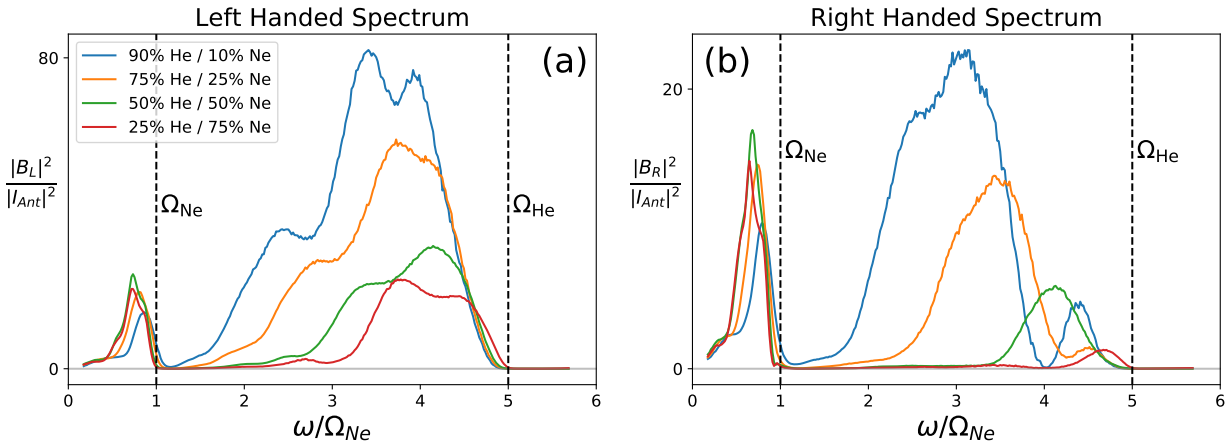

Figure 5.8: Power spectra for the (a) left and (b) right handed components of a wave launched by a magnetic dipole antenna, for various fill pressures of helium and neon.

concentration.

Next, we are interested in how the ratio of left-to-right handed magnetic field energy changes under varying plasma conditions, so it can be compared to the theoretical model derived in section 5.2. Figures 5.9a and 5.9b show the polarized energy ratio for different mixes and background fields, respectively. The field is fixed at $B_0 = 1500$ G in figure 5.9a, whereas the neutral pressure is fixed at 50% He/50% Ne in figure 5.9b. Data points where the failed to meet a coherence threshold of $r^2 > .98$ with the antenna current were deemed too noisy, and omitted from the plots. For $\omega < \Omega_{Ne}$, both figures scale consistently with the theoretical prediction shown in figure 5.1. In particular, the wave has roughly equal parts LHP and RHP at low frequency, indicating the wave is linearly polarized, and then becomes increasingly left-handed as it approaches the neon cyclotron frequency.

Above $\omega > \Omega_{Ne}$, the wave is observed to be left-hand dominant for nearly all mixes and background field cases. We expect a crossover frequency, defined by equation 5.8, where the wave switches from being right-hand dominant to left handed, but this is not observed in the data. The predicted (normalized) crossover frequency is labelled with a dashed line in figure 5.9b, as its value is independent of field. A large dip can be seen in the polarized

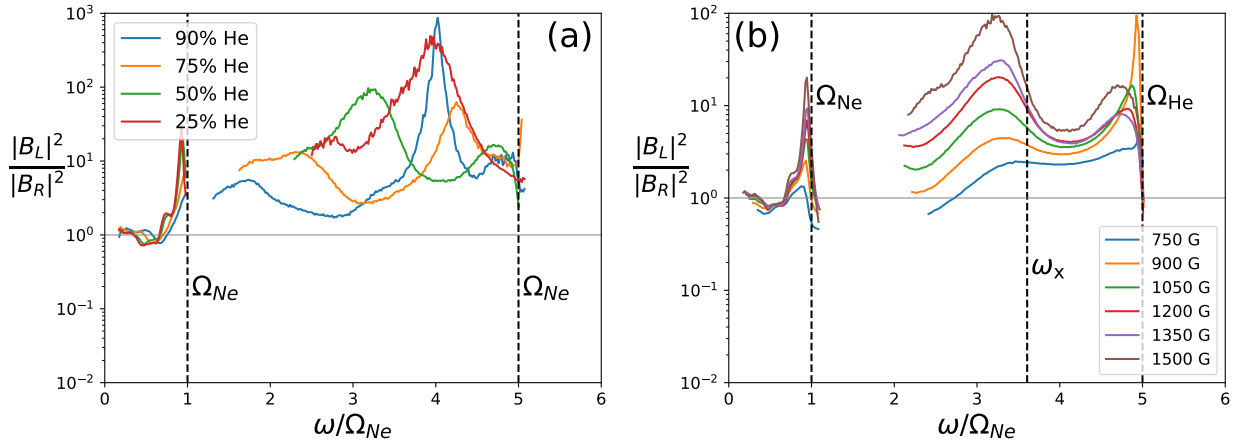

Figure 5.9: Ratio of left-to-right handed power for various (a) mixes and (b) background fields, for a shear wave launched from a magnetic dipole.

power ratio around $\omega/\Omega_{Ne} = 4.1$, which corresponds to the peak of the RHP component's upper band that was observed in figure 5.8b. The left-hand dominance of the upper band becomes much more pronounced with increasing background field.

5.4.3 Damping and Dispersion

It is unclear the cause of the discrepancy between the theoretical prediction of the upper band's polarization and the observed results, namely why the wave is almost completely left-hand polarized across the entire band despite the theory predicting it to be close to linearly polarized. One possibility that was considered is that the antenna is, in fact, coupling a linearly polarized wave onto the plasma, but the right-handed component of the wave experiences significantly more spatial damping as it propagates, resulting in the left-hand dominant wave far from the antenna. The left and right handed power spectra are shown in figure 5.10 at various distances from the antenna. Both figures are for a 50% He/50% Ne plasma, with $B_0 = 1500$ G. In the lower band, the LHP and RHP components of the wave decay at roughly the same rate with z, suggesting the lower band retains its linear polarization as it propagates. In the upper band, the wave's LHP component contains a

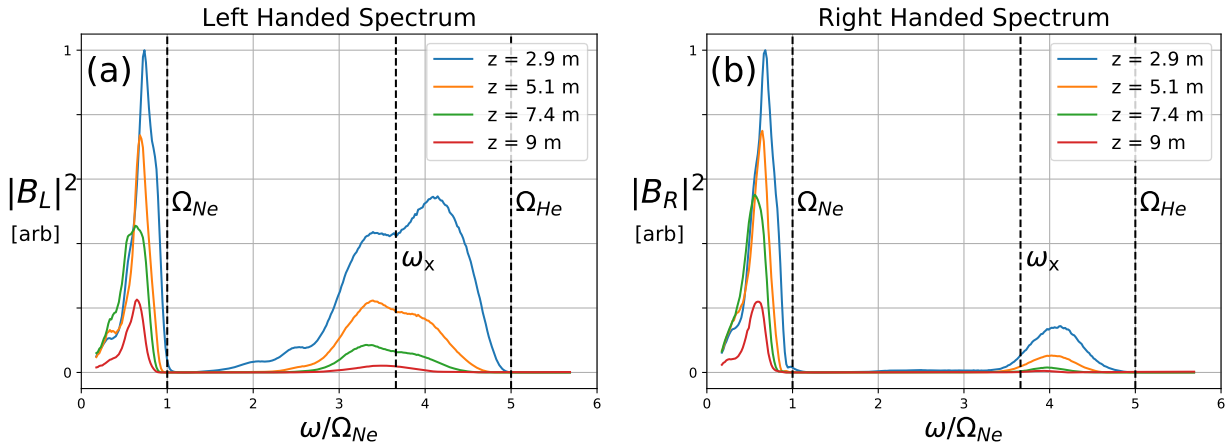

Figure 5.10: (a) Left and (b) right handed power spectra of a 50% He/50% Ne, 1500 G plasma, at four different distances from the antenna. The predicted crossover frequency ω_x is marked with a vertical dashed line.

lot of power at frequencies near the cutoff ($\omega_{ii} \sim 2.24\Omega_{Ne}$), but it rapidly dissipates with increasing z.

Past LAPD shear wave experiments have shown that the dominant mechanism for loss of wave energy along the machine is due to electron-ion collisions [39]. Assuming binary collisions, the electron-ion collison frequency is given by [62]:

$$\nu_e = \frac{\pi}{\sqrt{2}} \frac{n_e e^4 \ln \Lambda}{m_e^{1/2} T_e^{3/2}}, \tag{5.11}$$

where $\ln \Lambda$ is the Coulomb logarithm. Assuming $\ln \Lambda$ is largely unvarying with changing plasma conditions, it is easy to verify that the electron-ion collision frequency does not scale with background field. The parallel dielectric response can be modified to account for electron-ion collisions, which results in the following modified inertial Alfvén wave dispersion relation:

$$n_\parallel^2 = S\left(1 + k_\perp^2 \delta_e^2\right) + iS\frac{\nu_e}{\omega}\delta_e^2 k_\perp^2. \tag{5.12}$$

This can be solved for the real and imaginary parts of the parallel wavenumber:

$$\mathrm{Re}\left[k_{\parallel}\right]^2 \equiv k_{||}^2 = \frac{1}{2}\frac{\omega^2}{c^2}S\left(\sqrt{(1+k_\perp^2\delta_e^2)^2 + \left(\frac{\nu_e}{\omega}k_\perp^2\delta_e^2\right)^2} + 1 + k_\perp^2\delta_e^2\right), \tag{5.13}$$

$$\mathrm{Im}\left[k_{\parallel}\right]^2 \equiv \kappa^2 = \frac{1}{2}\frac{\omega^2}{c^2}S\left(\sqrt{(1+k_\perp^2\delta_e^2)^2 + \left(\frac{\nu_e}{\omega}k_\perp^2\delta_e^2\right)^2} - 1 - k_\perp^2\delta_e^2\right). \tag{5.14}$$

In the absence of collisionality, equation 5.13 reduces to the inertial Alfvén wave dispersion given by equation 4.4. Noting that the quantity $\omega^2 S(\bar{\omega})$ is independent of background field, where $\bar{\omega} \equiv \omega/\Omega_{Ne}$, it can be shown that $k_R(\bar{\omega})$ is independent of background field in the collisionless limit, and weakly dependent when weak collisions are accounted for. In light of equation 5.12, we define "weakly collisional" as the following condition:

$$\frac{\nu_e}{\omega} \ll 1 + \frac{1}{k_\perp^2\delta_e^2}.$$

This condition allows us to expand equation 5.14 to get the spatial damping of the inertial Alfvén wave in weakly collisional plasmas:

$$\kappa \approx \frac{1}{2}\frac{\nu_e}{c}\sqrt{S}\frac{k_\perp^2\delta_e^2}{\sqrt{1+k_\perp^2\delta_e^2}}. \tag{5.15}$$

Equation 5.15 shows that large-$k_\perp$ features of the wave will damp more rapidly with z, resulting in a "smoothing out" of the wavefront far from the antenna. It can be shown from equation 5.15 that $\kappa(\bar{\omega}) \propto 1/B$, meaning waves will experience stronger damping with decreasing background field. A similar derivation can be done to show $\kappa(\bar{\omega}) \propto 1/\sqrt{B}$ for a highly collisional plasma.

For a wave with a given frequency in the upper band, figure 5.7 says that all $k_\perp$ components of the wave will share the same handedness, with larger $k_\perp$ waves being closer to linearly polarized. Since equation 5.15 suggests that large-$k_\perp$ features damp faster, it follows

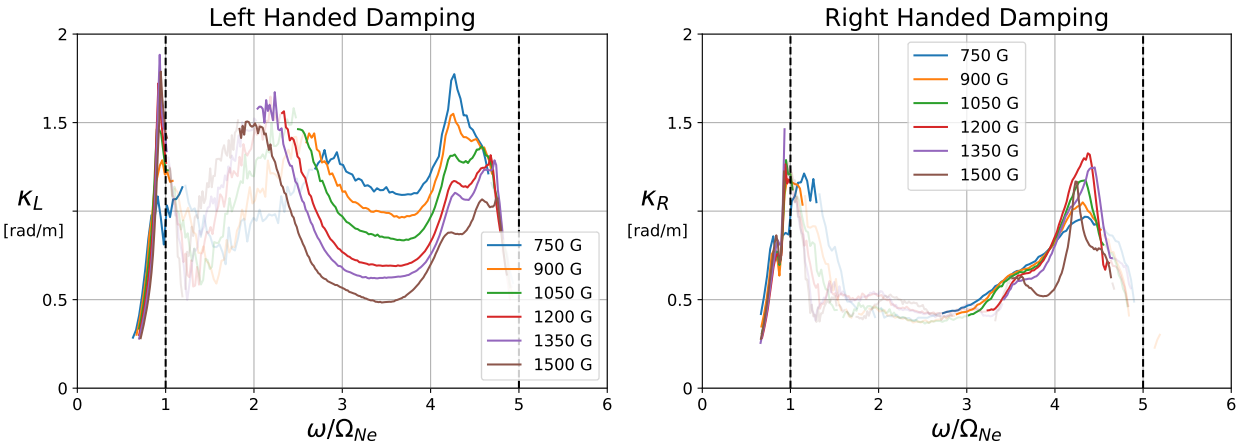

Figure 5.11: Spatial damping κ of the (a) left and (b) right hand polarized components of a shear wave launched from a magnetic dipole.

that the polarization of a wave will gradually increase as it propagates. In other words, collisionality will have the effect of making a slightly left-handed wave gradually more left-handed as it propagates in z, and similarly for right-handed waves. This means that collisions cannot explain the observed left-hand dominance in the part of the upper band where right-handed waves are expected.

The power spectra of the four B-dot probes from figure 5.10 were fit to a negative exponential $e^{-2\kappa z}$ via least squares in order to estimate the spatial damping κ. This was done for both the LHP and RHP components of the wave, and the results can be seen in figure 5.11. Data points which failed to meet a coherence threshold of $\gamma^2 > .8$ are included but faded out. In the lower band, both the left and right handed damping is relatively unchanged with background field, with is contrary to the $1/B$ scaling predicted for damping due to weak electron-ion collisions. As the frequency approaches the helium cyclotron frequency, it was shown in chapter 3 that the wavefront spreads out radially in a conical pattern (see equation 3.45). As the angle of the propagation cone is independent of B, it is suspected that the primary damping mechanism in the lower band is due to radial spreading of the wavefront.

In the upper band, figure 5.11 shows that the LH damping scales inversely with increasing

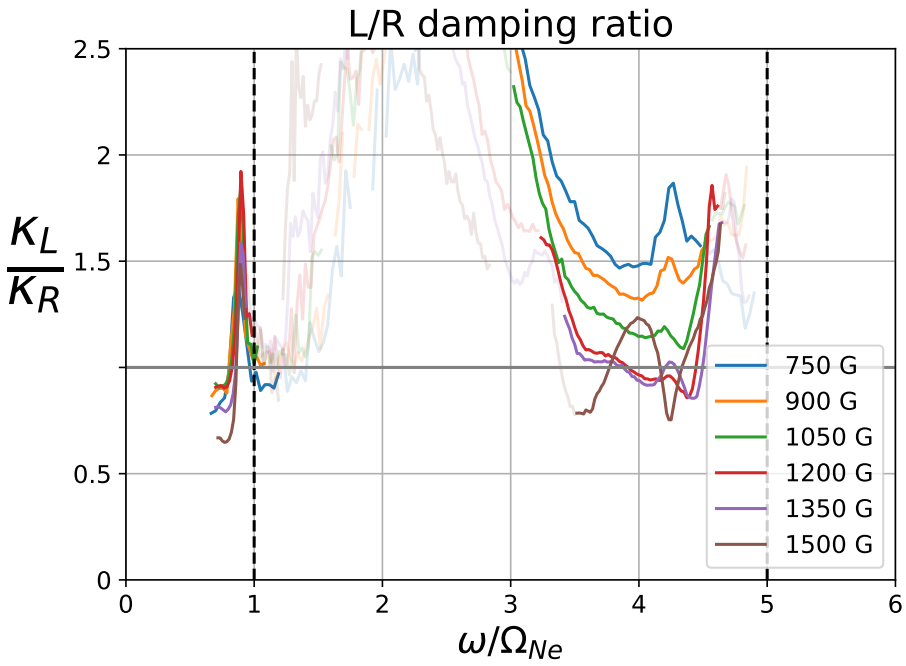

Figure 5.12: Ratio of the local damping coefficients along $r = 0$ for the left and right handed components of a shear wave launched by a magnetic dipole, in a 50% He/50% Ne plasma. The expected crossover frequency ω_x is estimated from the neutral fill pressures and designated with a vertical dashed line.

background field, which is consistent with the $1/B$ predicted scaling due to weak Coulomb collisions. The RH damping, however, is relatively unchanged with background field, meaning it cannot be explained by electron-ion collisions alone. Damping due purely to radial spreading would result in $\kappa \sim 0$ near the ion-ion hybrid frequency ω_{ii} ($\sim 2.24\Omega_{Ne}$ for a 50% He/50% Ne plasma), and monotonically increasing κ as one approaches the helium cyclotron frequency. This behavior is in agreement with the measured RH damping everywhere in the upper band, except for frequencies close to Ω_{He}, suggesting the RH damping is primarily due to conical spreading.

Figure 5.12 plots the ratio of the LHP and RHP damping, taken from the data in figure 5.11. At low frequencies, $\kappa_L \sim \kappa_R$, suggesting the wave is linearly polarized and retains

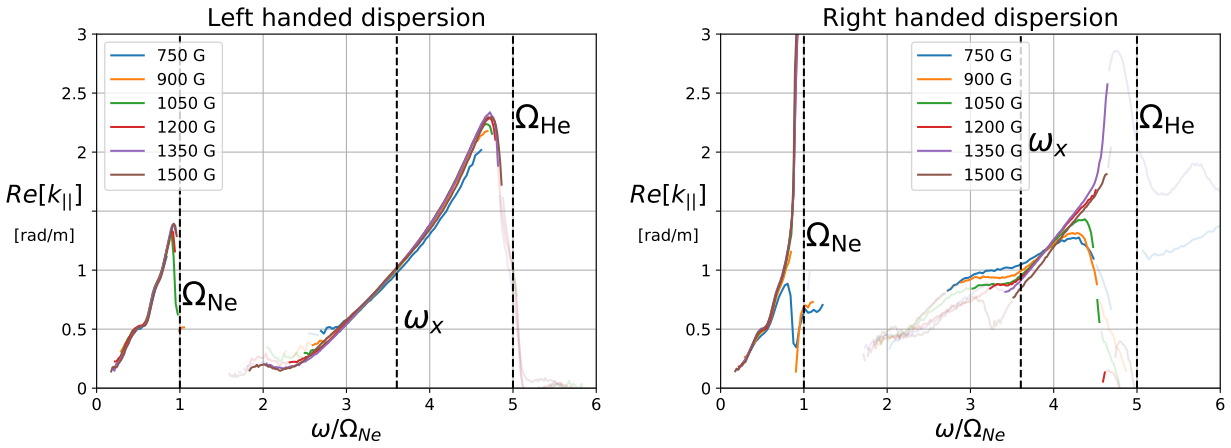

Figure 5.13: Real part of the parallel wavenumber, for the (a) left and (b) right handed components of the wave, in a 50% He/50% Ne plasma. The wavenumber was computed from the crossphase of two axially-separated B-dot probes.

its linear polarization as it propagates in z. In the upper band, the LH component of the wave experiences stronger damping than the RH component for nearly all frequencies and background fields. This means that preferential right-handed damping *cannot* explain the observed left-handed dominance of the upper band.

Figure 5.13 shows the real part of the parallel dispersion, measured from the crossphase of two axially-separated B-dot probes, for both the LHP and RHP components of a wave in a 50% He/50% Ne plasma. Data points which failed to exceed a coherence threshold of $\gamma^2 > .9$ between the two probes were faded out. The LHP dispersion is largely independent of background field, which is consistent with the predicted scaling of equation 5.13 for the inertial Alfvén wave. Additionally, the lower band's dispersion is nearly identical for the LHP and RHP components of the wave, suggesting they propagate at the same phase velocity. In the upper band, the LHP dispersion is consistent with the predicted dispersion of the inertial Alfvén wave, given by equation 4.4 and shown in figure 4.1. This observation, along with the observed $1/B$ scaling of the LH damping, suggests that the physics of the LHP component of the wave is primarily due to the propagation of collisional inertial Alfvén waves. The RHP

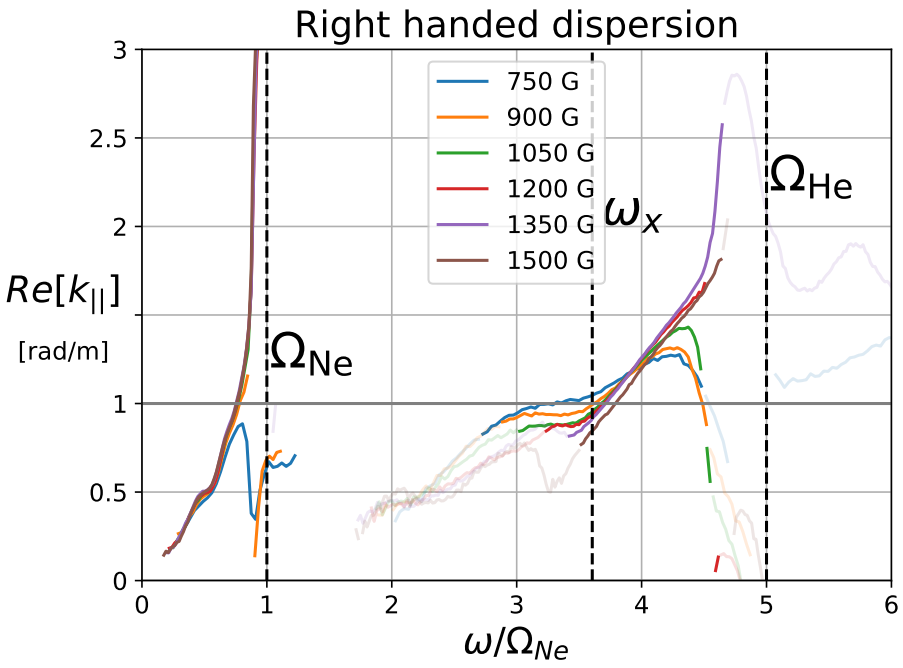

Figure 5.14: Ratio of the left and right handed parallel wavenumbers of a shear wave launched by a magnetic dipole, in a 50% He/50% Ne plasma. The expected crossover frequency ω_x is estimated from the neutral fill pressures and designated with a vertical dashed line.

dispersion in the upper band has some variation with field, with the wavenumber increasing as it approaches Ω_{He}. Figure 5.14 shows the ratio of the measured $k_{\|}$ for the left and right handed components of the wave. For the part of the upper band where both the left and right handed components have appreciable power, figure 5.14 shows that they have similar phase velocities. This suggests that the small pocket of right-handed energy that was observed in the upper band may be governed by inertial Alfvén wave physics as well, although this still doesn't explain the wave's polarization.

5.4.4 Spatial Distribution of Left and Right Handed Power

Previous experiments have shown that magnetic dipole antennas tend to drive two antiparallel current channels in the plasma, centered on either edge of the antenna loop. This was observed in past experiments with the RMF antenna [41], and verified in 3D simulations [60]. In the low frequency limit ($\omega < \Omega_{Ne}$), we showed in section 5.4 that the resulting magnetic field at the midpoint of the two current channels is a linearly polarized wave, which is consistent with the field one would expect from the symmetry of the two current channels. Above $\omega > \Omega_{Ne}$, the observed polarization diverges from what the theoretical model predicted in figure 5.1. The measured results, however, were taken along $r = 0$, and so in order to properly compare to the dispersion theory we need to consider the polarization across the entire wave front.

Figure 5.15a shows the time-evolving spatial structure of the wavefront at $\omega = .72\Omega_{Ne}$, for a 50% He / 50% Ne plasma at $B_0 = 1500$ G (field coming out of the page), 3 meters from the antenna. The vector field represents the magnetic field fluctuations of the wave, while the colored contour represents the parallel current density, calculated from Ampere's law. The field lines near $r = 0$ cm are observed to be linearly polarized, agreeing with the power spectra in figure 5.1. Two current channels can be clearly identified, equal and opposite in magnitude, centered on either edge of the antenna at $x = \pm 4.5\ cm$. As time elapses, the peaks of the two current channels are observed to drift radially outward. This causes the field

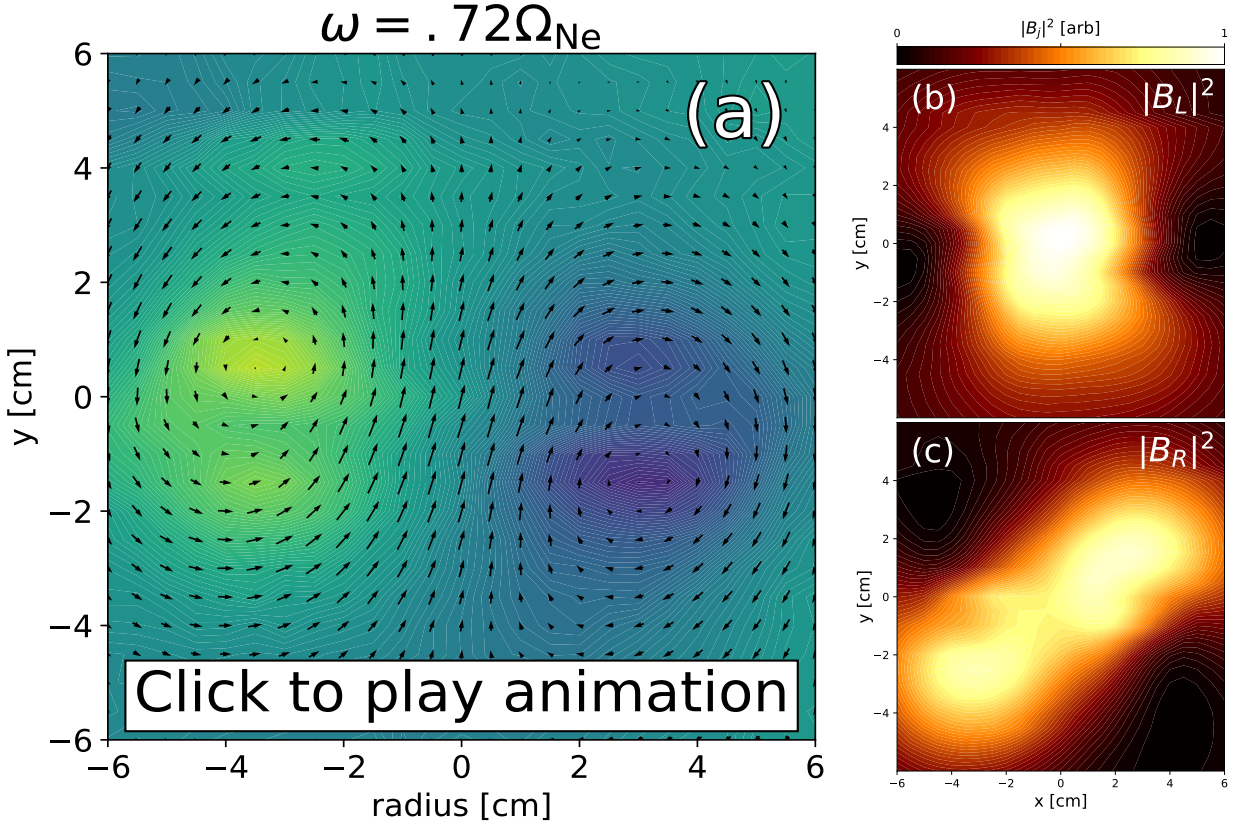

Figure 5.15: (a) Animation of the wave front of a shear wave launched by a magnetic dipole, taken 3 m from the antenna, in the upper propagation band of a 50% He/50% Ne plasma. Black vectors represent the perpendicular magnetic field, and the color contour is the parallel current (found from Ampere's law). (b) Left and (c) right handed power spectra of the wave, normalized to the same scale so as to show their relative strength to one another.

lines above and below each current channel to rotate in opposite directions, resulting in the left-right asymmetry seen in the right-handed spectrum shown in figure 5.15c. However, since both current channels remain on the $y = 0$ line as they grow and drift outward, symmetry is preserved at $r = 0$ and the resulting magnetic field is linearly polarized. The local energy density at $r = 0$ was found to be approximately 56% left handed (and 44% right), whereas the *total* energy of the wavefront (integrated across the XY plane) is 49% left handed.

Figure 5.16a shows the time evolution of the wave at $\omega = 3.4\Omega_{Ne}$, for similar plasma conditions. This frequency corresponds to a frequency in the upper band, where the dispersion physics of figure 5.1 predicts the wave to be right hand dominant. We again note the existence of two distinct current channels. However, at this frequency they appear to drift azimuthally around $r = 0$ as they evolve with time, in the direction of ion gyromotion. This causes the field between the current channels to rotate in the left handed direction as well. Conversely, this results in the field lines outside the two current channels to rotate in the right-handed direction. This is reflected in the distribution of left and right handed power, shown in figures 5.16b and 5.16c, respectively. The local energy density was found to be 98.3% left-handed at $r = 0$, while the total integrated power of the wavefront was closer to 74% left-handed, suggesting that there is some right-handed power present but it tends to inhabit the region outside the current channels.

Finally, figure 5.17 shows the time evolution at $\omega = 4.2\Omega_{Ne}$ - the frequency which corresponds to the peak of the right-handed spectrum seen previously in figure 5.8b. As each new peak of the current channels begins to materialize, there is a brief period where they revolve around each other, similar to the $3.4\Omega_{Ne}$ case, but then ultimately they drift out radially in a way that is more closely reminiscent of the $.72\Omega_{Ne}$ case. This results in a spectrum that is left-hand dominant at $r = 0$, due to the rotation of the current channels, but still has an appreciable amount of right-handed energy. The local energy density at $r = 0$ is 86.8% left-handed while the total integrated energy of the wavefront is 63.3% left-handed.

Many other frequencies were looked at on a global scale, and they all tell the same story

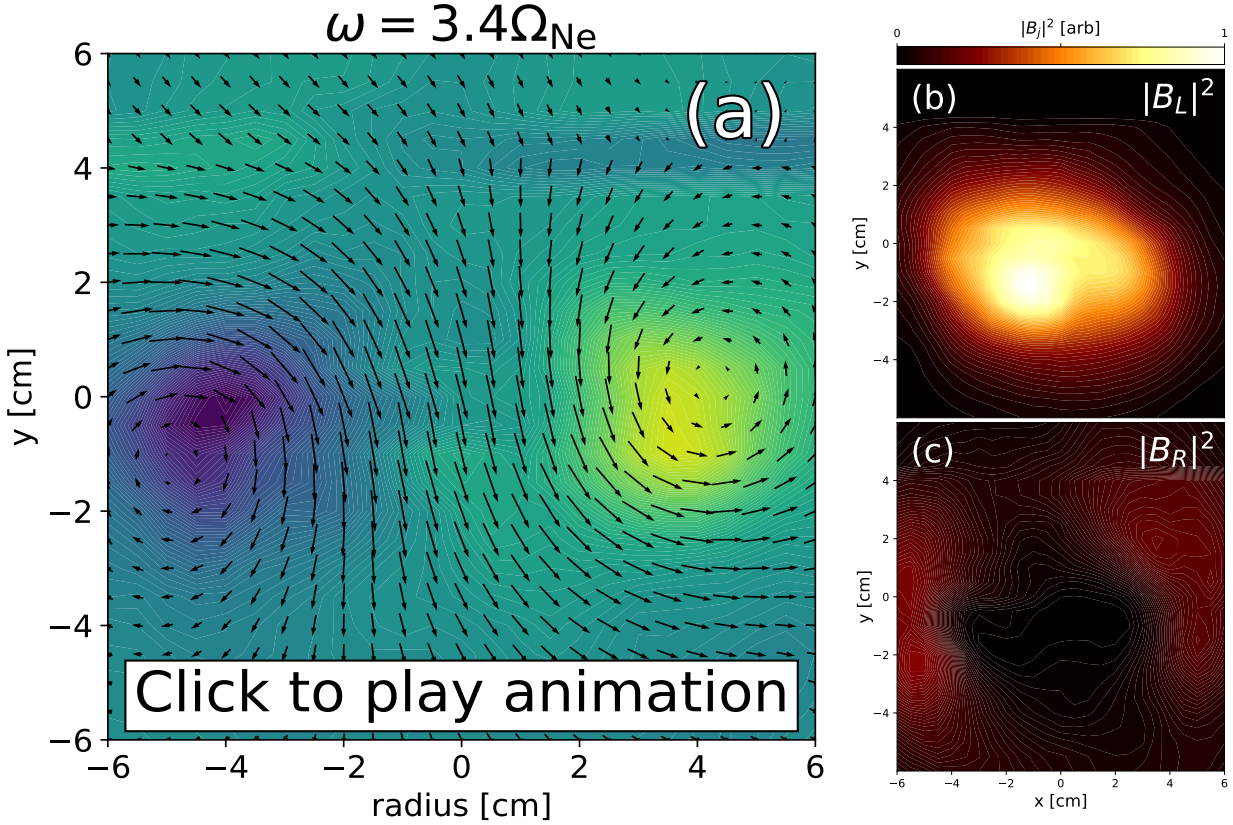

Figure 5.16: (a) Animation of the wave front of a shear wave launched by a magnetic dipole, taken 3 m from the antenna, in the upper propagation band of a 50% He/50% Ne plasma. Black vectors represent the perpendicular magnetic field, and the color contour is the parallel current (found from Ampere's law). (b) Left and (c) right handed power spectra of the wave, normalized to the same scale so as to show their relative strength to one another.

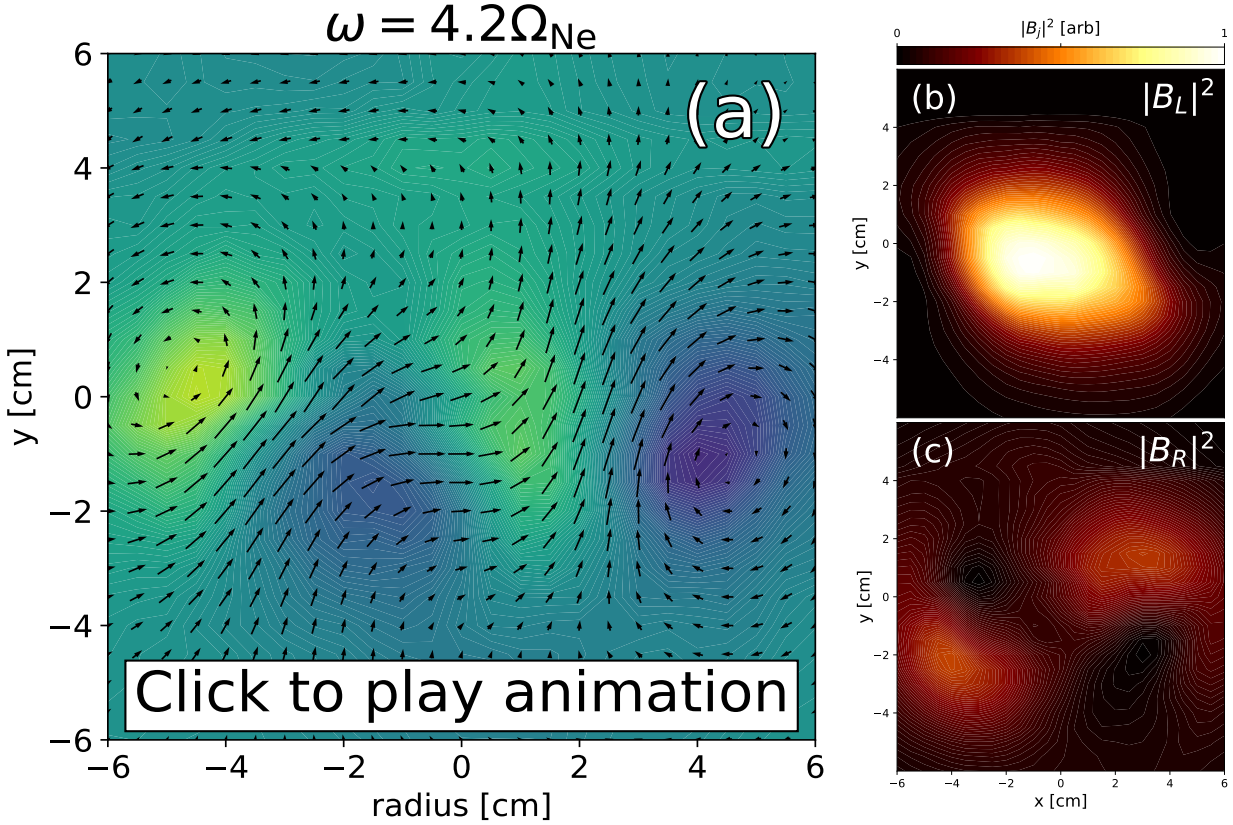

Figure 5.17: (a) Animation of the wave front of a shear wave launched by a magnetic dipole, taken 3 m from the antenna, in the upper propagation band of a 50% He/50% Ne plasma. Black vectors represent the perpendicular magnetic field, and the color contour is the parallel current (found from Ampere's law). (b) Left and (c) right handed power spectra of the wave, normalized to the same scale so as to show their relative strength to one another.

as the spectra that were taken along $r = 0$. Specifically, the upper band appears to be heavily left-handed for all frequencies, despite the dispersion theory predicting otherwise.

5.4.5 Effect of antenna coupling on wave polarization

In section 5.4.2 we showed that the upper band was observed to be left-handed everywhere, in direct contradiction with the theoretical prediction that said there should be a right-hand dominant frequency band. We looked at both the predicted and measured spatial damping rates, and showed that neither of these could explain the discrepancy between experiment and dispersion theory. In this section, we consider the impact that antenna coupling has on the wave's polarization. In other words, is this left-hand dominance of the upper band unique to the RMF antenna, and if not, how does it vary between different antenna configurations? In this section we consider the behavior of shear waves launched from several other antennas, and see how they affect the distribution of left and right handed power in the wave.

Symmetry of the two induced antiparallel electron currents by the magnetic dipole would suggest that the magnetic field along $r = 0$ is linearly polarized pointing in the $\hat{y}$ direction, but this is not what is observed in the upper band. Directly in front of the dipole, the vacuum electric field points in the $\hat{x}$ direction, exciting an ion polarization current in $\hat{x}$ and E×B current in $\hat{y}$. The phase difference between these cross-field currents will induce an elliptically polarized wave, and so one explanation is that it is this contribution to the polarization that results in the observed left-handed dominance of the upper band. This theory was tested by launching shear waves from two disk exciter antennas, located at the same z position and 9 cm apart (the same distance as the diameter of the RMF antenna). The disks were biased with equal and opposite AC signals, resulting in two antiparallel current channels in the plasma. More details on the disks and electronics used can be found in section 5.3. This antenna configuration is a way to recreate the parallel current conditions of the magnetic dipole antenna, while eliminating the near-field cross-field coupling that was speculated to exist.

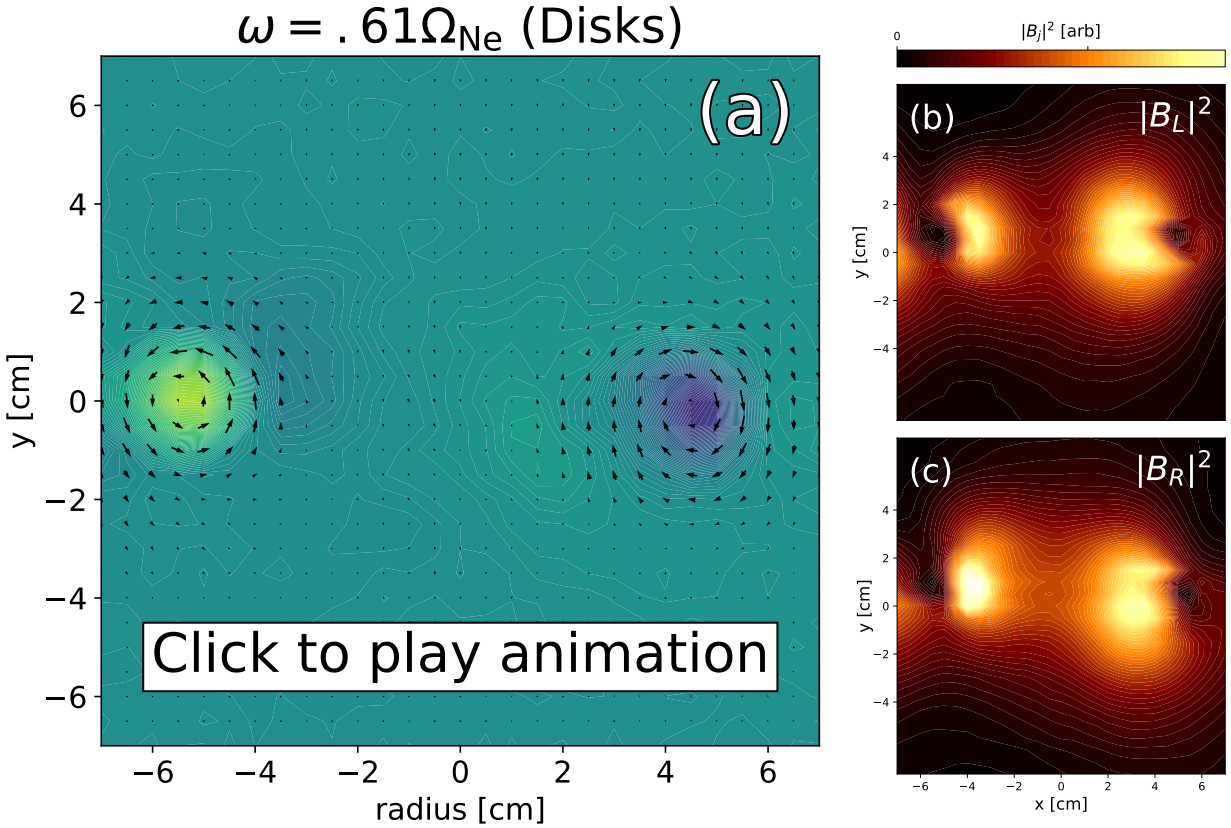

Figure 5.18: (a) Animation of the wave front of a shear wave launched by two disk exciters, taken 3 m from the antenna, in the lower propagation band of a 50% He/50% Ne plasma. Black vectors represent the perpendicular magnetic field, and the color contour is the parallel current (found from Ampere's law). (b) Left and (c) right handed power spectra of the wave, normalized to the same scale so as to show their relative strength to one another.

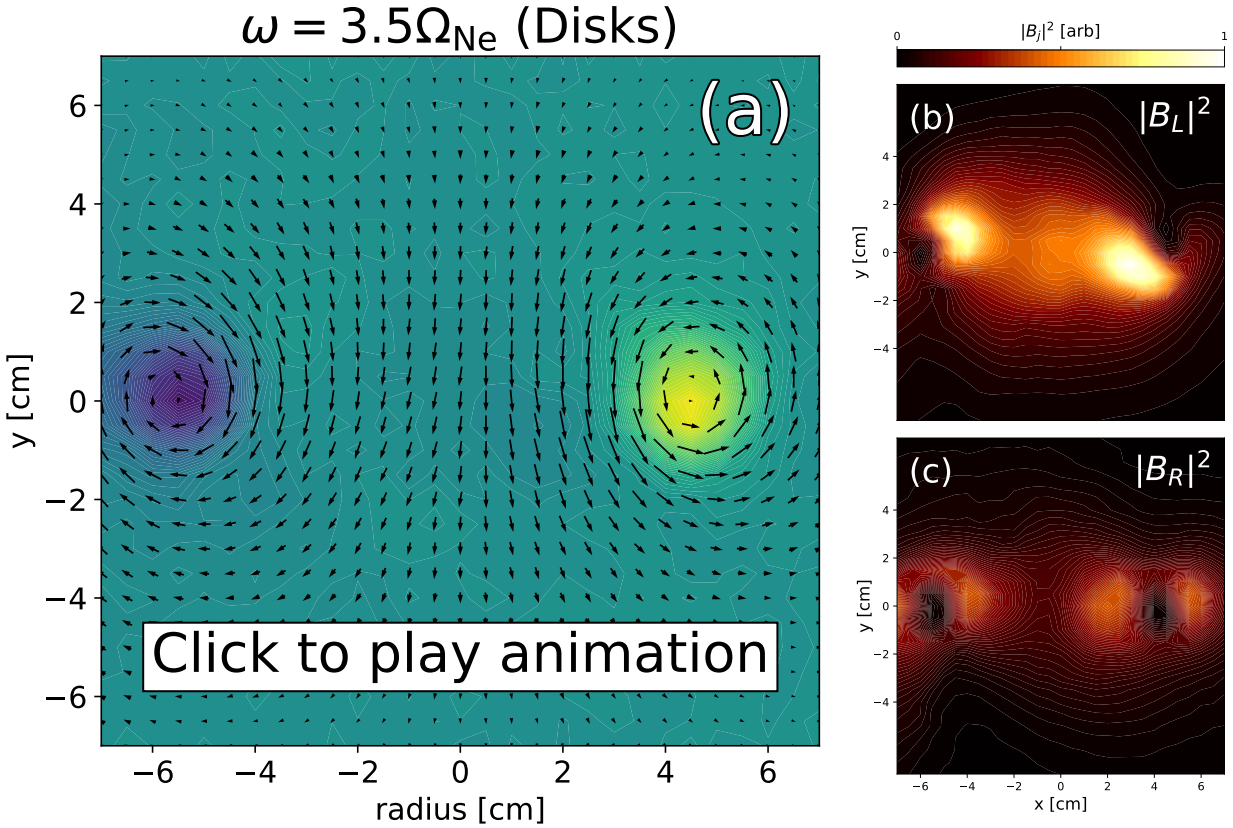

Figure 5.19: (a) Animation of the wave front of a shear wave launched by two disk exciters, taken 3 m from the antenna, in the upper propagation band of a 50% He/50% Ne plasma. Black vectors represent the perpendicular magnetic field, and the color contour is the parallel current (found from Ampere's law). (b) Left and (c) right handed power spectra of the wave, normalized to the same scale so as to show their relative strength to one another.

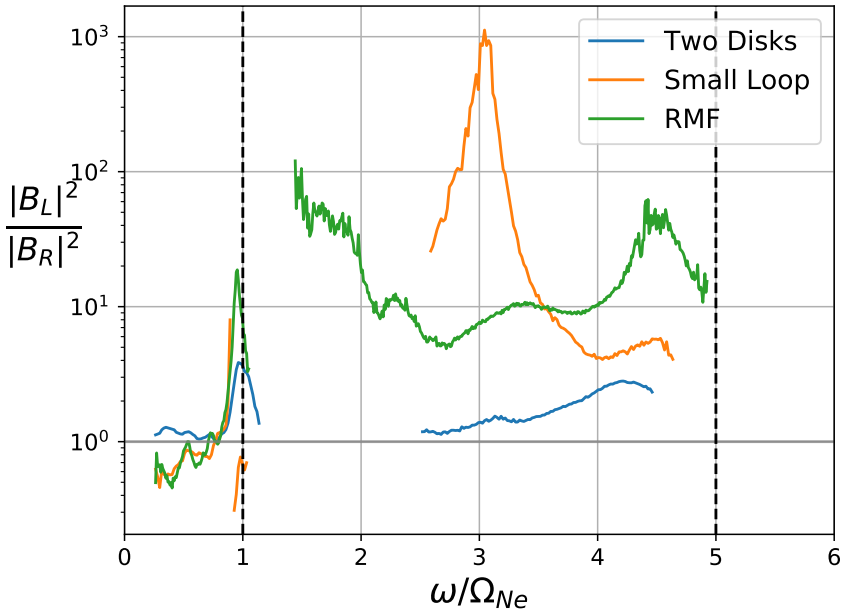

Figure 5.20: Comparison of the ratio of left-to-right handed power for the magnetic dipole, RMF antenna, and two disk exciters, in a 50% He/50% Ne plasma. A vertical dashed line denotes the predicted crossover frequency ω_x, calculated from equation 5.8.

Figures 5.18 and 5.19 show planes similar to the ones described in section 5.4.4, but for two disk exciters. The lower band is linearly polarized everywhere, as expected. Previous studies on the radiation pattern due to a disk exciter showed that the field was linearly polarized, and so figure 5.18 shows that the total field is just the superposition of each disk. The upper band, shown in figure 5.19, again shows a preference for left-handed energy at $r = 0$, although it is much less pronounced than what was observed for the dipole antenna. The LH dominance of the wave is accompanied by a left-handed rotation of the two current channels, centered on either antenna. Note that this is at a frequency where the wave was expected to be RH dominant based on the shear wave dispersion.

Figure 5.20 shows the ratio of left-to-right handed power, in a 50% He/50% Ne plasma, for the RMF antenna and two disk exciter setups, as well as for the smaller loop antenna described in section 4.3. All measurements were taken the same distance away from their

respective antenna, around 3 meters. The two disk exciters still produce a shear wave that is left-hand dominant across the entire upper band, although it is less pronounced than that of the RMF antenna. The loop antenna is also observed to be left-hand dominant across the upper band. So while the degree of coupled left-handed energy clearly depends on the antenna configuration being used, it appears that the observed left-hand dominance of the upper band is not unique to the RMF antenna.

5.5 Modelling via the Antenna Wave Equation

In this section we will employ several methods for numerically determining the field due to our magnetic loop antenna, in an effort to see if numerical results may explain some of the unexplained behavior observed in the wave's polarization (namely, the left-hand dominance in the upper band). We will first use the analytic method that was derived in chapter 3 (specifically, the Cartesian formulation derived in 3.4), which uses the vacuum field of the antenna in order to calculate the electromagnetic field in the rest of the plasma. The model assumes a cold, uniform plasma, and ignores reflection of waves at the boundary of the plasma. Unless otherwise specified, the simulations/numerical solutions in this section will assume an evenly mixed helium/neon plasma, with $n_e = .5 \times 10^{12}$ cm^{-3}, $B_0 = 1500$ G, and $\nu_e = 5$ MHz.

Consider an infinitely thin loop of current, with radius $a = 4.5$ cm and current $I = 6$ A, as these values are comparable to the ones from the preceding experiment. Additionally, we will assume a driven frequency of $\omega = .75\Omega_{He}$, as it was the upper band where the measured polarization was in contradiction with the theoretical model. We define the loop's coordinate system with origin at center of the loop, and z axis along the centerline of the loop (such that the loop lies in the XZ plane). The vector potential $\vec{A}$ is entirely azimuthal in the loop's frame, which we denote using primed coordinates, and is given by the following expression [55]:

$$A_{\theta'}(r', z') = \frac{\mu_0 I a}{4\pi} \int_0^{2\pi} \frac{\cos\theta' \mathrm{d}\theta'}{\sqrt{r'^2 + a^2 + z'^2 - 2ar'\cos\theta'}}, \tag{5.16}$$

where (r', θ', z') denotes cylindrical coordinates in the loop's frame of reference. The resulting magnetic field of the loop follows from the curl of equation 5.16:

$$B_{r'}(r', z') = \frac{\mu_0 I z'}{2\pi r'} \frac{1}{\sqrt{(r'-a)^2 + z'^2}} \left[\left(\frac{a^2 + r'^2 + z'^2}{(r'+a)^2 + z'^2} \right) E(\Lambda) - K(\Lambda) \right], \tag{5.17}$$

$$B_{z'}(r', z') = \frac{\mu_0 I}{2\pi} \frac{1}{\sqrt{(r'-a)^2 + z'^2}} \left[\left(\frac{a^2 - r'^2 - z'^2}{(r'+a)^2 + z'^2} \right) E(\Lambda) + K(\Lambda) \right], \tag{5.18}$$

where $K(\Lambda)$ and $E(\Lambda)$ are the complete elliptic integrals of the first and second kind, respectively, and we define Λ as:

$$\Lambda = \frac{-4ar'}{(r'-a)^2 + z'^2}. \tag{5.19}$$

We are interested in the field due to a loop lying in the XZ plane of the LAPD. Placing the origin at the center of the loop, equations 5.17 and 5.18 can be transformed into the LAPD's coordinate system via the following transformation:

$$\begin{aligned} B_x &= \frac{x}{\sqrt{x^2+z^2}} B_{r'} \\ B_y &= B_{z'} \\ B_z &= \frac{z}{\sqrt{x^2+z^2}} B_{r'} \end{aligned} \quad , \qquad \begin{aligned} r' &= \sqrt{x^2+z^2} \\ z' &= y \end{aligned} \quad . \tag{5.20}$$

Equations 5.17–5.20 contain all the necessary information to determine the vacuum field of the loop antenna in the LAPD's coordinates. These expressions for the vacuum field were then fed into equation 3.63 in order to find the field of the resulting wave in the plasma.

Figure 5.21 shows the calculated amplitude of the shear wave's magnetic field along $y = 0$, at various axial distances from the antenna. The results here are in qualitative agreement

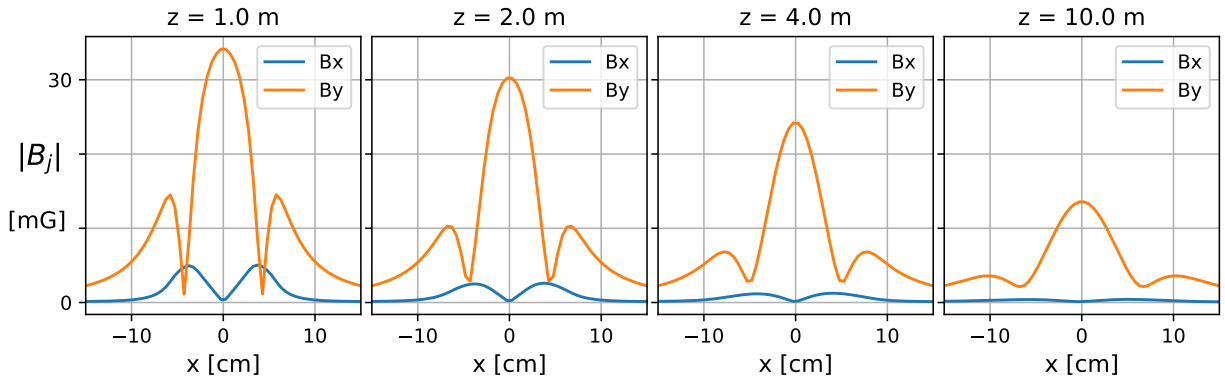

Figure 5.21: Magnetic field amplitude of the wave along $y = 0$, at various axial positions from the antenna, for frequency $\omega = .75\Omega_{He}$. The fact that $B_y \gg B_x$ almost everywhere in the plasma suggests that the wave is almost completely linearly polarized, which is in contradiction with the measured polarization in the upper band.

with previously published three dimensional simulations of the RMF antenna [60], and are consistent with past measurements [41]. It can be seen in figure 5.21 that $B_y >> B_x$ nearly everywhere in the plasma, suggesting the wave is overwhelmingly linearly polarized. The amplitude of the wave drops with increasing z as expected, which can be attributed entirely to electron collisionality and radial spreading of the wave energy.

Figure 5.22 shows two contour plots of the XZ plane along $y = 0$ - one without collisions, and one with $\nu_e = 5$ MHz. Electron collisionality has two noticeable effects on the wave structure. The first is an exponential decay of the wave energy with increasing z. In the absence of collisions, the wave energy density along $r = 0$ gradually decreases with z due to the radial spreading of the wavefront, although it can be shown that the total *integrated* energy across the wavefront remains constant. When collisionality is introduced, it becomes the dominant mechanism for axial energy dissipation in the upper band. Second, there are many "fine structure" interference patterns in the collisionless case that get washed out when collisions are introduced.In other words, collisionality tends to more rapidly dissipate large $k_\perp$ features in the wave, which is consistent with the scaling predicted in section 5.4.3.

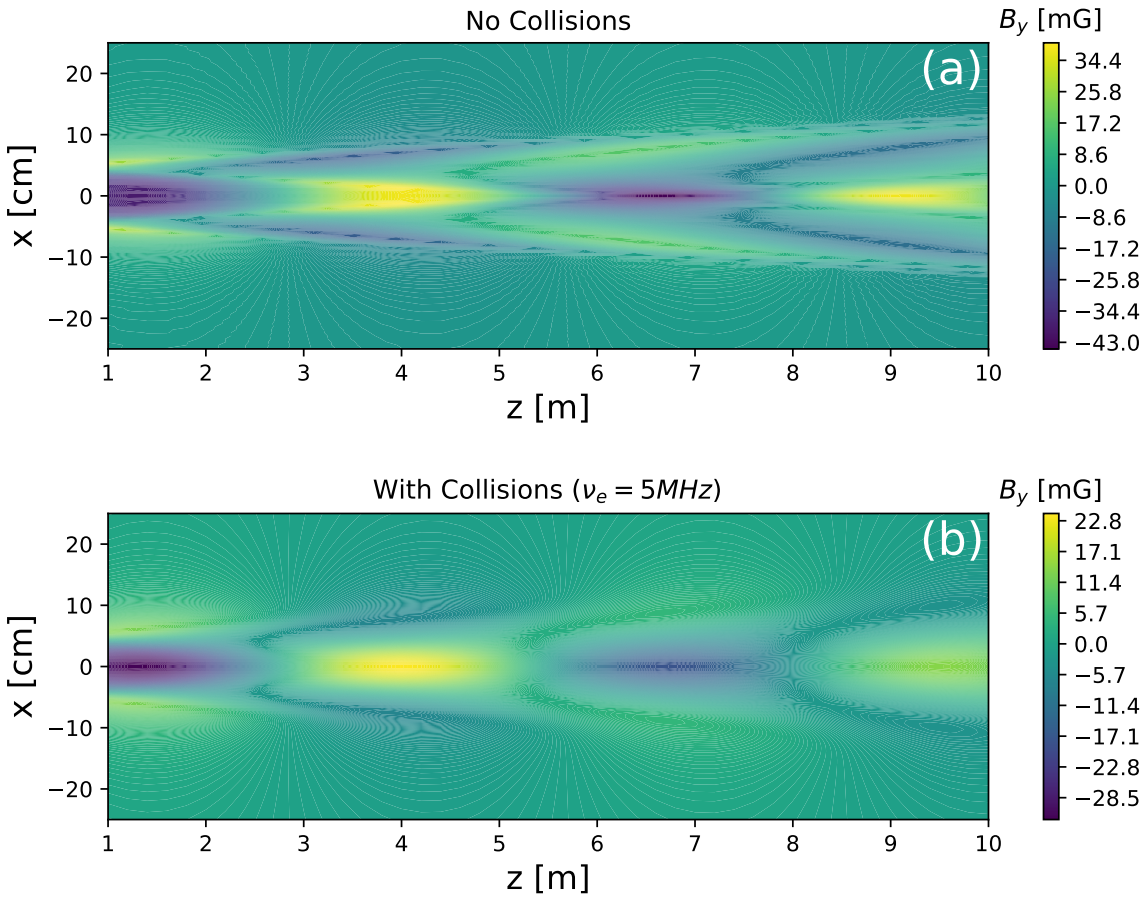

Figure 5.22: Contour plot of B_y at an instance in time, along the $y = 0$ plane. Antenna is centered on $x = y = 0$, outside the bounds of the figure. (a) With an electron collision frequency $\nu_e = 5$ MHz, which is typical of LAPD plasmas, and (b) without collisions.

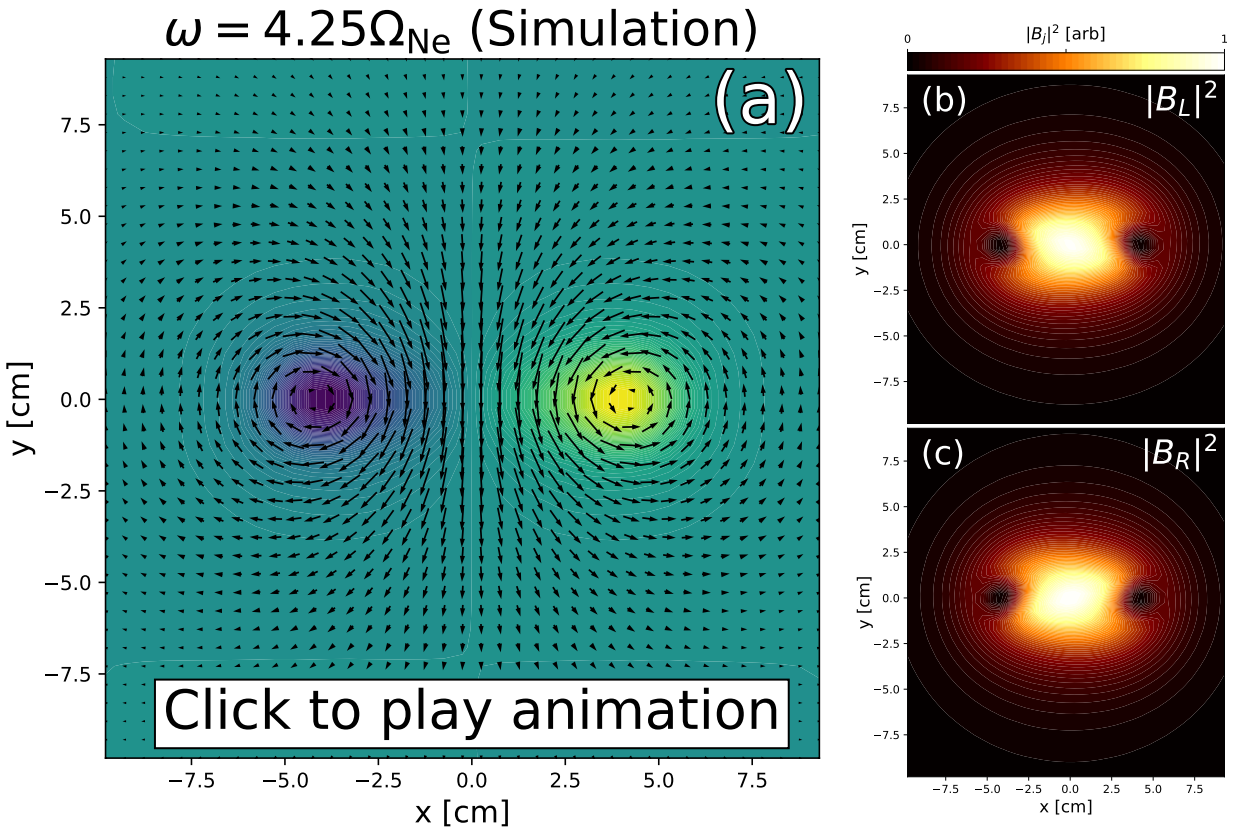

Figure 5.23: (a) Simulation of the wave front of a shear wave launched by the RMF antenna, taken 3 m from the antenna, with plasma/antenna conditions similar to figure 5.17. The wave is linearly polarized at the center of the two current channels, which is in direct contradiction with the observed left-handedness that was observed in figure 5.17.

In figure 5.23, we show the time evolution of the perpendicular magnetic field (vectors) and parallel plasma current (color contour), in the XY plane 3 m from the antenna. The plasma/antenna conditions showcased in this plot are most similar to the experimental data shown in figure 5.17. While we see two antiparallel current channels, which is consistent with the experimental data, the field at the midpoint of the current channels is linearly polarized. This is in contradiction with figure 5.17, which showed a clear left hand dominance in the upper band. There *is* some asymmetry in the left-right power distribution of the wave, which can be seen in figures 5.23b and 5.23c, but not enough to explain the experimental observations.

It's worth mentioning that similar simulations were also performed in the lower band, and they were in good qualitative agreement with the experimental data. Because of this, this section focused solely on simulating the upper band so as to (hopefully) better understand the observed anomaly in the polarization of the upper band.

5.5.1 Verification of the antenna wave model: Comparison with past studies

Previous publications have successfully carried out 3-D simulations of the loop antenna, which were shown to agree with experimental measurements [60]. In this section we will take a moment to compare the results of our antenna model from chapter 3 for the loop antenna to this past study, in order to validate the results of our new model.

Figures 5.24 and 5.25 show the XZ plane of a slow wave excited by a loop antenna of radius $R = 4.5$ cm, in a helium plasma with density $n_e = 1.4 \times 10^{12} cm^{-3}$, $B_0 = 1000G$, and collision frequency $\nu_e = 0$. The antenna frequency is set at $\omega = .5\Omega_{He}$. Figure 5.24 is the simulation result taken from [60], whereas figure 5.25 shows the resulting wave for when the same plasma/antenna parameters are pushed through our antenna model. Both figures are in excellent agreement, therefore validating the antenna model derived in chapter 3.

Figures 5.26 and 5.27 show a second comparison between previously simulated results and

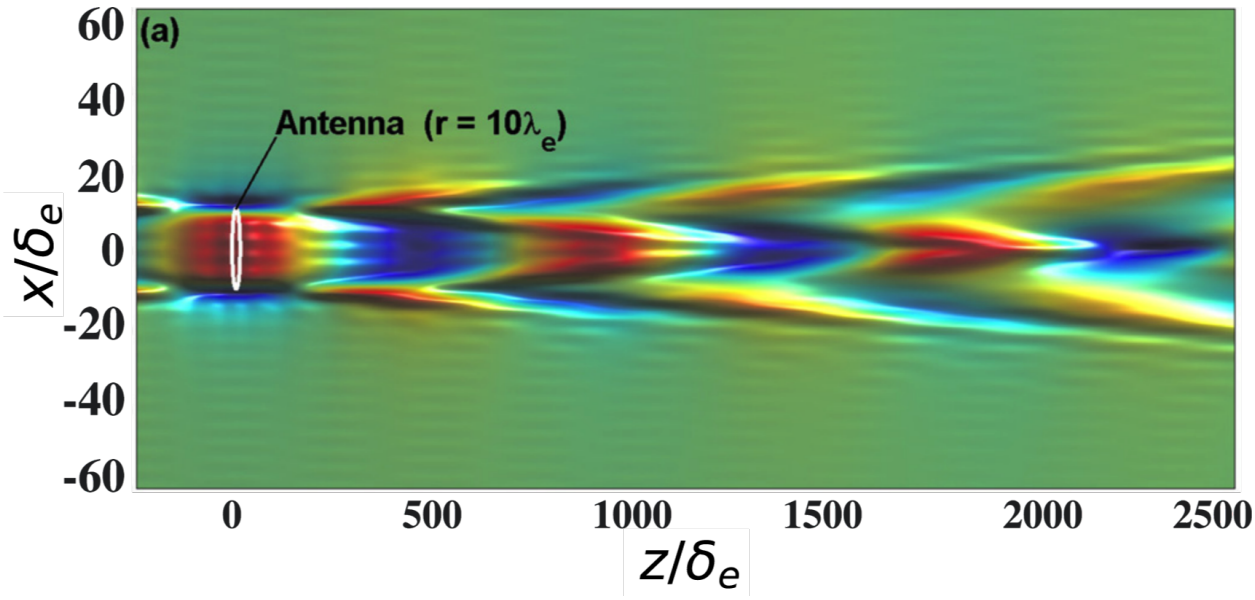

Figure 5.24: Simulation result of an XZ plane of the shear wave for a plasma with $n_e = 10^{12} cm^{-3}$, $B_0 = 1000G$, and $\nu_e = 0$, and antenna with frequency $\omega = .5\Omega_{He}$. Plane taken from [60].

our antenna model, this time of the XY plane. For this comparison, the same density and field are assumed but with $\nu_e = 4.75$ MHz and $\omega = .2\Omega_{He}$. These plots are again in excellent agreement, further supporting the antenna model outlined in chapter 3 and validating our use of it moving forward.

5.5.2 Wave polarization along $r = 0$ and globally

The majority of power spectra in the preceding sections were taken along the field line passing through the midpoint of the loop antenna, or $r = 0$ in the LAPD's coordinate system. At sufficiently large enough $k_\perp$, the induced parallel electron current is entirely responsible for setting the perpendicular magnetic field of the wave, resulting in linear polarization (with $\vec{B} = B_y \hat{y}$). In this section we are interested in determining the wave's polarization along the $r = 0$ line, using the analytic method outlined in chapter 3.

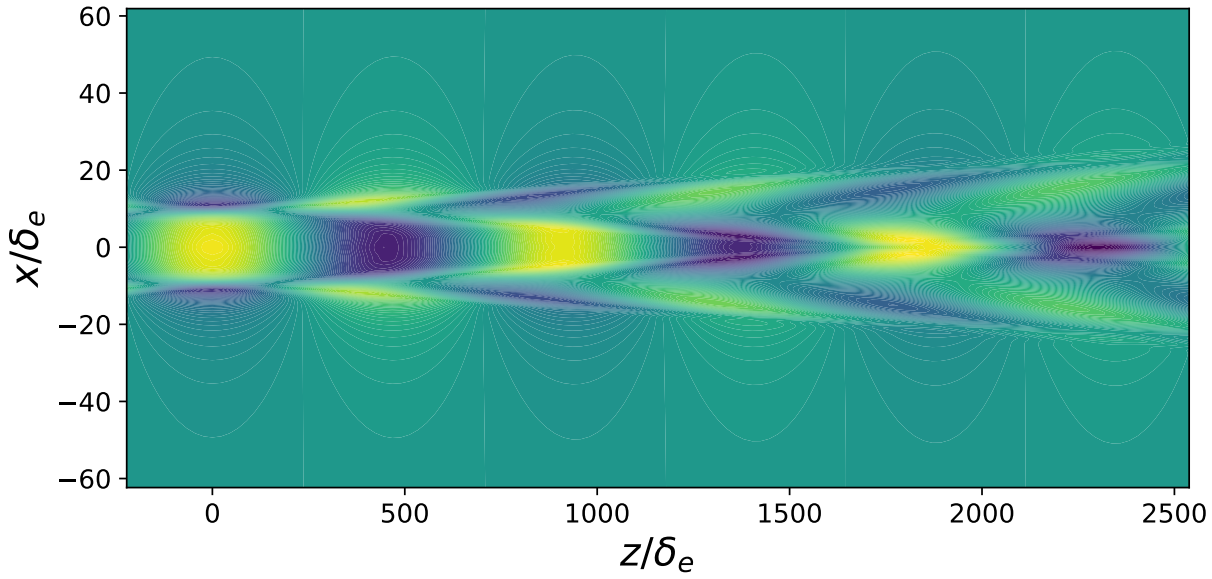

Figure 5.25: Model result of an XZ plane of the shear wave for a plasma with $n_e = 10^{12} cm^{-3}$, $B_0 = 1000G$, and $\nu_e = 0$, and antenna with frequency $\omega = .5\Omega_{He}$. Plane calculated using the model derived in chapter 3. The model result is in excellent agreement with the simulated XZ plane shown in figure 5.24.

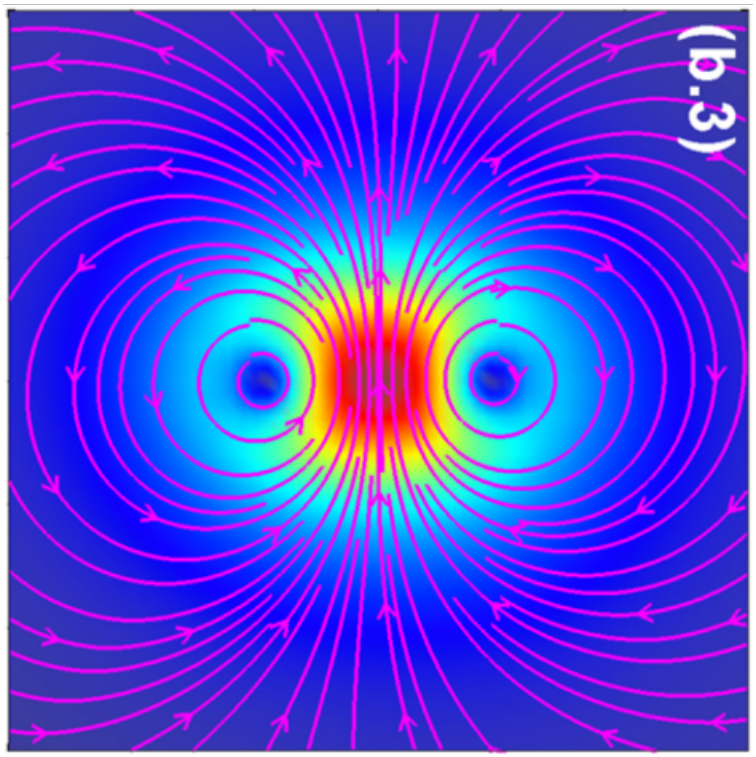

Figure 5.26: Simulation result of the XY plane of the shear wave for a plasma with $n_e = 10^{12} cm^{-3}$, $B_0 = 1000G$, and $\nu_e = 4.75$ MHz, and antenna with frequency $\omega = .2\Omega_{He}$. Plane taken from [60].

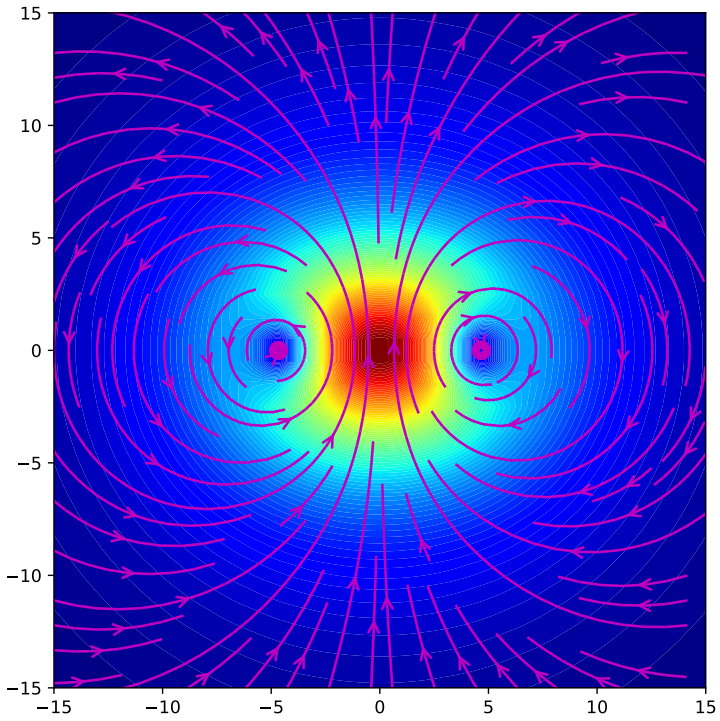

Figure 5.27: Model result of the XY plane of the shear wave for a plasma with $n_e = 10^{12} cm^{-3}$, $B_0 = 1000G$, and $\nu_e = 4.75$ MHz, and antenna with frequency $\omega = .2\Omega_{He}$. Plane calculated using the model derived in chapter 3. The model result is in excellent agreement with the simulated XY plane shown in figure 5.26.

The vacuum field of the loop antenna is given by equations 5.17–5.20. For simplicity, we will consider the region of space where the near-field of the antenna is negligible, which we define as the radiation field. In this region, the Cartesian solution to the antenna wave equation, given by equation 3.63, can be expressed as the following:

$$\tilde{B}_x(k_x,k_y,z) = i\frac{\omega^4}{c^4}\frac{e^{ik_\parallel z}}{2k_\parallel(k_\parallel^2-k_{\parallel-}^2)}\left[\left(S(n_\parallel^2+n_y^2)-in_xn_yD-RL(1-\frac{n_x^2}{P})\right)\tilde{B}_{x0}\right.$$
$$\left.+\left(-iD(n_\parallel^2+n_y^2)-n_xn_yS+n_xn_y\frac{RL}{P}\right)\tilde{B}_{y0}\right], \quad (5.21)$$

$$\tilde{B}_y(k_x,k_y,z) = 2i\frac{\omega^4}{c^4}\frac{e^{ik_\parallel z}}{2k_\parallel(k_\parallel^2-k_{\parallel-}^2)}\left[\left(iD(n_\parallel^2+n_x^2)-n_xn_yS+n_xn_y\frac{RL}{P}\right)\tilde{B}_{x0}\right.$$
$$\left.+\left(S(n_\parallel^2+n_x^2)+in_xn_yD-RL(1-\frac{n_y^2}{P})\right)\tilde{B}_{y0}\right], \quad (5.22)$$

where $k_\parallel$ and $k_{\parallel-}$ are the parallel wavenumbers of the slow and fast wave, respectively. Note that we have omitted the fast wave solution, as it is mostly evanescent in LAPD plasmas for this frequency regime. In equations 5.21 and 5.22, $\tilde{B}_{x0} = \tilde{B}_{x0}(k_x,k_y,k_{||})$ is the three-dimensional Fourier transform of B_{x0}, evaluated at $k_z = k_\parallel$ (where $k_\parallel$ is found from the dispersion relation given by equation 4.3), and likewise for $\tilde{B}_{y0}$. The spatial structure of the field is found from the inverse Fourier transform of $\tilde{B}_x$ and $\tilde{B}_y$. Since we are interested specifically in the field at $x = y = 0$, this amounts to the following integral:

$$B_j(x=0,y=0,z) = \int_{-\infty}^{\infty}\int_{-\infty}^{\infty}\tilde{B}_j(k_x,k_y,z)\mathrm{d}k_x\mathrm{d}k_y. \quad (5.23)$$

Several terms in equations 5.21–5.22 will not contribute to the integral of equation 5.23, by virtue of symmetry. It is straightforward to show that B_{x0} is odd in both x and y, and since B_{x0} is real it follows that $\tilde{B}_{x0}$ will be odd in k_x and k_y as well. A similar argument can be used to show that $\tilde{B}_{y0}$ is even in both k_x and k_y. Noting that $k_\parallel$ is even in k_x and k_y,

terms in equations 5.21 and 5.22 which are odd will not contribute to the integral of equation 5.23. This allows us to drop several terms, and after some rearranging we can express our field along $r = 0$ as the following:

$$B_x(0,0,z) = 2D\frac{\omega^4}{c^4}\int_0^\infty\int_0^\infty \frac{e^{ik_\parallel z}}{k_\parallel(k_\parallel^2 - k_{\parallel-}^2)}\left[n_x n_y \tilde{B}_{x0} + (n_\parallel^2 + n_y^2)\tilde{B}_{y0}\right]\mathrm{d}k_x\mathrm{d}k_y, \tag{5.24}$$

$$B_y(0,0,z) = 2i\frac{\omega^4}{c^4}\int_0^\infty\int_0^\infty \frac{e^{ik_\parallel z}}{k_\parallel(k_\parallel^2 - k_{\parallel-}^2)}\Big[-Sn_x n_y \tilde{B}_{x0} + \left(S(n_\parallel^2 + n_x^2) - RL(1 - \frac{n_y^2}{P})\right)\tilde{B}_{y0}\Big]\mathrm{d}k_x\mathrm{d}k_y. \tag{5.25}$$

The power distribution in $k_\perp$-space of the vacuum field is related to the radius a of the loop - i.e., a larger radius will push more power to smaller $k_\perp$. Figure 5.28 shows the field along $r = 0$ as a function of z, for a slow wave with frequency $\omega = 4.2\Omega_{Ne}$. It can be seen that B_y leads B_x by a phase of roughly $\pi/2$, indicating a left handed polarization, but the fact that $B_y \gg B_x$ means the wave will be almost completely linearly polarized in the y direction. The amplitude decreasing with z is due to radial spreading of the wavefront's energy, as we assumed $\nu_e = 0$ for demonstrative purposes.

The ratio of left-to-right handed power of the wave along $r = 0$ was calculated from equations 5.21 and 5.22 for a range of frequencies, and the results can be seen in figure 5.29. The results predict the wave to be slightly left-handed across the entire upper band, although not nearly enough to explain the left-hand dominance that was observed in the data. Figure 5.30 shows the *global* ratio of left-to-right handed power. This was calculated by adding up all the left and right handed power in the XY plane, and then computing the ratio of these quantities. The global power ratio is in qualitative agreement with the dispersion plot shown in figure 5.1. This is expected, as the crossover frequency was shown to be independent of $k_\perp$ and therefore any calculations which sample the entire perpendicular plane should be

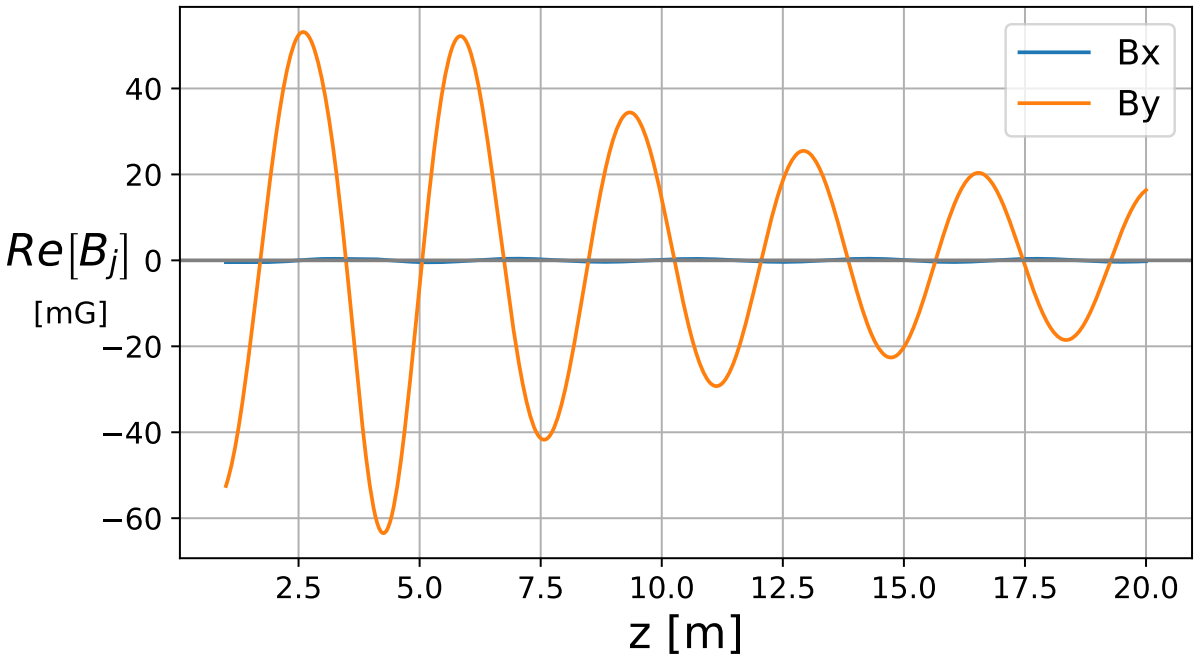

Figure 5.28: Magnetic field of a slow wave with frequency $\omega = 4.2\Omega_{Ne}$, along $r = 0$. The field is almost completely linearly polarized in the y direction. A small B_x can be seen that is $\pi/2$ phase behind B_y, indicating the wave is slightly left handed.

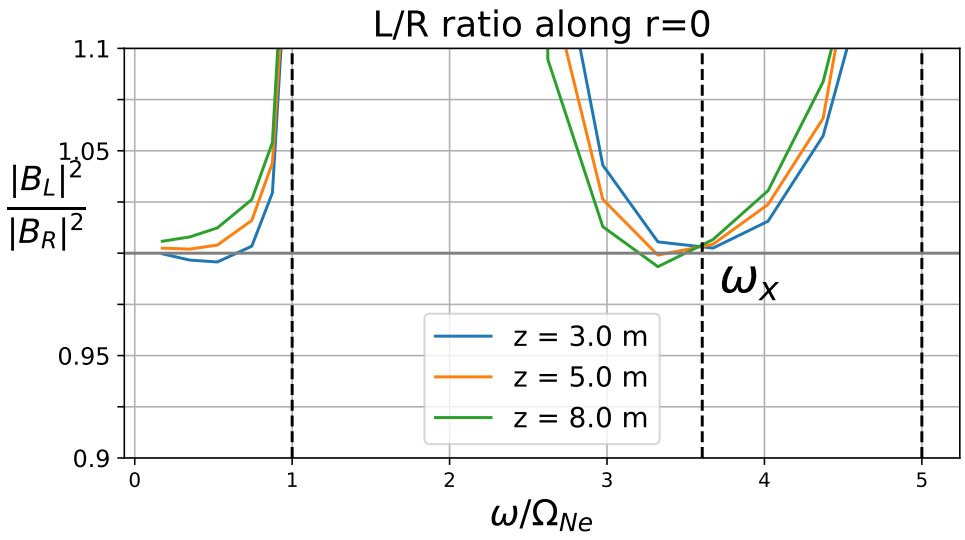

Figure 5.29: Predicted ratio of the left-to-right handed power of a wave launched by a magnetic loop antenna in a 50% He/50% Ne plasma, at varying axial positions along $r = 0$.

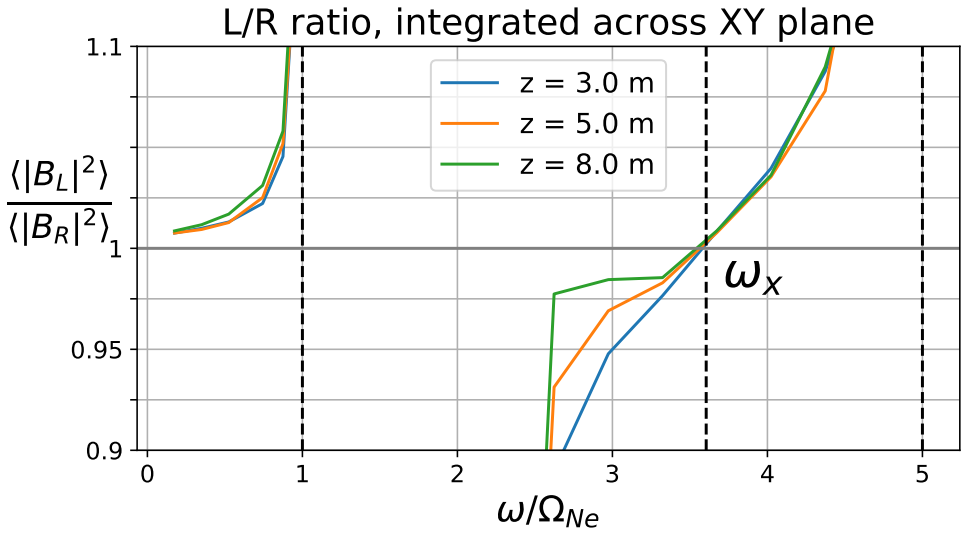

Figure 5.30: Predicted ratio of the global left-to-right handed power of a wave launched by a magnetic loop antenna in a 50% He/50% Ne plasma, at varying axial positions. The global polarization power ratio exhibits a crossover frequency at $\omega = \omega_X$, similar to the dispersion theory outlined in section 5.2.

reminiscent of the plane wave dispersion model. While our model appears to agree with the simple plane wave dispersion model, it unfortunately does not explain the observations of the upper band's polarization.

5.5.3 Comparison of predicted and measured radial profiles

The final comparison of our antenna model in this section will be to calculate radial lines of the left and right handed power of the wave, and compare to measured results. The results are shown in figure 5.31. A 50% He/50% Ne plasma with $n_e = 10^{12}$ cm^{-3}, $B_0 = 1500$ G, and $\nu_e = 4$ MHz was assumed for the model, as these values most closely match the experimental conditions. The frequency $\omega = 3.4\Omega_{Ne}$ was chosen for comparison, corresponding to a frequency in the upper band where previous model results (as well as the slab dispersion model) have predicted close to linear polarization. Both the modelled and measured data were taken 2.5 meters away from the RMF antenna, which has a radius of $r = 4.5$ cm. Figure 5.31 shows that the model prediction is very close to linearly polarized at all radial positions for this frequency, whereas the measured results are overwhelming left-hand dominant. This side-by-side comparison confirms that the antenna model derived in chapter 3 fails to predict the left-hand dominance that has been consistently observed in the upper band of the shear wave.

The total perpendicular power of the wave's magnetic field was computed, using $|B_\perp|^2 = |B_L|^2 + |B_R|^2$, for both the antenna model's prediction as well as the measured wave power. The results can be seen in figure 5.32. The same plasma and antenna parameters as figure 5.31 were assumed. While the two radial profiles are not in perfect agreement, they are similar enough to validate the results of the antenna model. The main difference between the two is that the measured profile is much wider, whereas the predicted profile has a local minimum around $r \approx \pm 4.7$ cm.

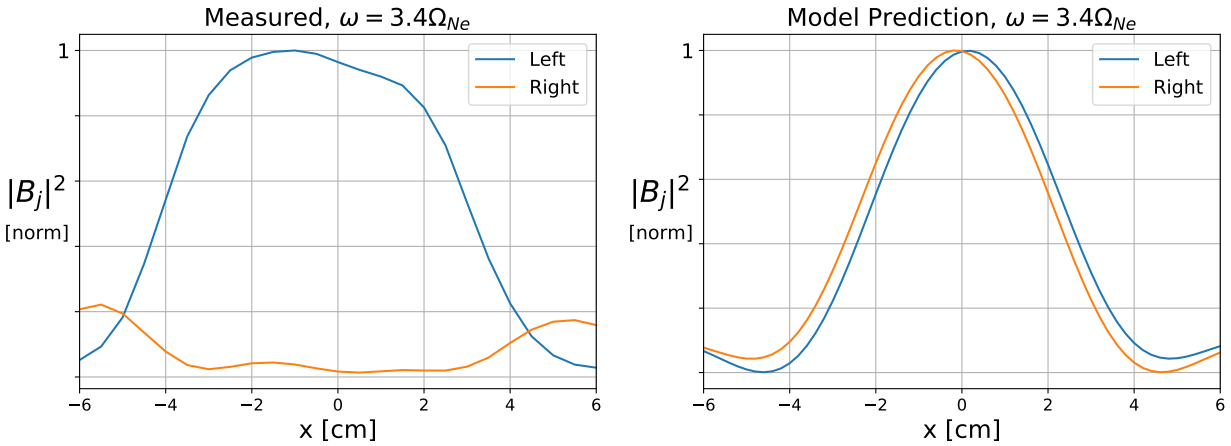

Figure 5.31: Radial profile of the left and right handed power, taken 2.5 meters away from the RMF antenna, (a) experimentally measured and (b) predicted by the antenna model. The measured profile is left-hand dominant, whereas the model predicts close to linear polarization at all radial positions.

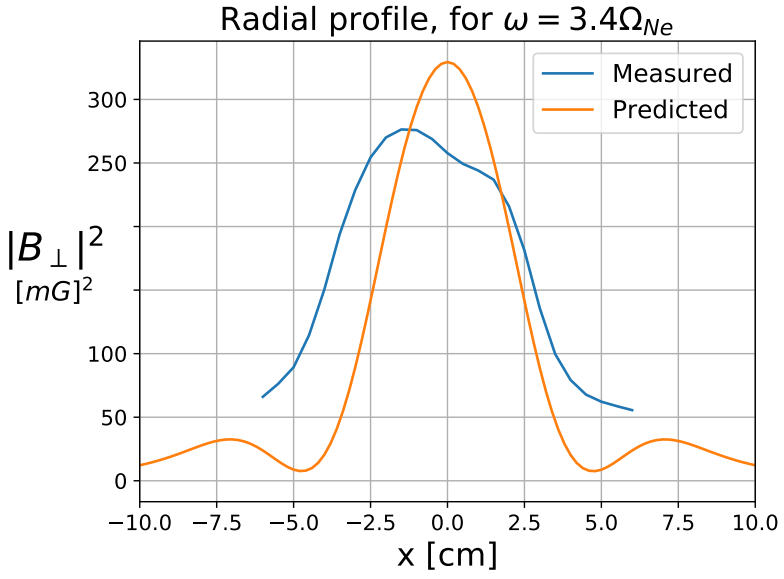

Figure 5.32: Radial profile of the squared amplitude of the wave's perpendicular magnetic field, for both the experimental measurement as well as the prediction of the antenna model.

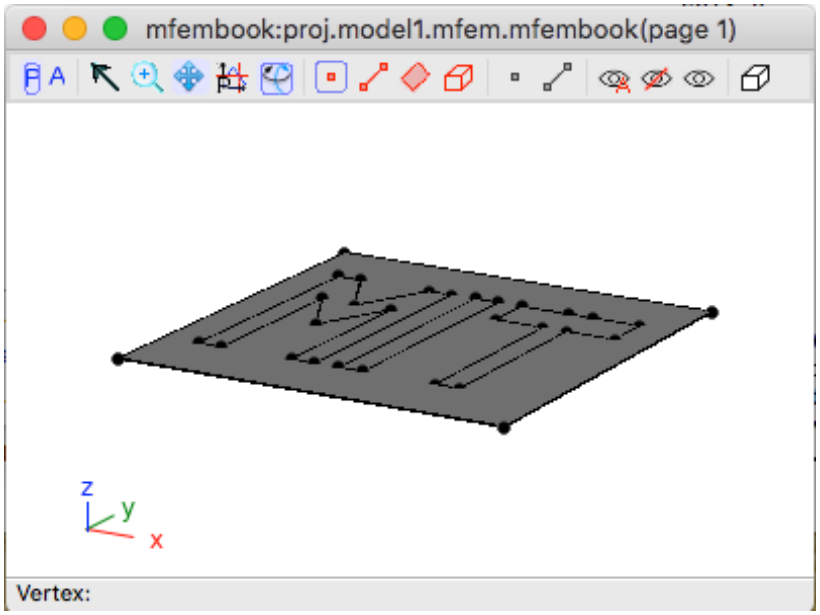

Figure 5.33: Petra-M's CAD interface allows the user to design intricate antenna geometries, and then designate the current distribution within them.

5.6 Full Wave Simulations using Petra-M

The full wave simulation tool Petra-M was employed in order to further investigate the anomaly of the upper band's left-hand dominance, in addition to our antenna model. Petra-M, short for Physics Equation Translator in MFEM, is a simulation framework that leverages the MFEM finite element library in order to solve a variety of wave propagation problems [88]. One of the original motivations of the framework was to use it to solve the problem of RF wave propagation in cold plasmas, which we will do here.

All simulations and subsequent plots in this section were generated by Kunal Sanwalka, the lab's Petra-M guru.

The framework has a CAD interface which allows the user to create a 3D model of their antenna, and then designate the current distribution within the antenna, as shown in figure 5.33. There are several well known differential equations that Petra-M can solve, such as the heat diffusion equation and waveguide equation, and for each problem the user can specify

parameters that are specific to that differential equation. For our purposes, we use Petra-M to solve the wave equation in a dielectric medium, where we specify the dielectric as the cold plasma dielectric tensor. The dielectric can be written to be a function of position, for example if one wanted to model wave propagation through density or background field gradients, but for our purposes we assume the dielectric to be uniform.

Figure 5.34 shows the XY plane generated by a Petra-M simulation, 2.5 m from the loop antenna. The plasma conditions, antenna parameters, and frequency are similar to the ones shown in figure 5.17. The wave is shown to be very close to linearly polarized at $r = 0$, with two parallel electron current channels on either side. The results from this simulation are similar to the animation that was created from our antenna model, shown in figure 5.23, but do not agree with the experimental observations of the upper band.

Next, Petra-M simulations were performed for several frequencies in order to calculate the ratio of left-to-right handed power globally. The results can be seen in figures 5.35. A crossover frequency can be seen in the results, which is consistent with the results of the antenna model (figure 5.30) as well as the dispersion theory (figure 5.1). Unfortunately, the Petra-M model predicted close to linear polarization throughout the entire upper band, meaning it is unable to explain the observed left-hand dominance of the upper band.

5.7 Conclusion

Shear waves were systematically launched in a helium/neon plasma for a wide range of conditions in the LAPD, using a magnetic dipole antenna. The resulting wave patterns were analytically decomposed into their left and right handed circularly polarized constituents, as it was shown in section 5.4 that the resulting spectra were qualitatively consistent with those obtained from launching "pure" left and right handed waves. Two distinct propagation bands were observed, bounded by $\omega < \Omega_{Ne}$ and $\omega_{ii} < \omega < \Omega_{He}$, where ω_{ii} is the ion-ion hybrid frequency. The lower band is linearly polarized at low frequency ($\omega < .67\Omega_{Ne}$)

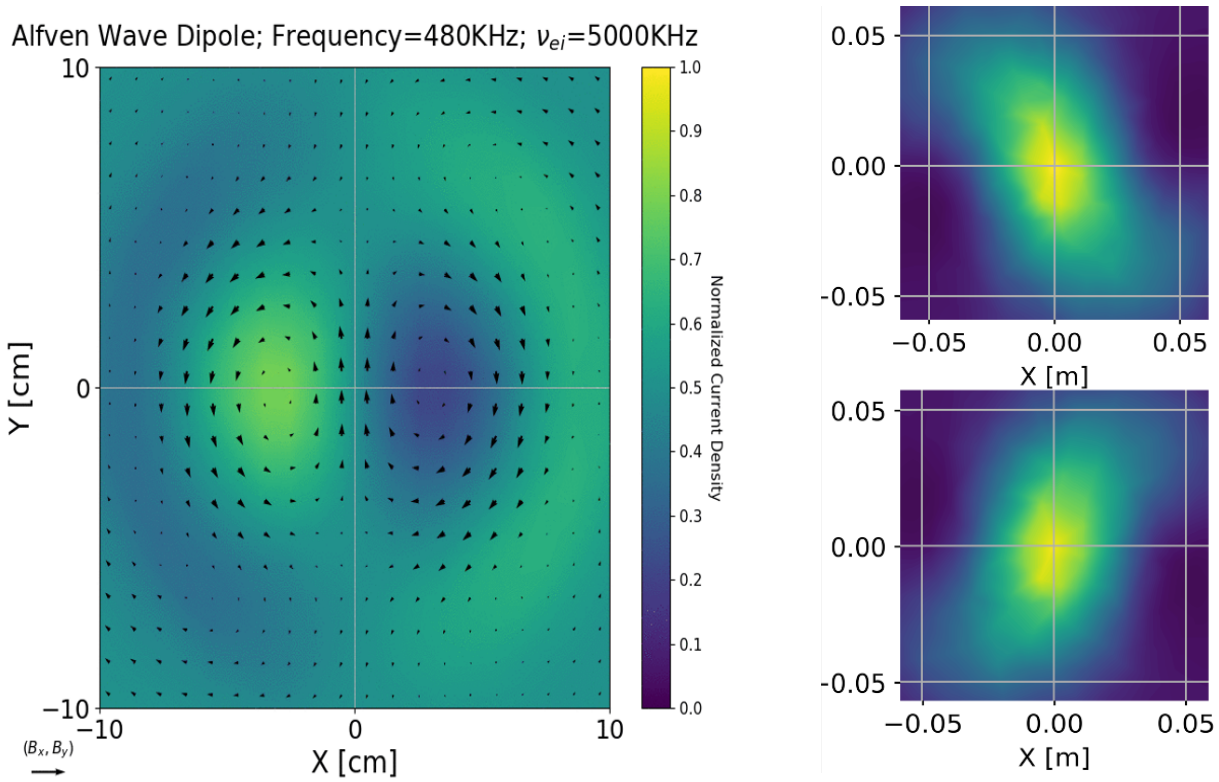

Figure 5.34: (a) Petra-M simulation of the wave front of a shear wave launched by a loop antenna, taken 3 m from the antenna, at frequency in the upper band of a helium/neon plasma. The wave is linearly polarized at the center of the two current channels, which is in direct contradiction with the observed left-hand dominance that was seen in the data. (b) Left and (c) right handed power spectra of the wave, normalized to each other.

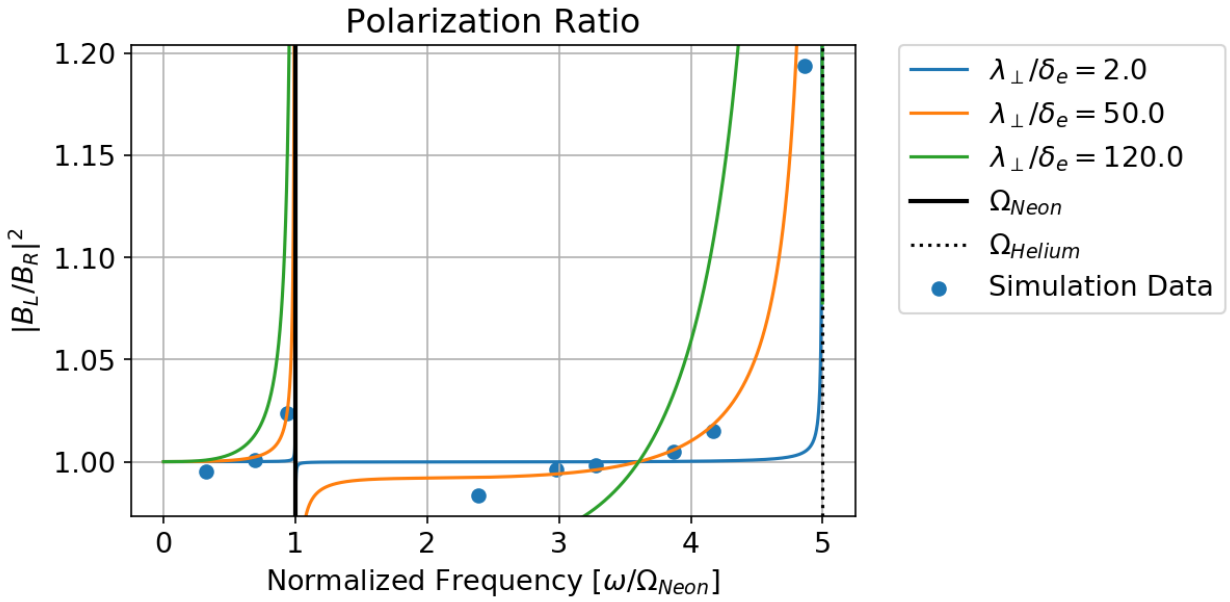

Figure 5.35: Global ratio of left-to-right handed power, calculated using simulations from Petra-M.

but becomes increasingly left handed closer to the neon cyclotron frequency. This is in agreement with the predicted polarization derived in section 5.2, which is based on the dispersion physics of the shear wave. The upper band, however, was found to be left-hand dominant at nearly all frequencies and plasma conditions. This is in direct contradiction with the theoretical prediction, which suggests that the lower half of the upper band should be right-hand dominant and the upper half left handed.

One possibility for the observed left-hand dominance of the upper band was that the right-handed component of the wave experiences significantly more damping than the left, and so this was explored both theoretically and experimentally. The spatial damping of both the left and right hand polarized components of the wave were calculated from a series of B-dot probes, for several different background field cases. It was found that the lower band experiences equal damping rates for the left and right handed components, whereas the upper band tends to experience more left-handed damping than right. Therefore it seems

unlikely that asymmetrical damping is the cause of the upper band's polarization. Another possible explanation that was considered was the effect of antenna coupling. It was shown that the left-hand dominance of the upper band is not unique to the RMF antenna, and was recreated for both the two-disk exciter configuration as well as the smaller loop antenna.

In sections 5.5 and 5.6, we simulated the expected wave patterns from a loop antenna using our antenna model, derived in chapter 3, as well as the full wave Petra-M framework. Both models were in excellent agreement with each other and the dispersion theory outlined in section 5.2 - namely, both models showed that the wave should be close to linearly polarized throughout the upper band. A comparison of the antenna model to measured radial lines of the left and right handed power, however, show that the antenna model fails to predict the left-hand dominance that is consistently observed in the data.

CHAPTER 6

Summary and Future Work

Several years ago, this dissertation started as an effort to find a robust and accurate method for measuring the ion-ion hybrid frequency ω_{ii}, the results of which are detailed in chapter 4. While experimenting with various diagnostic techniques, an anomaly in the polarization of the shear wave's upper band was observed, warranting a deeper investigation into the polarization of two-ion shear waves that ultimately culminated in its own study, which is presented in chapter 5. In an effort to try and understand the observed polarization, a theoretical framework for predicting the radiation fields excited by antennas immersed in a cold, magnetized plasma was developed, which can be found in chapter 3. While the contents of chapters 3, 4, and 5 are all closely related, they ultimately became their own independent works which are intended to stand on their own.

For the diagnostic discussed in chapter 4, the goal was to be able to make localized measurements of the ion density ratio in a two-ion plasma. One of the early renditions of such a probe can be seen in figure 2.11. The idea was fairly simple - bias the two mesh squares against each other with frequency ω, aligned across the background field, and measure the current response. Since the plasma between the two mesh squares is responsible for closing the current, it was expected that the circuit would experience a cross-field resonance at $\omega = \omega_{ii}$. Many variations of this scheme were tested, including several different antenna and electronic configurations. In the end, we were unsuccessful in exciting the ion-ion hybrid resonance, and so none of these results were ultimately included in this dissertation.

One of the reasons we were unable to excite the cross-field resonance is because, for the

plasma conditions typical in the LAPD, it is much easier to couple to the slow wave than the fast wave. As we showed in chapter 3, the majority of slow wave energy travels along narrow cones along the background field lines, leaving very little current which actually makes it across the field to the receiving end of the antenna. This led us down an alternate path, in which we excited slow waves and attempted to measure the ion-ion hybrid cutoff frequency, and became the central topic of chapter 4. The cutoff can be observed in several common laboratory diagnostics, including the ion saturation current, floating potential, and B-dot fluctuations, both in their respective spectra as well as the crossphase between axially-displaced probes. The cutoff was most evident in the B-dot's spectrum and crossphase, and so this was the data that was showcased throughout most of this dissertation. One of the biggest breakthroughs in this diagnostic was the development of a least-squares-fitting algorithm which is able to very efficiently find the local ion density ratio from a measured $k_{\parallel}$ plot, while requiring very little information about the plasma. This algorithm was applied to dispersion data taken from waves launched by a scaled down loop antenna and measured using two B-dot probes, centered on the same field line as the antenna and several meters away. The algorithm was successfully applied in order to obtain radially-localized measurements of the ion density ratio measurements, as can be seen in chapter 4. This diagnostic could prove useful in many magnetized plasma environments which permit direct contact with diagnostics and antennas, including both laboratory and space plasmas. When used in conjunction with an electron density measurement, this information can then be used to construct density profiles of the individual ion species.

At one point, our search for a robust method for measuring the ion density ratio led us to look at the polarization of the slow wave in two-ion plasmas, and how it varied with frequency and varying plasma conditions. Some of the observations went against what was initially expected based on the understood physics of the slow wave, and this motivated a deeper investigation which eventually culminated in chapter 5. The lower band behaved as expected - namely, it was linearly polarized at low frequency and became increasingly left-

handed near the ion cyclotron frequency. This is also the observed behavior in plasmas with a single ion species. The upper band, bounded by ω_{ii} and the larger of the two ion cyclotron frequencies, was observed to be overwhelmingly left-handed at (nearly) all frequencies and plasma conditions. This seems to be at odds with the dispersion theory, which predicts the bottom half of the upper band to be slightly right-handed and the upper half slightly left-handed. Many, *many* variations of this experiment were attempted over the course of 1-2 years. Countless antenna geometries and configurations were used, as well as nearly all possible plasma conditions that the LAPD is capable of facilitating. While the degree of left-handedness in the upper band varied between attempts, it always exhibited left-hand dominance across the entire frequency band. Simulations were performed using both a custom analytic model developed by the author as well as a full wave simulation framework known as Petra-M. Both modeling tools agreed with the dispersive plane wave theory as well as each other, but neither could explain the observed left-hand dominance in the upper band. While exploring different plasma environments using Petra-M, we discovered that decreasing the electron collisionality led to the polarization of the wave being altered. It is speculated that the lower collisionality results in the formation of reflected waves off the ends of the machine, which combine with the incident wave and modify the polarization. This warrants further investigation into the impact of reflection on shear wave polarization, and is currently being actively pursued as a possible lead in our polarization mystery.

Motivated by the dispersion theory's inability to predict the upper band's observed polarization, a more complete antenna wave theory was developed, the results of which are contained in chapter 3. Antenna-driven waves in a laboratory setting can rarely be considered as plane waves (consisting of a single wave vector $\vec{k}$), but rather consist of a continuous spectrum of $\vec{k}$ with varying amplitudes. Often times, the aggregate sum of these waves results in polarization behavior not captured by a simple dispersion theory, and so a full description of the spatial structure of the wave is required in order to have a complete picture of the wave's polarization. It was shown that Maxwell's equations can be reformulated

in order to express the vacuum field of the antenna as a source term to the plasma wave equation. A general solution was derived under this framework, expressed as a volume integral across the vacuum field of the antenna. One of the advantages of this model is the degree of analyticity, as it allows the user to solve many steps analytically, thereby saving significant computation time. This is best showcased in section 3.3, in which we solved the general solution for a 1-D electric dipole aligned along the background field. In chapter 5 this model was used to determine the field from a magnetic loop antenna, and the results were nearly identical to previously published simulation results of the same antenna [60] - verifying the results of the antenna model. The wave polarization was calculated using the antenna model, both globally and along $r = 0$, and found to be in close agreement with the simulation results from Petra-M as well as the dispersion theory. This analytic model for antenna-driven waves provides a useful alternative to other modeling techniques, in which symmetries in the vacuum field of the antenna can be exploited in order to substantially simply many problems.

If some hapless graduate student or researcher is reading this, perhaps looking for motivation for a project of their own: The diagnostic described in chapter 4 is successful in measuring the radially-localized ion density ratio, but it requires three probes (one antenna, two B-dot probes) stretched out across several meters in the z direction. The reason for this is because the wavelength of the shear wave is typically on the order of several meters, and so it is difficult to localize the diagnostic axially while simultaneously sampling a significant portion of the wave's parallel phase. An improvement on this diagnostic would be to modify it such that it is localized not only radially but also in the z direction. This would also allow this diagnostic to be used in curved magnetic field configurations, such as in the scrape off layer of tokamaks. Additionally, an antenna which could make measurements of the parallel phase without direct contact with the plasma (i.e. via reflectometry or interferometry) could be used in harsher plasma conditions, such as the core of a tokamak where knowledge of the ion-density ratio is of monumental importance.

The theoretical model in chapter 3 was shown to yield accurate results when compared to past simulations, but it is limited to considering cold plasmas that are uniform and infinite. This model remains to be generalized to account for kinetic effects, as well as the effect of reflected waves due to boundary conditions surrounding the plasma. Petra-M simulations shown in chapter 5 showed that reflected waves can have a significant impact on the wave physics, and so this would be a valuable addition to the model. Finally, generalizing the model to account for spatial inhomogeneities, such as density or field gradients, could capture additional wave physics that is known to exist in the LAPD and other magnetized plasmas. Lastly, the anomaly of the observed left-hand dominance in the shear wave's upper band remains a mystery, although chapter 5 explored and eliminated many possible causes. Reflections at the ends of the machine are currently being investigated via Petra-M simulations as a possible cause. An experimental counterpart to these simulations would be to deliberately facilitate the reflection of waves in the LAPD, and systematically document the changes in wave polarization. In addition, other higher order effects, such as plasma inhomogeneities and nonlinearities, remain to be explored in terms of their impact on wave polarization.

APPENDIX A

Derivation of Circularly Polarized Coordinates

A.1 Circularly Polarized Coordinates

Consider a vector field which has the following time dependence:

$$\vec{B}(t) = B_0 cos(\omega t)\hat{x} - B_0 sin(\omega t)\hat{y}, \tag{A.1}$$

where B_0 is a constant. It is straightforward to verify that equation A.1 represents a wave of constant magnitude B_0, that rotates in a circular motion in the direction of ion gyromotion (assuming a background magnetic field that points in $+\hat{z}$) - which we call the left-handed direction. Replacing *sin* and *cos* with their complex exponential forms, equation A.1 can be rewritten in the alternate form:

$$\vec{B}(t) = \mathrm{Re}\{B_0 e^{-i\omega t}\,(\hat{x} - i\hat{y})\}. \tag{A.2}$$

A right handed wave will yield a similar result, but in the direction $\hat{x} + i\hat{y}$. The form of equation A.2 motivates us to define the left and right-handed unit vectors $\hat{l}$ and $\hat{r}$, respectively, as:

$$\begin{aligned} \hat{l} &= \frac{1}{\sqrt{2}}\,(\hat{x} - i\hat{y})\,, \\ \hat{r} &= \frac{1}{\sqrt{2}}\,(\hat{x} + i\hat{y})\,. \end{aligned} \tag{A.3}$$

It can be shown that the complex unit vectors $\hat{l}$, $\hat{r}$, and $\hat{z}$ form an orthonormal basis in R^3. Any 3-dimensional vector field in Euclidian space, then, can be represented in the circularly polarized coordinate system defined by equation A.3. The components of $\vec{B}$ in circularly polarized coordinates can be found by projecting $\vec{B}$ onto $\hat{l}$ and $\hat{r}$ (recall that the inner product of two complex vectors is defined by $a \cdot b = \Sigma a_i b_i^*$). For a vector field with arbitrary time dependence, this gives us the following forms for the left and right handed components:

$$\begin{aligned} \tilde{B}_L &= \frac{1}{\sqrt{2}} \left(\tilde{B}_x(\omega) + i\tilde{B}_y(\omega) \right), \\ \tilde{B}_R &= \frac{1}{\sqrt{2}} \left(\tilde{B}_x(\omega) - i\tilde{B}_y(\omega) \right), \end{aligned} \tag{A.4}$$

where, for a signal with arbitrary time dependence, $\tilde{B}_j(\omega)$ is the Fourier transform of component $B_j(t)$, defined by:

$$\tilde{B}_j(\omega) = \frac{1}{2\pi} \int_{-\infty}^{\infty} B_j(t) e^{i\omega t} dt \quad \Longleftrightarrow \quad B_j(t) = \int_{-\infty}^{\infty} \tilde{B}_j(\omega) e^{-i\omega t} d\omega. \tag{A.5}$$

Our definition for the left and right-handed unit vectors in equation A.3 assume the convention $\partial_t \rightarrow -i\omega$, which is typical in plasma literature. Many FFT algorithms, as well as some other branches of physics, use the opposite sign convention, in which case the complex conjugates of equations A.3 and A.4 should be used. There is another pitfall that we haven't addressed, which is that our definitions for left and right-handedness are only valid for $\omega > 0$, whereas the inverse Fourier transform in equation A.5 is taken across all frequencies. For negative frequencies, the complex conjugates of equations A.3 and A.4 would have to be used. Any confusion involving negative frequencies can be avoided, however, by recognizing that if $B_j(t)$ is real (as any time signal should be), then its Fourier transform obeys the symmetry property $\tilde{B}_j(-\omega) = \tilde{B}_j^*(\omega)$. We can exploit this symmetry to avoid negative frequencies altogether, and change the limits of integration in the inverse FT to go from $\omega = 0$ to $+\infty$. For a vector field with arbitrary time dependence, then, the left and

right handed components of the wave can be extracted and isolated from the total signal by the following equation:

$$\left\{ \begin{array}{c} B_L(t) \\ B_R(t) \end{array} \right\} = 2\mathrm{Re}\left[\int_0^\infty \left\{ \begin{array}{c} \tilde{B}_L(\omega)\hat{l} \\ \tilde{B}_R(\omega)\hat{r} \end{array} \right\} e^{-i\omega t} d\omega \right]. \tag{A.6}$$

A.1.1 Circular Polarization of an Elliptical Wave

Consider an elliptical wave, defined by:

$$\vec{B}(t) = B_{x0} cos(\omega_0 t)\hat{x} - B_{y0} sin(\omega_0 t)\hat{y}, \tag{A.7}$$

where $B_{x0}, B_{y0} > 0$ and are not time dependent. It is straightforward to verify that the field of equation A.7 maps out an ellipse which rotates in the left-handed direction. The left and right handed components of the wave, in frequency space, are found to be:

$$\begin{array}{l} \tilde{B}_L(\omega) = \dfrac{1}{2\sqrt{2}} \left[(B_{x0} - B_{y0})\delta(\omega + \omega_0) + (B_{x0} + B_{y0})\delta(\omega - \omega_0) \right] \\ \tilde{B}_R(\omega) = \dfrac{1}{2\sqrt{2}} \left[(B_{x0} + B_{y0})\delta(\omega + \omega_0) + (B_{x0} - B_{y0})\delta(\omega - \omega_0) \right] \end{array}. \tag{A.8}$$

Inserting these into equation A.6 gives the following left and right handed waves:

$$\begin{array}{l} B_L(t) = \dfrac{1}{2}(B_{x0} + B_{y0}) \left[cos(\omega t)\hat{x} - sin(\omega t)\hat{y} \right] \\ B_R(t) = \dfrac{1}{2}(B_{x0} - B_{y0}) \left[cos(\omega t)\hat{x} + sin(\omega t)\hat{y} \right] \end{array}. \tag{A.9}$$

The time evolution of equation A.9 is shown in figure A.1, and shows how the left and right handed components add up to produce the original elliptical wave. This has strong implications for polarization studies. If one were to attempt to launch a left handed wave from an antenna, but the B_x and B_y components of the wave were not perfectly matched, equation A.9 suggests the antenna signal will contain a small right handed component of the wave whose power is proportional to the squared difference of the two amplitudes.

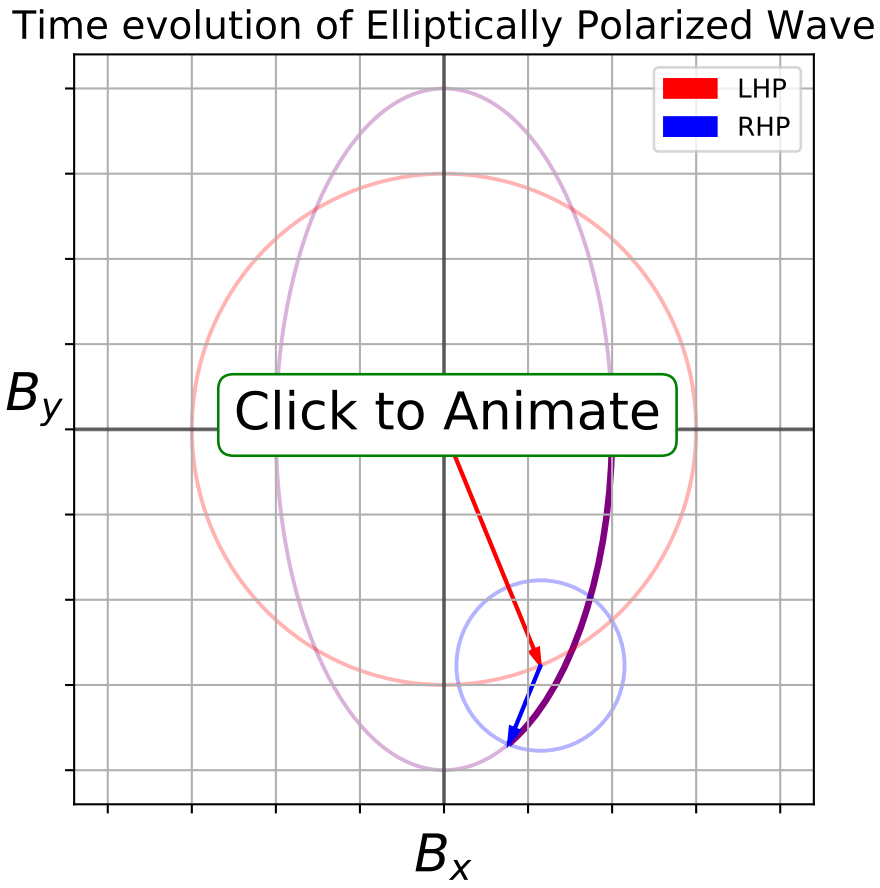

Figure A.1: Time evolution of an elliptically polarized wave, with $B_{y0} = 2B_{x0}$. Red and blue circles show the magnitude/direction of the left and right handed components of the field, respectively. The wave is primarily left-handed, but picks up a small right handed component due to the mismatch in B_{x0} and B_{y0}.

A.2 Recasting the Dispersion Matrix in Circularly Polarized Coordinates

A uniform, magnetized plasma, subjected to a small monochromatic perturbation, is described by equation 3.3. If we Fourier transform equation 3.3 in space, we can recast it in Cartesian coordinates as:

$$\begin{bmatrix} \varepsilon_\perp - n_y^2 - n_z^2 & \varepsilon_{xy} + n_x n_y & n_x n_z \\ -\varepsilon_{xy} + n_x n_y & \varepsilon_\perp - n_x^2 - n_z^2 & n_y n_z \\ n_x n_z & n_y n_z & \varepsilon_\parallel - n_x^2 - n_y^2 \end{bmatrix} \cdot \begin{pmatrix} E_x \\ E_y \\ E_z \end{pmatrix} = 0. \tag{A.10}$$

We wish to rewrite equation A.10 in circularly polarized coordinates, defined by equations A.3 and A.4. This can be achieved if we define the unitary transformation matrix $\mathbf{U}$, such that:

$$\begin{pmatrix} \tilde{E}_L \\ \tilde{E}_R \\ \tilde{E}_z \end{pmatrix} = \mathbf{U} \cdot \begin{pmatrix} \tilde{E}_x \\ \tilde{E}_y \\ \tilde{E}_z \end{pmatrix}, \quad \text{where} \quad \mathbf{U} = \begin{bmatrix} 1/\sqrt{2} & i/\sqrt{2} & 0 \\ 1/\sqrt{2} & -i/\sqrt{2} & 0 \\ 0 & 0 & 1 \end{bmatrix}. \tag{A.11}$$

The transformation matrix satisfies the condition for unitarity $\mathbf{U} \cdot \mathbf{U}^\dagger = \mathbf{I}$, where $\mathbf{U}^\dagger$ is the Hermitian of $\mathbf{U}$. Equation A.10 can be recast into circularly polarized coordinates by the transformation $\mathbf{U} \cdot \mathbf{W} \cdot \mathbf{U}^\dagger$, where $\mathbf{W}$ is the 3×3 Cartesian matrix in equation A.10. This gives us the following system of equations:

$$\begin{bmatrix} \varepsilon_L - n_L n_R - n_z^2 & n_L^2 & n_z n_L \\ n_R^2 & \varepsilon_R - n_L n_R - n_z^2 & n_z n_R \\ n_z n_R & n_z n_L & \varepsilon_\parallel - 2 n_L n_R \end{bmatrix} \cdot \begin{pmatrix} \tilde{E}_L \\ \tilde{E}_R \\ \tilde{E}_z \end{pmatrix} = 0, \tag{A.12}$$

where $\varepsilon_{R,L} = \varepsilon_\perp \pm i\varepsilon_{xy}$. The possible dispersion relations of the system can be found from either the determinant of equation A.12 or of equation A.10 - both will yield the same

dispersion relation, solved previously in section 3.2.2 and given by equation 3.19. If FLR effects are ignored, then ε_L and ε_R can be expressed as:

$$\varepsilon_{L,R} = 1 + \sum_s \frac{\omega_{ps}^2}{\omega^2} \zeta_{0,s} Z\left(\zeta_{\pm 1,s}\right), \tag{A.13}$$

where $\zeta_{n,s} = (\omega - n\Omega_{c,s})/\sqrt{2}k_\parallel v_{Th,s}$ and s refers to the particle species.

A.2.1 Polarization Energy of Shear Alfvén Waves

The ratio of left-to-right handed electric field energy, for a given frequency, can be found by combining the first and second lines of equation A.12, and gives the following:

$$\frac{E_L}{E_R} = \frac{n^2 - \varepsilon_R}{n^2 - \varepsilon_L} \frac{n_L}{n_R} \quad \Longrightarrow \quad \frac{|E_L|^2}{|E_R|^2} = \left| \frac{n^2 - \varepsilon_R}{n^2 - \varepsilon_L} \right|^2, \tag{A.14}$$

where $n^2 = n_\perp^2 + n_\parallel^2$. Note that equation A.14 is, in general, true for all dispersion modes of the system. The handedness of waves is traditionally discussed in the context of the polarization of the wave's transverse electric field. The RMF antenna used to study circularly polarized waves (described in detail in section 2.3), however, operates by driving the x and y components of the *magnetic* field $\pm\pi/2$ out of phase in order to excite circularly polarized waves. The ratio of the left-to-right handed magnetic field energy can be found through Faraday's law:

$$\frac{B_L}{B_R} = \frac{\left(\vec{n} \times \vec{E}\right) \cdot \hat{l}^*}{\left(\vec{n} \times \vec{E}\right) \cdot \hat{r}^*} = \frac{n_z E_L - n_L E_z}{n_R E_z - n_z E_R}. \tag{A.15}$$

We can combine equation A.14 with the third line of equation A.12 to get expressions for E_L/E_z and E_R/E_z, and then substitute these into equation A.15. The resulting expression is as follows:

$$\frac{B_L}{B_R} = -\frac{n^2 - \varepsilon_R + n_\perp^2(\varepsilon_{xy}/\varepsilon_\parallel)}{n^2 - \varepsilon_L - n_\perp^2(\varepsilon_{xy}/\varepsilon_\parallel)} \frac{n_L}{n_R} \quad \Longrightarrow \quad \frac{|B_L|^2}{|B_R|^2} = \left| \frac{n^2 - \varepsilon_R + n_\perp^2(\varepsilon_{xy}/\varepsilon_\parallel)}{n^2 - \varepsilon_L - n_\perp^2(\varepsilon_{xy}/\varepsilon_\parallel)} \right|^2 . \tag{A.16}$$

Note the similarities between equations A.15 and A.14. In the limit $n_\perp^2 \to 0$, the power ratios of the electric and magnetic fields are identical. Additionally, in the frequency limit $\omega \ll \Omega_{c,i}$, the $E \times B$ slippage current (captured by the ε_{xy} dielectric term) goes to zero and equations A.14 and A.15 are identical. We are interested in the polarization of inertial Alfvén waves, whose dispersion is defined by the upper branch of equation 3.19 for frequencies below the ion cyclotron frequency, and how the energy imparted by an antenna naturally distributes between right and left handedness. Substituting equation 3.37 into A.16 gives us the following power ratio:

$$\frac{|B_L|^2}{|B_R|^2} = \left| \frac{n_\perp^2 \left(1 - \frac{\varepsilon_L}{\varepsilon_\parallel}\right) - \varepsilon_{xy}}{n_\perp^2 \left(1 - \frac{\varepsilon_R}{\varepsilon_\parallel}\right) + \varepsilon_{xy}} \right|^2 . \tag{A.17}$$

Equation A.17 is valid in the kinetic and inertial limits, as well as the intermediate regime, but assumes ignorable FLR effects. The forms of the various dielectric terms are given by equation 4.10.

APPENDIX B

Hankel Transform of the Electric Dipole Field

Consider an infinitely thin wire element of length ℓ, carrying current $Ie^{-i\omega t}$, that is aligned parallel to the background magnetic field $B_0\hat{z}$. As the current has nowhere to go, charge conservation results in a point charge buildup of $q = \pm I/i\omega$ on either end of the wire element. Therefore, by virtue of charge conservation, a finite wire element with an alternating current is mathematically equivalent to an electric dipole. The magnetic field of the wire element in vacuum, in the quasi-magnetostatic limit, is given by the following:

$$B_{\theta 0}(r,z) = \frac{\mu_0 I}{4\pi r}\left[\frac{z+\ell/2}{\sqrt{r^2+(z+\ell/2)^2}} - \frac{z-\ell/2}{\sqrt{r^2+(z-\ell/2)^2}}\right], \tag{B.1}$$

where an $e^{-i\omega t}$ time dependence is understood. Equation B.1 can alternatively be obtained by finding the electric field due to the charge buildup on the ends, and then the magnetic field via Ampere's law. The Hankel transform of equation B.1 is found from the following integral:

$$\tilde{B}_{\theta 0}(r,z) = \frac{\mu_0 I}{4\pi}\int_0^\infty \frac{(z+\ell/2)J_1(k_\perp r)\mathrm{d}r}{\sqrt{r^2+(z+\ell/2)^2}} - \frac{\mu_0 I}{4\pi}\int_0^\infty \frac{(z-\ell/2)J_1(k_\perp r)\mathrm{d}r}{\sqrt{r^2+(z-\ell/2)^2}}. \tag{B.2}$$

In order to solve equation B.2, we need to know how to solve integrals of the following form:

$$\int_0^\infty \frac{J_1(\alpha x)\mathrm{d}x}{\sqrt{1+x^2}}.$$

This can be solved, interestingly enough, by considering the *Laplace* transform of J_1:

$$\int_0^\infty J_1(t)e^{-st}\mathrm{d}t = 1 - \frac{s}{\sqrt{1+s^2}} \qquad \text{for } s > 0. \tag{B.3}$$

A change of variables allows equation B.3 to be written in the following alternate form:

$$\int_0^\infty \frac{e^{-\alpha}}{\alpha} J_1(\alpha x)\alpha\mathrm{d}\alpha = \frac{1}{x}\left(1 - \frac{1}{\sqrt{1+x^2}}\right) \qquad \text{for } x > 0. \tag{B.4}$$

The left-hand side of equation B.4 is readily identified as the first-order Hankel transform of $e^{-\alpha}/\alpha$. It follows then that the inverse transform must also be true:

$$\frac{e^{-\alpha}}{\alpha} = \int_0^\infty \frac{1}{x}\left(1 - \frac{1}{\sqrt{1+x^2}}\right) J_1(\alpha x)x\mathrm{d}x. \tag{B.5}$$

The first term in the integral can be solved by noting that $\int J_1(x)\mathrm{d}x = 1$. We then arrive at the following:

$$\int_0^\infty \frac{J_1(\alpha x)\mathrm{d}x}{\sqrt{1+x^2}} = \frac{1}{\alpha}\left(1 - e^{-\alpha}\right) \qquad \text{for } \alpha > 0. \tag{B.6}$$

The requirement $\alpha > 0$ in equation B.6 means that equation B.2 must be solved separately for the following 3 regions:

1. $z \geq \ell/2$
2. $-\ell/2 < z < \ell/2$
3. $z \leq -\ell/2$

We will consider the region $z > \ell/2$ first. Defining the variables $x_\pm = r/(z \pm \ell/2)$ and $\alpha_\pm = k_\perp(z \pm \ell/2)$, equation B.2 can be rewritten as:

$$\tilde{B}_{\theta 0}(k_\perp, z) = \frac{\mu_0 I}{4\pi}(z+\ell/2)\int_0^\infty \frac{J_1(\alpha_+ x_+)\mathrm{d}x_+}{\sqrt{1+x_+^2}} - \frac{\mu_0 I}{4\pi}(z-\ell/2)\int_0^\infty \frac{J_1(\alpha_- x_-)\mathrm{d}x_-}{\sqrt{1+x_-^2}}. \tag{B.7}$$

The identity from equation B.6 can then be used, giving us the following:

$$\tilde{B}_{\theta 0}(k_\perp, z) = \frac{\mu_0 I}{2\pi k_\perp} e^{-k_\perp z}\sinh\left(k_\perp \frac{\ell}{2}\right) \qquad \text{for } z > \ell/2. \tag{B.8}$$

In the region $-\ell/2 < z < \ell/2$, we must choose our variable substitutions carefully such that equation B.6 can still be used. We define the variables $x_+ = r/(z+\ell/2)$, $x_- = r/(\ell/2 - z)$, $\alpha_+ = k_\perp(z+\ell/2)$, and $\alpha_- = k_\perp(\ell/2-z)$, and can rewrite equation B.2 as the following:

$$\tilde{B}_{\theta 0}(r, z) = \frac{\mu_0 I}{4\pi}(z+\ell/2)\int_0^\infty \frac{J_1(\alpha_+ x_+)\mathrm{d}x_+}{\sqrt{1+x_+^2}} + \frac{\mu_0 I}{4\pi}(\ell/2-z)\int_0^\infty \frac{J_1(\alpha_- x_-)\mathrm{d}x_-}{\sqrt{1+x_-^2}}. \tag{B.9}$$

We redefined our variable substitutions slightly differently in order to ensure that $\alpha_\pm$ is positive-definite in the region of interest, so that identity B.6 may be used. In the last region, defined by $z < -\ell/2$, we would use the variable substitutions $x_\pm = -r/(z \pm \ell/2)$ and $\alpha_\pm = -k_\perp(z \pm \ell/2)$.

The full solution of equation B.2 is then the following:

$$\tilde{B}_{\theta 0}(k_\perp, z) = \tfrac{\mu_0 I}{2\pi k_\perp} \begin{cases} e^{-k_\perp z}\sinh k_\perp \frac{\ell}{2} & \text{for } z > \ell/2 \\ \left(1 - e^{-k_\perp \frac{\ell}{2}}\cosh k_\perp z\right) & \text{for } -\ell/2 < z < \ell/2\,. \\ e^{k_\perp z}\sinh k_\perp \frac{\ell}{2} & \text{for } z < -\ell/2 \end{cases} \tag{B.10}$$

APPENDIX C

Plasma Dispersion Relation - Kinetic Theory

Much of the theoretical work in this dissertation assumes a cold, highly magnetized plasma. It can be shown that this approximation is more than satisfactory for most of the plasma conditions considered, and has the advantage of being much more mathematically tractable. There are certain plasma conditions, however, where this model breaks down, and a proper theoretical treatment should account for various kinetic effects. In this appendix we will discuss the relevant kinetic effects that sometimes emerge in LAPD plasmas, and their effects on the plasma dispersion relation and resulting wave propagation. This appendix is intended to only serve as a reference, and will not cover a full derivation of kinetic theory. For a derivation of the general solution to the Vlasov equation and the complete kinetic dielectric tensor, see [23] or [93].

The plasma wave equation, which arises from the combination of Ampere's and Faraday's laws, can be expressed in Fourier space as the following:

$$\vec{n} \times \vec{n} \times \vec{E} + \overleftrightarrow{\varepsilon} \cdot \vec{E} = 0. \tag{C.1}$$

Equation C.1 can then be expressed in Cartesian coordinates by the following 3×3 matrix:

$$\begin{bmatrix} \varepsilon_{xx} - n_y^2 - n_z^2 & \varepsilon_{xy} + n_x n_y & \varepsilon_{xz} + n_x n_z \\ -\varepsilon_{xy} + n_x n_y & \varepsilon_{yy} - n_x^2 - n_z^2 & \varepsilon_{yz} + n_y n_z \\ \varepsilon_{xz} + n_x n_z & -\varepsilon_{yz} + n_y n_z & \varepsilon_{zz} - n_x^2 - n_y^2 \end{bmatrix} \cdot \begin{pmatrix} E_x \\ E_y \\ E_z \end{pmatrix} = 0. \tag{C.2}$$

The components of the dielectric tensor are found from the solution to the collisionless

Vlasov equation. It is typical to rotate the coordinate system such that $\vec{n} = n_\perp \hat{x} + n_\parallel \hat{z}$, which can be done without loss of generality. Assuming all particle species obey a Maxwellian distribution with zero net drift, as well as an isotropic temperature ($T_\perp = T_\parallel$), the dielectric terms are given by the following:

$$
\begin{aligned}
\varepsilon_{xx} &= 1 + \sum_s \frac{\omega_{ps}^2}{\omega^2} \zeta_{0,s} \frac{e^{-\lambda_s}}{\lambda_s} \sum_{n=-\infty}^{\infty} n^2 I_n Z(\zeta_{n,s}), \\
\varepsilon_{xy} &= i \sum_s \frac{\omega_{ps}^2}{\omega^2} \zeta_{0,s} e^{-\lambda_s} \sum_{n=-\infty}^{\infty} n \left(I_n' - I_n \right) Z(\zeta_{n,s}), \\
\varepsilon_{xz} &= - \sum_s \frac{\omega_{ps}^2}{\omega^2} \zeta_{0,s} \frac{e^{-\lambda_s}}{\sqrt{2\lambda_s}} \sum_{n=-\infty}^{\infty} n I_n Z'(\zeta_{n,s}), \\
\varepsilon_{yy} &= 1 + \sum_s \frac{\omega_{ps}^2}{\omega^2} \zeta_{0,s} \lambda_s e^{-\lambda_s} \sum_{n=-\infty}^{\infty} \left[\left(2 + \frac{n^2}{\lambda_s^2} \right) I_n - 2 I_n' \right] Z(\zeta_{n,s}), \\
\varepsilon_{yz} &= i \sum_s \frac{\omega_{ps}^2}{\omega^2} \zeta_{0,s} \sqrt{\frac{\lambda_s}{2}} e^{-\lambda_s} \sum_{n=-\infty}^{\infty} (I_n' - I_n) Z'(\zeta_{n,s}), \\
\varepsilon_{zz} &= 1 - \sum_s \frac{\omega_{ps}^2}{\omega^2} \zeta_{0,s} e^{-\lambda_s} \sum_{n=-\infty}^{\infty} \zeta_{n,s} I_n Z'(\zeta_{n,s}).
\end{aligned}
\tag{C.3}
$$

The derivation in [23] contains a solution that is valid for net particle drifts and anisotropic temperature conditions, but these effects are not present in the LAPD so they are omitted here. In equation C.3, $I_n = I_n(\lambda_s)$ is the modified Bessel function of order n, and $Z(\zeta_{n,s})$ is the plasma dispersion function. The summations are over all particle species s. The definitions of λ_s and $\zeta_{n,s}$ can be found in table XYZ, as well as the definitions of any other variables not explicitly defined in the text.

C.1 Parallel Kinetic Electrons

To start, we will only consider kinetic effects of the parallel electron motion, while continuing to assume the ions are cold. A particle species is considered "cold" if the parallel phase velocity is much larger than the thermal speed, or $\zeta_{n,s} \gg 1$. In this limit, equation C.2 can

be reduced to the following:

$$\begin{bmatrix} S - n_y^2 - n_z^2 & -iD + n_x n_y & n_x n_z \\ iD + n_x n_y & S - n_x^2 - n_z^2 & n_y n_z \\ n_x n_z & n_y n_z & \varepsilon_\parallel - n_x^2 - n_y^2 \end{bmatrix} \cdot \begin{pmatrix} E_x \\ E_y \\ E_z \end{pmatrix} = 0. \tag{C.4}$$

For frequencies $\omega \ll |\Omega_{ce}|$, the dielectric terms can be expressed to good accuracy in the following form:

$$\begin{aligned} S(\omega) &= -\sum_{ions} \frac{\omega_{pi}^2}{\omega^2 - \Omega_{ci}^2}, \\ D(\omega) &= \sum_{ions} \frac{\omega}{\Omega_{ci}} \frac{\omega_{pi}^2}{\omega^2 - \Omega_{ci}^2}, \\ \varepsilon_\parallel(k_\parallel, \omega) &= -\frac{\omega_{pe}^2}{\omega^2} \zeta_{0,e}^2 Z'(\zeta_{0,e}). \end{aligned} \tag{C.5}$$

The $Z'(\zeta_{0,e})$ term in the parallel electron response is responsible for electron Landau damping, one of the main kinetic effects observed for LAPD plasma conditions. Note that the cold ion assumption breaks down for frequencies close to the ion cyclotron frequencies, as $\zeta_{n,s} \gg 1$ is no longer true. The plasma dispersion relation for kinetic electrons is given by the following:

$$n_\parallel^2 = S - \frac{n_\perp^2}{2}\left(1 + \frac{S}{\varepsilon_\parallel}\right) \pm \sqrt{\left(\frac{n_\perp^2}{2}\right)^2 \left(1 - \frac{S}{\varepsilon_\parallel}\right)^2 + D^2 \left(1 - \frac{n_\perp^2}{\varepsilon_\parallel}\right)}. \tag{C.6}$$

Note that since $\varepsilon_\parallel$ is a function of $k_\parallel$, equation C.6 will have to be solved numerically to find $k_\parallel(k_\perp, \omega)$. In the limits $\zeta_{0,e} \gg 1$ or $\zeta_{0,e}$, however, analytic expressions can be found for the parallel dispersion. If unsure, this form of the dielectric is probably the safest bet for LAPD plasmas, as it is valid for nearly all accessible plasma conditions in the machine.

C.2 Finite Ion Larmor Radius (FLR) effects

The inclusion of finite Larmor radius (FLR) effects drastically complicates the situation, as all nine terms of the dielectric tensor must be included. FLR effects arise when $\lambda_s \ll 1$ is not satisfied, giving rise to the $|n| > 1$ terms present in the summations in equation C.3. There are certain plasma conditions where ion FLR effects may be present in LAPD plasmas. Without loss of generality, we can rotate our coordinate system such that $\vec{n} = n_\perp \hat{x} + n_\parallel \hat{z}$. If we assume the ions and electrons are cold ($\zeta_{n,s} \gg 1$), equation C.2 can be expressed in the following form:

$$\begin{bmatrix} \varepsilon_{xx} - n_\parallel^2 & \varepsilon_{xy} & \alpha n_\parallel + n_\perp n_\parallel \\ -\varepsilon_{xy} & \varepsilon_{yy} - n_\parallel^2 - n_\perp^2 & \beta n_\parallel \\ \alpha n_\parallel + n_\perp n_\parallel & -\beta n_\parallel & \varepsilon_{zz} - n_\perp^2 \end{bmatrix} \cdot \begin{pmatrix} E_x \\ E_y \\ E_z \end{pmatrix} = 0, \tag{C.7}$$

where

$$\begin{aligned}
\varepsilon_{xx} &= -2\sum_{ions} \omega_{pi}^2 \frac{e^{-\lambda_i}}{\lambda_i} \sum_{n=1}^{\infty} \frac{n^2 I_n}{\omega^2 - (n\Omega_{ci})^2}, \\
\varepsilon_{xy} &= -i\frac{\omega_{pe}^2}{\omega\,|\Omega_{ce}|} - 2i\sum_{ions} \frac{\Omega_{ci}}{\omega} \omega_{pi}^2 e^{-\lambda_i} \sum_{n=1}^{\infty} \frac{n^2 (I_n' - I_n)}{\omega^2 - (n\Omega_{ci})^2}, \\
\varepsilon_{yy} &= \varepsilon_{xx} - 2\frac{\omega_{pe}^2}{\omega^2} \frac{k_\perp^2 v_{Th,e}^2}{\Omega_{ce}^2} + 2\sum_{ions} \frac{\omega_{pi}^2}{\omega} \lambda_i e^{-\lambda_i} \sum_{n=-\infty}^{\infty} \frac{I_n' - I_n}{\omega - n\Omega_{ci}}, \\
\varepsilon_{zz} &= -\frac{\omega_{pe}^2}{\omega^2}, \\
\alpha &= -\frac{4}{n_\perp} \sum_{ions} \omega_{pi}^2 \Omega_{ci}^2 e^{-\lambda_i} \sum_{n=1}^{\infty} \frac{n^2 I_n}{\left[\omega^2 - (n\Omega_{ci})^2\right]^2}, \\
\beta &= -in_\perp \frac{\omega_{pe}^2 v_{Th,e}^2}{c^2 |\Omega_{ce}| \omega} + ik_\perp \sum_{ions} \frac{\omega_{pi}^2 v_{Th,i}^2}{c\Omega_{ci}} e^{-\lambda_i} \sum_{n=-\infty}^{\infty} \frac{I_n' - I_n}{(\omega - n\Omega_{ci})^2},
\end{aligned} \tag{C.8}$$

where we redefined the dielectric terms $\varepsilon_{xz} \equiv \alpha n_\parallel$ and $\varepsilon_{yz} \equiv \beta n_\parallel$, where α and β are independent of $k_\parallel$. In this way, all the terms defined in equation C.8 are independent of $k_\parallel$ and the $n_\parallel$ dependence of equation C.7 is explicitly shown. This coordinate system

is directly analogous to cylindrical coordinates via the variable substitutions $\hat{x} \to \hat{r}$ and $\hat{y} \to \hat{\theta}$ – therefore it follows that any analysis performed in Cartesian coordinates is directly transferable to a cylindrical system with azimuthal symmetry. We have also assumed cold parallel electron motion here, although it is straightforward to replace ε_{zz} with its kinetic counterpart.

The dispersion relation of the system is found by taking the determinant of equation C.7, and the resulting characteristic equation is a quadratic in $n_\parallel^2$:

$$0 = An_\parallel^4 - Bn_\parallel^2 + C, \tag{C.9}$$

where

$$\begin{aligned} A &= \varepsilon_{zz} + \alpha^2 - \beta^2 + 2\alpha n_\perp, \\ B &= (\varepsilon_{yy} - n_\perp^2)(\varepsilon_{zz} + \alpha^2 + 2\alpha n_\perp) + \varepsilon_{xx}(\varepsilon_{zz} - n_\perp^2 - \beta^2) - 2\beta\varepsilon_{xy}(\alpha + n_\perp), \\ C &= (\varepsilon_{zz} - n_\perp^2)\left[\varepsilon_{xx}(\varepsilon_{yy} - n_\perp^2) + \varepsilon_{xy}^2\right]. \end{aligned} \tag{C.10}$$

Equation C.9 can then be readily solved for $k_\parallel(\omega, k_\perp)$, using the definitions provided by equations C.10 and C.8, without having to resort to numerical methods.

C.3 Comparison of Kinetic Dispersion Relation in Various Limits

We will consider now a plasma with typical LAPD conditions, and compare the various slow wave dispersion relations that have been discussed in the preceding sections. The plasma parameters considered here are similar to the ones in table 5.3.1. We will assume $\lambda_\perp = 4$ cm - this is a little smaller than the values imposed by the RMF antenna, but better for highlighting differences between the various limits of the dielectric. The following three cases are compared:

1. Cold plasma, defined by dispersion 3.19 and plasma dielectric 3.6.

2. Cold ions and warm (kinetic) electrons, defined by dispersion C.6 and plasma dielectric C.5.

3. The exact kinetic solution, given by the determinant of equation C.2 and plasma dielectric C.3.

When $|\zeta_{0,e}| \gg 1$, the electrons can be considered cold[1], whereas for $|\zeta_{0,e}| \sim 1$ the electrons are defined as warm. As $\zeta_{0,e}$ is a function of frequency, some frequencies may satisfy the cold condition while others will not. Figure C.2 shows $|\zeta_{0,e}|$ as a function of frequency. The "exact" solution of $k_{\parallel}(\omega)$ from figure C.1 was used in this calculation. Close to the cutoff frequency ($\omega \sim 2.24\Omega_{Ne}$), the condition $|\zeta_{0,e}| \gg 1$ is satisfied and the cold fluid model is deemed accurate. But for the majority of frequencies considered, it is evident that the cold condition is not satisfied and kinetic theory must be used to describe parallel electron motion.

C.4 Plasma Dispersion Function

The plasma dispersion function $Z(\zeta_{n,s})$ arises in the dielectric tensor when one assumes a Maxwellian velocity distribution of particle species s, and is defined by the following integral expressions:

$$\sqrt{\pi}Z(\zeta_{n,s}) = \begin{cases} \int_{-\infty}^{\infty} \frac{e^{-x^2}}{x-\zeta_{n,s}} dx & \text{for} \quad \mathrm{Im}(\zeta_{n,s}) > 0 \\ \mathcal{P}\int_{-\infty}^{\infty} \frac{e^{-x^2}}{x-\zeta_{n,s}} dx + i\pi e^{-\zeta_{n,s}^2} & \text{for} \quad \mathrm{Im}(\zeta_{n,s}) = 0 \\ \int_{-\infty}^{\infty} \frac{e^{-x^2}}{x-\zeta_{n,s}} dx + 2i\pi e^{-\zeta_{n,s}^2} & \text{for } \mathrm{Im}(\zeta_{n,s}) < 0 \end{cases} , \tag{C.11}$$

where $\mathcal{P}$ is the Cauchy principal value operator [113]. The $i\pi e^{-\zeta_{n,s}^2}$ terms in equation C.11 arise from the analytic continuation of the integral function, which is done by deforming the complex integration path below $\zeta_{n,s}$ [65]. Equation C.11 can alternatively be expressed as:

[1]With the exception of when $\mathrm{Im}\zeta \gg \mathrm{Re}\zeta$, as discussed in section C.4.

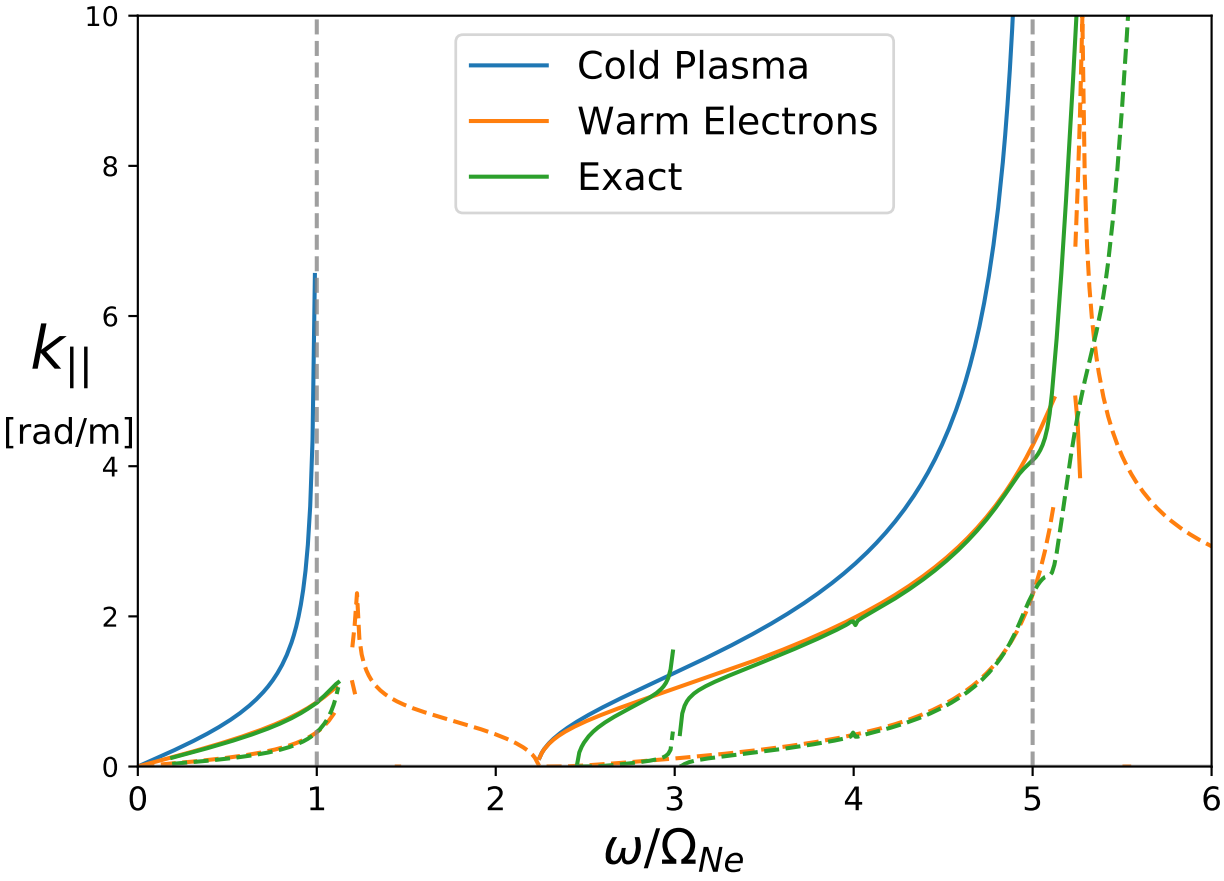

Figure C.1: Comparison of the shear wave dispersion relation resulting from three different plasma models, in a 50% He/ 50% Ne plasma for typical LAPD conditions. The dashed colored lines denote the imaginary part of $k_{||}$ for their respective color. Vertical dashed lines mark the ion cyclotron frequencies.

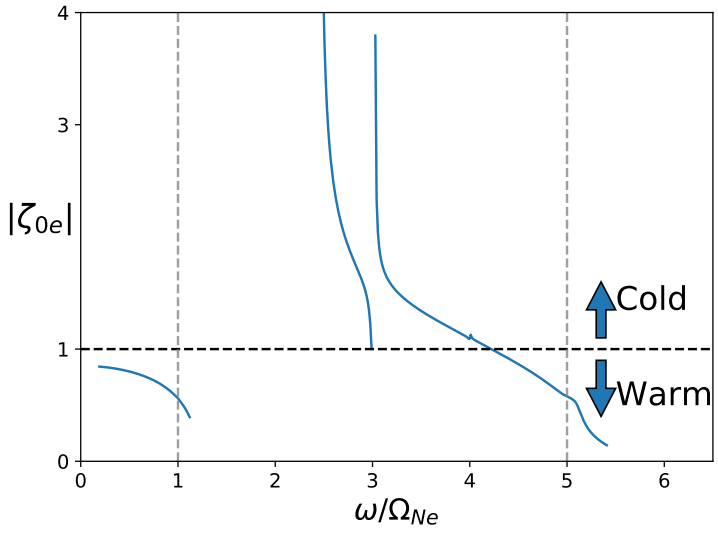

Figure C.2: Plot of $|\zeta_{0,e}|$ vs. frequency, for a 50% He/50% Ne plasma. When $|\zeta_{0,e}| \gg 1$, the cold fluid model of the plasma is valid. Otherwise, warm kinetic electron effects must be considered.

$$Z(\zeta_{n,s}) = i\sqrt{\pi}e^{-\zeta_{n,s}^2}\left[1 - \mathrm{erf}(-i\zeta_{n,s})\right] = e^{-\zeta_{n,s}^2}\mathrm{erfc}(-i\zeta_{n,s}), \tag{C.12}$$

where $\mathrm{erfc}(\zeta_{n,s})$ is the complex error function. Equation C.12 is valid in the entire complex plane, and since the error function is readily available in many standard programming languages[2], equation C.12 is generally more convenient to use for numerical solvers.

For a driven wave with a complex-valued $k_\parallel = k_R + ik_I$, both the real and imaginary parts of $k_\parallel$ will in general be positive, as this corresponds to a forward propagating wave that is damped. When $k_I < k_R$, the plasma dispersion function is well behaved. But consider a frequency where $k_I \gg k_R$. This gives the following value for $\zeta_{0,s}$:

$$\zeta_{0,s} = \frac{\omega}{\sqrt{2}v_{Th,s}(k_R + ik_I)} = \frac{\omega}{\sqrt{2}v_{Th,s}|k_\parallel|^2}(k_R - ik_I). \tag{C.13}$$

[2]For example, ERFC() in IDL, and scipy.special.wofz in the scipy package for python.

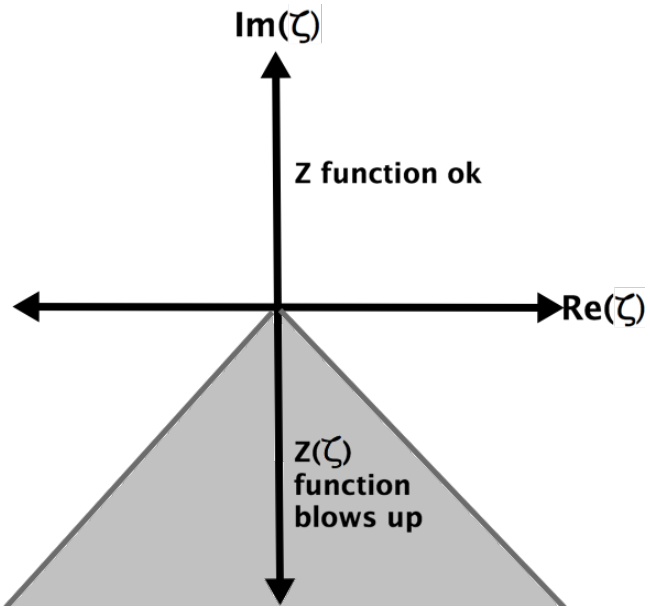

Figure C.3: Diagram of the complex plane of ζ, showing where the plasma dispersion function $Z(\zeta)$ blows up.

For a real-valued frequency, it follows that $\mathrm{Im}(\zeta_{0,s}) < 0$. The exponential in equation C.11 that arises from analytic continuation becomes:

$$e^{-\zeta_{0,s}^2} = e^{A^2(k_I^2 - k_R^2)} e^{i2A^2 k_R k_I}, \tag{C.14}$$

where $A = \omega/\sqrt{2} v_{Th,s} |k_\parallel|^2$. We can immediately see that for $k_I \gg k_R$, the exponential blows up and we run into a serious problem. Unfortunately this problem is not resolved by a situation of "infinities cancelling each other out" when this is plugged into the dielectric terms. What this means is that the fully-generalized kinetic dispersion relation (such as in equation C.3) *cannot* give solutions where $k_I \gg k_R$. The cold fluid model predicts regions of evanescence, where $k_R = 0$. But the "cold" model is predicated on the mathematical assertion that $Z(\zeta) \sim -1/\zeta$ in the limit $|\zeta| \gg 1$. This statement is true when $|\mathrm{Re}(\zeta)| > |\mathrm{Im}(\zeta)|$, but is not valid in regions of the complex plane where this inequality is not satisfied (as can be clearly seen by equation C.14). The implication of this, then, is that the evanescent

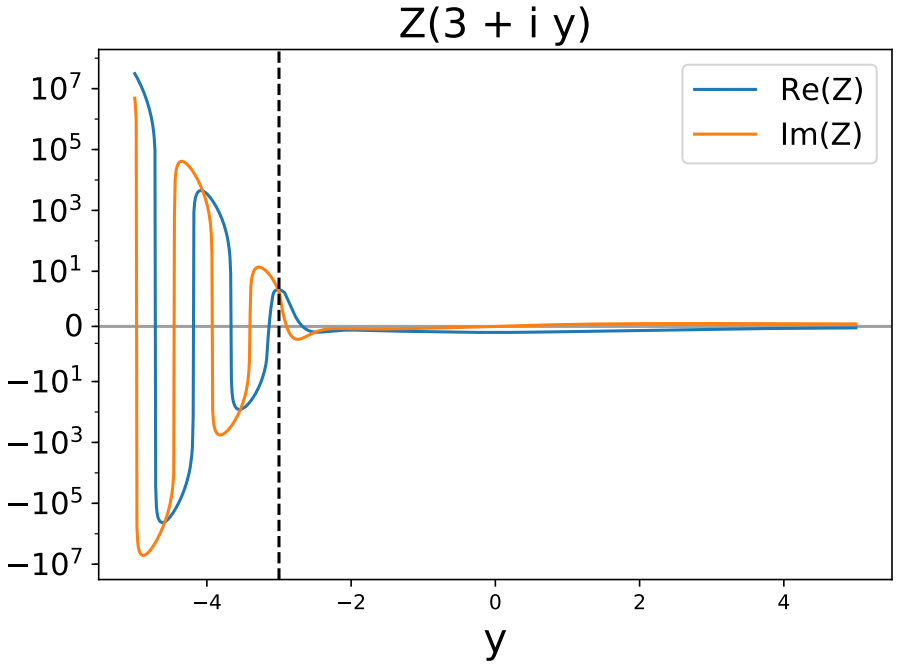

Figure C.4: Plot of $Z(\zeta)$ vs. Imζ for Re$\zeta = 3$, showing how the function blows up when Im$\zeta >$ Reζ (marked by a dashed vertical line).

solutions of the cold model are simply wrong, as the cold limit is naively being applied in a frequency regime where it is technically not valid. More information on numerical methods of computing the plasma dispersion function can be found in [34], or for a more modern treatment see [110].

REFERENCES

[1] Compressional alfvén and ion–ion hybrid waves in tokamak plasmas with two ion species. *Plasma Phys. Control. Fusion*, 56:125017, 2014.

[2] H. Alfvén. Existence of electromagnetic-hydrodynamic waves. *Nature*, 150:405–406, October 1942.

[3] W. P Allis, S. J. Buchsbaum, and A. Bers. *Waves in Anisotropic Plasmas*. The MIT Press, 2003.

[4] B. J. Anderson, R. E. Denton, G. Ho, D. C. Hamilton, S. A. Fuselier, and R. J. Strangeway. Observational test of local proton cyclotron instability in the earth's magnetosphere. *Journal of Geophysical Research*, 101(A10):527–543, October 1996.

[5] B. J. Anderson, R. E. Erlandson, and L. J. Zanetti. A statistical study of Pc1-2 magnetic pulsations in the equatorial magnetosphere: 1. equatorial occurrence distributions. *Journal of Geophysical Research*, 97(A3):3075–3088, March 1992.

[6] B. J. Anderson, R. E. Erlandson, and L. J. Zanetti. A statistical study of pc1-2 magnetic pulsations in the equatorial magnetosphere: 1. wave properties. *Journal of Geophysical Research*, 97(A3):3089–3101, March 1992.

[7] J. M. Anderson and L. Goldstein. Interaction of electromagnetic waves of radio-frequency in isothermal plasmas: Collision cross section of helium atoms and ions for electrons. *Physical Review Letters*, 100(4):1037–1045, June 1955.

[8] D. Arnush and F. F. Chen. Generalized theory of helicon waves. II. excitation and absorption. *Physics of Plasmas*, 5(5), 1998.

[9] W. I. Axford and J. F. McKenzie. The acceleration of the solar wind. *AIP Conference Proceedings*, 382(1):72–75, 1996.

[10] S. D. Baalrud and C. C. Hegna. Determining the Bohm criterion in plasmas with two ion species. *Physics of Plasmas*, 18, February 2011.

[11] D. Baker and S. Lee. Dual laser interferometer for plasma density measurements on large tokamaks. *Review of Scientific Instruments*, 49(7), 1978.

[12] J. W. Belcher and L. Davis Jr. Large amplitude Alfvén waves in the interplanetary medium, 2. *Journal of Geophysical Research*, 76(16):3534–3563, 1971.

[13] A. Boboc, L. Zabeo, A. Murari, and JET Contributors. Simultaneous Cotton-Mouton and Faraday rotation angle measurements on JET. *Review of Scientific Instruments*, 77(10), June 2006.

[14] G. G. Borg, M. H. Brennan, R. C. Cross, L. Giannone, and I. J. Donnelly. Guided propagation of Alfvén waves in a toroidal plasma. *Plasma Physics and Controlled Fusion*, 27(10):1125–1149, 1985.

[15] M. Brambilla. *Kinetic Theory of Plasma Waves: Homogeneous Plasmas*. Oxford University Press, New York, 1998.

[16] S. J. Buchsbaum. Resonance in a plasma with two ion species. *The Physics of Fluids*, 3(3):418–420, January 1960.

[17] F. F. Chen. *Introduction to Plasma Physics and Controlled Fusion*, volume 1. Plenum Press, New York and London, second edition, 1990.

[18] F. F. Chen and D. Arnush. Generalized theory of helicon waves. I. normal modes. *Physics of Plasmas*, 4(9), 1997.

[19] F. F. Chen, G. Dimonte, T. Christensen, G. R. Neil, and T. E. Romesser. Use of the two-ion hybrid as an impurity diagnostic. *The Physics of Fluids*, 29(5):1651–1658, January 1986.

[20] John M. Cornwall. Cyclotron instabilities and electromagnetic emission in the ultra low frequency and very low frequency ranges. *Journal of Geophysical Research*, 70(1):61–69, January 1965.

[21] John M. Cornwall, F. V. Coroniti, and R. M. Thorne. Turbulent loss of ring current protons. *Journal of Geophysical Research*, 75(25):4699– 4709, September 1970.

[22] Rodney Cross. *An Introduction to Alfvén Waves*. Taylor and Francis, first edition, 1988.

[23] Wu Dejin. *Kinetic Alfvén Waves: Theory, Experiment, and Application*. Science Press, 2012.

[24] T. Drozdenko and G. J. Morales. Nonlinear effects resulting from the interaction of a large-scale Alfvén wave with a density filament. *Physics of Plasmas*, 8(7):3265–3276, 2001.

[25] B. Eliasson and K. Papadopoulos. Pitch angle scattering of relativistic electrons near electromagnetic ion cyclotron resonances in diverging magnetic fields. *Plasma Phys. Control. Fusion*, 59(10):104003, 2017.

[26] J. D. Strachan et. al. Deuterium and tritium experiments on tftr. *Plasma Physics and Controlled Fusion*, 36(12B):B3–B15, 1994.

[27] S. D. Scott et. al. Isotope scaling of transport in deuterium-tritium plasmas. *Physica Scripta*, 51(3):394–401, November 1994.

[28] E. T. Everson, P. Pribyl, C. G. Constantin, A. Zylstra, D. Shaeffer, N. L. Kugland, and C. Niemann. Design, construction, and calibration of a three-axis, high frequency magnetic probe (B-dot probe) as a diagnostic for exploding plasmas. *Review of Scientific Instruments*, 80(11), November 2009.

[29] W. A. Farmer and G. J. Morales. Cherenkov radiation of shear Alfvén waves in plasmas with two ion species. *Phys. Plasmas*, 19(9):092109, 2012.

[30] W. A. Farmer and G. J. Morales. The ion-ion hybrid Alfvén resonator in a fusion environment. *Phys. Plasmas*, 21(6):0625707, 2014.

[31] A. Fasoli, D. Testa, S. Sharapov, H. L. Berk, B. Breizman, A. Gondhalekar, R. F. Heeter, and M. Mantsinen. MHD spectroscopy. *Plasma Physics and Controlled Fusion*, 44(12B):B159–172, November 2002.

[32] R. N. Franklin. Plasmas with more than one species of positive ion and the Bohm criterion. *Journal of Physics D: Applied Physics*, 33:3186–3188, May 1990.

[33] B. J. Fraser and T. S. Nguyen. Is the plasmapause a preferred source region of electromagnetic ion cyclotron waves in the magnetosphere? *Journal of Atmospheric and Solar-Terrestrial Physics*, 63(11):1225–1247, 2001.

[34] Burton D. Fried and Samuel D. Conte. *The Plasma Dispersion Function*, volume 1. Elsevier, Inc., 1961.

[35] W. Gekelman, H. Pfister, Z. Lucky, J. Bamber, D. Leneman, and J. Maggs. Design, construction, and properties of the large plasma research device - the LAPD at UCLA. *Review of Scientific Instruments*, 62(12):2875–2883, August 1991.

[36] W. Gekelman, P. Pribyl, Z. Lucky, M. Drandell, D. Leneman, J. Maggs, S. Vincena, B. Van Campernolle, S. K. P. Tripathi, G. Morales, T. A. Carter, Y. Wang, and T. DeHaas. The upgraded large plasma device, a machine for studying frontier basic plasma physics. *Review of Scientific Instruments*, 87(025105), 2016.

[37] W. Gekelman, S. Vincena, B. Van Compernolle, G. J. Morales, J. E. Maggs, P. Pribyl, and T. A. Carter. The many faces of shear Alfvén waves. *Phys. Plasmas*, 18(5):032113, 2011.

[38] W. Gekelman, S. Vincena, D. Leneman, and J. Maggs. Laboratory experiments on shear Alfvén waves and their relationship to space plasmas. *Journal of Geophysical Research*, 102(A4):7225–7236, April 1994.

[39] W. Gekelman, S. Vincena, D. Leneman, and J. Maggs. Laboratory experiments on shear Alfvén waves and their relationship to space plasmas. *Journal of Geophysical Research*, 102(A4):7225–7236, April 1997.

[40] W. Gekelman, S. Vincena, D. Leneman, and J. Maggs. Review of laboratory experiments on Alfvén waves and their relationship to space observations. *Journal of Geophysical Research*, 104(A7):14417–14435, 1999.

[41] A. Gigliotti, W. Gekelman, P. Pribyl, S. Vincena, A. Karavaev, X. Shao, A. Surjalal Sharma, and D. Papadopoulos. Generation of polarized shear Alfvén waves by a rotating magnetic field source. *Physics of Plasmas*, 16(9), September 2009.

[42] A. H. Glasser, C. R. Sovinec, R. A. Nebel, T. A. Gianakon, S. J. Plimpton, M. S. Chu, D. D. Schnak, and the NIMROD team. The NIMROD code: a new approach to numerical plasma physics. *Plasma Physics and Controlled Fusion*, 41(3A), 1999.

[43] A. V. Guglielmi, A. S. Potapov, and C. T. Russell. The ion cyclotron resonator in the magnetosphere. *JETP Letters*, 72(6):298–300, August 2000.

[44] Akira Hasegawa and Kunioki Mima. Anomalous transport produced by kinetic Alfvén wave turbulence. *Journal of Geophysical Research*, 83(A3):1117–1123, March 1978.

[45] W. W. Heidbrink. Basic physics of Alfvén instabilities driven by energetic particles in toroidally confined plasmas. *Physics of Plasmas*, 15(5), February 2008.

[46] W. W. Heidbrink, E. J. Strait, M. S. Chu, and A. D. Turnbull. Observation of beta-induced Alfvén eigenmodes in the DIII-D tokamak. *Physical Review Letters*, 71(6):855–858, August 1993.

[47] J. Hillairet, D. Voyer, A. Ekedahl, M. Goniche, M. Kazda, O. Meneghini, D. Milanesio, and M. Preynas. ALOHA: an advanced lower hybrid antenna coupling code. *Nuclear Fusion*, 50(12), 2010.

[48] J. C. Hillesheim, C. Holland, L. Schmitz, S. Kubota, T. L. Rhodes, and T. A. Carter. 2D full wave modeling for a synthetic Doppler backscattering diagnostic. *Review of Scientific Instruments*, 83(12), 2012.

[49] M. Hirsch, E. Holzhauer, J. Baldzuhn, B. Kurzan, and B. Scott. Doppler reflectometry for the investigation of propagating density perturbations. *Plasma Physics and Controlled Fusion*, 43(12), 2001.

[50] Richard B. Horne. Convective instabilities of electromagnetic ion cyclotron waves in the outer magnetosphere. *Journal of Geophysical Research*, 99(A9):259–273, September 1994.

[51] Y. Hu and R. E. Denton. Two-dimensional hybrid code simulation of electromagneticion cyclotron waves in a dipole magnetic field. *Journal of Geophysical Research*, 114, December 2009.

[52] Y. Hu, R. E. Denton, and J. R. Johnson. Two-dimensional hybrid code simulation of electromagnetic ion cyclotron waves of multi-ion plasmas in a dipole magnetic field. *Journal of Geophysical Research*, 115, December 2010.

[53] S. Ichimaru. *Basic Principles of Plasma Physics: A Statistical Approach*. 2. Statistical Physics. Addison-Wesley, Reading, Massachusetts, second edition, 1980.

[54] H. Ikezi, J. S. deGrassie, R. I. Pinkster, and R. T. Snider. Plasma mass density, species mix, and fluctuations diagnostic using a fast Alfvén wave. *Review of Scientific Instruments*, 68(1):478–479, 1996.

[55] J. D. Jackson. *Classical Electrodynamics*, volume 1. John Wiley and Sons, Inc., first edition, 1962.

[56] E. F. Jaeger, L. A. Berry, J. S. Tolliver, and D. B. Batchelor. Power deposition in high-density inductively coupled plasma tools for semiconductor processing. *Physics of Plasmas*, 2(6), 1995.

[57] JET. Fusion energy production from a deuterium-tritium plasma in the JET tokamak. *Nuclear Fusion*, 32(2):187–203, 1992.

[58] P. J. Coleman Jr. Hydromagnetic waves in the interplanetary plasma. *Physical Review Letters*, 17(4):207–211, July 1966.

[59] P. J. Coleman Jr. Wavelike behavior in the interplanetary plasma: Mariner 2. *Planetary and Space Science*, 15(6):953–973, June 1967.

[60] A. V. Karavaev, N. A. Gumerov, K. Papadopoulos, X. Shao, A. S. Sharma1, W. Gekelman, Y. Wang, B. Van Compernolle, P. Pribyl, and S. Vincena. Generation of shear Alfvén waves by a rotating magnetic field source: Three-dimensional simulations. *Physics of Plasmas*, 2011.

[61] C. A. Kletzing, D. J. Thuecks, F. Skiff, S. R. Bounds, and S. Vincena. Measurement of inertial limit Alfvén wave dispersion for finite perpendicular wave number. *Physical Review Letters*, 104(9), 2010.

[62] R. A. Koch and Wendell Horton. Effects of electron angle scattering in plasma waves. *The Physics of Fluids*, 18(7):861–865, January 1975.

[63] A. M. Kolmogorov. The local structure of turubulence in incompressible viscous fluids for very large Reynolds numbers. *Proceedings of the Royal Society A*, 434(1890):9–13, July 1991.

[64] V. Lancellotti, D. Milanesio, R. Maggiora, G. Vecchi, and V. Kyrytsya. TOPICA: an accurate and efficient numerical tool for analysis and design of ICRF antennas. *Nuclear Fusion*, 46(7), 2006.

[65] L. Landau. On the vibration of the electronic plasma. *Journal of Experimental and Theoretical Physics*, 10(25), 1944.

[66] Dongsoo Lee, Lutfi Oksuz, and Noah Hershkowitz. Exact solution for the generalzed Bohm criterion in a two-ion-species plasma. *Physical Review Letters*, 99, October 2007.

[67] S. Lundquist. Experimental investigations of magneto-hydrodynamic waves. *Physical Review Letters*, 76(12):1805–1809, August 1949.

[68] A. Messiaen, R. Koch, R. R. Weynants, P. Dumortier, F. Louche, R. Maggiora, and D. Milanesio. Performance of the ITER ICRH system as expected from TOPICA and ANTITER II modelling. *Nuclear Fusion*, 50(2), 2010.

[69] D. Milanesio, O. Meneghini, V. Lancellotti, R. Maggiora, and G. Vecchi. A multi-cavity approach for enhanced efficiency in TOPICA RF antenna code. *Nuclear Fusion*, 49(11), 2009.

[70] Kyungguk Min, Jeongwoo Lee, Kunihiro Keika, and Wen Li. Global distribution of EMIC waves derived from THEMIS observations. *Journal of Geophysical Research*, 117(A5), May 2012.

[71] C. Mitchell, S. Vincena, J. Maggs, and W. Gekelman. Laboratory observation of Alfvén resonance. *Journal of Geophysical Research*, 28(5):923–926, 1999.

[72] G. J. Morales, R. S. Loritsch, and J. E. Maggs. Structure of Alfvén waves at the skin-depth scale. *Physics of Plasmas*, 1(12):3765–3774, August 1994.

[73] G. J. Morales and J. E. Maggs. Structure of kinetic Alfvén waves with small transverse scale length. *Physics of Plasmas*, 4(11):4118–4125, July 1997.

[74] H. Ogata. A numerical integration formula based on the bessel functions. *Publications of the Research Institute for Mathematical Sciences*, 41(4), 2005.

[75] M. Ono. Cold, electrostatic ion-cyclotron waves and ion-ion hybrid resonances. *Physical Review Letters*, 42(19):1267–1270, May 1979.

[76] F. W. Perkins. Heating tokamaks via the ion-cyclotron and ion-ion hybrid resonances. *Nuclear Fusion*, 17(6):1197–1224, 1977.

[77] S. Perraut, R. Gendrin, A. Roux, and C. de Villedary. Ion cyclotron waves: Direct comparison between ground-based measurements and observations in the source region. *Journal of Geophysical Research*, 89(A1):195–202, January 1984.

[78] A. K. Ram and K. Hizanidis. Scattering of radio frequency waves by cylindrical density filaments in tokamak plasmas. *Physics of Plasmas*, 23(2), 2016.

[79] C. Riccardi, M. Fontanesi, A. Galassi, and E. Sindoni. Plasma diagnostic through ion bernstein waves. *Il Nuovo Cimento*, 16(5):505–515, May 1994.

[80] K-U Riemann. The Bohm criterion and sheath formation. *Journal of Physics D: Applied Physics*, 24:493–518, December 1990.

[81] A. Roux, S. Perraut, J. L. Rauch, and C. de Villedary. Wave-particle interactions near Ω_{He^+} observed on board GEOS 1 and 2: 2. generation of ion cyclotron waves and heating of He^+ ions. *Journal of Geophysical Research*, 87(A10):8174–8190, October 1982.

[82] D. A. Schaffner, T. A Carter, G. D. Rossi, D. S. Guice, J. E. Maggs, S. Vincena, and B. Friedman. Modification of turbulent transport with continuous variation of flow shear in the large plasma device. *Physical Review Letters*, 109(13), 2012.

[83] J. E. Scharer, B. D. McVey, and T. K. Mau. Fast wave ion-cyclotron and first-harmonic heating of tokamaks. *Nuclear Fusion*, 17(2):297–304, 1977.

[84] G. Schmidt. *Physics of High Temperature Plasmas*. Academic Press, "second" edition, 1979.

[85] J. P. M. Schmitt. Dispersion and cyclotron damping of pure ion Bernstein waves. *Physical Review Letters*, 31(16):982–985, April 1973.

[86] S. E. Segre. Plasma polarimetry for large Cotton-Mouton and Faraday effects. *Physics of Plasmas*, 2(8):2908–2914, April 1995.

[87] X. Shao, K. Papadopoulos, and A. S. Sharma. Control of the energetic proton flux in the inner radiation belt by artificial means. *Journal of Geophysical Research*, 114, July 2009.

[88] S. Shiraiwa, J. C. Wright, P. T. Bonoli, T. Kolev, and M. Stowell. RF wave simulation for cold edge plasmas using the MFEM library. *EPJ Web of Conference*, 157(03048), 2017.

[89] M. M. Shoucri and G. J. Morales. Generation of Alfvén waves caused by thermal modulation of the electrical conductivity. *The Physics of Fluids*, 28(8):2458–2465, 1985.

[90] A. P. Smirnov. The GENRAY ray tracing code. Technical report, Moscow State University, 2003.

[91] D. E. Smith and E. J. Powers. Experimental determination of the spectral index of a turbulent plasma from digitally computed power spectra. *Physics of Fluids*, 16:1373–1374, 1973.

[92] R. L. Smith and Neil Brice. Propagation in multi-component plasmas. *Journal of Geophysical Research*, 69(23):5020–5040, December 1964.

[93] T. H. Stix. *The Theory of Plasma Waves*. McGraw-Hill, 1962.

[94] D. Summers and R.M. Thorne. Relativistic electron pitch-angle scattering by electromagnetic ion cyclotron waves during geomagnetic storms. *J. Geophys. Res.*, 108:1143, 2003.

[95] D. G. Swanson. *Theory of Mode Conversion and Tunneling in Inhomogeneous Plasmas*. John Wiley and Sons, Inc., New York, New York, first edition, 1998.

[96] D. G. Swanson. *Plasma Waves*. Academic Press, 2012.

[97] Richard M. Thorne, Richard B. Horne, Vania K. Jordanova, Jacob Bortnik, and Sarah Glauert. Interaction of EMIC waves with thermal plasma and radiation belt particles. *Magnetospheric ULF Waves: Synthesis and New Directions*, 169:213–223, 2006.

[98] L. V. Tverskaya. Dynamics of the earth's radiation belts. *Moscow University Physics*, 65(4):246–251, November 2009.

[99] Theodore W. J. Unti and Marcia Neugebauer. Alfvén waves in the solar wind. *The Physics of Fluids*, 11(3):563–568, March 1968.

[100] S. Vincena. *Propagation of the Shear Alfvén Wave from a Skin Depth Scale Source into Nonuniform Plasmas*. PhD dissertation, University of California, Los Angeles, Department of Physics, 1999.

[101] S. T. Vincena, W. A. Farmer, J. E. Maggs, and G. J. Morales. Laboratory realization of an ion-ion hybrid Alfvén wave resonator. *Geophysical Research Letters*, 38, 2011.

[102] S. T. Vincena, W. A. Farmer, J. E. Maggs, and G. J. Morales. Investigation of an ion-ion hybrid Alfvén wave resonator. *Physics of Plasmas*, 20(1), December 2013.

[103] S. T. Vincena, G. J. Morales, and J. E. Maggs. Effect of two ion species on the propagation of shear Alfvén waves of small transverse scale. *Physics of Plasmas*, 17(5), April 2010.

[104] Y. Wang, W. Gekelman, P. Pribyl, and K. Papadopoulos. Scattering of magnetic mirror trapped fast electrons by a shear Alfvén wave. *Physical Review Letters*, 108(10), March 2012.

[105] Y. Wang, W. Gekelman, P. Pribyl, and K. Papadopoulos. Enhanced loss of magnetic-mirror-trapped fast electrons by a shear Alfvén wave. *Physics of Plasmas*, 21(5), May 2014.

[106] G. W. Watson, W. W. Heidbrink, K. H. Burrell, and G. J. Kramer. Plasma species mix diagnostic using ion-ion hybrid layer reflectometry. *Plasma Physics and Controlled Fusion*, 46:471–487, February 2004.

[107] R. B. White, E. Fredrickson, D. Darrow, M. Zarnstroff, R. Wilson, S. Zweben, K. Hill, Yang Chen, and Guoyong Fu. Toroidal Alfvén eigenmode-induced ripple trapping. *Physics of Plasmas*, 2(8), April 1995.

[108] C. S. Wu. Alfvén waves in the solar wind. *Physica Scripta*, T60:91–96, July 1995.

[109] Hong Xie and Leon Ofman. Multiple ions resonant heating and acceleration by Alfvén/cyclotron fluctuations in the corona and the solar wind. *Journal of Geophysical Research*, 109, August 2004.

[110] Hua-Sheng Xie. Generalized plasma dispersion function: One-solve-all treatment, visualizations, and application to landau damping. *Physics of Plasmas*, 20(9), September 2013.

[111] D. T. Young, S. Perraut, A. Roux, C. de Villedary, R. Gendrin, A. Korth, G. Kremser, and D. Jones. Wave-particle interactions near Ω_{He^+} observed on GEOS 1 and 2: 1. propagation of ion cyclotron waves in He^+-rich plasma. *Journal of Geophysical Research*, 86(A8):6755–6772, August 1981.

[112] Andrew Zangwill. *Modern Electrodynamics*. Cambridge University Press, New York, first edition, 2012.

[113] Dennis G. Zill and Patrick D. Shanahan. *Complex Analysis: A first Course with Applications*. Jones and Bartlett Learning, 2015.